Regional Climate Modelling over Europe at Glacial Times

Inauguraldissertation

der Philosophisch–naturwissenschaftlichen Fakultät
der Universität Bern

vorgelegt von

Patricio Andrés Velásquez Álvarez

von Iquique, Chile

Leiter der Arbeit:

Prof. Dr. Christoph C. Raible

Abteilung für Klima– und Umweltphysik
Physikalisches Institut der Universität Bern

Regional Climate Modelling over Europe at Glacial Times

Inauguraldissertation

der Philosophisch–naturwissenschaftlichen Fakultät
der Universität Bern

vorgelegt von

Patricio Andrés Velásquez Álvarez

von Iquique, Chile

Leiter der Arbeit:

Prof. Dr. Christoph C. Raible

Abteilung für Klima– und Umweltphysik
Physikalisches Institut der Universität Bern

Von der Philosophisch–naturwissenschaftlichen Fakultät angenommen.

Der Dekan

Bern, 23. August 2021 Prof. Dr. Zoltan Balogh

Thesis summary

The climate on Earth has continuously fluctuated throughout the world's history under the influence of internal and external forcing factors. A key challenge for climate science is the understanding of the different drivers and mechanisms that define the climate of the past and its fluctuations. Glacial climate states are of great interest in climate research as their conditions are highly different compared to today's climate. Climate modelling functions as a complementary tool to further investigate the role of forcing factors such as surface conditions in glacial climates. Global climate models are used to describe the Earth's system; however, they show wide disagreement when simulating the climate of the past over the continents. This disagreement may be related to a variety of factors, including the coarse model resolution and an incomplete representation of Earth system processes. The application of regional climate models improves the representation of these processes due to their higher spatial resolution. Still, the accuracy of the simulated regional climate strongly depends on the representation of the surface conditions in the models. Even though the surface conditions become more realistic, deviations can still be evident in the simulations, especially in precipitation. These biases may impact the results obtained through hydrological and glacier modelling that follows next in the modelling chain. Accordingly, the central goal of this thesis is to investigate the role of the glacial surface conditions in the European glacial climate using the regional climate model WRF. Two studies are carried out to achieve this central goal. An additional study presents a method to adjust deviations in simulated precipitation at glacial times, e.g., the simulated precipitation of the previous two studies.

The first study assesses the importance of resolution and land–atmosphere feedbacks on the climate of Europe. To that end, a more accurate glacial land cover is generated using an asynchronous coupled land–atmosphere modelling experiment that combines a global climate model, a regional climate model, and a dynamic vegetation model. The regional climate and land cover models are run at high (18 km) resolution. The asynchronous coupling shows that the land–atmosphere coupling achieves quasi-equilibrium after four iterations. Simulated climate and land cover agree reasonably well with independent reconstructions based on paleoenvironmental proxies. This study determines the importance of land cover on the climate of Europe at the Last Glacial Maximum (LGM) using a sensitivity simulation with an LGM climate but present-day land cover. Results show that the LGM land cover leads to colder and drier summer conditions around the Alps and warmer and drier climate in southeastern Europe. This finding does not only demonstrate that LGM land cover plays an important role

in regulating the regional climate, but it also indicates the need of using realistic glacial land cover estimates to accurately simulate the regional glacial climate.

The second study investigates the sensitivity of the glacial Alpine hydro-climate to northern hemispheric and local ice-sheet changes. Therefore, sensitivity simulations are carried out with a 2 km horizontal resolution over the Alps for the LGM and the Marine Isotope Stage 4 (MIS4). During winter, the findings show wetter conditions in the southern part of the Alps under LGM conditions compared to present day. This wetting can be traced back to dynamical processes, i.e., changes in the wind speed and direction. In summer, drier conditions are found in most of the Alpine region during LGM. These drier conditions can be attributed to thermodynamic processes, i.e., lower temperatures. The MIS4 climate shows enhanced winter precipitation compared to the LGM, which is explained by its warmer climate compared to the LGM, i.e., by thermodynamics. An increase of the northern hemispheric ice-sheet thickness leads to a significant intensification of glacial Alpine hydro-climate conditions, which is mainly explained by dynamical processes. Changing only the Fennoscandian ice sheet is less influential on the Alpine precipitation, whereas modifications in the local Alpine ice-sheet topography significantly alter the Alpine precipitation. These findings demonstrate that the northern hemispheric and local ice-sheet topography are of great importance at regulating the Alpine hydro-climate.

The third study presents a new correction method for precipitation over complex terrain that explicitly considers orographic characteristics. This method offers a good alternative to the standard empirical quantile mapping (EQM) method during colder climate states, in which the orography strongly deviates from the present-day state, e.g., at the LGM. The new method and its performance are presented for Switzerland using regional climate model simulations at 2 km resolution for present day and LGM conditions. In present-day conditions, the comparison between simulations and observations shows a strong seasonality and, especially during colder months, a height dependence of the bias in precipitation. The new method is able to fully correct the seasonal precipitation bias induced by the global climate model. A rigorous temporal and spatial cross-validation with independent data exhibits robust results. The application of the new bias-correction method to the LGM demonstrates that it is a more appropriate correction compared to the standard EQM under highly different climate conditions as the latter imprints present-day orographic features into the LGM climate.

The last chapter of this thesis is dedicated to highlight some key results of the studies of this thesis and to outline possible follow-up studies and potential benefits for other studies and the scientific community.

Contents

Chapter 1

Introduction

Changes in the climate become an interesting topic for the scientific community as they influence the human behaviour, e.g., they force humans to adapt. Climate sciences aim at understanding the different drivers and mechanisms that define the climate and its fluctuations under past, present and future conditions. In climate sciences, the climate of the past plays a key role as it provides information about the climate response to particular forcing factors. This serves as a basis for the analysis of changes in the present day and future climate. Climate scientists have demonstrated that the Earth's climate has experienced a large range of climate changes on different temporal and spatial scales throughout the world's history. Cold and warm periods are prominent indicators of these changes. For example in the Common Era, the last important warm and cold periods were the Medieval Warm Period (900–1300 AD) and the Little Ice Age (1400–1800 AD), respectively. Further back in time, there are even stronger changes in the climate. For instance, a warm period is the Holocene Thermal Maximum (9 to 5 ka, Wanner et al., 2008; Renssen et al., 2009) and a cold period is the Last Glacial Maximum (LGM, 21 ka; Clark et al., 2009). Focusing on the cold periods, the Little Ice Age was produced by a decreased solar incoming radiation and a high volcanic activity and it affected the Northern Hemisphere continents more strongly compared to the rest of the world (Mann et al., 2009). The LGM had a different setting of the Earth's orbital parameters and atmospheric composition. These orbital changes resulted in very cold conditions and thus led to the growth of extensive continental ice sheets, especially in the Northern Hemisphere. This produced the global sea-level drop of about 120 m compared to present day (Clark et al., 2009).

In this thesis, a regional climate model is used to increase the understanding of the European climate at glacial times. Particularly, this thesis investigates the role of the surface conditions in the climate response during the LGM and the Marine Isotope Stage 4 (MIS4, 65 ka). This thesis also presents a technique that adjusts deviations and thus makes the climate information more reliable in climate states when the topography strongly changed compared to today. Hence, this chapter provides a general introduction to the climate system, its modes of variability, the land-atmosphere interaction, the hydrological cycle and the forcing factors. Also, this chapter presents an overview of the different techniques to reconstruct the

climate of the past and the major features that define the LGM and MIS4. The research questions and the outline of this thesis are presented at the end of this chapter.

1.1 Climate System

Climate is usually defined as the *average weather* or the statistical description of important quantities in terms of the mean and its variability over a certain period and a particular area. In a broader sense, climate can also refer to the state of the entire climate system (IPCC, 2007, 2013a). The Earth's climate system consists of five major components: the atmosphere, the hydrosphere, the cryosphere, the land surface, and the biosphere. These components constantly interact with each other interchanging energy, mass and momentum (IPCC, 2001, 2007, 2013a). Hence, they build a complex coupled system, where a change in one component directly results in adjustments of the other components. The climate system's components are outlined in the following subsections and summarised in Fig. 1.1.

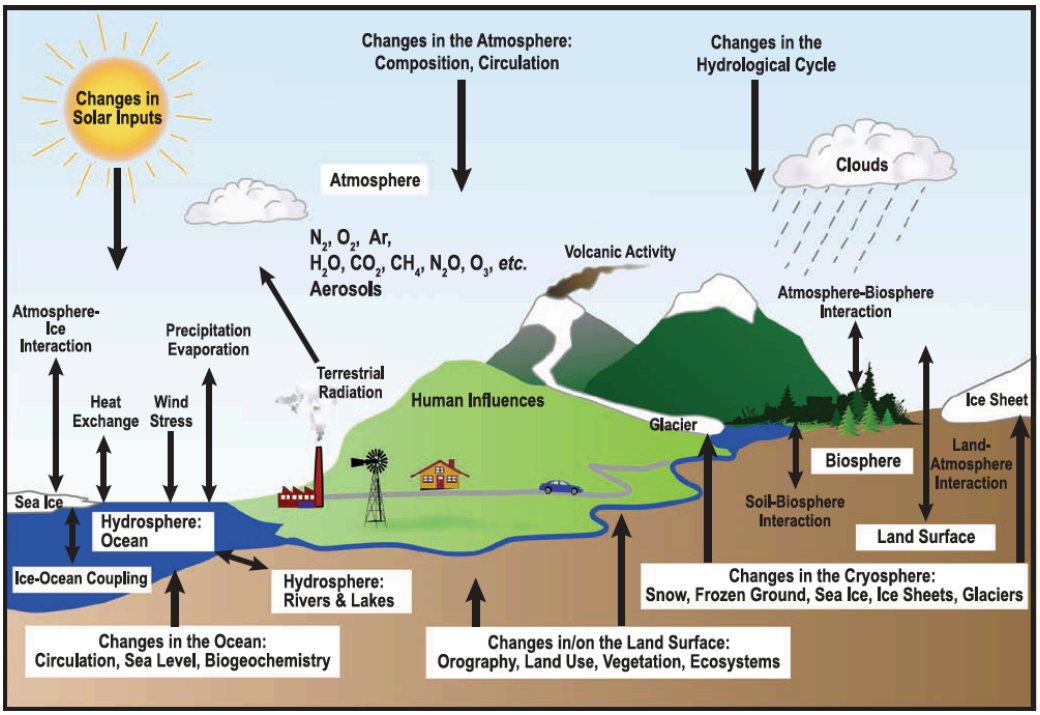

Figure 1.1: Schematic view of the components of the climate system, their processes and interactions. Source: FAQ 1.2, Fig. 1 from IPCC (2007).

The single major energy source of the Earth's climate system is the incoming short-wave radiation from the Sun. In the present-day climate system, the incoming solar radiation is approximately 340 Wm^{-2}, from which only 100 Wm^{-2} is reflected back to the space (Hartmann et al., 2013; Wild et al., 2013). The rest of this incoming radiation is absorbed and distributed across the globe. Around 239 Wm^{-2} from the incoming radiation is compensated by long-wave (infrared) outgoing radiation (Wild et al., 2013), which gives only 0.6 Wm^{-2} for the Earth's energy budget (Fig. 1.2; Loeb et al., 2009; Hansen et al., 2011). Note that the Earth's energy

budget is referred to the balance between the energy that Earth receives from the Sun and radiates back into outer space after having been distributed throughout the components of the climate system. An equilibrium in the energy balance is never reached as various types of variability shape and modify the radiation balance (the so-called forcing). The amount of incoming solar radiation can change through variations in the Earth's orbit or in solar activity. The amount of radiation that is reflected back to the space can be also modified by changes in clouds, atmospheric particles, ice coverage, land use and vegetation (Fig. 1.2). Outgoing, i.e., towards the space, infrared radiation can be influenced by changes in the atmospheric composition, i.e., different concentration of disposing and absorbing species (IPCC, 2013b). Radiative balance over oceans can be modified by natural internal variability, i.e., alterations in the uptake or release of heat by the ocean. Remarkable examples of climate forcing are not only natural phenomena such as changes in the orbital parameters and volcanic eruptions, but also anthropogenic phenomena such as the human-induced changes in the atmospheric composition in the recent past (IPCC, 2013b; Nisbet et al., 2019).

1.1.1 Atmosphere

The atmosphere is a thin gaseous layer surrounding the Earth that mainly consists of diatomic nitrogen (N_2) with a volume mixing ratio of 78.08 %, oxygen (O_2) with a volume mixing ratio of 20.95 %, argon (Ar) with a volume mixing ratio of 0.93 %, and many other trace gases and small particles (Wallace and Hobbs, 2006). The atmosphere is the least stable component of the climate system; also, it experiences the most rapidly changes compared to the other components (IPCC, 2001, 2007). The most variable element of the atmosphere is water (H_2O) in its various phases such as vapour, cloud droplets, and ice crystals. The transition between these phases is a key role in the climate system and its variability as this transition absorbs and releases much energy influencing air temperature and motion. A considerable amount of water vapour exists in the atmosphere (1–4 % volume mixing ratio), which together with some trace gases such as ozone (O_3) play a crucial role in the Earth's life as they absorb solar radiation in several wavelengths. Especially, ozone absorbes solar radiation in wavelengths that can be lethal for the terrestrial biosphere (less than 290 nm; fifth chapter of Wallace and Hobbs (2006), and second chapter of Rowland (2009)). Additionally, water vapour, carbon dioxide (CO_2), methane (CH_4), nitrous oxide (N_2O), O_3 and chlorofluorocarbons are very important in the global energy balance as they can absorb and scatter radiation (Wallace and Hobbs, 2006; IPCC, 2013b). In particular, water vapour and these trace gases are known as greenhouse gases (GHGs), since they are highly effective in trapping the infrared radiation. This trapped radiation is the result of the difference between the energy emitted back to the space and the emitted energy by the surface (Raval and Ramanathan, 1989). The trapped radiation results in an atmospheric temperature increase of around 33 K (Mitchell, 1989), which is one important basement for the development of life on Earth.

Besides the gaseous elements, the atmosphere also contains small particles that are suspended in the air, the so-called aerosols. They influence the global energy balance, since they

can considerably absorb and scatter radiation. Aerosols from volcanic eruptions such as sulphur dioxide (SO_2) and volcanic dust reflect some of the incoming solar radiation and, thus resulting in a negative forcing, i.e., in a decrease of the atmospheric temperature (IPCC, 2013b; Tomasi et al., 2017). Some species such as black carbon and dust are highly effective in absorbing radiation in different wavelengths, which is then emitted back as infrared radiation increasing the atmospheric temperature (Tomasi et al., 2017). Dust, marine and human-produced aerosols influence clouds properties and their formation mechanisms. This does not only affect the precipitation processes and the hydrological cycle (e.g., Casazza et al., 2018; Dave et al., 2019; Zhao et al., 2019), but also their capacity of absorbing and reflecting radiation (e.g., Rosenfeld et al., 2019; Christensen et al., 2020; Zhang et al., 2020). Consequently, any change in the atmospheric concentration of the such as GHGs or aerosols, e.g., through natural or anthropogenic sources, directly impacts the global radiation balance and thus alters the Earth's energy budget.

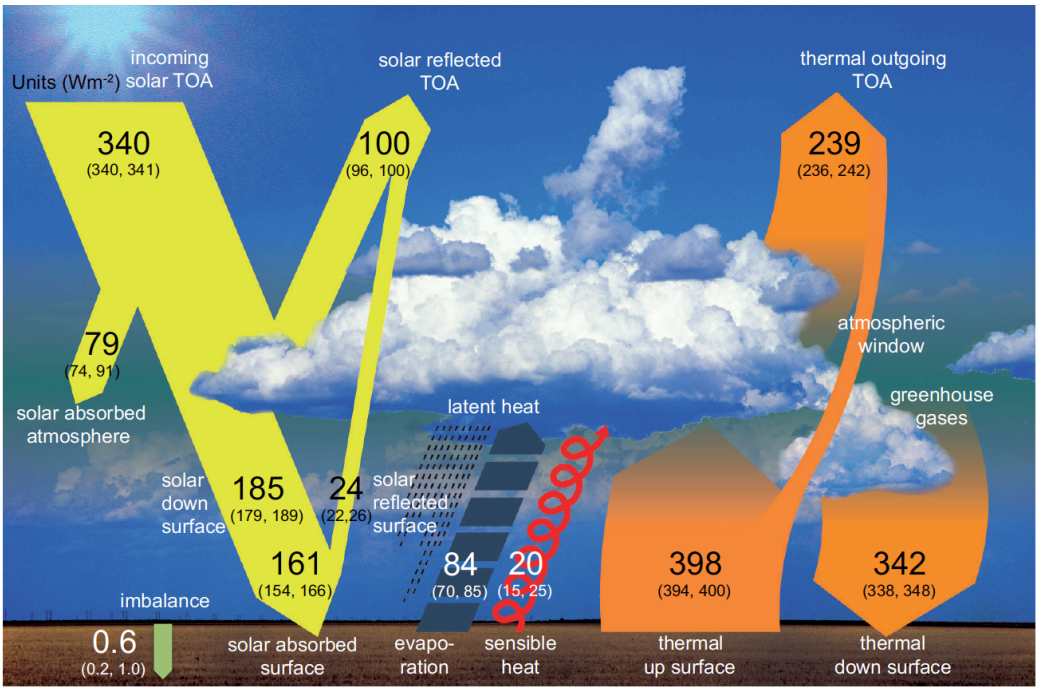

Figure 1.2: Schematic view of the global mean energy budget under present-day climate conditions. Numbers state magnitudes of the individual energy fluxes in Wm^{-2}, adjusted within their uncertainty ranges to close the energy budgets. Numbers in parentheses attached to the energy fluxes cover the range of values in line with observational constraints (Adapted from Wild et al., 2013). Source: Figure 2.11 from IPCC (2013b).

1.1.2 Hydrosphere

The hydrosphere comprises the total amount of liquid surface and subterranean water and both fresh and saline water. The fresh water includes rivers, lakes and aquifers, and the saline water oceans and seas (IPCC, 2001, 2007). Most of the water is stored in the oceans (∼97 %) which cover around 70 % of the Earth's surface. The oceans also store a large amount of energy that is redistributed across the global ocean basins through its circulation. This

circulation is rather slow, compared to the one of the atmosphere, and commonly consists of two parts: a wind-driven circulation that governs the uppermost layer (topmost few hundred meters), and a density-driven circulation that dominates below (the so-called thermohaline circulation). The latter is due to density differences that are produced by thermal and salinity gradients within the ocean (Wyrtki, 1961; Toggweiler and Key, 2001).

The oceans play an important role in regulating the atmospheric concentration of CO_2 as they are able to take up CO_2 from the atmosphere, redistribute it and; inversely, they can also release it back to the atmosphere (IPCC, 2019b). The oceans also function as regulator of the global air temperature as they can damp strong temperature changes due to their large heat capacity (Wallace and Hobbs, 2006) and their large overturning times (from several hundred to thousand years; Primeau, 2005). This consequently acts as a climate regulator and as a source of natural climate variability (IPCC, 2001).

1.1.3 Cryosphere

The cryosphere includes the frozen water part of the Earth system at and below the land and ocean surface. This includes snow cover, glaciers, ice sheets, ice shelves, icebergs, sea ice, lake ice, river ice, permafrost and frozen ground (IPCC, 2007, 2019b). Some parts of the cryosphere such as snow and ice on lakes exist only during colder months, especially in mid-latitude locations. Other parts of the cryosphere such as glaciers and ice sheets stay frozen much longer, not only throughout the year, but also from thousands to even hundreds of thousands of years. The largest parts of the cryosphere are the ice sheets covering around 10 % of Earth's land surface (e.g., the Greenland and Antarctic ice sheets).

The cryosphere influences the climate system through a variety of effects. Cryosphere's surface importantly contributes to the reflectivity of solar radiation (albedo effect; IPCC, 2001, 2019b). This capacity of reflecting can be modified by the deposition of some absorbing natural and human-produced aerosols such as dust and black carbon, respectively. The cryosphere also influences the global sea level as its large content of frozen water can melt and thus be discharged into the oceans (IPCC, 2001; Church et al., 2013). This particularly happens in warmer conditions as the melting becomes more important than the formation of frozen water. Variations in the global sea level directly impact the global capacity of reflecting solar radiation. The reason is that these changes modify the amount of global land surface coverage which has a different albedo compared to the oceans. Thus, the global radiation balance can be affected by a higher amount of deposited absorbing species on the cryosphere and by a global sea level rise, which can directly alter the Earth's energy budget (IPCC, 2019b). Additionally, the cryosphere inhibits ocean-atmosphere exchange of heat (low thermal conductivity; Wallace and Hobbs, 2006), momentum (large inertia) and gases (including CO_2) when it covers large water bodies such as oceans. The global ocean circulation that is mainly driven by density gradients can be also influenced by the cryosphere, since melting and formation of frozen water can modify these gradients. Compared to the surrounding water, melting at the border of the ice

sheets forms fresh water that is less dense and the formation of sea ice crystals produces salty water that is more dense (Wyrtki, 1961; Clark et al., 2002; IPCC, 2019b).

1.1.4 Land Surface

The Earth's land surface is an active and complex place at the interface of the lithosphere, the hydrosphere, the atmosphere, and the biosphere (Phillips, 1999). It covers about 29 % of the Earth's surface and its processes refer to various biogeophysical and biogeochemical processes that also interact with atmospheric processes (Niu and Zeng, 2012). The land surface is often considered as a static component as it changes very slowly compared to the other components of the climate system (Gettelman and Rood, 2016).

The land surface plays a central role in controlling the amount of solar radiation that is returned back to the atmosphere (IPCC, 2001). Part of this incoming radiation is directly reflected back (albedo-effect), which strongly depends on the vegetation cover at the surface and on seasonal factor such as snow or ice during wintertime (IPCC, 2019a). For instance, desert areas reflect more radiation than forests; however, the albedo of the latter can be increased even more than desert areas when it is covered by snow during wintertime. Some of this solar radiation is also sent back as infrared radiation which heats the atmosphere. In addition, the shape and the roughness of the land surface can influence the ocean and the atmosphere, respectively. The shape determines the geometry of the oceans affecting the patterns of their circulation (Gettelman and Rood, 2016). Roughness influences the atmosphere dynamically as winds blow over it. This cannot only blow dust from the surface into the air, i.e., dust aerosols, modifying the atmospheric capacity of reflecting and dispersing radiation (IPCC, 2019a), but also influence the atmospheric circulation and thus the precipitation patterns. For instance, an air parcel would rise when facing a orographical barrier and its water content could condense forming clouds and producing rainfalls (orographic precipitation). The same air parcel becomes dry when flowing down the opposite flunk resulting in dissipation of cloud or low-precipitation (the so-called rain-shadow effect).

1.1.5 Biosphere

The biosphere is defined as the part of the Earth's system that comprises all ecosystems and living organisms in the atmosphere, on land (terrestrial biosphere) or in the oceans (marine biosphere). This also includes derived dead organic matter, such as litter, soil organic matter and oceanic detritus (Hutchinson, 1970; Gettelman and Rood, 2016; IPCC, 2007). The biosphere influences fluxes of energy, water and aerosols between the Earth surface and atmosphere. It is also central to the biogeochemistry of our planet (Overpeck et al., 2003).

The biosphere has a major impact on the atmosphere's composition. It regulates the water in the soil through uptake into plant structures and release water into the atmosphere (e.g., through evapotranspiration). This has an effect on the atmospheric water content, which does not only influences precipitation processes, but also the atmospheric capacity of reflecting

and dispersing radiation (as explained in Sect. 1.1.1). The biosphere influences the uptake and release of greenhouse gases and also plays a central role in the carbon cycle, as well as in the budgets of many other gases such as methane and nitrous oxide (Overpeck et al., 2003). Marine and terrestrial plants, especially forests, store significant amounts of carbon from carbon dioxide through the photosynthetic process (Overpeck et al., 2003). This effect (carbon storage) is particularly important as the influence of climate on the biosphere is preserved as fossils, tree rings, pollen and other records, so that much of what is known of past climates comes from such biotic indicators (IPCC, 2001; Wallace and Hobbs, 2006). The biosphere also influences the surface radiation balance as its capacity of absorbing and reflecting radiation depends on changes in vegetation cover fraction (IPCC, 2001). Consequently, any change in the biosphere, e.g., through natural or anthropogenic causes, directly impacts the global radiation balance and thus alters the Earth's energy budget.

1.2 Present Climate

1.2.1 Planetary Atmospheric Circulation

The planetary atmospheric circulations describes the air movement on the Earth. The description assumes the air to behave as a fluid. Thus, the air movement can be described using the thermodynamical and hydrodynamical laws of fluids, i.e, the laws of conversation of momentum, energy and mass. The atmospheric motion is triggered by the following forces: gravity, pressure gradient, surface friction, Coriolis and centrifugal. The latter two are known as pseudo forces as they emerge from the rotation of the Earth. Therefore, considering these forces and other assumptions, the atmospheric motion can be formulated as follows (Holton and Hakim, 2013):

$$\underbrace{\frac{d\vec{v}}{dt}}_{\text{A}} = \underbrace{-\frac{1}{\rho}\vec{\nabla}p}_{\text{B}} + \underbrace{\vec{g}}_{\text{C}} - \underbrace{2\vec{\Omega}\times\vec{v}}_{\text{D}} + \underbrace{\vec{F}_R}_{\text{E}} \quad , \tag{1.1}$$

where the left-side term A denotes the temporal change of the velocity (momentum per mass unit) and right-side terms B, C, D and E represent the forces acting per unit mass (i.e., accelerations). The term B describes the force driven by pressure gradients, the term C the gravitational force, the term D the Coriolis force and the term E the force due to friction. Note that this formulation cannot be solved analytically; thus, numerical methods are used to calculate approximate solutions. Moreover, additional information is required to fully describe the fluid features of the atmosphere, which encompasses the laws of mass and energy conservation and the equation of state. In the following, the description focuses on the lower part of the atmosphere, the so-called troposphere.

The radiation distribution over the Earth's surface is the first major driver of the global atmospheric circulation. The equatorial region receives much more solar radiation compared to the polar areas and constantly absorbs more energy than the emitted to the space throughout the year, i.e, positive net radiation. Thus, the equatorial region presents a warming in contrast to the high altitudes which show a cooling due to the emission of more energy to the space than the one absorbed, i.e., negative net radiation. According to the second law of thermodynamics (thermodynamic equilibrium), the resulting meridional gradient leads to a poleward energy (heat) transport (Trenberth and Caron, 2001), which substantially maintains the planetary wind fields. Air parcels rise over the tropics due to the differential heating and flow poleward aloft due to the mass conservation. On a non-rotating Earth-like, the aloft poleward flow would reach the Poles to sink to the Earth's surface, where it eventually flows back to the equator forming the structure of a single convection cell in each hemisphere (Fig. 1.3a). However, the Earth's rotation is the other major driver of the global atmospheric circulation determining its shape (Lockwood, 1987). Thus, any meridional motion will end up generating a latitudinal flow due to the influence of the Coriolis effect, which is accelerated poleward due to the conservation of angular momentum. This results in breaking up the single convective cell into a structure of three cells in each hemisphere: the Hadley cell, the Ferrel cell and the Polar cell (Fig. 1.3b).

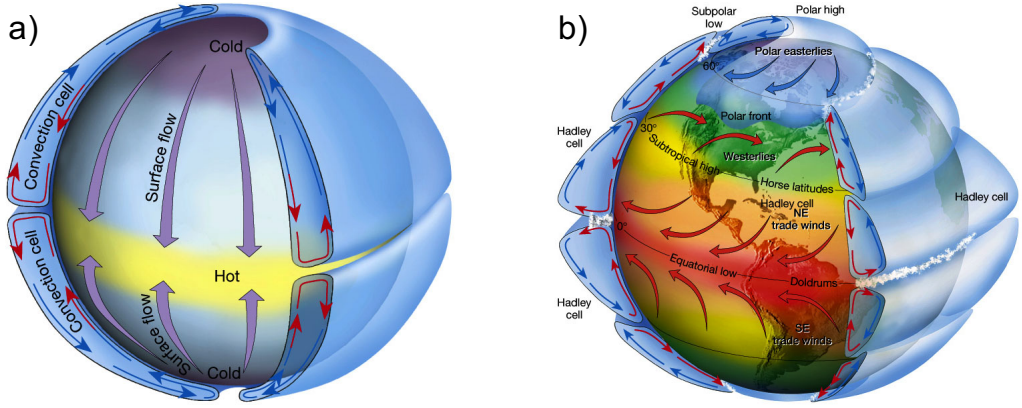

Figure 1.3: Illustration of the global atmospheric circulation. (a) represents a simple and single cell atmospheric convection in a non-rotating Earth. "Single cell" being either a single cell north or south of the equator. (b) shows and idealized three cell atmospheric convection in a rotating Earth. "Three cell" being either three cells north or south of the equator. The deflections of the winds within each cell is caused by the Coriolis Force. Source: Figure 7.5 in Lutgens and Tarbuck (2001).

The Hadley cell consists of the circulation that takes places from the equator to the subtropics (∼30° latitude) (Hadley, 1735). This circulation is directly driven by the radiative heating in the tropics, which produces warm air parcels that release latent heat when arising and condensing. This produces a decrease of the surface pressure, the so-called Equatorial Low, and eventually forms significantly thunderstorms afterwards. These air parcels then flow poleward aloft and sink at the subtropics that are colder than the tropics, the so-called subsidence (Fig. 1.3b). The poleward flow is deflected to the right in the North Hemisphere (NH) and to the left in the South Hemisphere (SH), which triggers the westerly winds aloft, the so-called westerlies (Fig. 1.3b). Note that the Hadley circulation is also referred to a thermally direct circulation as the air parcels arise from a warm place and sink over a cold location.

The subsidence does not only dry out the subtropical troposphere and causes the stationary subtropical high pressure systems, but also produces the major deserts of the world at this latitude. The air parcels return from the subtropical surface to the equator. This flow to the equator, as the aloft flow, is deflected by Coriolis, which produces the easterly winds that converge forming the Inter Tropical Convergence Zone (ITCZ), the so-called trade winds (Fig. 1.3b).

The Ferrel cell covers from ∼30° to ∼60° latitude (also called mid-latitude region) and is referred to a thermally indirect circulation as air parcels arise over a relatively cold region and thereafter sink over warmer areas. This cell is therefore considered to be driven by dynamical processes rather than by thermal processes, whose more important drivers are the large-scale eddies, i.e., mid-latitude cyclones and anticyclones. They are responsible for the transport of heat, mass and momentum in the mid-latitude circulation (Schneider, 2006). The Ferrell cell has its sinking branch at the same latitude as the Hadley cell (∼30°), from where the air parcels flow poleward at the surface with an eastward deflection due to Coriolis (i.e., westerly winds; Fig. 1.3b). The air parcels then rise in higher latitudes (approximately near 60°) and flow to the equator at upper levels with a westward deflection (i.e., easterly winds Ferrel, 1856) converging with the upper-level poleward branch of the Hadley cell (Fig. 1.3b). Still, the Ferrel cell moderately represents the reality as it needs that the upper-level winds flow westward (i.e., easterly winds) and the reality shows relatively strong eastward winds (i.e., westerly winds Harman, 1987) that are importantly connected to the eastward-flowing surface winds.

The Polar cell describes the circulation that takes place from ∼60° to the poles and is mainly driven by convection (Fig. 1.3b). Although the air parcels at about 60° are cool and dry compared to the ones in the tropics, they are still sufficiently warm and moist to undergo convection and drive a thermally direct circulation. The air parcels rise at ∼60° and flow poleward aloft with an eastward reflection. When the air parcels reach the polar areas, they are cooled through emission of radiation to space and is considerably denser than the underlying air; thus, they descend to the surface. This subsidence, as in the Hadley cell, dries out the polar troposphere and causes the cold stationary polar high pressure system. Then, the air parcels return from the polar surface to the ∼ 60 ° with a westward deflection, the so-called polar easterlies, where they converge with the surface poleward branch of the Ferrel cell (Fig. 1.3b). The cold polar air is mixed with the relatively warmer air at about 60°, which triggers the so-called sub-polar low and its underlying upward motion. Extratropical cyclones develop along this mixing boundary, the so-called polar front, and become the primary source of high precipitation amounts in the mid-latitudes.

The middle-to-upper troposphere usually have regions with maximum wind speeds (westerly winds) inside the Hadley and Ferrel cells. These stronger winds are known as jet streams and can be classified in two types: the subtropical thermally-driven jet stream and the mid-latitude eddy-driven jet stream (also called polar jets). Subtropical jet streams are often located at about 30° near to the sinking branch of the Hadley cell. They are mainly the result of thermal winds and the conservation of angular momentum. Thus, the Hadley cell does not

only show an increasing strength of the westerly winds with altitude (i.e., maximum speed in the upper troposphere), but also drives a source and sink of westerly momentum from the equator up to the subtropics contributing to the sharpness of the jet stream (Schneider, 2006). The mid-latitude jet streams are linked to frontogenesis and their maximum speed is observed in low-middle troposphere. They occur in areas of high baroclinicity, i.e., areas of substantial temperature gradients, where the transient eddies are produced (for more details about baroclinicity see: Holton and Hakim, 2013). These eddies propagate both poleward and to the equator and become the key of the meridional convergence of momentum that causes the acceleration of the westerly mean flow and thus the formation of the jet stream (Hoskins et al., 1983).

Consequently, the three-cell model explains reasonably well the surface wind distribution in the atmosphere and is therefore considered as the mean state of the atmospheric dynamics. However, this model can break down, especially in the lower troposphere. One reason is the interaction with the land surface and ocean. Another reason is that the atmosphere experiences fast changes and is influenced by many other perturbations in different spatial scales. The focus of this thesis is mostly on mid-latitudes, which is dominated by the westerlies and, in the zonal view, by the Ferrel cell. These phenomena control the European climate.

1.2.2 Modes of Variability

In the reality, the atmospheric circulation is influenced by the non-uniform landmass distribution and its underlying elevation, i.e., the topography. This significantly alters the schematic view of the general circulation (three-cell model) as it creates several land-sea contrasts and thus a deformation of the schematic zonal mean flow. Furthermore, the climate system presents phenomena that fluctuate on a broad variety of spatial scales. These fluctuations are known as modes of variability and have an oscillation without an exact periodicity (also called internal variability). Climate indexes are used to assess these modes (Viron et al., 2013). For instance, important modes of variability are, among others, the El Niño–Southern Oscillation (ENSO), Pacific Decadal Oscillation (PDO), North Atlantic Oscillation (NAO), and the Madden–Julian Oscillation (MJO). The modes of variability, on the global-to-synoptic scale, are the principal source of variability in climate elements on a regional-to-local scale (e.g., Keeley et al., 2008; Ault et al., 2011). Focusing on Europe, there are many studies about climate indexes which attempt at explaining the climate elements of Europe (e.g., Bartolini et al., 2009; Kalimeris et al., 2017; O'Reilly et al., 2017; Steirou et al., 2017; Kundzewicz et al., 2019; Piper et al., 2019; Hernández et al., 2020). Even though there are several modes of variability that are important to understand the European climate, I briefly describe in this section only two well-known global-to-synoptic modes of variability, i.e., ENSO and NAO. The reason for the selection is that ENSO and NAO represent a global and regional mode of variability, respectively.

The El Niño-Southern Oscillation (ENSO) phenomenon is the strongest natural fluctuation of climate on interannual time scales and is generated by ocean-atmosphere interactions over

the tropical Pacific (IPCC, 2001; Lin and Qian, 2019). In the long-term climatology, the sea level pressure is higher on the eastern side than on the western side of the tropical Pacific (pressure gradient), which is accompanied by the trade winds along the equator (Philander, 1989; Wallace and Hobbs, 2006). The atmospheric trade winds transport the warm tropical water to the west producing a "warm pool" in the tropical western Pacific and an upward slope of sea level along the equator of about 60 cm from east to west. According to the mass conservation, the ocean counteracts the loss of mass in the tropical eastern pacific by vertical and horizontal transport of water from colder oceanic regions, which produces a cold tongue along the equator that is most pronounced about October and weakest in March (Philander, 1989; IPCC, 2001). The climatological features of the tropical Pacific usually fluctuate between two phases that consist of an eastward (El Niño) and westward (La Niña) shift of the warm pool. This movement is mainly caused by a weakness (El Niño) or an intensification (La Niña) of the trade winds, which simultaneously moves the associated convective cell and influences the oceanic thermocline depth (Fig. 1.4). This directly has a strong impact on several regions of the globe such as changes of the precipitation patterns of Southeast Asia, Australia, North and South America. This phenomenon also affects other parts of the world that are not directly connected to the Pacific such as the North Atlantic Ocean and the Mediterranean region (Kalimeris et al., 2017; Lin and Qian, 2019). ENSO produces a NAO-like pattern (for details about NAO see following paragraph), thus affecting European region. This NAO-like pattern is mainly driven by large-scale dynamical mechanisms in the upper troposphere (Bell et al., 2009; Domeisen et al., 2015; Mezzina et al., 2020). Many studies found that ENSO can influence the temperature and precipitation patterns over Europe, especially from late autumn till late spring and sometimes delayed with respect to the Pacific anomalies (e.g., Fraedrich, 1994; Brönnimann et al., 2007; López-Parages et al., 2016; Herceg-Bulić et al., 2017; Ivasić et al., 2021). For instance, the El Niño (positive phase of ENSO) can produce negative and positive temperature anomalies in northeastern Europe and Turkey, respectively, and positive and negative precipitation anomalies around the European 45° N, in Norway and the southeastern Mediterranean area, respectively (Brönnimann et al., 2007; Lin and Qian, 2019). Moreover, ENSO influences the frequency and intensity of extreme rainfall events over Europe. This influence is much smaller than North Atlantic Oscillation but still significant in some areas such as southern and eastern Europe (Nobre et al., 2017).

The North Atlantic Oscillation (NAO) is an atmospheric phenomenon on monthly to decadal time scales over the North Atlantic Ocean (IPCC, 2001; Hurrell et al., 2003; Woollings, 2010; Pinto and Raible, 2012). Although NAO is present throughout the year, the description of NAO is here focused on wintertime as NAO has its more important manifestation during boreal winter and it explains most of the European variability in wintertime (around 40 %, Brandimarte et al., 2011; Pinto and Raible, 2012; Raible et al., 2014; Kalimeris et al., 2017; Steirou et al., 2017). In the longterm, the high-pressure system over the Azores (Azores High) and the low-pressure system over Iceland (Icelandic Low) mostly determine the atmospheric circulation of North Atlantic region, especially the lower-to-mid tropospheric winds and their underlying water transport towards Europe. NAO is generally represented by a north-south dipole of sea

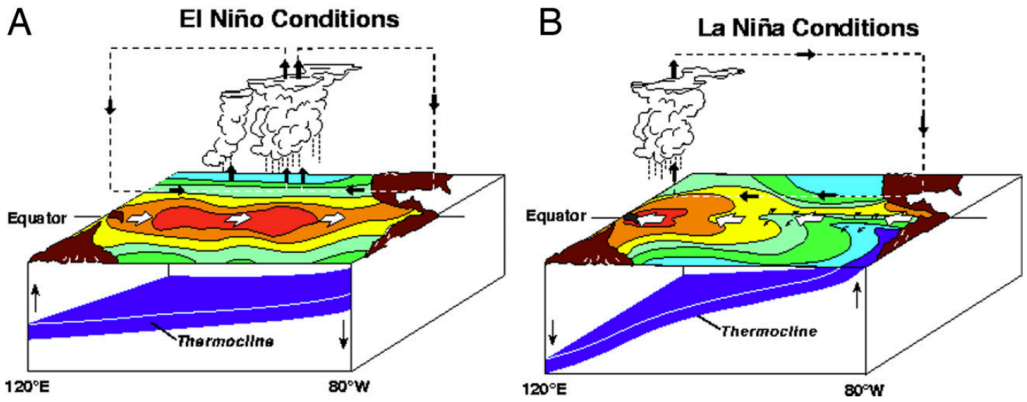

Figure 1.4: Schematic description of large-scale ocean-atmosphere interactions during the development of ENSO extremes. A represents El Niño and B La Niña according to the Bjerkness feedback. Source: Fig. 3 from Latif and Keenlyside (2009).

level surface pressure anomalies. NAO is also known as the index of the mid-latitude wind strength into Europe and fluctuates between a positive and negative phase. The positive (negative) NAO phase consists of an intensification (weakening) of the Azores High and the Iceland Low (Fig. 1.5). This results in a stronger (weaker) meridional pressure gradient over North Atlantic, which produces a stronger (weaker) zonal flow regime, especially over the mid-latitude eastern North Atlantic (van Loon and Rogers, 1978; Marshall et al., 2001; Wanner et al., 2001; Hurrell et al., 2003; Marshall et al., 2001; Hurrell and Deser, 2010; Woollings, 2010; Pinto and Raible, 2012; Kalimeris et al., 2017). These fluctuations affect the entire Atlantic Ocean and the surrounding continents. NAO does not only influence the air-sea interaction, but it is also connected to the overturning circulation in the North Atlantic Ocean (Marshall et al., 2001). Also, NAO regulates the intensity and the path of the mid-latitude cyclones and their underlying extreme-weather conditions shaping the European climate (Rogers, 1990; Steirou et al., 2017).

1.2.3 European Climate

Europe is a continent from the North Hemisphere whose area is bordered by the Atlantic Ocean to the west, the Mediterranean Sea to the south, Asia to the east, and the Arctic Ocean to the north. In general, the present-day European climate is determined by the predominant west-to-east atmospheric flow and the relatively warm surface water of the North Atlantic Ocean (Seager et al., 2002; Palter, 2015) and Mediterranean Sea (Lionello et al., 2006; Volosciuk et al., 2016; O'Reilly et al., 2017).

Focusing on the atmospheric flow, Europe is characterised by several key dynamical features such as the Northern Atlantic jet stream, the North Atlantic storm track and the stationary waves (Woollings, 2010). As mentioned in Sect. 1.2.1, two jet streams affect the extratropical regions, i.e., the subtropical and the eddy-driven jet stream (Held and Hou, 1980; Hoskins et al., 1983; Panetta and Held, 1988). Although these jet streams differ in their formation mechanisms, they are often indistinctly separated from each other in the North

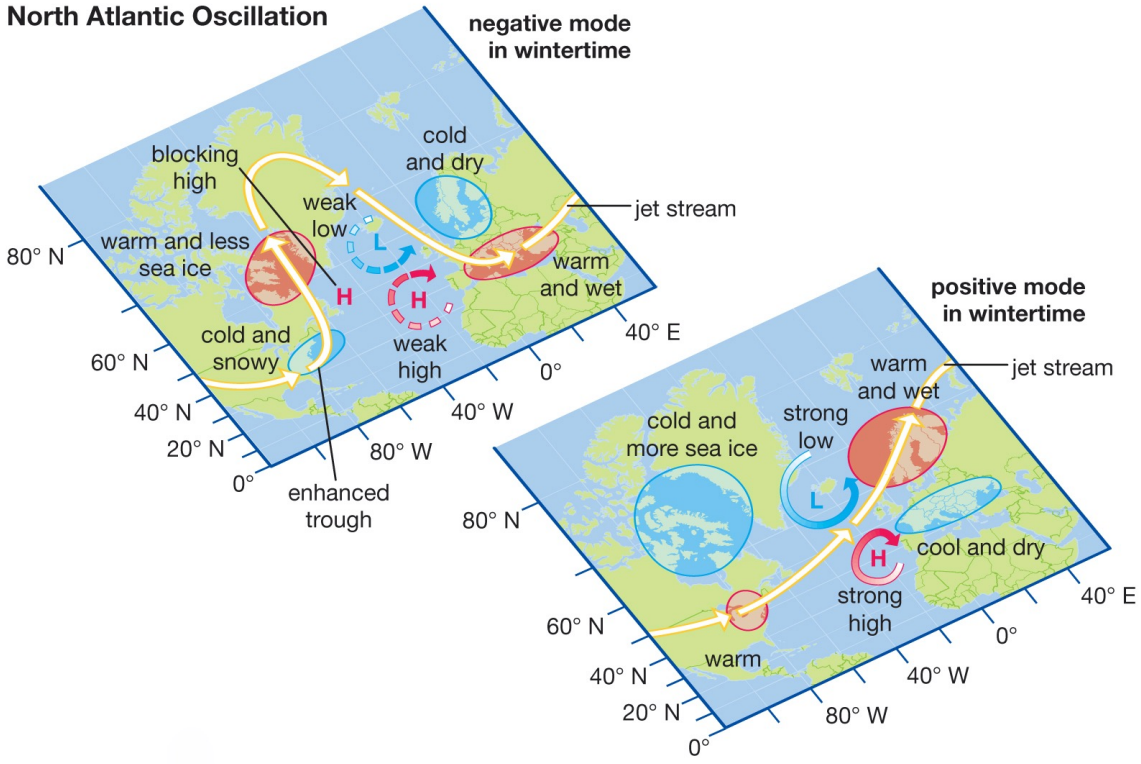

Figure 1.5: Schematic view of the North Atlantic Oscillation (NAO) in wintertime. The typical path of the polar-front jet stream (yellow) during negative (upper left) and positive modes (bottom right) of the North Atlantic Oscillation. Areas in blue (red) represent cold (warmer) conditions, L and H low- and high-pressure systems. Source: Rafferty (2019).

Hemisphere. For instance, this separation rarely happens over the North Atlantic towards Europe, particularly during winter, when only the eddy-driven jet stream is clearly distinguished (Boucher, 1987; Eichelberger and Hartmann, 2007; Woollings, 2010; Woollings et al., 2010; Li and Wettstein, 2012; Harnik et al., 2014). The eddy-driven jet stream controls the genesis of mid-latitude cyclones and anticyclones which travel preferentially over certain regions, the so-called storm track (Schultz et al., 2019). The storm track is also a common measure for the intensity of the cyclonic activity in the mid latitudes (Blackmon, 1976; Sickmöller et al., 2000). The North Atlantic storm track influences the European climate by not only shaping the precipitation and temperature pattern, but also the frequency and intensity of weather and climate extremes (Woollings, 2010; Dee et al., 2011; Hawcroft et al., 2012; Wernli and Schwierz, 2006; Ludwig et al., 2016; Schultz et al., 2019). This is particularly important in winter because over-land convective processes become more important during summer. Both eddy-driven jet stream and storm track are tilted poleward as a result of the strong Northern Hemisphere stationary wave pattern (Woollings et al., 2010). This zonal asymmetry is known as a stationary wave that is subset of the atmospheric Rossby waves. This can be interpreted as response to the asymmetry in the surface forcing such as orography and relatively warm surface water from the North Atlantic Ocean. This stationary wave causes two important tilts that influences the European climate. The atmospheric circulation

exhibits a southwest-northeast flow across the North Atlantic Ocean towards Europe, which advects relatively warm maritime air to western Europe. Also, it shows north-westerlies that advect relatively cold air to continental Europe (central-to-eastern part, Smagorinsky, 1953; Held et al., 2002; Nigam and DeWeaver, 2003; Brayshaw et al., 2009; Kaspi and Schneider, 2013; Van Niekerk, 2017). During summer, the jet-stream and storm track are weaker and shifted northward, which leads to drier and warmer conditions in central to southern Europe. Consequently, Europe is usually characterised by a temperate climate. Western Europe has moderately warm summers and cool winters with frequent overcast skies. Southern Europe typically presents hot dry summer, mild winters, and frequent sunny skies. Central and eastern Europe generally features warm-to-hot summers and cold winters (Boucher, 1987).

1.2.4 Alpine Climate

The European Alps are a dominant feature of the European landscape. In general, they are defined as an arc-shaped mountain range located in the middle of the continent. They are characterised as a region with a very complex topography: extensive lowlands, deep valleys and mountain peaks higher than 4000 m. The European Alps influence the regional atmospheric circulation by deflecting the flow horizontally and vertically, by altering the sensible and latent heat, and by inducing waves into the free atmosphere on different spatial scales (Schär et al., 1998).

Four flow conditions mostly modulate the heat and moisture transport toward the European Alps, thus influencing the Alpine climate. Westerly flow conditions introduce the relatively mild and moist air of the Atlantic Ocean. Northerly winds transport cold polar air from northern Europe. Easterly flow conditions provide continental air masses that are usually cold and dry in winter and hot in summer. Southerly winds transport warm and moist air from the Mediterranean Sea (Frei and Schär, 1998; Sturman and Wanner, 2001; Aubrey et al., 2020). The main sources that contributes to the Alpine moisture are the North Atlantic Ocean (westerly winds, 39.6 %), North Sea and Baltic Sea (northerly winds, 16.6 %), the Mediterranean Sea (southerly winds, 23.3 %), and the European land surface (transported by all flow conditions, 20.8 %). Overall, the North Atlantic contribution dominates in winter and the European land surface in summer (Sodemann and Zubler, 2010). These flow conditions create particular features over the Alpine region such as preferred spatial-temporal temperature and precipitation patterns (Schär et al., 1998). These patterns can be influenced by changes in the stability and in the atmospheric vertical profile which are produced by flow phenomena associated with gravity waves such as Föhn and valley winds (Frei and Schär, 1998; Schär et al., 1998).

The valleys and lowlands are overall warmer and drier than the surrounding mountains. Most of the valleys and lowlands on average reach temperatures below zero degree during winter and around 25 °C in summer. Very stable atmospheric conditions are frequent due to thermal inversions, especially producing fog in the valleys during autumn and winter. The moist areas, i.e., Alpine precipitation patterns, are mainly defined by two processes: (i) The

orographically forced upstream flow is evident throughout the year but especially stronger in wintertime. (ii) The topographically triggered convection dominates the summer precipitation, especially over the mountains (Frei and Schär, 1998; Schär et al., 1998; Aubrey et al., 2020).

At high altitudes (above 1500 m), the moisture that precipitates in form of snow during fall, winter and spring is stored and accumulates. This snow is then gradually converted into permanent glaciers. Snow and glaciers very slowly melt throughout the year with a relatively acceleration towards and during summertime, which in turn sustains flow streams. Thus, the European Alps play an important role in regulating the water supply of the region that is traversed by streams originated in the Alps such as Rhine and Rhone rivers. These and other streams does not only serve as water supply for human being, but also for flora and fauna of the surrounding Alpine region. The hydrological cycle and some of its important components are in detail explained in the following section (Sect. 1.3).

1.3 Hydrological Cycle

Water is an important ingredient of the Earth's climatic system. It is constantly changing states between solid, liquid, and gaseous, whose processes can happen within a millisecond or over millions of years. These three water phases can be found in all the components of the climate system in a continuous movement that occurs on, above and below the Earth's surface. This is defined as the natural water cycle, also known as the hydrological cycle (Peixóto and Oort, 1983; Hordon, 1998; IPCC, 2001; Pierrehumbert, 2002; Hack et al., 2006; Narasimhan, 2009).

The water cycle has no starting point (Hordon, 1998). But, to further describe it, I start in the oceans as they contain the most Earth's water and can be considered as the place where the water cycle is mainly driven (Narasimhan, 2009). The solar radiation mainly heats the superficial water layers of the ocean. These layers are normally in a liquid phase except in very cold areas where it can be solid (snow or ice). The water molecules evaporate (or sublimate) as water vapour into the atmosphere storing energy in the form of latent heat. This process importantly happens in the tropics due to the constantly higher insolation (Hordon, 1998) and results in relatively warmer and humid air parcels which drive the upward branch of the atmospheric Hadley cell (Sect. 1.2.1). Water is evaporated (or sublimated) from the soil and transpired from plants, which is known as evapotranspiration. The transpiration consists of moving liquid water from the soil through the plants till is release as water vapour into the atmosphere by their leaves. Additionally, volcanic eruptions also discharge water vapour into the atmosphere.

The atmospheric water vapour is then vertically and horizontally transported. This two-dimensional transport releases energy into the atmosphere: The water vapour incorporates sensible heat when it cools down. Latent heat is also released when the water vapour changes its phase to form water drops, i.e. condensation, or to form ice crystal, i.e. sublimation or solidification. The energy release happens during the upwards motion and when the horizontal

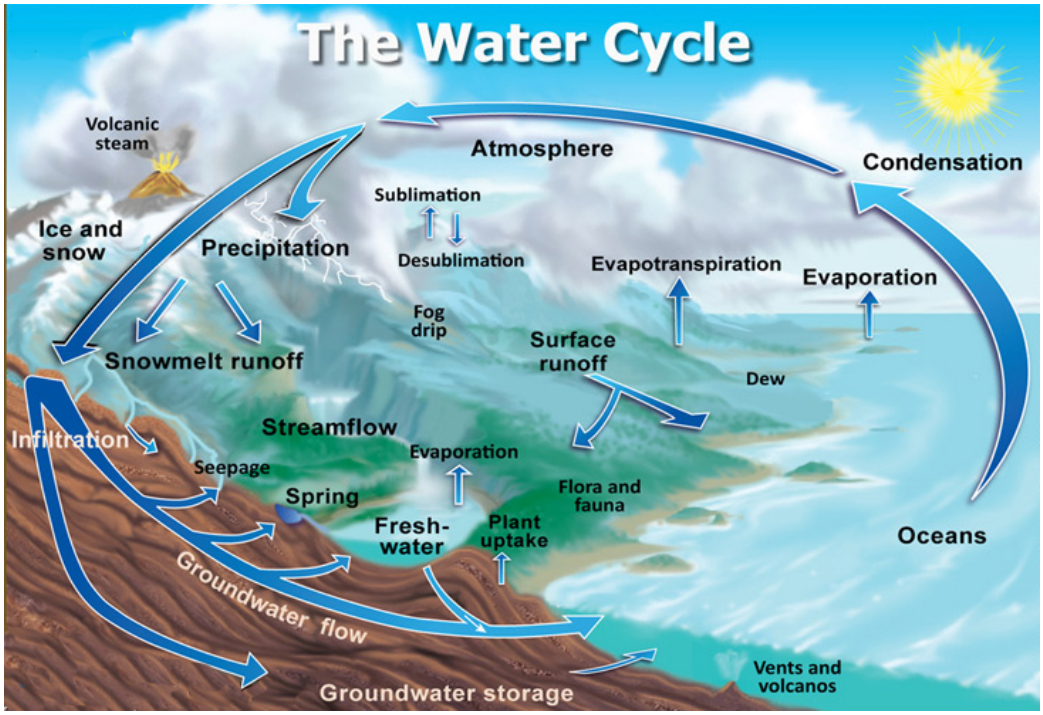

Figure 1.6: Schematic view of the components of the hydrological cycle, their processes and interactions. Source: The water cycle from the USGS Water Science School (https://www.usgs.gov/media/images/water-cycle-natural-water-cycle).

transport heads towards relatively colder regions. This builds one of the main modes of energy transport in the atmosphere (Pierrehumbert, 2002; Gettelman and Rood, 2016). Clouds mainly consist of water drops and ice crystals whose size and distribution contribute to determine cloud's properties. Under certain atmospheric conditions, the water drops and ice crystals fall out and reach the surface (land and ocean surface) as liquid (rain) or solid (snow or hail) precipitation (Wallace and Hobbs, 2006; Pruppacher and Klett, 2010). The water cycle remains open unless the precipitation directly occurs over the oceans.

At high altitudes, a small portion of the precipitation is stored as ice (or glacier) which very slowly melt. The other portion of precipitation with the melting water can then be intercepted by vegetation canopy before completely reaching the ground. As soon as the ground is reached, some of this water flows over land as surface water, also known as runoff, towards oceans or towards sunken areas where it is stored like lakes. The rest of water is infiltrated into the ground as soil moisture which can be percolated into deeper layers as groundwater (Narasimhan, 2009; Gettelman and Rood, 2016). In these deep layers, some of this water stays for hundred to thousand years as groundwater storage (Oki and Kanae, 2006) before continuing its way to the ocean. Another portion directly returns to the ocean as groundwater flow or comes to the surface to be part of the runoff. Both groundwater and lakes inside volcanos can return to the atmosphere as water vapour by volcanic eruptions. The water cycle is closed when the water finally reaches the oceans. The hydrological cycle is summarised in Fig. 1.6. This thesis focuses on two components of the water cycle, i.e., precipitation and ice cover, which are outlined in the following sections.

1.3.1 Precipitation

Precipitation consists of water drops and ice crystals falling out of the atmosphere on the Earth's surface (Houze, 2014; American Meteorological Society, 2019). The amount of precipitation is measured by the depth of liquid water over a horizontal surface, for example: 1 mm corresponds to 1 kg water mass that dropped out on 1 m^2. Physical processes that characterise the formation and fall of these drops and crystals are known as cloud microphysics. Some of these processes are briefly explained in the following.

Everything starts when the air becomes saturated with water vapour (reaching 100 % relative humidity). The saturation is caused by increasing the amount of water vapour in the atmosphere or by changes in air temperature and pressure (Wallace and Hobbs, 2006). The saturation leads to condensing the atmospheric water vapour into very small water droplets, the so-called cloud droplets ($\sim$ 0.02 mm in diameter, Fig. 1.7). This usually occurs on the surface of suspended particles called cloud condensation nuclei (CCN), whose size is much smaller ($\sim$ 0.2 μm in diameter, Fig.1.7). Cloud droplets are not only subject to gravitational force that makes them fall, but also by frictional force while falling as the accelerated motion is increasingly resisted by surrounding air. This makes cloud droplets have barely detectable fall speeds and they rather remain suspended in the air and form part of all visible clouds (Wang, 2013; Houze, 2014).

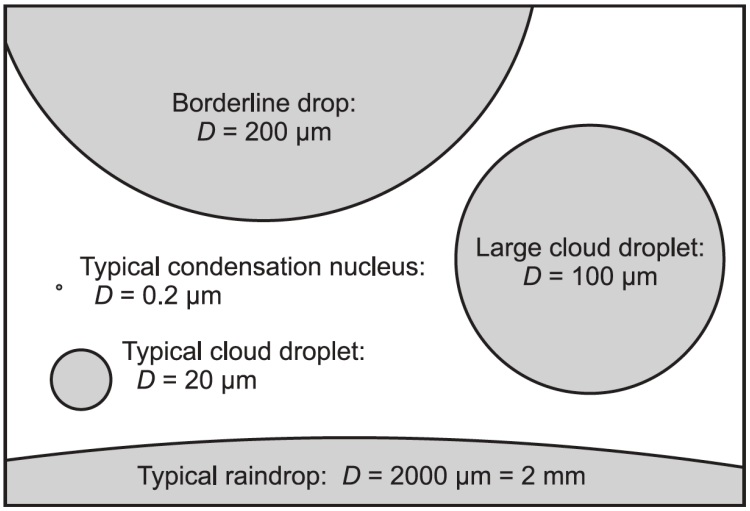

Figure 1.7: Typical diameters of water droplets/drops and aerosol in the atmosphere. Source: Figure 3.1 in Houze (2014).

From cloud droplets to the the falling particles, there is a mass increase of around million times. Some of this growth can be achieved in supersaturated environments, where cloud droplets and aerosols function as CCNs in further condensing water vapour on their surfaces. This growth process turn out to be neglected as soon as the condensation rate becomes less important compared to the evaporation rate that also happens on the surface of the CCNs. This is usually before reaching the size of raindrops and is explained by the fact that a supersaturated environment lasts for relatively short periods in the reality. Turbulence and gravity are the key

for the cloud droplets to become falling particles since they dominate the growth compared to the supersaturated environment. Turbulence and gravity move the atmospheric particles and make cloud droplets collide. The efficiency of colliding, i.e., coalescence and collisions of droplets, is determined by many physical properties such as polarisation, velocity and droplet's size. High efficiency of colliding then results in an important mass increase of the droplets and their underlying gravitational acceleration, which produces a raindrop capable of falling. However, this growth can importantly be diminished by characteristics of the surrounding air, e.g., relatively drier air, and other droplet-related physical properties that can break the raindrop into smaller parts. Similar processes are also observed in the formation of ice crystals. For an in-depth explanation of the growth mechanisms for both raindrops and crystals see Houghton (1950), Willis and Tattelman (1989), Wallace and Hobbs (2006), Wang (2013) and Houze (2014).

Raindrops normally loses mass on their falling path below the clouds. One reason is that the raindrops break up after collisions with other particles or after deformation. For instance, the bottom of the drop is affected by the air resistance and starts to flatten out with an inward curvature in the middle while growing. Then, the bottom of the bigger drop greatly expands to a form similar to a parachute, which leads to the large drop to split into smaller drops. The other reason is that they can evaporate by the increase of energy due to friction and to relatively warmer and drier surrounding air. Ice crystals can melt to become raindrops and then experience the same mass loss (Wallace and Hobbs, 2006; Wang, 2013; Houze, 2014).

1.3.2 Glaciers

A glacier is a large mass of ice that originates on the land surface by the recrystallisation of snow or other forms of solid precipitation (Meier, 2020). The recrystallisation process is also known as the accumulation process of falling ice crystals (snow or other forms of solid precipitation) to become a crystalline solid (glacier). Some other features and formation processes are briefly explained in the following.

Glaciers cover around 10 % of Earth's land surface (IPCC, 2019b). They can cover areas from 0.1 km ^{2}, e.g., the mountain glaciers, to some millions of km^2. The latter are called ice sheets due to their considerably large continent-coverage such as the Greenland and the Antarctic ice sheet ($\sim$1.8 million km^2 and $\sim$13.5 million km^2, respectively; Meier, 2020). For simplicity, the terms glaciers and ice sheets are considered interchangeable in this thesis.

Usually, glaciers undergo elastic deformation as response to long-term forces such as gravity (Meier and Ashton, 2020). This results in a constant downhill movement by sliding at their base with a very low speed (Cuffey and Paterson, 2010) compared to speeds of other fluids such as atmosphere (Holton and Hakim, 2013). The glacier speed is influenced by friction forces and ice-related pressure. Friction makes glaciers move more slowly at their borders, i.e., at the bottom of the glacier and also at the valley's sidewalls in Alpine glaciers. However, the lowermost layer of a glacier is subject of high pressures that can cause ice to melt. This produces a slippery layer that permits the rest of the ice to slide and to accelerate, the so-called

basal sliding (Weertman, 1957; Paterson, 1994; Cuffey and Paterson, 2010) (Fig. 1.8). Friction results in shaping the landscape by creating landforms such as cirques, moraines and fjords (Bridge and Demicco, 2008). Friction, soil and atmospheric temperatures can lead glaciers to melt. The melting rate is crucial as it needs to be lower than the recrystallisation process (accumulation rate) to allow ice crystals to be stored for longer periods compared to the temporal extent of its associated precipitation. This means that glaciers are located in places that experience a large amount of snow and their climate is relatively cold most of the time, e.g., Earth's polar regions and locations at high altitude.

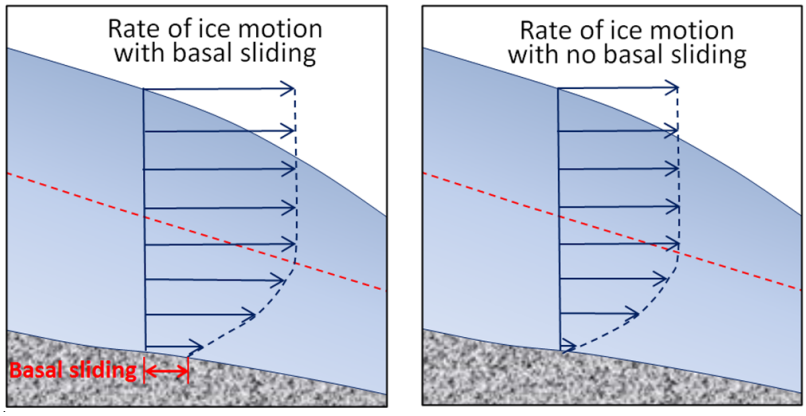

Figure 1.8: Schematic differences in glacial ice motion with basal sliding (left) and without basal sliding (right). The dashed red line indicates the upper limit of plastic internal flow. Source: Figure 16.2.9 in Earle (2019).

Glaciers play an important role in the flora and fauna as they are one of the source of fresh water (IPCC, 2019b). They are also important for human beings as source of energy supply. For instance, mountain glaciers are key contributors to seasonal river flows. They function as frozen water reservoirs that supply fresh-water runoff to river flow during warm and dry periods. A scenario of constant glacier retreats has important consequences for river flows, which directly impact water supplies, sustainability of aquatic ecosystems and hydropower generation (e.g., Immerzeel et al., 2010; Kaser et al., 2010; Huss, 2011; IPCC, 2019b).

1.4 Land Cover

Land cover is the physical material Earth's surface, which includes plants, asphalt, bare ground, water, etc. This section focuses on briefly explaining vegetation and its interactions with the atmosphere.

1.4.1 Vegetation

Vegetation is usually defined as the ground cover provided by an assemblage of plant species, which encompasses the most abundant living element in the biosphere. Plants are characterised as multicellular eukaryotic organisms made of cells with cellulose. These organisms are particularly different in terms of nutrition as they use a photosynthetic process. This

process provides energy from chemical reactions between water, minerals, carbon dioxide, pigments and solar energy (Dickinson et al., 2020).

Figure 1.9: Examples of vegetation types. (a) represents forest, (b) grassland, (c) desert steppe and (d) desert. Source: Figure 1 in Dugarsuren and Lin (2016).

Vegetation is also used as the term to describe main features of the plant cover in a specific area, the so-called vegetation type (some examples in Fig. 1.9). Vegetation types can for example define an area by using the dominant plant growth like forest vegetation, grassland vegetation (e.g., Machar et al., 2017; Zheng et al., 2019). A description can also use colloquial or technical descriptors and particular plant communities such as desert vegetation, arctic vegetation (e.g., Lu et al., 2019; Bjorkman et al., 2020) and peat bog vegetation (e.g., Segal, 1966; Levy et al., 2019), respectively. Vegetation types can be determined by the interaction with a variety of environmental factors such as predation, topography, soil characteristics and climate. Slope orientation and inclination influence the growth of vegetation types by determining the exposition to solar radiation and the movement of surface and soil water. This water motion is also an important factor as it can determine the soil moisture and the nutrient availability.

Vast diversity of animals, including humans and microorganisms, rely on vegetation in the food chain since vegetation serves as primary energy source and wildlife habitat. Vegetation is also the key in regulating numerous biogeochemical cycles such as water, carbon and nitrogen. It also influences soil features, particularly the density and chemistry (e.g., Benninghoff, 1952; Metzger et al., 2017; Veldkamp et al., 2020) as result of the soil-vegetation-atmosphere interaction (e.g., Jamalinia et al., 2019).

1.4.2 Atmosphere–Vegetation Interaction

Components of the climate system constantly interact between each other. Vegetation and atmosphere are strongly connected and they regulate the atmospheric branch of the hydrological cycle over the land surface. Vegetation for example influences the heat and moisture fluxes in the near-surface troposphere. Atmosphere in turn influences the plant's growth through precipitation (McPherson, 2007) and atmospheric CO_2 (e.g. Asshoff et al., 2006; Moore et al., 2006). The hydrological-related interaction is briefly explained in the following.

Vegetation vertically extends from few centimetres to tens of metres. High vegetation, e.g., tall trees, modify near-surface flow compared to bare soil, which increases atmospheric turbulence at low levels. An increase of low-level turbulence is usually associated with an intensification of convective processes on the local scale and frictional forces on synoptical scale, which can enhance precipitation processes (McPherson, 2007; Spracklen et al., 2018). Heat and moisture fluxes can vary from one to another area as a consequence of the different vegetation types across the land surface. This results in horizontal pressure and temperature gradients in the low-level troposphere, which can produce vertical and horizontal motions. The vertical motion influences precipitation processes. The horizontal motion, also called vegetation breezes, modifies the horizontal distribution of moisture that is used in the precipitation process. (Letzel and Raasch, 2003; McPherson, 2007; Garcia-Carreras et al., 2011; Kang and Bryan, 2011). This is particularly important between areas with strongly different vegetations types as they can cause circulations that increase rainfall over some regions and reduce it elsewhere (Fig. 1.10, e.g., Yan et al., 2017; Spracklen et al., 2018).

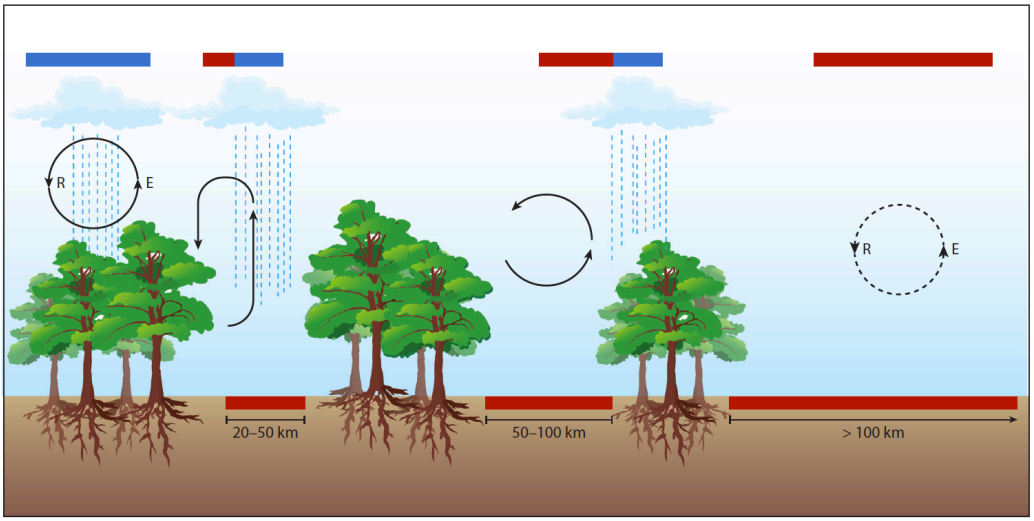

Figure 1.10: Schematic example of the circulation and precipitation effects between two vegetation types: tropical forest and a deforested area (bare soil). Bare soil illustrates a reduced evapotranspiration and a warmer land surface. Circulation between the two types cause regions of increased and decreased rainfall. E represents evapotranspiration, R rainfall. Soil with red rectangles indicates a warmer land surface. Blue and red rectangles on the top represent an increase of decrease of precipitation, respectively. Source: Figure 3 in Spracklen et al. (2018).

Atmosphere influences vegetation in different ways (Marquer et al., 2017). Vegetation growth is for example associated with temperature (e.g., Messaoud and Chen, 2011; Lloyd and Bunn, 2007), precipitation (e.g., Cienciala et al., 2018) and atmospheric CO_2 (e.g. Lamarche et al., 1984; Bond et al., 2003; Yang et al., 2019). Changes in either atmospheric temperature or moisture affect the atmospheric vapour pressure at low levels, i.e. near-surface relative humidity, which is crucial for photosynthesis processes (Rawson et al., 1977; Fletcher et al., 2007; Yuan et al., 2019). This is also true for some species in long-term freezing conditions (Rehm et al., 2021). Extreme atmospheric events such as dryness and extreme precipitation are associated with mortality of some species. Dryness strongly reduces the soil moisture and extreme precipitation saturates the soil with humidity, which both can dramatically affect vegetation survival (e.g., Zeppel et al., 2014; Renne et al., 2019; Li et al., 2019).

1.5 Past Climate

Earth's climate system has experienced a vast of fluctuations in long-term time scales throughout the world's history. These variations are the result of natural and anthropogenic changes in elements outside and inside the climate system, the so-called external and internal forcing, respectively (Mitchell, 1976; IPCC, 2013b). Besides the forcing factors, there are many complex internal mechanisms that influence the variations of the Earth's climate system, the so-called feedbacks. They are generally defined as the processes in which a perturbation in one quantity alters a second quantity that in turn modifies the first one. A positive feedback amplifies the variation in the first quantity while negative feedback diminish it (IPCC, 2013a,b). There are many positive and negative feedbacks in the Earth's climate system. For instance, water vapour functions as a positive feedback. The first perturbation is the increase of surface temperature which enhances the amount of atmospheric water vapour through the evaporation from water bodies such as the sea surface. Since water vapour functions as a GHG, the higher amount of water vapour in turn enhances the greenhouse effect and thus produces further warming on the Earth's surface. Another example is the long-wave radiation (LWR) that is emitted from the top of the atmosphere. An increase in the atmospheric temperature enhances the emission of energy through LWR (according to Stefan–Boltzmann law; Liou, 2002). This increase in amount of outgoing radiation cools down the Earth. Thus, it is described as a negative feedback as it diminishes the original warming, also called as the Planck feedback (IPCC, 2013b).

For simplicity, this thesis briefly mentions only natural forcing factors that mostly dominate the influence on the climate system in millennia time scales. The orbital forcing is the dominant external forcing factor and consists of three elements: the tilt of the Earth's axis (also called obliquity), its precession, and eccentricity of the Earth's orbit around the Sun. These elements change with a periodicity of around 100, 41 and 23 thousand years, respectively (Fig. 1.11). They determine the incoming solar radiation at the top of the atmosphere (Milankovitch, 1941), which is the main driver of the climate system (Sect. 1.1). Volcanic activity and atmospheric

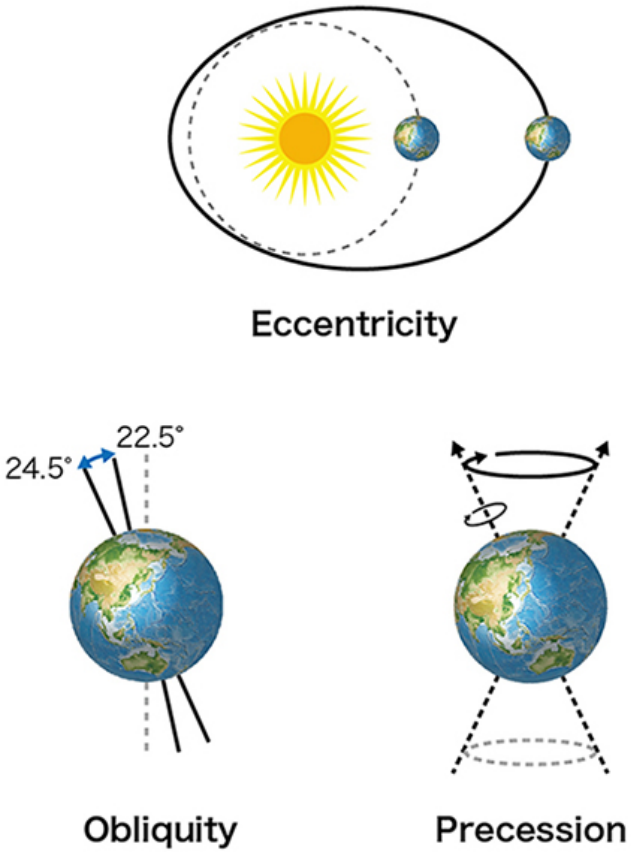

Figure 1.11: Illustration of the three elements of the orbital forcing. Upper panel represents the eccentricity, bottom left obliquity and bottom right precession. Source: Figure 2 in JAMSTEC (2014).

composition are considered the dominant internal forcing factors. They are part of the climate system and their changes can influence Earth's radiative balance (IPCC, 2013b).

Elements of the climate system have a different temporal response to changes in the external and internal forcing. This response ranges from days to millennia. For instance, the atmospheric response is no longer than a few months and the one of oceans and ice sheets can last for decades until centuries or millennia. It is important to mention that the interactions between the elements of the climate system are non-linear. This interaction and the different responses are together the reason that climate system is never in full equilibrium. Hence, they lead to additional fluctuations in the elements of the climate system, which is particularly important when there are no changes in the external and internal forcing. These fluctuations are known as internal variability, whose important consequence is that a great part of climate variations can hardly be predicted on relatively short time scales. El Niño Southern Oscillation (ENSO) is an example of internal variability in present-day climate. ENSO comes from the atmosphere-ocean interaction in the tropical Pacific (Sect. 1.2.2).

The climate of the past has changed from glacial to interglacial periods several times in the last 800 thousand years (Sigman and Boyle, 2000; Schilt et al., 2010). This thesis focuses on the climate state of the two last glacial periods. The following sections briefly

explain these climate states and the two available techniques to reconstruct them: proxy-based reconstructions and climate modelling.

1.5.1 Proxies

The present-day climate is characterised by spatial networks of stations that directly measure the elements of the climate system, e.g., temperature, precipitation and humidity. This has only been possible in the modern times. To reconstruct the climate conditions of the past, the scientific community has focussed on indirect measurements, the so-called natural climate proxy archives and their underlying proxy reconstructions. Proxy archives can be defined as the elements that preserve characteristics of the past that stand in for direct measurements (NCEI, 2018). There are several types of proxy archives, e.g., ice cores, lake and marine sediments, corals, pollen, stalagmites and tree rings (e.g., Li et al., 2010; Emile-Geay et al., 2017). They are sensitive to climate variables at different time scales as they preserve the climate information in different ways. One proxy archive may be good at short time scales, while another better at longer time scales. For instance, tree rings are used to infer the climate of the last few millennia whereas ice cores beyond tens of millennia. Proxy reconstructions are the climate information that is defined as the statistical relationships between characteristics in the proxy archives and climate variables. These relationships are normally based on present day to infer the climate of the past. Some proxy archives are briefly explained in the following.

Glaciers provide valuable information about the climate of more than tens of millennia ago. As mentioned in Sect 1.3.2, they are made of accumulated snow. While snow accumulates on the surface, air bubbles and particles can be captured and stored in glaciers. This process forms distinct layers as the air composition and particles vary across time. These layers are collected in deep-ice samples made by drilling the glaciers, the so-called ice cores. Some places on the Earth can offer ice cores with a very long temporal extension as they have permanently been frozen for very long periods, e.g. both poles and the tops of mountains (NCEI, 2018; USGS, 2021). Ice cores can provide information about temperature, precipitation, atmospheric composition, volcanic activity, and even wind patterns (e.g., Lambert et al., 2012; Adolphi et al., 2018; Brook and Buizert, 2018; Erhardt et al., 2019; Svensson et al., 2020).

Plants have existed for more than many million of years (Stewart and Rothwell, 2010). Each flowering plant produces distinctive pollen grains. This means that features of pollen grains permit to identify the type of plant from which they come. Pollen grains are deposited on the surface or in water bodies like lakes and oceans. Pollen grains can also be transported by wind for long distances before deposition. Some pollen grains do not become a plant and are preserved on the land surface or at the bottom of the water bodies for long periods, the so-called pollen records. They are part of layers that represent the deposition of other material as well, also known as sediment layers (NCEI, 2018; USGS, 2021). Pollen records can be used to infer the climate of an area based on the types of plants found in the layers (e.g., Camuera et al., 2019; Shi et al., 2020).

Figure 1.12: Elements of the climate system that are considered as proxy archives. Left panel represents pollen records, middle ice cores, and right stalagmites. Source: NCEI (2018).

Stalagmites are part of the natural calcium carbonate deposits (speleothems) that form in a cave environment. They are also considered as a type of rock formation whose shape is often similar to bamboo shoots. This rock formation arises from the floor of a cave due to the accumulation of deposited material that comes from drops enriched in Ca_2^+ and HCO_3 that fall from the cave ceiling onto the floor. A variety of measurable parameters in stalagmites are used to infer key aspects of climate variability. Some of them are stable isotope ratios, growth-rate changes, variations in trace element ratios, organic acid contents and the nature of trapped pollen grains. Stalagmites are often well preserved and their records can be continuous with relatively long-time coverage of hundreds to thousands years. Stalagmites can provide information about mean annual temperature, rainfall variability, atmospheric circulation changes and vegetation response (Schwarcz, 1986; Gascoyne, 1992; McDermott, 2004; Fairchild and Treble, 2009; Cheng et al., 2019; Tan et al., 2020).

1.5.2 Climate Models

Climate models have become a unique opportunity to study past, present and future climate states as they function as a complementary way to further characterise and understand the climate system. Climate models can be described as mathematical representation of the climate system. The representation is based on physical, chemical and biological principles that describe mechanisms of the Earth system, its elements and their interactions. Climate models are overall unable to analytically solve these mechanisms. They instead provide spatially and temporally discretised solutions, i.e., the equations are numerically solved. This means that climate models split the Earth into many boxes called grid cells. The size of these grid cells is known as spatial resolution and can vary from one to another climate model (e.g., Fig.

1.13). Climate models also use parametrisations to represent finer processes and to include approximations of mechanisms that cannot be expressed in a mathematical equation. The latter are based on empirical evidence.

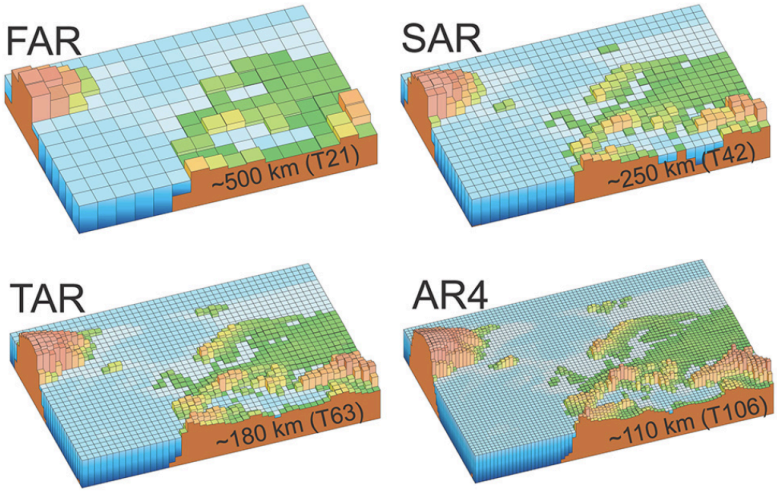

Figure 1.13: Geographic resolution characteristic of the generations of climate models used in the IPCC Assessment Reports. First ("FAR") published in 1990, second ("SAR") in 1995, third ("TAR") in 2001 and fourth ("AR4") in 2007. Source: adapted from Fig. 1.4 in IPCC (2007).

The choice of the model generally depends on the scientific purpose and on technical considerations such as available computing power and storage facilities. Studies often use less complex models when the research question focuses on large number of experiments or it aims attention at largely temporal and spatial scales. Available climate models are normally classified according to their complexity. Models range from very simple low-dimensional box models like one-dimensional energy balance models to very complex models, also called comprehensive climate models, e.g., Earth System Models (ESMs; examples in Fig. 1.13; Trenberth, 1992; IPCC, 2007). ESMs usually contain sub-models, e.g., ocean, the atmosphere, the ice, the land surface, that encompass all interactive three-dimensional processes of the climate system. It is important to mention that the spatial resolution can vary across these sub-models (e.g., Hofer et al., 2012b; Merz et al., 2014; Meehl et al., 2019; Lofverstrom et al., 2020). Two climate models are used in this thesis: the global climate model Community Climate System Model version 4 (CCSM4) and the regional climate model Weather Research and Forecasting (WRF) model. Besides the climate models, the vegetation model Lund-Potsdamn-Jena-LMfire (LPJ-LMfire) is employed in combination with the two climate models in this thesis. Both climate models and the vegetation model are in detail described in chapter 2.

1.5.3 Glacial Periods

Glacial climate states are of great interest for a variety of scientists as their climate conditions are highly different compared to today's climate. This offers the opportunity to further understand the Earth's system under different forcing factors. This thesis focuses on

two glacial climate states: the Last Glacial Maximum (LGM) and the Marine Isotope Stage 4 (MIS4). Both climate states are briefly introduced in the following.

The Last Glacial Maximum is the most recent glacial period and dates back to around 21 thousand years ago (Yokoyama et al., 2000; Clark et al., 2009; Van Meerbeeck et al., 2009; Hughes et al., 2013). Compared to present day, the LGM was characterised by large ice sheets in the Northern Hemisphere (e.g., Fig. 1.14), a global mean temperature roughly 5 to 6.5 °C colder (Otto-Bliesner et al., 2006; Löfverström et al., 2014), a global sea level of 115 to 130 m lower (Lambeck and Chappell, 2001; Lambeck et al., 2014; Peltier and Fairbanks, 2006), and the atmospheric greenhouse gases (GHGs) in a lower concentration (Brady et al., 2013; Cao et al., 2019). The global sea-level lowering led to global changes in the land-sea distribution and its associated coastlines (e.g., Fig. 1.14). Closure of the Bering Strait is for example one of the most prominent variations in the northern hemispheric land-sea geography (e.g. Hu et al., 2007, 2010, 2015). The atmospheric circulation was strongly altered by these global changes, especially by the large ice sheets (e.g., Laîné et al., 2009; Löfverström et al., 2014; Ullman et al., 2014; Beghin et al., 2015; Löfverström et al., 2016) and the different land-sea distribution (e.g., DiNezio and Tierney, 2013). This accordingly affected precipitation patterns (e.g. Bartlein et al., 2011; Beghin et al., 2016; Lora, 2018; Lofverstrom, 2020).

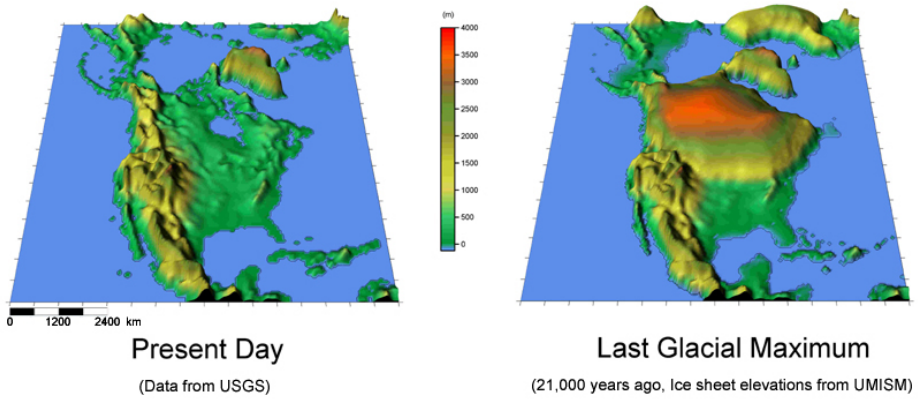

Figure 1.14: Schematic land surface and coastlines (topography) over North America at present day and LGM. Left panel represents the topography from present day and right from LGM. Elevated LGM topography is results of an increased ice-sheet thickness and the different coastlines is due to the lowered sea level. Source: http://polarmet.osu.edu/paleonwp/terrain.jpg.

In Europe, proxy reconstructions suggest that the LGM climate was 10 to 14 °C colder and around 200 mm year^{-1} drier compared to present day (Wu et al., 2007; Bartlein et al., 2011). These climatic conditions have strong implications not only for nature but also for humans as they drove the human behaviour during the LGM (Burke et al., 2017; Wren and Burke, 2019), e.g., the spatial distribution of populations and the influence on the cultural and biological evolution (Kaplan et al., 2016). For example, small groups of highly mobile Upper Paleolithic hunter-gatherers persisted in the face of inhospitable climate, while Neanderthals disappeared (Finlayson, 2004; Finlayson et al., 2006; Finlayson, 2008; Burke et al., 2014; Maier et al., 2016; Baena Preysler et al., 2019; Klein et al., 2021).

The Last Glacial Maximum is the most studied glacial period in terms of climate simulations, e.g., Earth system modelling. The reason is that its very different boundary conditions are well known (Mix et al., 2001), which makes the LGM be a good testbed of models' ability to faithfully reproduce a range of other climate states (e.g., Mix et al., 2001; Braconnot et al., 2012; Harrison et al., 2014, 2015; Janská et al., 2017; Cleator et al., 2020). Global climate models (GCMs) are generally consistent with the proxy reconstructions in simulating an LGM European climate that is largely colder than present day (e.g., Ludwig et al., 2016; Hofer et al., 2012a). However, GCMs partly disagree in comparison to proxy reconstructions, particularly concerning the magnitude and spatial patterning of temperature and precipitation (Harrison et al., 2015). The coarse spatial resolution of the GCMs is one possible reason for the disagreement. GCMs may not appropriately represent all the processes, especially the influences of mountains, ice sheets, and water bodies on the regional climate (Rauscher et al., 2010; Gómez-Navarro et al., 2011, 2012, 2013; Di Luca et al., 2012; Prein et al., 2013; Demory et al., 2020; Iles et al., 2020).

The application of regional climate models (RCMs) has led to improvements in the representation of regional and local climate (e.g., Kjellström et al., 2010; Strandberg et al., 2011; Gómez-Navarro et al., 2012, 2013; Ludwig et al., 2017, 2020). Regional climate models downscale the information of GCMs, which offers a clear benefit to answer paleoclimate research questions as it improves the interpretation of climate modelling and proxy reconstructions during the LGM (Ludwig et al., 2019). Still, studies have demonstrated that RCMs require appropriate surface boundary conditions to properly represent the lower troposphere as they play a crucial role in regulating water and energy fluxes between the land surface and the atmosphere (e.g., Crowley and Baum, 1997; Kjellström et al., 2010; Strandberg et al., 2011, 2014; Gómez-Navarro et al., 2015; Jia et al., 2019; Ludwig et al., 2017, 2019). This becomes the first focus of this thesis: a more accurate representation of the regional glacial climate. For the better representation, the regional climate model WRF is used in combination with the global climate model CCSM4 and the vegetation model LPJ-LMfire. Please see chapter 2 for a detailed information about WRF, CCSM4 and LPJ-LMfire.

The analysis of this thesis is extended to the glacial period Marine Isotope Stage 4 (MIS4) which is the predecessor glacial period of LGM and dates back to around 65 thousand years ago (Boch et al., 2011; Obrochta et al., 2014). Compared to present day, the available proxy reconstructions suggest that the MIS4 had a minimum summer insolation in the Northern Hemisphere (Goñi and D'Errico, 2005), a global mean temperature approximately 3 to 4 °C colder (Löfverström et al., 2014), a global sea-level drop of roughly 90 ± 10 m (e.g., Cutler et al., 2003; Siddall et al., 2008, 2010; De Deckker et al., 2019) and ocean temperatures up to 10 °C lower (Goñi and D'Errico, 2005). Compared to the LGM, proxy reconstructions characterise the MIS4 to be warmer (e.g., Eggleston et al., 2016; Newnham et al., 2017; De Deckker et al., 2019) with higher GHGs (e.g. CO_2; Eggleston et al., 2016). Note that these relatively warmer conditions are still enough to define MIS4 as glacial period since they were colder compared to the previous and after millennia (e.g., De Deckker et al., 2019). Also, these relatively higher GHGs were still low compared to present day. For humans, these MIS4 climatic conditions

have strong implications as Homo sapiens started migrating out-of-Africa towards Eurasia during this period (Tierney et al., 2017). Still, the MIS4 climate is less understood than the LGM as proxy-based data availability is reduced (López-García et al., 2018), especially on regional scales, e.g., over Europe. Moreover, there is very few evidence about the role of the ice-sheet topography in the regional climate like the Alps during glacial times, which becomes the second focuses of this thesis. To assess the MIS4 climate and the role of the topography, the regional climate model WRF is employed to carry out several sensitivity experiments.

Even though regional climate modelling provides a better understanding of the climate system, biases can still be evident in the simulations, especially in precipitation (e.g., Ban et al., 2014; Gómez-Navarro et al., 2018). These biases may impact the results obtained through hydrological and glacier modelling that follows next in the modelling chain (Allen and Ingram, 2002; Seguinot et al., 2014; Felder et al., 2018). The correction of these biases is the third focus of this thesis. A new correction method is presented for glacial conditions using an empirical quantile technique.

1.6 Outline

The central goal of this thesis is to investigate the impact of glacial surface conditions on the European climate using climate model simulations at glacial times. To achieve this, the thesis focuses on three specific aims. The first specific aim is to estimate the role of the land surface in the European glacial climate using the regional climate model WRF. To that end, a more accurate glacial land cover is created using an asynchronous coupled modelling design that combines the CCSM4, WRF and LPJ-LMfire models. The second specific aim is to determine the influence of the ice-sheet topography on the Alpine climate using several sensitive simulations done with the regional climate model WRF. The sensitive simulations consist of modifying the thickness of northern hemispheric ice sheets: either the Laurentide, Fennoscandian or Alpine ice sheet. Both specific aims are highly relevant for the interpretation of proxy records and the further understanding of the regional climate as they can more accurately represent regional-to-local processes compared to global climate simulations. The last specific objective is to build a bias-correction method whose application is more appropriate under highly different climate conditions such as glacial times. Thus, this thesis presents a new bias-correction method for precipitation based on an empirical quantile mapping technique and orographic features. This last objective is particularly important for glaciologists as they use climate information as input for their glacier models. Accordingly, the following leading research questions are formulated:

- *What is the role of the land surface on the European climate at glacial times?*
- *How does the ice-sheet topography influence the Alpine climate at glacial times?*

- *What method is more appropriate to correct precipitation biases in glacial simulations?*

Each research question is responded in an individual chapter. The thesis is structured as follows:

Chapter 2 describes the main tool of this thesis. It introduces the regional climate model WRF and briefly describes its components: The model's dynamical solvers are presented, which contain most physics packages. A preprocessing system is also explained as it is needed to prepare the terrestrial and meteorological data, i.e., input and boundary conditions, to run WRF. This chapter also describes the models used to create the terrestrial and meteorological data. Finally, the simulations that are analysed in this thesis are described in detail.

Chapter 3 estimates the role of the land surface in the European glacial climate. It explains the asynchronous coupled modelling design that is used for building the new land cover of Europe at the LGM. Results of the coupled model experiment are evaluated using independent reconstructions of land cover and climate. Additionally, sensitivity tests are performed to better understand the importance of land cover, which is done by forcing the regional climate model with an alternative set of land-surface boundary conditions. This study is published in the journal Climate of the Past (Velasquez et al., 2021).

Chapter 4 determines the influence of the ice-sheet topography on the Alpine glacial climate. It explains the performance of two sets of sensitive tests: changes in the ice-sheet topography of the North Hemisphere but not Alpine region, and changes only in the Alpine ice-sheet topography. This chapter investigates the atmospheric branch of the hydrological cycle over the Alpine region, particularly the changes in the precipitation patterns. To better understand the driving mechanisms of these changes, this chapter also investigates the changes in the atmospheric vertical profiles and wind fields over the Alpine region. This study has been submitted to the journal Climate of the Past and it is under review (preprint, Velasquez et al., 2021).

Chapter 5 presents a new bias correction that produces more reliable climate information. It describes the bias-correction method that is based on complex orographic features with focus on the Alpine region. Method's performance is evaluated using a present-day climate simulation and observational gridded data. The application to other climate states is assessed with a LGM simulation, where the Alpine topography is strongly changed. This study is published in the journal Geoscientific Model Development (Velasquez et al., 2020).

Chapter 6 provides a short discussion of the major results of this thesis. Additionally, some shortcomings and possible follow-up studies are mentioned.

Bibliography

Adolphi, F., Bronk Ramsey, C., Erhardt, T., Edwards, R. L., Cheng, H., Turney, C. S. M., Cooper, A., Svensson, A., Rasmussen, S. O., Fischer, H., and Muscheler, R.: Connecting the Greenland ice-core and U/Th timescales via cosmogenic radionuclides: testing the synchroneity of Dansgaard–Oeschger events, Climate of the Past, 14, 1755–1781, doi:10.5194/cp-14-1755-2018, 2018.

Allen, M. R. and Ingram, W. J.: Constraints on future changes in climate and the hydrologic cycle, doi: 10.1038/nature01092, 2002.

American Meteorological Society: Glossary of meteorology, URL http://glossary.ametsoc.org/wiki/Main_Page, 2019.

Asshoff, R., Zotz, G., and Körner, C.: Growth and phenology of mature temperate forest trees in elevated CO2, Global Change Biology, 12, 848–861, doi:10.1111/j.1365-2486.2006.01133.x, 2006.

Aubrey, D., Poulsen, T. M., and Veyret, P.: Alps | Britannica, URL https://www.britannica.com/place/Alps, 2020.

Ault, T. R., Macalady, A. K., Pederson, G. T., Betancourt, J. L., and Schwartz, M. D.: Northern Hemisphere modes of variability and the timing of spring in western North America, Journal of Climate, 24, 4003–4014, doi:10.1175/2011JCLI4069.1, 2011.

Baena Preysler, J., Carrión Santafé, E., Torres Navas, C., and Vaquero Rodríguez, M.: Mousterian inside the upper Paleolithic? The last interval of El Esquilleu (Cantabria, Spain) sequence, Quaternary International, 508, 153–163, doi:10.1016/j.quaint.2018.11.015, 2019.

Ban, N., Schmidli, J., and Schär, C.: Evaluation of the convection-resolving regional climate modeling approach in decade-long simulations, Journal of Geophysical Research: Atmospheres, 119, 7889–7907, doi:10.1002/2014JD021478, 2014.

Bartlein, P. J., Harrison, S. P., Brewer, S., Connor, S., Davis, B. A. S., Gajewski, K., Guiot, J., Harrison-Prentice, T. I., Henderson, A., Peyron, O., Prentice, I. C., Scholze, M., Seppä, H., Shuman, B., Sugita, S., Thompson, R. S., Viau, A. E., Williams, J., and Wu, H.: Pollen-based continental climate reconstructions at 6 and 21 ka: a global synthesis, Climate Dynamics, 37, 775–802, doi:10.1007/s00382-010-0904-1, 2011.

Bartolini, E., Claps, P., and D'Odorico, P.: Interannual variability of winter precipitation in the European Alps: relations with the North Atlantic Oscillation., Hydrology and Earth System Sciences, 13, 17–25, doi:10.5194/hess-13-17-2009, 2009.

Beghin, P., Charbit, S., Dumas, C., Kageyama, M., and Ritz, C.: How might the North American ice sheet influence the northwestern Eurasian climate?, Climate of the Past, 11, 1467–1490, doi:10.5194/cp-11-1467-2015, 2015.

Beghin, P., Charbit, S., Kageyama, M., Combourieu-Nebout, N., Hatté, C., Dumas, C., and Peterschmitt, J.-Y.: What drives LGM precipitation over the western Mediterranean? A study focused on the Iberian Peninsula and northern Morocco, Climate Dynamics, 46, 2611–2631, doi:10.1007/s00382-015-2720-0, 2016.

Bell, C. J., Gray, L. J., Charlton-Perez, A. J., Joshi, M. M., and Scaife, A. A.: Stratospheric communication of El Niño teleconnections to European winter, Journal of Climate, 22, 4083–4096, doi:10.1175/2009JCLI2717.1, 2009.

Benninghoff, W. S.: Interaction of vegetation and soil frost phenomena, Arctic, 5, 34–44, publisher: Arctic Institute of North America, 1952.

Bjorkman, A. D., García Criado, M., Myers-Smith, I. H., Ravolainen, V., Jónsdóttir, I. S., Westergaard, K. B., Lawler, J. P., Aronsson, M., Bennett, B., Gardfjell, H., Heiðmarsson, S., Stewart, L., and Normand, S.: Status and trends in Arctic vegetation: evidence from experimental warming and long-term monitoring, Ambio, 49, 678–692, doi:10.1007/s13280-019-01161-6, 2020.

Blackmon, M. L.: A climatological spectral study of the 500 mb geopotential height of the Northern Hemisphere, Journal of the Atmospheric Sciences, 33, 1607–1623, 1976.

Boch, R., Cheng, H., Spötl, C., Edwards, R. L., Wang, X., and Häuselmann, P.: NALPS: a precisely dated European climate record 120–60 ka, Climate of the Past, 7, 1247–1259, doi:10.5194/cp-7-1247-2011, 2011.

Bond, W. J., Midgley, G. F., and Woodward, F. I.: The importance of low atmospheric CO2 and fire in promoting the spread of grasslands and savannas, Global Change Biology, 9, 973–982, doi:10.1046/j.1365-2486.2003.00577.x, 2003.

Boucher, K. R.: Europe, climate of, in: Climatology, Encyclopedia of Earth Science, pp. 428–445, Springer, Boston, MA, US, doi:10.1007/0-387-30749-4_72, 1987.

Braconnot, P., Harrison, S. P., Kageyama, M., Bartlein, P. J., Masson-Delmotte, V., Abe-Ouchi, A., Otto-Bliesner, B., and Zhao, Y.: Evaluation of climate models using palaeoclimatic data, Nature Climate Change, 2, 417–424, doi:10.1038/nclimate1456, 2012.

Brady, E. C., Otto-Bliesner, B. L., Kay, J. E., and Rosenbloom, N.: Sensitivity to glacial forcing in the CCSM4, Journal of Climate, 26, 1901–1925, doi:10.1175/JCLI-D-11-00416.1, 2013.

Brandimarte, L., Di Baldassarre, G., Bruni, G., D'Odorico, P., and Montanari, A.: Relation between the North-Atlantic Oscillation and hydroclimatic conditions in Mediterranean areas, Water Resources Management, 25, 1269–1279, doi:10.1007/s11269-010-9742-5, 2011.

Brayshaw, D. J., Hoskins, B., and Blackburn, M.: The basic ingredients of the North Atlantic storm track. Part I: land–sea contrast and orography, Journal of Atmospheric Sciences, 66, 2539–2558, doi:10.1175/2009JAS3078.1, 2009.

Bridge, J. and Demicco, R.: Earth surface processes, landforms and sediment deposits, Cambridge University Press, Cambridge, United Kingdom and New York, NY, USA, 2008.

Brönnimann, S., Xoplaki, E., Casty, C., Pauling, A., and Luterbacher, J.: ENSO influence on Europe during the last centuries, Climate Dynamics, 28, 181–197, doi:10.1007/s00382-006-0175-z, 2007.

Brook, E. J. and Buizert, C.: Antarctic and global climate history viewed from ice cores, Nature, 558, 200–208, doi:10.1038/s41586-018-0172-5, 2018.

Burke, A., Levavasseur, G., James, P. M. A., Guiducci, D., Izquierdo, M. A., Bourgeon, L., Kageyama, M., Ramstein, G., and Vrac, M.: Exploring the impact of climate variability during the Last Glacial Maximum on the pattern of human occupation of Iberia, Journal of Human Evolution, 73, 35–46, doi:10.1016/j.jhevol.2014.06.003, 2014.

Burke, A., Kageyama, M., Latombe, G., Fasel, M., Vrac, M., Ramstein, G., and James, P. M. A.: Risky business: the impact of climate and climate variability on human population dynamics in Western Europe during the Last Glacial Maximum, Quaternary Science Reviews, 164, 217–229, doi:10.1016/j.quascirev.2017.04.001, 2017.

Camuera, J., Jiménez-Moreno, G., Ramos-Román, M. J., García-Alix, A., Toney, J. L., Anderson, R. S., Jiménez-Espejo, F., Bright, J., Webster, C., Yanes, Y., and Carrión, J. S.: Vegetation and climate changes during the last two glacial-interglacial cycles in the western Mediterranean: a new long pollen record from Padul (southern Iberian Peninsula), Quaternary Science Reviews, 205, 86–105, doi:10.1016/j.quascirev.2018.12.013, 2019.

Cao, J., Wang, B., and Liu, J.: Attribution of the Last Glacial Maximum climate formation, Climate Dynamics, 53, 1661–1679, doi:10.1007/s00382-019-04711-6, 2019.

Casazza, M., Lega, M., Liu, G., Ulgiati, S., and Endreny, T. A.: Aerosol pollution, including eroded soils, intensifies cloud growth, precipitation, and soil erosion: a review, Journal of Cleaner Production, 189, 135–144, doi:10.1016/j.jclepro.2018.04.004, 2018.

Cheng, H., Zhang, H., Zhao, J., Li, H., Ning, Y., and Kathayat, G.: Chinese stalagmite paleoclimate researches: a review and perspective, Science China Earth Sciences, 62, 1489–1513, doi:10.1007/s11430-019-9478-3, 2019.

Christensen, M. W., Jones, W. K., and Stier, P.: Aerosols enhance cloud lifetime and brightness along the stratus-to-cumulus transition, Proceedings of the National Academy of Sciences, 117, 17 591–17 598, doi:10.1073/pnas.1921231117, 2020.

Church, J. A., Clark, P. U., Cazenave, A., Gregory, J. M., Jevrejeva, S., Levermann, A., Merrifield, M. A., Milne, G. A., Nerem, R. S., Nunn, P. D., and others: Sea level change in: Climate Change 2013: The Physical Science Basis. Contribution of Working Group I to the Fifth Assessment Report of the Intergovernmental Panel on Climate Change [Stocker, T.F., D. Qin, G.-K. Plattner, M. Tignor, S.K. Allen, J. Boschung, A. Nauels, Y. Xia, V. Bex and P.M. Midgley (eds.)]., Cambridge University Press, Cambridge, United Kingdom and New York, NY, USA, 2013.

Cienciala, E., Altman, J., Doležal, J., Kopáček, J., Štěpánek, P., Ståhl, G., and Tumajer, J.: Increased spruce tree growth in Central Europe since 1960s, Science of The Total Environment, 619-620, 1637–1647, doi:10.1016/j.scitotenv.2017.10.138, 2018.

Clark, P. U., Pisias, N. G., Stocker, T. F., and Weaver, A. J.: The role of the thermohaline circulation in abrupt climate change, Nature, 415, 863–869, doi:10.1038/415863a, 2002.

Clark, P. U., Dyke, A. S., Shakun, J. D., Carlson, A. E., Clark, J., Wohlfarth, B., Mitrovica, J. X., Hostetler, S. W., and McCabe, A. M.: The Last Glacial Maximum, Science, 325, 710–714, doi:10.1126/science.1172873, 2009.

Cleator, S. F., Harrison, S. P., Nichols, N. K., Prentice, I. C., and Roulstone, I.: A new multivariable benchmark for Last Glacial Maximum climate simulations, Climate of the Past, 16, 699–712, doi:10.5194/cp-16-699-2020, 2020.

Crowley, T. J. and Baum, S. K.: Effect of vegetation on an ice-age climate model simulation, Journal of Geophysical Research: Atmospheres, 102, 16 463–16 480, doi:10.1029/97JD00536, 1997.

Cuffey, K. and Paterson, W. S. B.: The physics of glaciers, Elsevier and Academic Press, Kidlington, Oxford, United Kingdom and Burlington, MA, USA, 4th edn., 2010.

Cutler, K. B., Edwards, R. L., Taylor, F. W., Cheng, H., Adkins, J., Gallup, C. D., Cutler, P. M., Burr, G. S., and Bloom, A. L.: Rapid sea-level fall and deep-ocean temperature change since the last interglacial period, Earth and Planetary Science Letters, 206, 253–271, doi:10.1016/S0012-821X(02)01107-X, 2003.

Dave, P., Patil, N., Bhushan, M., and Venkataraman, C.: Aerosol influences on cloud modification and rainfall suppression in the south Asian monsoon region, in: Climate Change Signals and Response. A strategic knowledge compendium for India, edited by Venkataraman, C., Mishra, T., Ghosh, S., and Karmakar, S., pp. 21–37, Springer, Singapore, doi:10.1007/978-981-13-0280-0_2, 2019.

De Deckker, P., Arnold, L. J., van der Kaars, S., Bayon, G., Stuut, J.-B. W., Perner, K., Lopes dos Santos, R., Uemura, R., and Demuro, M.: Marine Isotope Stage 4 in Australasia: a full glacial culminating 65,000 years ago – global connections and implications for human dispersal, Quaternary Science Reviews, 204, 187–207, doi:10.1016/j.quascirev.2018.11.017, 2019.

Dee, D. P., Uppala, S. M., Simmons, A. J., Berrisford, P., Poli, P., Kobayashi, S., Andrae, U., Balmaseda, M. A., Balsamo, G., Bauer, P., Bechtold, P., Beljaars, A. C. M., Berg, L. v. d., Bidlot, J., Bormann, N., Delsol, C., Dragani, R., Fuentes, M., Geer, A. J., Haimberger, L., Healy, S. B., Hersbach, H., Hólm, E. V., Isaksen, L., Kållberg, P., Köhler, M., Matricardi, M., McNally, A. P., Monge-Sanz, B. M., Morcrette, J.-J., Park, B.-K., Peubey, C., Rosnay, P. d., Tavolato, C., Thépaut, J.-N., and Vitart, F.: The ERA-Interim reanalysis: configuration and performance of the data assimilation system, Quarterly Journal of the Royal Meteorological Society, 137, 553–597, doi:10.1002/qj.828, 2011.

Demory, M.-E., Berthou, S., Fernández, J., Sørland, S. L., Brogli, R., Roberts, M. J., Beyerle, U., Seddon, J., Haarsma, R., Schär, C., Buonomo, E., Christensen, O. B., Ciarlo ?, J. M., Fealy, R., Nikulin, G., Peano, D., Putrasahan, D., Roberts, C. D., Senan, R., Steger, C., Teichmann, C., and Vautard, R.: European daily precipitation according to EURO-CORDEX regional climate models (RCMs) and high-resolution global climate models (GCMs) from the High-Resolution Model Intercomparison Project (HighResMIP), Geoscientific Model Development, 13, 5485–5506, doi:10.5194/gmd-13-5485-2020, 2020.

Di Luca, A., de Elía, R., and Laprise, R.: Potential for added value in precipitation simulated by high-resolution nested regional climate models and observations, Climate Dynamics, 38, 1229–1247, doi:10.1007/s00382-011-1068-3, 2012.

Dickinson, W. C., Lambers, H., Yopp, J. H., Woodwell, G. M., Schmid, R., and Rothwell, G. W.: Plant, URL https://www.britannica.com/plant/plant, 2020.

DiNezio, P. N. and Tierney, J. E.: The effect of sea level on glacial Indo-Pacific climate, Nature Geoscience, 6, 485–491, doi:10.1038/ngeo1823, 2013.

Domeisen, D. I. V., Butler, A. H., Fröhlich, K., Bittner, M., Müller, W. A., and Baehr, J.: Seasonal predictability over Europe arising from El Niño and stratospheric variability in the MPI-ESM seasonal prediction system, Journal of Climate, 28, 256–271, doi:10.1175/JCLI-D-14-00207.1, 2015.

Dugarsuren, N. and Lin, C.: Simulation of net primary productivity in Mongolia using CASA Model, during 2000-2004, Mongolian Journal of Biological Sciences, 14, 43–51, doi:10.22353/mjbs.2016.14.06, 2016.

Earle, S.: Physical geology - 2nd edition, BCcampus, 2019.

Eggleston, S., Schmitt, J., Bereiter, B., Schneider, R., and Fischer, H.: Evolution of the stable carbon isotope composition of atmospheric CO2 over the last glacial cycle, Paleoceanography, 31, 434–452, doi:10.1002/2015PA002874, 2016.

Eichelberger, S. J. and Hartmann, D. L.: Zonal jet structure and the leading mode of variability, Journal of Climate, 20, 5149–5163, doi:10.1175/JCLI4279.1, 2007.

Emile-Geay, J., McKay, N. P., Kaufman, D. S., von Gunten, L., Wang, J., Anchukaitis, K. J., Abram, N. J., Addison, J. A., Curran, M. A., Evans, M. N., Henley, B. J., Hao, Z., Martrat, B., McGregor, H. V., Neukom, R., Pederson, G. T., Stenni, B., Thirumalai, K., Werner, J. P., Xu, C., Divine, D. V., Dixon, B. C., Gergis, J., Mundo, I. A., Nakatsuka, T., Phipps, S. J., Routson, C. C., Steig, E. J., Tierney, J. E., Tyler, J. J., Allen, K. J., Bertler, N. A., Björklund, J., Chase, B. M., Chen, M.-T., Cook, E., de Jong, R., DeLong, K. L., Dixon, D. A., Ekaykin, A. A., Ersek, V., Filipsson, H. L., Francus, P., Freund, M. B., Frezzotti, M., Gaire, N. P., Gajewski, K., Ge, Q., Goosse, H., Gornostaeva, A., Grosjean, M., Horiuchi, K., Hormes, A., Husum, K., Isaksson, E., Kandasamy, S., Kawamura, K., Kilbourne, K. H., Koç, N., Leduc, G., Linderholm, H. W., Lorrey, A. M., Mikhalenko, V., Mortyn, P. G., Motoyama, H., Moy, A. D., Mulvaney, R., Munz, P. M., Nash, D. J., Oerter, H., Opel, T., Orsi, A. J., Ovchinnikov, D. V., Porter, T. J., Roop, H. A., Saenger, C., Sano, M., Sauchyn, D., Saunders, K. M., Seidenkrantz, M.-S., Severi, M., Shao, X., Sicre, M.-A., Sigl, M., Sinclair, K., St. George, S., St. Jacques, J.-M., Thamban, M., Kuwar Thapa, U., Thomas, E. R., Turney, C., Uemura, R., Viau, A. E., Vladimirova, D. O., Wahl, E. R., White, J. W., Yu, Z., Zinke, J., and PAGES2k Consortium: A

global multiproxy database for temperature reconstructions of the Common Era, Scientific Data, 4, 170 088, doi:10.1038/sdata.2017.88, 2017.

Erhardt, T., Capron, E., Rasmussen, S. O., Schüpbach, S., Bigler, M., Adolphi, F., and Fischer, H.: Decadal-scale progression of the onset of Dansgaard–Oeschger warming events, Climate of the Past, 15, 811–825, doi:10.5194/cp-15-811-2019, 2019.

Fairchild, I. J. and Treble, P. C.: Trace elements in speleothems as recorders of environmental change, Quaternary Science Reviews, 28, 449–468, doi:10.1016/j.quascirev.2008.11.007, 2009.

Felder, G., Gómez-Navarro, J. J., Zischg, A. P., Raible, C. C., Röthlisberger, V., Bozhinova, D., Martius, O., and Weingartner, R.: From global circulation to local flood loss: Coupling models across the scales, Science of The Total Environment, 635, 1225–1239, doi:10.1016/j.scitotenv.2018.04.170, 2018.

Ferrel, W.: An essay on the winds and currents of ocean, Nashville journal of medicine and surgery, 11, 1856.

Finlayson, C.: Neanderthals and modern humans: an ecological and evolutionary perspective, vol. 38, Cambridge University Press, 2004.

Finlayson, C.: On the importance of coastal areas in the survival of Neanderthal populations during the Late Pleistocene, Quaternary Science Reviews, 27, 2246–2252, doi:10.1016/j.quascirev.2008.08.033, 2008.

Finlayson, C., Giles Pacheco, F., Rodríguez-Vidal, J., Fa, D. A., María Gutierrez López, J., Santiago Pérez, A., Finlayson, G., Allue, E., Baena Preysler, J., Cáceres, I., Carrión, J. S., Fernández Jalvo, Y., Gleed-Owen, C. P., Jimenez Espejo, F. J., López, P., Antonio López Sáez, J., Antonio Riquelme Cantal, J., Sánchez Marco, A., Giles Guzman, F., Brown, K., Fuentes, N., Valarino, C. A., Villalpando, A., Stringer, C. B., Martinez Ruiz, F., and Sakamoto, T.: Late survival of Neanderthals at the southernmost extreme of Europe, Nature, 443, 850–853, doi:10.1038/nature05195, 2006.

Fletcher, A. L., Sinclair, T. R., and Allen, L. H.: Transpiration responses to vapor pressure deficit in well watered 'slow-wilting' and commercial soybean, Environmental and Experimental Botany, 61, 145–151, doi:10.1016/j.envexpbot.2007.05.004, 2007.

Fraedrich, K.: An ENSO impact on Europe?, Tellus A, 46, 541–552, doi:10.1034/j.1600-0870.1994.00015.x, 1994.

Frei, C. and Schär, C.: A precipitation climatology of the Alps from high-resolution rain-gauge observations, International Journal of Climatology, 18, 873–900, doi:10.1002/(SICI)1097-0088(19980630)18:8⟨873::AID-JOC255⟩3.0.CO;2-9, 1998.

Garcia-Carreras, L., Parker, D. J., and Marsham, J. H.: What is the mechanism for the modification of convective cloud distributions by land surface–induced flows?, Journal of the Atmospheric Sciences, 68, 619–634, doi:10.1175/2010JAS3604.1, 2011.

Gascoyne, M.: Palaeoclimate determination from cave calcite deposits, Quaternary Science Reviews, 11, 609–632, doi:10.1016/0277-3791(92)90074-I, 1992.

Gettelman, A. and Rood, R. B.: Components of the climate system, in: Demystifying Climate Models: A Users Guide to Earth System Models, edited by Gettelman, A. and Rood, R. B., Earth Systems Data and Models, pp. 13–22, Springer, Berlin, Heidelberg, doi:10.1007/978-3-662-48959-8_2, 2016.

Gómez-Navarro, J. J., Montávez, J. P., Jerez, S., Jiménez-Guerrero, P., Lorente-Plazas, R., González-Rouco, J. F., and Zorita, E.: A regional climate simulation over the Iberian Peninsula for the last millennium, Climate of the Past, 7, 451–472, doi:10.5194/cp-7-451-2011, 2011.

Gómez-Navarro, J. J., Montávez, J. P., Jiménez-Guerrero, P., Jerez, S., Lorente-Plazas, R., González-Rouco, J. F., and Zorita, E.: Internal and external variability in regional simulations of the Iberian Peninsula climate over the last millennium, Climate of the Past, 8, 25–36, doi:10.5194/cp-8-25-2012, 2012.

Gómez-Navarro, J. J., Montávez, J. P., Wagner, S., and Zorita, E.: A regional climate palaeosimulation for Europe in the period 1500-1990 - Part 1: model validation, Climate of the Past, 9, 1667–1682, doi:10.5194/cp-9-1667-2013, 2013.

Gómez-Navarro, J. J., Bothe, O., Wagner, S., Zorita, E., Werner, J. P., Luterbacher, J., Raible, C. C., and Montávez, J. P.: A regional climate palaeosimulation for Europe in the period 1500–1990 – Part 2: shortcomings and strengths of models and reconstructions, Climate of the Past, 11, 1077–1095, doi:10.5194/cp-11-1077-2015, 2015.

Gómez-Navarro, J. J., Raible, C. C., Bozhinova, D., Martius, O., García Valero, J. A., and Montávez, J. P.: A new region-aware bias-correction method for simulated precipitation in areas of complex orography, Geoscientific Model Development, 11, 2231–2247, doi:10.5194/gmd-11-2231-2018, 2018.

Goñi, M. F. S. and D'Errico, F.: La historia de la vegetación y el clima del último ciclo climático (OIS5-OIS1, 140.000-10.000 BP) en la Península Ibérica y su posible impacto sobre los grupos paleolíticos, pp. 115–129, Museo Nacional y Centro de Investigación de Altamira, Ministerio de Cultura, Dirección General de Bellas Artes y Bienes Culturales, Subdirección General de Museos Estatales, Altamira Museum, Cantabria, Spain, 2005.

Hack, J. J., Caron, J. M., Yeager, S. G., Oleson, K. W., Holland, M. M., Truesdale, J. E., and Rasch, P. J.: Simulation of the global hydrological cycle in the CCSM Community Atmosphere Model Version 3 (CAM3): mean features, Journal of Climate, 19, 2199–2221, doi:10.1175/JCLI3755.1, 2006.

Hadley, G.: Concerning the cause of the general trade-winds, Philosophical Transactions of the Royal Society of London, 39, 58–62, 1735.

Hansen, J., Sato, M., Kharecha, P., and von Schuckmann, K.: Earth's energy imbalance and implications, Atmospheric Chemistry and Physics, 11, 13 421–13 449, doi:10.5194/acp-11-13421-2011, 2011.

Harman, J. R.: Westerlies, middle-latitude west winds, in: Climatology, pp. 922–928, Springer US, Boston, MA, doi:10.1007/0-387-30749-4_197, 1987.

Harnik, N., Galanti, E., Martius, O., and Adam, O.: The anomalous merging of the African and North Atlantic jet dtreams during the Northern Hemisphere winter of 2010, Journal of Climate, 27, 7319–7334, doi:10.1175/JCLI-D-13-00531.1, 2014.

Harrison, S. P., Bartlein, P. J., Brewer, S., Prentice, I. C., Boyd, M., Hessler, I., Holmgren, K., Izumi, K., and Willis, K.: Climate model benchmarking with glacial and mid-Holocene climates, Climate Dynamics, 43, 671–688, doi:10.1007/s00382-013-1922-6, 2014.

Harrison, S. P., Bartlein, P. J., Izumi, K., Li, G., Annan, J., Hargreaves, J., Braconnot, P., and Kageyama, M.: Evaluation of CMIP5 palaeo-simulations to improve climate projections, Nature Climate Change, 5, 735–743, doi:10.1038/nclimate2649, 2015.

Hartmann, D. L., Tank, A. M. G. K., Rusticucci, M., Alexander, L. V., Brönnimann, S., Charabi, Y. A. R., Dentener, F. J., Dlugokencky, E. J., Easterling, D. R., Kaplan, A., Soden, B. J., Thorne, P. W., Wild, M., and Zhai, P.: Observations: atmosphere and surface, Climate Change 2013. The Physical Science Basis: Working Group I Contribution to the Fifth Assessment Report of the Intergovernmental Panel on Climate Change, pp. 159–254, doi:10.1017/CBO9781107415324.008, 2013.

Hawcroft, M. K., Shaffrey, L. C., Hodges, K. I., and Dacre, H. F.: How much Northern Hemisphere precipitation is associated with extratropical cyclones?, Geophysical Research Letters, 39, doi:10.1029/2012GL053866, 2012.

Held, I. M. and Hou, A. Y.: Nonlinear axially symmetric circulations in a nearly inviscid atmosphere, Journal of Atmospheric Sciences, 37, 515–533, doi:10.1175/1520-0469(1980)037⟨0515:NASCIA⟩2.0.CO;2, 1980.

Held, I. M., Ting, M., and Wang, H.: Northern winter stationary waves: theory and modeling, Journal of Climate, 15, 2125–2144, doi:10.1175/1520-0442(2002)015⟨2125:NWSWTA⟩2.0.CO;2, 2002.

Herceg-Bulić, I., Mezzina, B., Kucharski, F., Ruggieri, P., and King, M. P.: Wintertime ENSO influence on late spring European climate: the stratospheric response and the role of North Atlantic SST, International Journal of Climatology, 37, 87–108, doi:10.1002/joc.4980, 2017.

Hernández, A., Martin-Puertas, C., Moffa-Sánchez, P., Moreno-Chamarro, E., Ortega, P., Blockley, S., Cobb, K. M., Comas-Bru, L., Giralt, S., Goosse, H., Luterbacher, J., Martrat, B., Muscheler, R., Parnell, A., Pla-Rabes, S., Sjolte, J., Scaife, A. A., Swingedouw, D., Wise, E., and Xu, G.: Modes of climate variability: synthesis and review of proxy-based reconstructions through the Holocene, Earth-Science Reviews, 209, 103 286, doi:10.1016/j.earscirev.2020.103286, 2020.

Hofer, D., Raible, C. C., Dehnert, A., and Kuhlemann, J.: The impact of different glacial boundary conditions on atmospheric dynamics and precipitation in the North Atlantic region, Climate of the Past, 8, 935–949, doi:10.5194/cp-8-935-2012, 2012a.

Hofer, D., Raible, C. C., Merz, N., Dehnert, A., and Kuhlemann, J.: Simulated winter circulation types in the North Atlantic and European region for preindustrial and glacial conditions: glacial circulation types, Geophysical Research Letters, 39, L15 805, doi:10.1029/2012GL052296, 2012b.

Holton, J. R. and Hakim, G. J.: An introduction to dynamic meteorology, Elsevier, doi:10.1016/C2009-0-63394-8, 2013.

Hordon, R. M.: Hydrological cycle, in: Encyclopedia of Hydrology and Lakes, Encyclopedia of Earth Science, pp. 367–371, Springer, Dordrecht, Netherlands, doi:10.1007/1-4020-4497-6_116, 1998.

Hoskins, B. J., James, I. N., and White, G. H.: The shape, propagation and mean-flow interaction of large-scale weather systems, Journal of the Atmospheric Sciences, 40, 1595–1612, doi:10.1175/1520-0469(1983)040⟨1595:TSPAMF⟩2.0.CO;2, 1983.

Houghton, H. G.: A preliminary quantitative analysis of precipitation mechanisms, Journal of Atmospheric Sciences, 7, 363–369, doi:10.1175/1520-0469(1950)007⟨0363:APQAOP⟩2.0.CO;2, 1950.

Houze, R. A.: Cloud dynamics, Elsevier and Academic Press, 2nd edn., 2014.

Hu, A., Meehl, G. A., and Han, W.: Role of the Bering Strait in the thermohaline circulation and abrupt climate change, Geophysical Research Letters, 34, doi:10.1029/2006GL028906, 2007.

Hu, A., Meehl, G. A., Otto-Bliesner, B. L., Waelbroeck, C., Han, W., Loutre, M.-F., Lambeck, K., Mitrovica, J. X., and Rosenbloom, N.: Influence of Bering Strait flow and North Atlantic circulation on glacial sea-level changes, Nature Geoscience, 3, 118–121, doi:10.1038/ngeo729, 2010.

Hu, A., Meehl, G. A., Han, W., Otto-Bliestner, B., Abe-Ouchi, A., and Rosenbloom, N.: Effects of the Bering Strait closure on AMOC and global climate under different background climates, Progress in Oceanography, 132, 174–196, doi:10.1016/j.pocean.2014.02.004, 2015.

Hughes, P. D., Gibbard, P. L., and Ehlers, J.: Timing of glaciation during the last glacial cycle: evaluating the concept of a global 'Last Glacial Maximum' (LGM), Earth-Science Reviews, 125, 171–198, doi:10.1016/j.earscirev.2013.07.003, 2013.

Hurrell, J. W. and Deser, C.: North Atlantic climate variability: the role of the North Atlantic Oscillation, Journal of Marine Systems, 79, 231–244, doi:10.1016/j.jmarsys.2009.11.002, 2010.

Hurrell, J. W., Kushnir, Y., Ottersen, G., and Visbeck, M.: An overview of the North Atlantic Oscillation, in: The North Atlantic Oscillation: Climatic Significance and Environmental Impact, Geophysical Monograph Series, pp. 1–35, American Geophysical Union, doi:10.1029/134GM01, 2003.

Huss, M.: Present and future contribution of glacier storage change to runoff from macroscale drainage basins in Europe, Water Resources Research, 47, doi:10.1029/2010WR010299, 2011.

Hutchinson, G. E.: The biosphere, Scientific American, 223, 44–53, 1970.

Iles, C. E., Vautard, R., Strachan, J., Joussaume, S., Eggen, B. R., and Hewitt, C. D.: The benefits of increasing resolution in global and regional climate simulations for European climate extremes, Geoscientific Model Development, 13, 5583–5607, doi:10.5194/gmd-13-5583-2020, 2020.

Immerzeel, W. W., Beek, L. P. H. v., and Bierkens, M. F. P.: Climate change will affect the Asian water towers, Science, 328, 1382–1385, doi:10.1126/science.1183188, 2010.

IPCC: Climate Change 2001: The Scientific Basis. Contribution of Working Group I to the Third Assessment Report of the Intergovernmental Panel on Climate Change [Houghton, J.T., Y. Ding, D.J. Griggs, M. Noguer, P.J. van der Linden, X. Dai, K. Maskell, and C.A. Johnson (eds.)], Cambridge University Press, Cambridge, United Kingdom and New York, NY, USA, 881 pp., 2001.

IPCC: Climate Change 2007: The Physical Science Basis: Working Group I Contribution to the Fourth Assessment Report of the Intergovernmental Panel on Climate Change [Solomon, S., D. Qin, M. Manning, Z. Chen, M. Marquis, K.B. Averyt, M. Tignor and H.L. Miller (eds.)], Cambridge University Press, Cambridge, United Kingdom and New York, NY, USA, 996 pp., 2007.

IPCC: Annex III: Glossary [Planton, S. (ed.)]. In: Climate Change 2013: The Physical Science Basis. Contribution of Working Group I to the Fifth Assessment Report of the Intergovernmental Panel on Climate Change [Stocker, T.F., D. Qin, G.-K. Plattner, M. Tignor, S.K. Allen, J. Boschung, A. Nauels, Y. Xia, V. Bex and P.M. Midgley (eds.)]., Cambridge University Press, Cambridge, United Kingdom and New York, NY, USA, 1535 pp, 2013a.

IPCC: Climate Change 2013: The Physical Science Basis. Contribution of Working Group I to the Fifth Assessment Report of the Intergovernmental Panel on Climate Change [Stocker, T.F., D. Qin, G.-K. Plattner, M. Tignor, S.K. Allen, J. Boschung, A. Nauels, Y. Xia, V. Bex and P.M. Midgley (eds.)], Cambridge University Press, Cambridge, United Kingdom and New York, NY, USA, 1535 pp, 2013b.

IPCC: Climate Change and Land: an IPCC special report on climate change, desertification, land degradation, sustainable land management, food security, and greenhouse gas fluxes in terrestrial ecosystems [P.R. Shukla, J. Skea, E. Calvo Buendia, V. Masson-Delmotte, H.-O. Pörtner, D. C. Roberts, P. Zhai, R. Slade, S. Connors, R. van Diemen, M. Ferrat, E. Haughey, S. Luz, S. Neogi, M. Pathak, J. Petzold, J. Portugal Pereira, P. Vyas, E. Huntley, K. Kissick, M. Belkacemi, J. Malley, (eds.)], in press., 2019a.

IPCC: IPCC Special Report on the Ocean and Cryosphere in a Changing Climate [H.-O. Pörtner, D.C. Roberts, V. Masson-Delmotte, P. Zhai, M. Tignor, E. Poloczanska, K. Mintenbeck, A. Alegría, M. Nicolai, A. Okem, J. Petzold, B. Rama, N.M. Weyer (eds.)], in press, 2019b.

Ivasić, S., Herceg-Bulić, I., and King, M. P.: Recent weakening in the winter ENSO teleconnection over the North Atlantic-European region, Climate Dynamics, doi:10.1007/s00382-021-05783-z, 2021.

Jamalinia, E., Vardon, P. J., and Steele-Dunne, S. C.: The effect of soil–vegetation–atmosphere interaction on slope stability: a numerical study, Environmental Geotechnics, pp. 1–12, doi:10.1680/jenge.18.00201, 2019.

JAMSTEC: How does orbital variations affect ancient Antarctica?: East Antarctic ice volume change during Pliocene and Early Pleistocene, Press release, Japan Agency for Marine-Earth Science and Technology, Japan, URL https://www.jamstec.go.jp/e/about/press_release/20141027/, 2014.

Janská, V., Jiménez-Alfaro, B., Chytrý, M., Divíšek, J., Anenkhonov, O., Korolyuk, A., Lashchinskyi, N., and Culek, M.: Palaeodistribution modelling of European vegetation types at the Last Glacial Maximum

using modern analogues from Siberia: prospects and limitations, Quaternary Science Reviews, 159, 103–115, doi:10.1016/j.quascirev.2017.01.011, 2017.

Jia, G., Shevliakova, E., Artaxo, P., Noblet-Ducoudré, N. D., Houghton, R., House, J., Kitajima, K., Lennard, C., Popp, A., Sirin, A., Sukumar, R., and Verchot, L.: Land–climate interactions. In: Climate Change and Land: an IPCC special report on climate change, desertification, land degradation, sustainable land management, food security, and greenhouse gas fluxes in terrestrial ecosystems [P.R. Shukla, J. Skea, E. Calvo Buendia, V. Masson-Delmotte, H.-O. Pörtner, D.C. Roberts, P. Zhai, R. Slade, S. Connors, R. van Diemen, M. Ferrat, E. Haughey, S. Luz, S. Neogi, M. Pathak, J. Petzold, J. Portugal Pereira, P. Vyas, E. Huntley, K. Kissick, M, Belkacemi, J. Malley, (eds.)]. In press., 2019.

Kalimeris, A., Ranieri, E., Founda, D., and Norrant, C.: Variability modes of precipitation along a Central Mediterranean area and their relations with ENSO, NAO, and other climatic patterns, Atmospheric Research, 198, 56–80, doi:10.1016/j.atmosres.2017.07.031, 2017.

Kang, S.-L. and Bryan, G. H.: A large-eddy Simulation study of moist convection initiation over heterogeneous surface fluxes, Monthly Weather Review, 139, 2901–2917, doi:10.1175/MWR-D-10-05037.1, 2011.

Kaplan, J. O., Pfeiffer, M., Kolen, J. C. A., and Davis, B. A. S.: Large scale anthropogenic reduction of forest cover in Last Glacial Maximum Europe, PLOS ONE, 11, e0166 726, doi:10.1371/journal.pone.0166726, 2016.

Kaser, G., Großhauser, M., and Marzeion, B.: Contribution potential of glaciers to water availability in different climate regimes, Proceedings of the National Academy of Sciences, 107, 20 223–20 227, doi:10.1073/pnas.1008162107, 2010.

Kaspi, Y. and Schneider, T.: The role of stationary eddies in shaping midlatitude storm tracks, Journal of Atmospheric Sciences, 70, 2596–2613, doi:10.1175/JAS-D-12-082.1, 2013.

Keeley, S. P. E., Collins, M., and Thorpe, A. J.: Northern Hemisphere winter atmospheric climate: modes of natural variability and climate change, Climate Dynamics, 31, 195–211, doi:10.1007/s00382-007-0346-6, 2008.

Kjellström, E., Brandefelt, J., Näslund, J.-O., Smith, B., Strandberg, G., Voelker, A. H. L., and Wohlfarth, B.: Simulated climate conditions in Europe during the Marine Isotope Stage 3 stadial, Boreas, 39, 436–456, doi:10.1111/j.1502-3885.2010.00143.x, 2010.

Klein, K., Wegener, C., Schmidt, I., Rostami, M., Ludwig, P., Ulbrich, S., Richter, J., Weniger, G.-C., and Shao, Y.: Human existence potential in Europe during the Last Glacial Maximum, Quaternary International, 581-582, 7–27, doi:10.1016/j.quaint.2020.07.046, 2021.

Kundzewicz, Z. W., Szwed, M., and Pińskwar, I.: Climate variability and floods—a global review, Water, 11, 1399, doi:10.3390/w11071399, 2019.

Laîné, A., Kageyama, M., Salas-Mélia, D., Voldoire, A., Rivière, G., Ramstein, G., Planton, S., Tyteca, S., and Peterschmitt, J. Y.: Northern hemisphere storm tracks during the last glacial maximum in the PMIP2 ocean-atmosphere coupled models: energetic study, seasonal cycle, precipitation, Climate Dynamics, 32, 593–614, doi:10.1007/s00382-008-0391-9, 2009.

Lamarche, V. C., Graybill, D. A., Fritts, H. C., and Rose, M. R.: Increasing atmospheric carbon dioxide: tree ring evidence for growth enhancement in natural vegetation, Science, 225, 1019–1021, doi:10.1126/science.225.4666.1019, 1984.

Lambeck, K. and Chappell, J.: Sea level change through the last glacial cycle, Science, 292, 679–686, doi:10.1126/science.1059549, 2001.

Lambeck, K., Rouby, H., Purcell, A., Sun, Y., and Sambridge, M.: Sea level and global ice volumes from the Last Glacial Maximum to the Holocene, Proceedings of the National Academy of Sciences, 111, 15 296–15 303, doi:10.1073/pnas.1411762111, 2014.

Lambert, F., Bigler, M., Steffensen, J. P., Hutterli, M., and Fischer, H.: Centennial mineral dust variability in high-resolution ice core data from Dome C, Antarctica, Climate of the Past, 8, 609–623, doi:10.5194/cp-8-609-2012, 2012.

Latif, M. and Keenlyside, N. S.: El Niño/Southern Oscillation response to global warming, Proceedings of the National Academy of Sciences, 106, 20 578–20 583, doi:10.1073/pnas.0710860105, 2009.

Letzel, M. O. and Raasch, S.: Large eddy simulation of thermally induced oscillations in the convective boundary layer, Journal of the Atmospheric Sciences, 60, 2328–2341, doi:10.1175/1520-0469(2003)060⟨2328:LESOTI⟩2.0.CO;2, 2003.

Levy, P., Dijk, N. v., Gray, A., Sutton, M., Jones, M., Leeson, S., Dise, N., Leith, I., and Sheppard, L.: Response of a peat bog vegetation community to long-term experimental addition of nitrogen, Journal of Ecology, 107, 1167–1186, doi:10.1111/1365-2745.13107, 2019.

Li, B., Nychka, D. W., and Ammann, C. M.: The value of multiproxy reconstruction of past climate, Journal of the American Statistical Association, 105, 883–895, doi:10.1198/jasa.2010.ap09379, 2010.

Li, C. and Wettstein, J. J.: Thermally driven and eddy-driven jet variability in reanalysis, Journal of Climate, 25, 1587–1596, doi:10.1175/JCLI-D-11-00145.1, 2012.

Li, Y., Guan, K., Schnitkey, G. D., DeLucia, E., and Peng, B.: Excessive rainfall leads to maize yield loss of a comparable magnitude to extreme drought in the United States, Global Change Biology, 25, 2325–2337, doi:10.1111/gcb.14628, 2019.

Lin, J. and Qian, T.: A new picture of the global impacts of El Nino-Southern Oscillation, Scientific Reports, 9, 17 543, doi:10.1038/s41598-019-54090-5, 2019.

Lionello, P., Malanotte-Rizzoli, P., Boscolo, R., Alpert, P., Artale, V., Li, L., Luterbacher, J., May, W., Trigo, R., Tsimplis, M., Ulbrich, U., and Xoplaki, E.: The Mediterranean climate: an overview of the main characteristics and issues, in: Developments in Earth and Environmental Sciences, edited by Lionello, P., Malanotte-Rizzoli, P., and Boscolo, R., vol. 4 of *Mediterranean*, pp. 1–26, Elsevier, doi:10.1016/S1571-9197(06)80003-0, 2006.

Liou, K. N.: An introduction to atmospheric radiation, vol. 84 of *International geophysics series*, Elsevier, San Diego, CA, USA and London, UK, 2nd edn., 2002.

Lloyd, A. H. and Bunn, A. G.: Responses of the circumpolar boreal forest to 20th century climate variability, Environmental Research Letters, 2, 045 013, doi:10.1088/1748-9326/2/4/045013, 2007.

Lockwood, J. G.: Atmospheric circulation, global, in: Climatology, pp. 131–140, Springer, Boston, MA, doi:10.1007/0-387-30749-4_20, 1987.

Loeb, N. G., Wielicki, B. A., Doelling, D. R., Smith, G. L., Keyes, D. F., Kato, S., Manalo-Smith, N., and Wong, T.: Toward optimal closure of the Earth's top-of-atmosphere radiation budget, Journal of Climate, 22, 748–766, doi:10.1175/2008JCLI2637.1, 2009.

Lofverstrom, M.: A dynamic link between high-intensity precipitation events in southwestern North America and Europe at the Last Glacial Maximum, Earth and Planetary Science Letters, 534, 116 081, doi:10.1016/j.epsl.2020.116081, 2020.

Löfverström, M., Caballero, R., Nilsson, J., and Kleman, J.: Evolution of the large-scale atmospheric circulation in response to changing ice sheets over the last glacial cycle, Climate of the Past, 10, 1453–1471, doi:10.5194/cp-10-1453-2014, 2014.

Löfverström, M., Caballero, R., Nilsson, J., and Messori, G.: Stationary wave reflection as a mechanism for zonalizing the Atlantic winter jet at the LGM, Journal of the Atmospheric Sciences, 73, 3329–3342, doi:10.1175/JAS-D-15-0295.1, 2016.

Lofverstrom, M., Fyke, J. G., Thayer-Calder, K., Muntjewerf, L., Vizcaino, M., Sacks, W. J., Lipscomb, W. H., Otto-Bliesner, B. L., and Bradley, S. L.: An efficient ice sheet/Earth system model spin-up procedure for CESM2-CISM2: description, evaluation, and broader applicability, Journal of Advances in Modeling Earth Systems, 12, e2019MS001 984, doi:10.1029/2019MS001984, 2020.

López-García, J. M., Livraghi, A., Romandini, M., and Peresani, M.: The De Nadale Cave (Zovencedo, Berici Hills, northeastern Italy): a small-mammal fauna from near the onset of Marine Isotope Stage 4 and its palaeoclimatic implications, Palaeogeography, Palaeoclimatology, Palaeoecology, 506, 196–201, doi:10.1016/j.palaeo.2018.06.033, 2018.

López-Parages, J., Rodríguez-Fonseca, B., Dommenget, D., and Frauen, C.: ENSO influence on the North Atlantic European climate: a non-linear and non-stationary approach, Climate Dynamics, 47, 2071–2084, doi:10.1007/s00382-015-2951-0, 2016.

Lora, J. M.: Components and mechanisms of hydrologic cycle changes over North America at the Last Glacial Maximum, Journal of Climate, 31, 7035–7051, doi:10.1175/JCLI-D-17-0544.1, 2018.

Lu, K.-Q., Li, M., Wang, G.-H., Xu, L.-S., Ferguson, D. K., Trivedi, A., Xuan, J., Feng, Y., Li, J.-F., Xie, G., Yao, Y.-F., and Wang, Y.-F.: New pollen classification of Chenopodiaceae for exploring and tracing desert vegetation evolution in eastern arid central Asia, Journal of Systematics and Evolution, 57, 190–199, doi:10.1111/jse.12462, 2019.

Ludwig, P., Schaffernicht, E. J., Shao, Y., and Pinto, J. G.: Regional atmospheric circulation over Europe during the Last Glacial Maximum and its links to precipitation, Journal of Geophysical Research: Atmospheres, 121, 2130–2145, doi:10.1002/2015JD024444, 2016.

Ludwig, P., Pinto, J. G., Raible, C. C., and Shao, Y.: Impacts of surface boundary conditions on regional climate model simulations of European climate during the Last Glacial Maximum, Geophysical Research Letters, 44, 5086–5095, doi:10.1002/2017GL073622, 2017.

Ludwig, P., Gómez-Navarro, J. J., Pinto, J. G., Raible, C. C., Wagner, S., and Zorita, E.: Perspectives of regional paleoclimate modeling, Annals of the New York Academy of Sciences, 1436, 54–69, doi:10.1111/nyas.13865, 2019.

Ludwig, P., Gavrilov, M. B., Markovic, S. B., Ujvari, G., and Lehmkuhl, F.: Simulated regional dust cycle in the Carpathian Basin and the Adriatic Sea region during the Last Glacial Maximum, Quaternary International, 581-582, 114–127, doi:10.1016/j.quaint.2020.09.048, 2020.

Lutgens, F. K. and Tarbuck, E. J.: The atmosphere: an introduction to meteorology, Prentince Hall/Pearson Education, New York City, USA, 8th edn., URL ISBN-13:9780130879578, 512 pp., 2001.

Machar, I., Vlckova, V., Bucek, A., Vozenilek, V., Salek, L., and Jerabkova, L.: Modelling of climate conditions in forest vegetation zones as a support tool for forest management strategy in European Beech dominated forests, Forests, 8, 82, doi:10.3390/f8030082, 2017.

Maier, A., Lehmkuhl, F., Ludwig, P., Melles, M., Schmidt, I., Shao, Y., Zeeden, C., and Zimmermann, A.: Demographic estimates of hunter–gatherers during the Last Glacial Maximum in Europe against the background of palaeoenvironmental data, Quaternary International, 425, 49–61, doi:10.1016/j.quaint.2016.04.009, 2016.

Mann, M. E., Zhang, Z., Rutherford, S., Bradley, R. S., Hughes, M. K., Shindell, D., Ammann, C., Faluvegi, G., and Ni, F.: Global Signatures and Dynamical Origins of the Little Ice Age and Medieval Climate Anomaly, Science, 326, 1256–1260, doi:10.1126/science.1177303, 2009.

Marquer, L., Gaillard, M.-J., Sugita, S., Poska, A., Trondman, A.-K., Mazier, F., Nielsen, A. B., Fyfe, R. M., Jönsson, A. M., Smith, B., Kaplan, J. O., Alenius, T., Birks, H. J. B., Bjune, A. E., Christiansen, J., Dodson, J., Edwards, K. J., Giesecke, T., Herzschuh, U., Kangur, M., Koff, T., Latałowa, M., Lechterbeck, J., Olofsson, J., and Seppä, H.: Quantifying the effects of land use and climate on Holocene vegetation in Europe, Quaternary Science Reviews, 171, 20–37, doi:10.1016/j.quascirev.2017.07.001, 2017.

Marshall, J., Kushnir, Y., Battisti, D., Chang, P., Czaja, A., Dickson, R., Hurrell, J., McCartney, M., Saravanan, R., and Visbeck, M.: North Atlantic climate variability: phenomena, impacts and mechanisms, International Journal of Climatology, 21, 1863–1898, doi:10.1002/joc.693, 2001.

McDermott, F.: Palaeo-climate reconstruction from stable isotope variations in speleothems: a review, Quaternary Science Reviews, 23, 901–918, doi:10.1016/j.quascirev.2003.06.021, 2004.

McPherson, R. A.: A review of vegetation—atmosphere interactions and their influences on mesoscale phenomena, Progress in Physical Geography: Earth and Environment, 31, 261–285, doi:10.1177/0309133307079055, 2007.

Meehl, G. A., Yang, D., Arblaster, J. M., Bates, S. C., Rosenbloom, N., Neale, R., Bacmeister, J., Lauritzen, P. H., Bryan, F., Small, J., Truesdale, J., Hannay, C., Shields, C., Strand, W. G., Dennis, J., and Danabasoglu, G.: Effects of model resolution, physics, and coupling on Southern Hemisphere storm tracks in CESM1.3, Geophysical Research Letters, 46, 12 408–12 416, doi:10.1029/2019GL084057, 2019.

Meier, M. F.: Glacier, URL https://www.britannica.com/science/glacier, 2020.

Meier, M. F. and Ashton, G. D. A.: Ice, URL https://www.britannica.com/science/ice, 2020.

Merz, N., Gfeller, G., Born, A., Raible, C. C., Stocker, T. F., and Fischer, H.: Influence of ice sheet topography on Greenland precipitation during the Eemian interglacial, Journal of Geophysical Research: Atmospheres, 119, 10,749–10,768, doi:10.1002/2014JD021940, 2014.

Messaoud, Y. and Chen, H. Y. H.: The influence of tecent climate change on tree height growth differs with species and spatial environment, PLOS ONE, 6, e14 691, doi:10.1371/journal.pone.0014691, 2011.

Metzger, J. C., Wutzler, T., Valle, N. D., Filipzik, J., Grauer, C., Lehmann, R., Roggenbuck, M., Schelhorn, D., Weckmüller, J., Küsel, K., Totsche, K. U., Trumbore, S., and Hildebrandt, A.: Vegetation impacts soil water content patterns by shaping canopy water fluxes and soil properties, Hydrological Processes, 31, 3783–3795, doi:10.1002/hyp.11274, 2017.

Mezzina, B., García-Serrano, J., Bladé, I., and Kucharski, F.: Dynamics of the ENSO teleconnection and NAO variability in the North Atlantic–European Late winter, Journal of Climate, 33, 907–923, doi:10.1175/JCLI-D-19-0192.1, 2020.

Milankovitch, M. K.: Kanon der Erdbestrahlung und seine Anwendung auf das Eiszeitenproblem, Royal Serbian Academy Special Publication, 133, 1–633, 1941.

Mitchell, J. F. B.: The "Greenhouse" effect and climate change, Reviews of Geophysics, 27, 115–139, doi:10.1029/RG027i001p00115, 1989.

Mitchell, J. M.: An overview of climatic variability and its causal mechanisms, Quaternary Research, 6, 481–493, doi:10.1016/0033-5894(76)90021-1, 1976.

Mix, A. C., Bard, E., and Schneider, R.: Environmental processes of the ice age: land, oceans, glaciers (EPILOG), Quaternary Science Reviews, 20, 627–657, doi:10.1016/S0277-3791(00)00145-1, 2001.

Moore, D. J. P., Aref, S., Ho, R. M., Pippen, J. S., Hamilton, J. G., and Lucia, E. H. D.: Annual basal area increment and growth duration of Pinus taeda in response to eight years of free-air carbon dioxide enrichment, Global Change Biology, 12, 1367–1377, doi:10.1111/j.1365-2486.2006.01189.x, 2006.

Narasimhan, T. N.: Hydrological cycle and water budgets, in: Encyclopedia of Inland Waters, edited by Likens, G. E., pp. 714–720, Academic Press, Oxford, doi:10.1016/B978-012370626-3.00010-7, 2009.

NCEI: National Centers of Enviromental Information: What Are Proxy Data?. National Oceanic and Atmospheric Administration (NOAA), URL http://www.ncei.noaa.gov/news/what-are-proxy-data, 2018.

Newnham, R. M., Alloway, B. V., Holt, K. A., Butler, K., Rees, A. B. H., Wilmshurst, J. M., Dunbar, G., and Hajdas, I.: Last Glacial pollen–climate reconstructions from Northland, New Zealand, Journal of Quaternary Science, 32, 685–703, doi:10.1002/jqs.2955, 2017.

Nigam, S. and DeWeaver, E.: Stationary waves (orographic and thermally forced), in: Ecyclopedia of Atmospheric Sciences, edited by Holton, J. R. and et al., pp. 2121–2137, Academi Press, 2003.

Nisbet, E. G., Manning, M. R., Dlugokencky, E. J., Fisher, R. E., Lowry, D., Michel, S. E., Myhre, C. L., Platt, S. M., Allen, G., Bousquet, P., Brownlow, R., Cain, M., France, J. L., Hermansen, O., Hossaini, R., Jones, A. E., Levin, I., Manning, A. C., Myhre, G., Pyle, J. A., Vaughn, B. H., Warwick, N. J., and White, J. W. C.: Very strong atmospheric methane growth in the 4 years 2014–2017: implications for the Paris agreement, Global Biogeochemical Cycles, 33, 318–342, doi:10.1029/2018GB006009, 2019.

Niu, G.-Y. and Zeng, X.: Earth system model, modeling the land component of, in: Climate Change Modeling Methodology: Selected Entries from the Encyclopedia of Sustainability Science and Technology, edited by Rasch, P. J., pp. 139–168, Springer, New York, NY, doi:10.1007/978-1-4614-5767-1_7, 2012.

Nobre, G. G., Jongman, B., Aerts, J., and Ward, P. J.: The role of climate variability in extreme floods in Europe, Environmental Research Letters, 12, 084 012, doi:10.1088/1748-9326/aa7c22, 2017.

Obrochta, S. P., Yokoyama, Y., Morén, J., and Crowley, T. J.: Conversion of GISP2-based sediment core age models to the GICC05 extended chronology, Quaternary Geochronology, 20, 1–7, doi:10.1016/j.quageo.2013.09.001, 2014.

Oki, T. and Kanae, S.: Global hydrological cycles and world water resources, Science, 313, 1068–1072, doi:10.1126/science.1128845, 2006.

O'Reilly, C. H., Minobe, S., Kuwano-Yoshida, A., and Woollings, T.: The Gulf Stream influence on wintertime North Atlantic jet variability, Quarterly Journal of the Royal Meteorological Society, 143, 173–183, doi:10.1002/qj.2907, 2017.

O'Reilly, C. H., Woollings, T., and Zanna, L.: The Dynamical Influence of the Atlantic Multidecadal Oscillation on Continental Climate, Journal of Climate, 30, 18, 2017.

Otto-Bliesner, B. L., Brady, E. C., Clauzet, G., Tomas, R., Levis, S., and Kothavala, Z.: Last Glacial Maximum and Holocene climate in CCSM3, Journal of Climate, 19, 2526–2544, doi:10.1175/JCLI3748.1, 2006.

Overpeck, J., Whitlock, C., and Huntley, B.: Terrestrial biosphere dynamics in the climate system: past and future, in: Paleoclimate, Global Change and the Future, edited by Alverson, K. D., Pedersen, T. F., and Bradley, R. S., Global change — The IGBP series, pp. 81–103, Springer Berlin Heidelberg, Berlin, Heidelberg, doi:10.1007/978-3-642-55828-3_5, 2003.

Palter, J. B.: The role of the gulf stream in European climate, Annual Review of Marine Science, 7, 113–137, doi:10.1146/annurev-marine-010814-015656, 2015.

Panetta, R. L. and Held, I. M.: Baroclinic eddy fluxes in a one-dimensional model of quasi-geostrophic turbulence, Journal of Atmospheric Sciences, 45, 3354–3365, doi:10.1175/1520-0469(1988)045⟨3354:BEFIAO⟩2.0.CO;2, 1988.

Paterson, W. S. B.: Physics of glaciers, Butterworth-Heinemann, 1994.

Peixóto, J. P. and Oort, A. H.: The atmospheric branch of the hydrological cycle and climate, in: Variations in the Global Water Budget, edited by Street-Perrott, A., Beran, M., and Ratcliffe, R., pp. 5–65, Springer Netherlands, Dordrecht, doi:10.1007/978-94-009-6954-4_2, 1983.

Peltier, W. R. and Fairbanks, R. G.: Global glacial ice volume and Last Glacial Maximum duration from an extended Barbados sea level record, Quaternary Science Reviews, 25, 3322–3337, doi:10.1016/j.quascirev.2006.04.010, 2006.

Philander, S. G.: El niño, la niña, and the southern oscillation, vol. 46 of *Academic Press, International geophysics series*, Princeton University, geophysical fluid dynamics lab. NOAA, Princeton New Jersey, United States, 1989.

Phillips, J. D.: Earth surface systems, Blackwell Oxford, 1999.

Pierrehumbert, R. T.: The hydrologic cycle in deep-time climate problems, Nature, 419, 191–198, doi:10.1038/nature01088, 2002.

Pinto, J. G. and Raible, C. C.: Past and recent changes in the North Atlantic oscillation, WIREs Climate Change, 3, 79–90, doi:10.1002/wcc.150, 2012.

Piper, D. A., Kunz, M., Allen, J. T., and Mohr, S.: Investigation of the temporal variability of thunderstorms in central and western Europe and the relation to large-scale flow and teleconnection patterns, Quarterly Journal of the Royal Meteorological Society, 145, 3644–3666, doi:10.1002/qj.3647, 2019.

Prein, A. F., Holland, G. J., Rasmussen, R. M., Done, J., Ikeda, K., Clark, M. P., and Liu, C. H.: Importance of regional climate model grid spacing for the simulation of heavy precipitation in the Colorado headwaters, Journal of Climate, 26, 4848–4857, doi:10.1175/JCLI-D-12-00727.1, 2013.

Primeau, F.: Characterizing transport between the surface mixed layer and the ocean interior with a forward and adjoint global ocean transport model, Journal of Physical Oceanography, 35, 545–564, doi:10.1175/JPO2699.1, 2005.

Pruppacher, H. and Klett, J.: Microstructure of atmospheric clouds and precipitation, in: Microphysics of Clouds and Precipitation, edited by Pruppacher, H. and Klett, J., Atmospheric and Oceanographic Sciences Library, pp. 10–73, Springer Netherlands, Dordrecht, doi:10.1007/978-0-306-48100-0_2, 2010.

Rafferty, J. P.: North Atlantic Oscillation | climatology | Britannica, URL https://www.britannica.com/science/North-Atlantic-Oscillation, 2019.

Raible, C. C., Lehner, F., González-Rouco, J. F., and Fernández-Donado, L.: Changing correlation structures of the Northern Hemisphere atmospheric circulation from 1000 to 2100 AD, Climate of the Past, 10, 537–550, doi:10.5194/cp-10-537-2014, 2014.

Rauscher, S. A., Coppola, E., Piani, C., and Giorgi, F.: Resolution effects on regional climate model simulations of seasonal precipitation over Europe, Climate Dynamics, 35, 685–711, doi:10.1007/s00382-009-0607-7, 2010.

Raval, A. and Ramanathan, V.: Observational determination of the greenhouse effect, Nature, 342, 758–761, doi:10.1038/342758a0, 1989.

Rawson, H. M., Begg, J. E., and Woodward, R. G.: The effect of atmospheric humidity on photosynthesis, transpiration and water use efficiency of leaves of several plant species, Planta, 134, 5–10, doi:10.1007/BF00390086, 1977.

Rehm, E. M., Yelenik, S., and D'Antonio, C.: Freezing temperatures restrict woody plant recruitment and restoration efforts in abandoned montane pastures, Global Ecology and Conservation, p. e01462, doi:10.1016/j.gecco.2021.e01462, 2021.

Renne, R. R., Schlaepfer, D. R., Palmquist, K. A., Bradford, J. B., Burke, I. C., and Lauenroth, W. K.: Soil and stand structure explain shrub mortality patterns following global change–type drought and extreme precipitation, Ecology, 100, e02 889, doi:10.1002/ecy.2889, 2019.

Renssen, H., Seppä, H., Heiri, O., Roche, D. M., Goosse, H., and Fichefet, T.: The spatial and temporal complexity of the Holocene thermal maximum, Nature Geoscience, 2, 411–414, doi:10.1038/ngeo513, 2009.

Rogers, J. C.: Patterns of low-frequency monthly sea level pressure variability (1899–1986) and associated wave cyclone frequencies, Journal of Climate, 3, 1364–1379, doi:10.1175/1520-0442(1990)003⟨1364:POLFMS⟩2.0.CO;2, 1990.

Rosenfeld, D., Zhu, Y., Wang, M., Zheng, Y., Goren, T., and Yu, S.: Aerosol-driven droplet concentrations dominate coverage and water of oceanic low-level clouds, Science, 363, doi:10.1126/science.aav0566, 2019.

Rowland, F. S.: Stratospheric ozone depletion, in: Twenty Years of Ozone Decline, edited by Zerefos, C., Contopoulos, G., and Skalkeas, G., pp. 23–66, Springer Netherlands, Dordrecht, doi:10.1007/978-90-481-2469-5_5, 2009.

Schär, C., Davies, T. D., Frei, C., Wanner, H., Widmann, M., Wild, M., and Davies, H. C.: Current alpine climate, Views from the Alps: Regional perspectives on climate change, pp. 21–170, 1998.

Schilt, A., Baumgartner, M., Blunier, T., Schwander, J., Spahni, R., Fischer, H., and Stocker, T. F.: Glacial–interglacial and millennial-scale variations in the atmospheric nitrous oxide concentration during the last 800,000 years, Quaternary Science Reviews, 29, 182–192, doi:10.1016/j.quascirev.2009.03.011, 2010.

Schneider, T.: The general circulation of the atmosphere, Annual Review of Earth and Planetary Sciences, 34, 655–688, doi:10.1146/annurev.earth.34.031405.125144, 2006.

Schultz, D. M., Bosart, L. F., Colle, B. A., Davies, H. C., Dearden, C., Keyser, D., Martius, O., Roebber, P. J., Steenburgh, W. J., Volkert, H., and Winters, A. C.: Extratropical cyclones: a century of research on meteorology's centerpiece, Meteorological Monographs, 59, 16.1–16.56, doi:10.1175/AMSMONOGRAPHS-D-18-0015.1, 2019.

Schwarcz, H. P.: Chapter 7 - Geochronology and isotopic geochemistry of speleothems, in: The Terrestrial Environment, B, edited by Fritz, P. and Fontes, J. C., Handbook of Environmental Isotope Geochemistry, pp. 271–303, Elsevier, Amsterdam, doi:10.1016/B978-0-444-42225-5.50012-7, 1986.

Seager, R., Battisti, D. S., Yin, J., Gordon, N., Naik, N., Clement, A. C., and Cane, M. A.: Is the Gulf Stream responsible for Europe's mild winters?, Quarterly Journal of the Royal Meteorological Society, 128, 2563–2586, doi:10.1256/qj.01.128, 2002.

Segal, S.: Ecological studies of peat-bog vegetation in the north-western part of the province of Overijsel (The Netherlands), Wentia, 15, 109–141, 1966.

Seguinot, J., Khroulev, C., Rogozhina, I., Stroeven, A. P., and Zhang, Q.: The effect of climate forcing on numerical simulations of the Cordilleran ice sheet at the Last Glacial Maximum, The Cryosphere, 8, 1087–1103, doi:10.5194/tc-8-1087-2014, 2014.

Shi, W., Jiang, H., Mao, X., and Xu, H.: Pollen record of climate change during the last deglaciation from the eastern Tibetan Plateau, PLOS ONE, 15, e0232 803, doi:10.1371/journal.pone.0232803, 2020.

Sickmöller, M., Blender, R., and Fraedrich, K.: Observed winter cyclone tracks in the northern hemisphere in re-analysed ECMWF data, Quarterly Journal of the Royal Meteorological Society, 126, 591–620, doi:10.1002/qj.49712656311, 2000.

Siddall, M., Rohling, E. J., Thompson, W. G., and Waelbroeck, C.: Marine isotope stage 3 sea level fluctuations: data synthesis and new outlook, Reviews of Geophysics, 46, doi:10.1029/2007RG000226, 2008.

Siddall, M., Kaplan, M. R., Schaefer, J. M., Putnam, A., Kelly, M. A., and Goehring, B.: Changing influence of Antarctic and Greenlandic temperature records on sea-level over the last glacial cycle, Quaternary Science Reviews, 29, 410–423, doi:10.1016/j.quascirev.2009.11.007, 2010.

Sigman, D. M. and Boyle, E. A.: Glacial/interglacial variations in atmospheric carbon dioxide, Nature, 407, 859–869, doi:10.1038/35038000, 2000.

Smagorinsky, J.: The dynamical influence of large-scale heat sources and sinks on the quasi-stationary mean motions of the atmosphere, Quarterly Journal of the Royal Meteorological Society, 79, 342–366, doi:10.1002/qj.49707934103, 1953.

Sodemann, H. and Zubler, E.: Seasonal and inter-annual variability of the moisture sources for Alpine precipitation during 1995–2002, International Journal of Climatology, 30, 947–961, doi:10.1002/joc.1932, 2010.

Spracklen, D., Baker, J., Garcia-Carreras, L., and Marsham, J.: The effects of tropical vegetation on rainfall, Annual Review of Environment and Resources, 43, 193–218, doi:10.1146/annurev-environ-102017-030136, 2018.

Steirou, E., Gerlitz, L., Apel, H., and Merz, B.: Links between large-scale circulation patterns and streamflow in Central Europe: a review, Journal of Hydrology, 549, 484–500, doi:10.1016/j.jhydrol.2017.04.003, 2017.

Stewart, W. N. and Rothwell, G. W.: Paleobotany and the evolution of plants, Cambridge University Press, Cambridge, United Kingdom and New York, NY, USA, 2nd edn., 2010.

Strandberg, G., Brandefelt, J., Kjellstro M., E., and Smith, B.: High-resolution regional simulation of Last Glacial Maximum climate in Europe, Tellus A: Dynamic Meteorology and Oceanography, 63, 107–125, doi:10.1111/j.1600-0870.2010.00485.x, 2011.

Strandberg, G., Kjellström, E., Poska, A., Wagner, S., Gaillard, M.-J., Trondman, A.-K., Mauri, A., Davis, B. a. S., Kaplan, J. O., Birks, H. J. B., Bjune, A. E., Fyfe, R., Giesecke, T., Kalnina, L., Kangur, M., van der Knaap, W. O., Kokfelt, U., Kuneš, P., Lata\l owa, M., Marquer, L., Mazier, F., Nielsen, A. B., Smith, B., Seppä, H., and Sugita, S.: Regional climate model simulations for Europe at 6 and 0.2 k BP: sensitivity to changes in anthropogenic deforestation, Climate of the Past, 10, 661–680, doi:10.5194/cp-10-661-2014, 2014.

Sturman, A. and Wanner, H.: A comparative review of the weather and climate of the southern Alps of New Zealand and the European Alps, Mountain Research and Development, 21, 359–369, doi:10.1659/0276-4741(2001)021[0359:ACROTW]2.0.CO;2, 2001.

Svensson, A., Dahl-Jensen, D., Steffensen, J. P., Blunier, T., Rasmussen, S. O., Vinther, B. M., Vallelonga, P., Capron, E., Gkinis, V., Cook, E., Kjær, H. A., Muscheler, R., Kipfstuhl, S., Wilhelms, F., Stocker, T. F., Fischer, H., Adolphi, F., Erhardt, T., Sigl, M., Landais, A., Parrenin, F., Buizert, C., McConnell, J. R., Severi, M., Mulvaney, R., and Bigler, M.: Bipolar volcanic synchronization of abrupt climate change in Greenland and Antarctic ice cores during the last glacial period, Climate of the Past, 16, 1565–1580, doi:10.5194/cp-16-1565-2020, 2020.

Tan, L., Liu, W., Wang, T., Cheng, P., Zang, J., Wang, X., Ma, L., Li, D., Lan, J., Edwards, R. L., Cheng, H., Xu, H., Ai, L., Gao, Y., and Cai, Y.: A multiple-proxy stalagmite record reveals historical deforestation in central Shandong, northern China, Science China Earth Sciences, 63, 1622–1632, doi:10.1007/s11430-019-9649-1, 2020.

Tierney, J. E., deMenocal, P. B., and Zander, P. D.: A climatic context for the out-of-Africa migration, Geology, 45, 1023–1026, doi:10.1130/G39457.1, 2017.

Toggweiler, J. R. and Key, R. M.: Thermohaline circulation, in: Encyclopedia of Ocean Sciences, edited by Steele, J. H., pp. 2941–2947, Academic Press, Oxford, doi:10.1006/rwos.2001.0111, 2001.

Tomasi, C., Fuzzi, S., and Kokhanovsky, A.: Atmospheric aerosols: life cycles and effects on air quality and climate, John Wiley & Sons, 2017.

Trenberth, K. E.: Climate system modeling, Cambridge University Press, Cambridge, United Kingdom and New York, NY, USA, 1992.

Trenberth, K. E. and Caron, J. M.: Estimates of meridional atmosphere and ocean heat transports, Journal of Climate, 14, 3433–3443, doi:10.1175/1520-0442(2001)014⟨3433:EOMAAO⟩2.0.CO;2, 2001.

Ullman, D. J., LeGrande, A. N., Carlson, A. E., Anslow, F. S., and Licciardi, J. M.: Assessing the impact of Laurentide Ice Sheet topography on glacial climate, Climate of the Past, 10, 487–507, doi:10.5194/cp-10-487-2014, 2014.

USGS: U.S. Geological survey, paleoclimate research: proxies, URL https://www2.usgs.gov/landresources/lcs/paleoclimate/proxies.asp, 2021.

van Loon, H. and Rogers, J. C.: The seesaw in winter temperatures between Greenland and Northern Europe. Part I: general description, Monthly Weather Review, 106, 296–310, doi:10.1175/1520-0493(1978)106⟨0296:TSIWTB⟩2.0.CO;2, 1978.

Van Meerbeeck, C. J., Renssen, H., and Roche, D. M.: How did Marine Isotope Stage 3 and Last Glacial Maximum climates differ? – Perspectives from equilibrium simulations, Climate of the Past, 5, 33–51, doi:10.5194/cp-5-33-2009, 2009.

Van Niekerk, A.: The role of orographic drag in modelled atmospheric circulation, phd, University of Reading, URL http://centaur.reading.ac.uk/74795/, 2017.

Velasquez, P., Messmer, M., and Raible, C. C.: A new bias-correction method for precipitation over complex terrain suitable for different climate states: a case study using WRF (version 3.8.1), Geoscientific Model Development, 13, 5007–5027, doi:10.5194/gmd-13-5007-2020, 2020.

Velasquez, P., Kaplan, J. O., Messmer, M., Ludwig, P., and Raible, C. C.: The role of land cover in the climate of glacial Europe, Climate of the Past, 17, 1161–1180, doi:10.5194/cp-17-1161-2021, 2021.

Veldkamp, E., Schmidt, M., Powers, J. S., and Corre, M. D.: Deforestation and reforestation impacts on soils in the tropics, Nature Reviews Earth & Environment, 1, 590–605, doi:10.1038/s43017-020-0091-5, 2020.

Viron, O. d., Dickey, J. O., and Ghil, M.: Global modes of climate variability, Geophysical Research Letters, 40, 1832–1837, doi:10.1002/grl.50386, 2013.

Volosciuk, C., Maraun, D., Semenov, V. A., Tilinina, N., Gulev, S. K., and Latif, M.: Rising mediterranean sea surface temperatures amplify extreme summer precipitation in Central Europe, Scientific Reports, 6, 32 450, doi:10.1038/srep32450, 2016.

Wallace, J. M. and Hobbs, P. V.: Atmospheric science: an introductory survey, vol. 92, Elsevier, 2006.

Wang, P. K.: Physics and dynamics of clouds and precipitation, Cambridge University Press, Cambridge, doi:10.1017/CBO9780511794285, 2013.

Wanner, H., Brönnimann, S., Casty, C., Gyalistras, D., Luterbacher, J., Schmutz, C., Stephenson, D. B., and Xoplaki, E.: North Atlantic Oscillation – concepts and studies, Surveys in Geophysics, 22, 321–381, doi:10.1023/A:1014217317898, 2001.

Wanner, H., Beer, J., Bütikofer, J., Crowley, T. J., Cubasch, U., Flückiger, J., Goosse, H., Grosjean, M., Joos, F., Kaplan, J. O., Küttel, M., Müller, S. A., Prentice, I. C., Solomina, O., Stocker, T. F., Tarasov, P., Wagner, M., and Widmann, M.: Mid- to Late Holocene climate change: an overview, Quaternary Science Reviews, 27, 1791–1828, doi:10.1016/j.quascirev.2008.06.013, 2008.

Weertman, J.: On the sliding of glaciers, Journal of Glaciology, 3, 33–38, doi:10.3189/S0022143000024709, 1957.

Wernli, H. and Schwierz, C.: Surface cyclones in the ERA-40 dataset (1958–2001). Part I: novel identification method and global climatology, Journal of Atmospheric Sciences, 63, 2486–2507, doi:10.1175/JAS3766.1, 2006.

Wild, M., Folini, D., Schär, C., Loeb, N., Dutton, E. G., and König-Langlo, G.: The global energy balance from a surface perspective, Climate Dynamics, 40, 3107–3134, doi:10.1007/s00382-012-1569-8, 2013.

Willis, P. T. and Tattelman, P.: Drop-size distributions associated with intense rainfall, Journal of Applied Meteorology, 28, 3–15, doi:10.1175/1520-0450(1989)028⟨0003:DSDAWI⟩2.0.CO;2, 1989.

Woollings, T.: Dynamical influences on European climate: an uncertain future, Philosophical Transactions of the Royal Society A: Mathematical, Physical and Engineering Sciences, 368, 3733–3756, doi:10.1098/rsta.2010.0040, 2010.

Woollings, T., Hannachi, A., and Hoskins, B.: Variability of the North Atlantic eddy-driven jet stream, Quarterly Journal of the Royal Meteorological Society, 136, 856–868, doi:10.1002/qj.625, 2010.

Wren, C. D. and Burke, A.: Habitat suitability and the genetic structure of human populations during the Last Glacial Maximum (LGM) in Western Europe, PLOS ONE, 14, e0217 996, doi:10.1371/journal.pone.0217996, 2019.

Wu, H., Guiot, J., Brewer, S., and Guo, Z.: Climatic changes in Eurasia and Africa at the last glacial maximum and mid-Holocene: reconstruction from pollen data using inverse vegetation modelling, Climate Dynamics, 29, 211–229, doi:10.1007/s00382-007-0231-3, 2007.

Wyrtki, K.: The thermohaline circulation in relation to the general circulation in the oceans, Deep Sea Research (1953), 8, 39–64, doi:10.1016/0146-6313(61)90014-4, 1961.

Yan, D., Xu, T., Girma, A., Yuan, Z., Weng, B., Qin, T., Do, P., and Yuan, Y.: Regional correlation between precipitation and vegetation in the Huang-Huai-Hai river basin, China, Water, 9, 557, doi:10.3390/w9080557, 2017.

Yang, Y., Roderick, M. L., Zhang, S., McVicar, T. R., and Donohue, R. J.: Hydrologic implications of vegetation response to elevated CO 2 in climate projections, Nature Climate Change, 9, 44–48, doi:10.1038/s41558-018-0361-0, 2019.

Yokoyama, Y., Lambeck, K., De Deckker, P., Johnston, P., and Fifield, L. K.: Timing of the Last Glacial Maximum from observed sea-level minima, Nature, 406, 713–716, doi:10.1038/35021035, 2000.

Yuan, W., Zheng, Y., Piao, S., Ciais, P., Lombardozzi, D., Wang, Y., Ryu, Y., Chen, G., Dong, W., Hu, Z., Jain, A. K., Jiang, C., Kato, E., Li, S., Lienert, S., Liu, S., Nabel, J. E. M. S., Qin, Z., Quine, T., Sitch, S., Smith, W. K., Wang, F., Wu, C., Xiao, Z., and Yang, S.: Increased atmospheric vapor pressure deficit reduces global vegetation growth, Science Advances, 5, eaax1396, doi:10.1126/sciadv.aax1396, 2019.

Zeppel, M. J. B., Wilks, J. V., and Lewis, J. D.: Impacts of extreme precipitation and seasonal changes in precipitation on plants, Biogeosciences, 11, 3083–3093, doi:10.5194/bg-11-3083-2014, 2014.

Zhang, L., Fu, T.-M., Tian, H., Ma, Y., Chen, J.-P., Tsai, T.-C., Tsai, I.-C., Meng, Z., and Yang, X.: Anthropogenic aerosols significantly reduce mesoscale convective system occurrences and precipitation over Southern China in April, Geophysical Research Letters, 47, e2019GL086 204, doi:10.1029/2019GL086204, 2020.

Zhao, A. D., Stevenson, D. S., and Bollasina, M. A.: The role of anthropogenic aerosols in future precipitation extremes over the Asian Monsoon region, Climate Dynamics, 52, 6257–6278, doi:10.1007/s00382-018-4514-7, 2019.

Zheng, K., Wei, J.-Z., Pei, J.-Y., Cheng, H., Zhang, X.-L., Huang, F.-Q., Li, F.-M., and Ye, J.-S.: Impacts of climate change and human activities on grassland vegetation variation in the Chinese Loess Plateau, Science of The Total Environment, 660, 236–244, doi:10.1016/j.scitotenv.2019.01.022, 2019.

Chapter 2

Regional Climate Modelling

Modelling tools such as global climate models (GCMs) are used to describe the Earth's system (Sect. 1.5.2). Still, GCMs poorly represent processes that govern the regional-to-local scale due to their coarse resolution (e.g., Demory et al., 2020); thus, these processes need to be parameterised (Leung et al., 2003; Su et al., 2012). Regional climate models (RCMs) are another modelling tools. A regional climate model (RCM) is generally defined as the technique to dynamically downscale global climate information over a limited area. The American Meteorological Society in more detail defines a RCM as "a numerical climate prediction model forced by specified lateral and ocean conditions from a general circulation model (GCM) or observation-based dataset (reanalysis) that simulates atmospheric and land surface processes, while accounting for high-resolution topographical data, land-sea contrasts, surface characteristics, and other components of the Earth-system" (American Meteorological Society, 2019). RCMs overall improve the representation of the climate simulated by their driver GCMs (e.g. Armstrong et al., 2019; Solman and Blázquez, 2019). The main reason is that RCMs have an increased horizontal resolution compared to their driver GCMs and thus better represent the topography and the interaction with other components of the climate system (Ludwig et al., 2019). This is particularly important for topography-influenced phenomena such as Föhn, the orographically forced upstream flow and the triggered summer convection. For example, Bozkurt et al. (2019) found that RCMs represents temperature and precipitation fields better than their driving GCMs in areas with complex topography, particularly, the coastal-valley transitions. Ciarlo‘ et al. (2020) also observed that RCMs have a positive added value, especially when analysing the tail-end of the precipitation distribution in areas of complex topography and coast-lines. RCMs are used to directly resolve several processes (no parameterisation, e.g., convection-permitting, Giorgi et al., 2016; Messmer et al., 2017). Convection-permitting model resolutions are in general preferred as many recent studies show a better performance in simulating precipitation (e.g., Ban et al., 2014; Prein et al., 2015; Kendon et al., 2017; Berthou et al., 2018; Finney et al., 2019). Thus, RCMs improve the representation of the elements of the Earth's system that belongs to finer spatial scales (e.g., Kjellström et al., 2010; Strandberg et al., 2011; Gómez-Navarro et al., 2012, 2013; Ludwig et al., 2017, 2020). Still, uncertainties arise in the RCMs when comparing them to observations. Some

uncertainties are transferred from their driving GCMs in the initial and boundary conditions. Other ones are originated by shortcomings in the parametrisations and selection of the model domain (Flato et al., 2013)

This thesis is mainly based on simulations performed with the regional climate model Weather Research and Forecasting (WRF) model which is a numerical weather prediction and atmospheric simulation system. WRF model has collaboratively been developed since the latter 1990's by the National Center for Atmospheric Research (NCAR), the National Oceanic and Atmospheric Administration (represented by the National Centers for Environmental Prediction (NCEP) and the Earth System Research Laboratory), the U.S. Air Force, the Naval Research Laboratory, the University of Oklahoma, and the Federal Aviation Administration (FAA) (Skamarock and Klemp, 2008). WRF has been used in many studies across spatial scales from thousands of kilometres at the relatively high spatial resolutions of some kilometres (e.g., Zhang et al., 2012; González-Rojí et al., 2018; Ludwig et al., 2020) to hundreds of metres at the exceedingly high horizontal resolutions of 10 to 500 metres (e.g., Wyszogrodzki et al., 2012; Kochanski et al., 2013; Fiori et al., 2017; Siewert and Kroszczynski, 2020). The following sections provide a brief description of WRF, its requirements to run and the sets of simulations that are carried out for this thesis.

2.1 Weather Research and Forecast (WRF) Model

WRF model is a non-hydrostatic mesoscale model with a compressible atmosphere. Its software infrastructure contains dynamical solvers, physics packages and initialisation programs. Additionally, it accommodates two optional systems such as WRF-Var and WRF-Chem. WRF-Var is a data assimilation system that that converts observational data sets in driving climate information for WRF model. WRF-Chem is the chemistry system that permits the air chemistry modelling in WRF model (Skamarock et al., 2008). Figure 2.1 depicts the WRF components.

Dynamical solvers are technically the core of WRF and can either be the Advanced Research WRF (ARW) solver, also known as Eulerian mass solver, developed primarily at NCAR or the Non-hydrostatic Mesoscale Model (NMM) solver developed at NCEP. Most physics packages are shared by both the ARW and NMM solvers; however, some specific compatibility can vary between the schemes considered (Skamarock et al., 2008). The simulations of this thesis are carried out using the version 3.8.1 of WRF and its underlying ARW solver. WRF-Var and WRF-Chem are not implemented in the simulations. The equations are then presented in the Eulerian flux form using variables with conservative properties. The equations are formulated using terrain-following vertical coordinates whose uppermost level is on a constant pressure level of 50 hPa. The terrain-following vertical coordinate (η) is defined as

$$\eta = \frac{p_h - p_{ht}}{\mu} \quad \text{, where} \quad \mu = p_{hs} - p_{ht} \,, \tag{2.1}$$

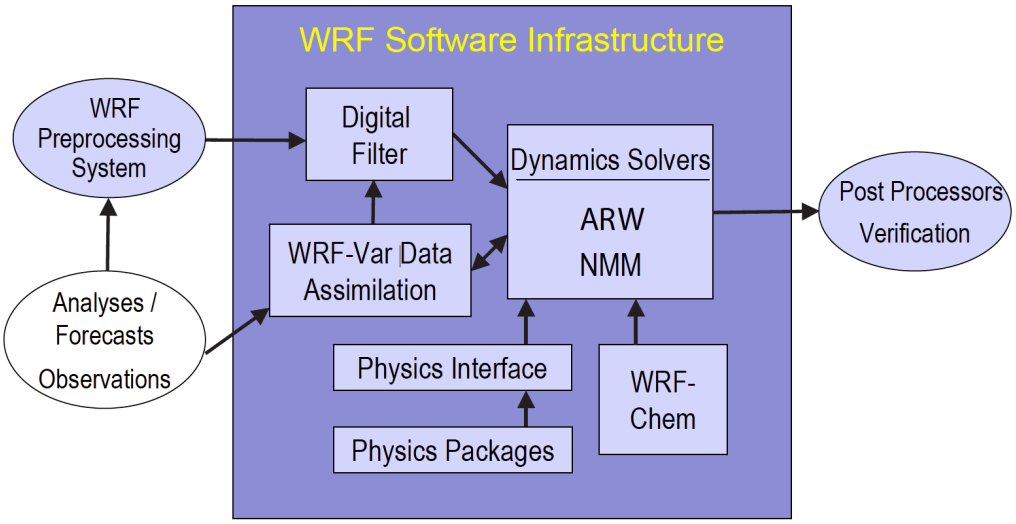

Figure 2.1: WRF system components. Source: Fig. 1.1 in Skamarock et al. (2008).

where p_h is the hydrostatic component of the pressure, and p_{hs} and p_{ht} are values along the surface and top boundaries, respectively. The η values vary from 1 at the surface to 0 at the upper boundary of the model domain. μ(x, y) represents the mass per unit area within the column in the model domain at the grid point (x, y); thus, the flux form variables employed in the governing equations are:

$$(U, V, W) \;=\; \mathbf{V} \;=\; \mu \mathbf{v} \;, \qquad \Omega \;=\; \mu \dot{\eta} \qquad \text{and} \qquad \Theta \;=\; \mu \theta \;. \tag{2.2}$$

$\mathbf{v} = (u, v, w)$ refers to the covariant velocities in the two horizontal and vertical directions, respectively. $\omega = \dot{\eta}$ is the contravariant 'vertical' velocity and θ the potential temperature. There are other non-conserved variables used in the governing equations of the ARW such as $\Phi = gz$ (the geopotential), p (pressure), and $\alpha = 1/\rho$ (the inverse density). Accordingly, the flux-form Euler equations can be written as follows:

The momentum equation in x-direction is

$$F_U = \frac{\partial U}{\partial t} + (\nabla \cdot \mathbf{V} u) - \frac{\partial (p \phi_\eta)}{\partial x} + \frac{\partial (p \phi_x)}{\partial \eta}. \tag{2.3}$$

The momentum equation in y-direction is

$$F_V = \frac{\partial V}{\partial t} + (\nabla \cdot \mathbf{V} v) - \frac{\partial (p \phi_\eta)}{\partial y} + \frac{\partial (p \phi_y)}{\partial \eta}. \tag{2.4}$$

The momentum equation in z-direction is

$$F_W = \frac{\partial W}{\partial t} + (\nabla \cdot \mathbf{V} \omega) - g \left(\frac{\partial p}{\partial \eta} - \mu \right). \tag{2.5}$$

The thermodynamic energy equation is

$$F_\Theta = \frac{\partial \Omega}{\partial t} + (\nabla \cdot \mathbf{V}\theta) \ . \tag{2.6}$$

The continuity equation is

$$\frac{\partial \mu}{\partial t} = -(\nabla \cdot \mathbf{V}) \ . \tag{2.7}$$

The geopotential height equation is

$$\mu \frac{\partial \phi}{\partial t} = -(\mathbf{V} \cdot \nabla \phi) + gW. \tag{2.8}$$

The equation of state is

$$p = p_0 \left(\frac{R_d \theta}{p_0 \alpha} \right)^\gamma . \tag{2.9}$$

The hydrostatic equation is

$$\frac{\partial \phi}{\partial \eta} = -\alpha \mu. \tag{2.10}$$

R_d is the gas constant for dry air, p_0 indicates the reference pressure that is commonly 10^5 Pascals and $\gamma = c_p/c_v = 1.4$ represents the ratio of the heat capacities for dry air. Additionally, the following equations are used in the Eq. 2.3 to 2.8:

$$\nabla \cdot \mathbf{V}a = \frac{\partial U a}{\partial x} + \frac{\partial V a}{\partial y} + \frac{\partial \Omega a}{\partial \eta} \tag{2.11}$$

and

$$\mathbf{V} \cdot \nabla a = U \frac{\partial a}{\partial x} + V \frac{\partial a}{\partial y} + \Omega \frac{\partial a}{\partial \eta}, \tag{2.12}$$

where "a" represents a generic variable. The left-hand-side terms F_U, F_V, F_W and F_Θ (Eq. 2.3 – 2.6) represent forcing terms that appear from the model physics, turbulent mixing, spherical projections and the Earth's rotation. The here-presented equations are definitely not complete. For simplicity, the terms for moisture, map projection, Coriolis and curvature are omitted. Further details are presented in Skamarock et al. (2008) and Skamarock and Klemp (2008).

The ARW solver uses the 3rd-order Runge-Kutta scheme for the time integration and the second to the sixth order advection schemes for the spatial discretisation. The ARW solver also uses an Arakawa C-grid staggered for the horizontal and vertical model grid. This means that

mass and thermodynamic variables are staggered on-half grid from the wind components. Namely, the mass and thermodynamic variables are located in the centre of the grid cell and the wind components are at the border of the grid cell (Fig. 2.2).

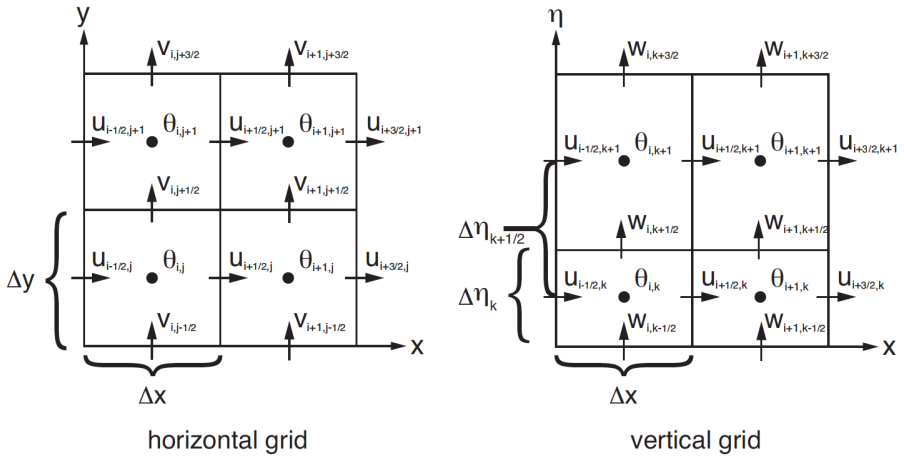

Figure 2.2: Schematic diagram of the horizontal and vertical grids of the ARW. u and v represent the horizontal wind components, W the vertical wind component, θ the mass and thermodynamic variable, Δx, Δy, $\Delta\eta$ the grid lengths. Source: Fig. 3.2 in Skamarock et al. (2008).

Nesting approach is supported by ARW solver. ARW-nesting permits to only increase the temporal and horizontal resolution over a specific region. This means that ARW allows the introduction of additional grids into the simulation. These grids are rectangular and aligned with the parent grid. Only integer values are allowed to be used for the temporal and horizontal refinements. A nest ratio of 1:3 is used for the grid refinement in the simulations of this thesis. The simulations are carried out with a two-way nesting approach. This allows the interface between the parent and the nested domain. The parent domain in each time step provides the nested domain with information through lateral boundary conditions. The nested domain at the same time delivers information back to the parent domain in the way that the finer grid information replaces the one of the parent domain. There are three of options of time-step approaches in ARW solver. In this thesis, the simulations are run using an adaptive time step, i.e., the integration time step can vary from time to time. This time-step scheme selects a time step based on the temporally-evolving wind fields which are typically bigger than usual fixed time steps (Skamarock et al., 2008; Skamarock and Klemp, 2008). The adaptive time step results in a throughput increase on the available computer facilities till around 50 % (Hutchinson, 2007).

There are many physics options in WRF and they are organised in categories, the so-called parametrisations, as follows: microphysics, cumulus, planetary boundary layer (PBL), atmospheric surface layer, land-surface model (LSM), and atmospheric radiation. The interactions between the parametrisations are depicted in Fig. 2.3. Each category offers several options that need to be selected before running a simulation. For the simulations of this thesis, the selection of the parametrisations are mostly based on previous studies that used similar domains and GCMs and focused their investigation over the same region (e.g., Messmer et al.,

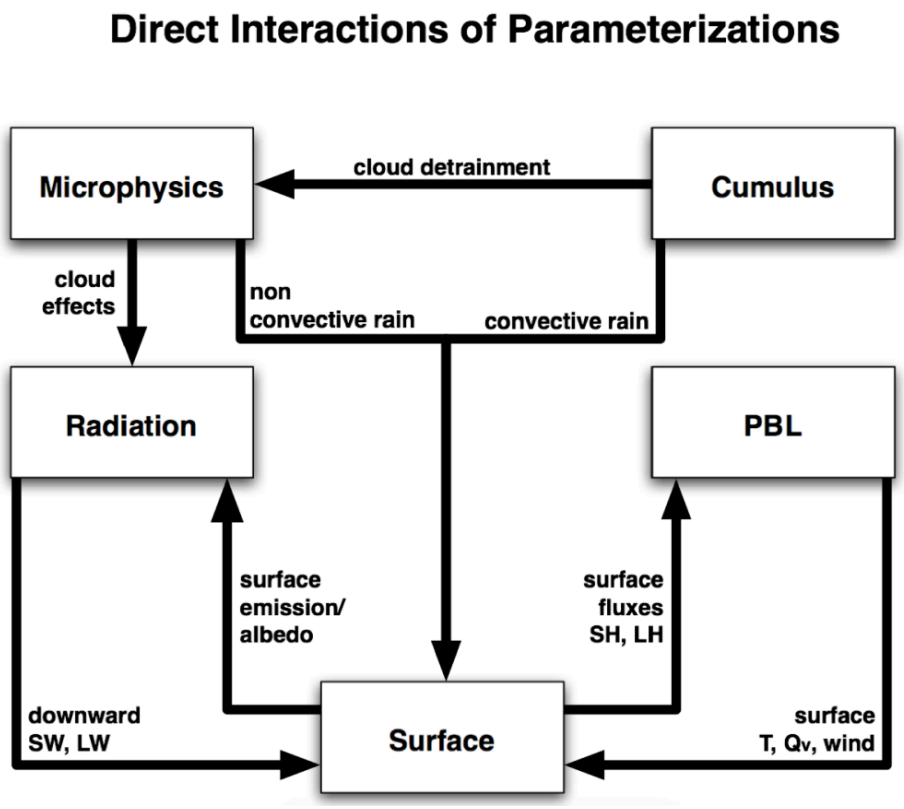

Figure 2.3: Schematic diagram of interactions between WRF parametrisations (physics components). Source: Fig. 8.1 in Skamarock et al. (2019).

2017; Gómez-Navarro et al., 2018). The chosen parametrisations are enlisted in Table 2.1. Note that the cumulus parametrisation can be switched off below a certain grid spacing that is usually defined between 4 and 6 kilometres (e.g., Prein et al., 2013; Pennelly et al., 2014; Bonekamp et al., 2018; Gómez-Navarro et al., 2018) and rarely reaches 9 kilometres (e.g., Li et al., 2020). This permits the explicit solution of the convection-related equations, the so-called convection-permitting.

2.2 Initial and Boundary Conditions for WRF

2.2.1 WRF Preprocessing System (WPS)

WRF Processing System (WPS) is the key for running WRF model and very important in downscaling. WPS is a set of programs that prepare terrestrial and meteorological data for prognostic calculation and data assimilation, i.e, the initial and boundary conditions to run the ARW pre-processor program.

Geogrid is the first program that acts. It defines the physical grid which includes the domains' location, the projection type, the number of grid points and their in-between distances (Fig. 2.4). Note that the ARW solver supports four projections to the sphere: the Lambert conformal, the polar stereographic, the Mercator, and the latitude-longitude (Skamarock et al.,

Table 2.1: Parameterisations used to run WRF.

Parameterisation	**Chosen parameterisation**
Microphysics	WRF single moment 6-class scheme
Cumulus	Kain–Fritsch scheme
Planetary boundary layer	Yonsei University scheme
Surface layer	MM5 similarity
Land/water surface	Noah–Multiparameterization LSM
Longwave radiation	RRTM scheme
Shortwave radiation	Dudhia scheme

2008). This thesis uses the Lambert conformal. Additionally, Geogrid interpolates static fields to the prescribed domains. These static geographical data contains, among others, information about the digital terrain model, vegetation indexes, soil type, albedo, terrain coverage, and land use.

An external analysis is processed by the WPS GriB decoder independently of the domain configuration, the so-called Ungrib program. This decoder diagnoses required fields which are also known as the driving information, e.g., a GCM. This driving information is typically in GRIB format and is converted by Ungrib program into an internal binary format (Fig. 2.4).

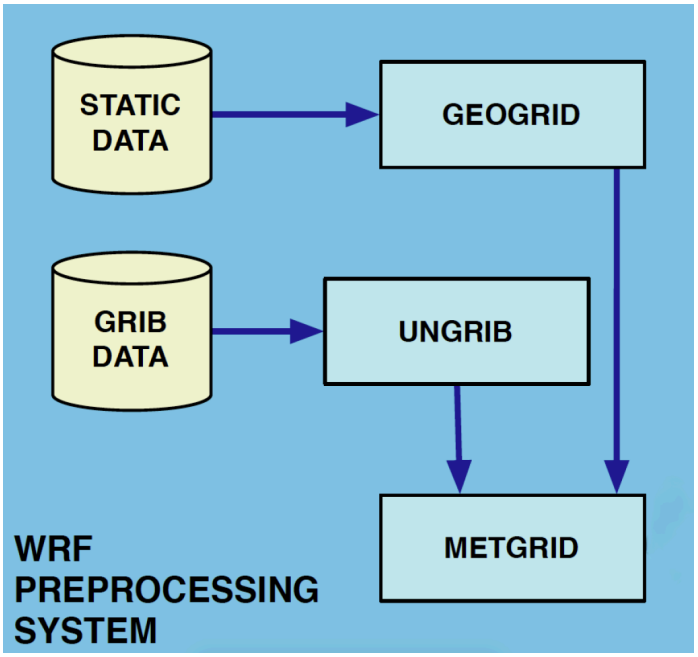

Figure 2.4: Scheme of data flow and program components in WPS. Source: Fig. 5.1 in Skamarock et al. (2008).

After Geogrid and Ungrib programs are successfully carried out, Meteogrid program horizontally interpolates the meteorological data onto the projected domains (Fig. 2.4). The resulting data is a snapshot of the atmosphere on the selected model grid's horizontal staggering

at the selected time slice. Each snapshot contains two- and three-dimensional fields. These fields are known as initial and boundary conditions for running WRF. Two-dimensional fields contain the static terrestrial fields already mentioned above. It also includes time-dependent fields from the external model: surface and sea-level pressure, layers of soil temperature and moisture, snow depth, skin temperature, sea surface temperature and a sea ice flag (also known as mask). Three-dimensional fields contain: temperature, relative humidity and the horizontal wind components already rotated to the model projection.

2.2.2 Community Climate System Model version 4 (CCSM4)

The global climate model (GCM) that drives WRF is the Community Climate System Model (version 4; CCSM4, Gent et al., 2011). CCSM4 was run by Hofer et al. (2012a,b) and Merz et al. (2015). Their simulations provide the initial and boundary conditions for WRF.

CCSM4 is the fourth generation of the fully-coupled Community Climate System Model (CCSM) developed by NCAR. The code of the CCSM models is freely available to the scientific community. CCSM4 consist of four models that simultaneously simulate elements of the Earth's climate system: atmosphere, ocean, land surface and sea ice. There is also a coupler that exchanges information between these components. CCSM4 replaces its predecessor CCSM3 in 2010 with further developments in all components that improve the representation of the Earth's system. For example, there are important improvements in the frequency of ENSO variability and the SST correlations with the whole Pacific Ocean. The land water storage is improved together with the heat flux into the atmosphere and the runoff into the ocean. CCMS4 better represents the frequency distribution of tropical precipitation, MJO variability, the worldwide heat waves and very heavy rainfall. There is a much better representation of the sea ice and its underlying albedo. Further improvements are presented in Gent et al. (2011). In the same line of the GCMs from NCAR, CSSM4 is the predecessor of Community Earth System Model 1 (CESM1; Hurrell et al., 2013). The main difference between CCSM4 and CESM1 is the additional biology- and chemistry-related features.

CCSM4's atmospheric and land component is described by the Community Atmosphere Model version 4 (CAM4, Neale et al., 2010) and by the Community Land Model version 4 (CLM4, Oleson et al., 2010), respectively. These two components are coupled to so-called *data models* for the ocean and sea ice. These surface boundary conditions are obtained from a fully coupled simulation with CCSM3 at lower resolution (see details in: Hofer et al., 2012a). CCSM3 provided monthly mean time-varying sea-ice cover and sea-surface temperatures. Furthermore, the Community Ice Code (version 4, CICE4; Hunke and Lipscomb, 2010) is set to its thermodynamic-only mode. This means that sea-ice cover is prescribed and surface fluxes through the ice are computed by considering snow depth, albedo, and surface temperature as simulated by CAM4 (Merz et al., 2015). The atmosphere-land-only model provides 6-hourly output at horizontal resolution of 1.25 $^\circ \times 0.9^\circ$ (longitude $\times$ latitude), 26 vertical hybrid sigma-pressure levels. The model is run under perpetual forcing conditions, i.e., it uses fixed forcing factors, which leads to a climate state that statistically shows no trends. This is also

known as a climate state in equilibrium. The CCSM4 simulations used to run WRF are further described in Sect. 2.3.

2.2.3 Vegetation Model Lund-Potsdamn-Jena-LMfire (LPJ-LMfire)

An addition model provides the initial and boundary conditions for WRF (Jed O. Kaplan pers. comm.; Velasquez et al., 2021). The dynamic global vegetation model LPJ-LMfire (Pfeiffer et al., 2013) is used to generate the land cover for the present day and LGM climate. Note that LPJ-LMfire is an evolution of the vegetation model Lund-Potsdamn-Jena (LPJ, Sitch et al., 2003). At each grid cell, LPJ-LMfire simulates land cover in the form of the fractional coverage of population of different plant functional types (PFTs). These PFTs are overall defined to account for the variety of structure and function among plants (Smith et al., 1993). LPJ-LMfire uses nine plant functional types (PFTs) that include tropical, temperate, and boreal trees, and tropical and extratropical herbaceous vegetation (Sitch et al., 2003). LPJ-LMfire is a processed-based, large-scale and explicit representation of the vegetation structure and dynamics, the competition between PFT populations and the soil biochemistry. LPJ-LMfire simulates the land cover patterns in response to the climate and soil conditions, and the atmospheric CO_2 concentrations, which includes land-atmosphere water and carbon exchanges (Prentice et al., 1992; Haxeltine and Prentice, 1996; Haxeltine et al., 1996; Kaplan, 2001; Kaplan et al., 2016). Note that LPJ-LMfire also considers bioclimatic features that constrain the survival and regeneration of the PFTs.

A typically LPJ-LMfire simulation begins from the "bare ground" (no plant biomass present) and spins up many years until approximate equilibrium is reached with respect to carbon pools and vegetation cover. In this thesis, the LPJ-LMfire simulations are run for 1020 years with the climate state and forcing (greenhouse gases: CO_2, N_2O and CH_4) from the CCSM4 and WRF, and the present-day soil physical properties extrapolated out on to the continental shelves (Kaplan et al., 2016). Such a long simulation is not necessary to bring above-ground vegetation into equilibrium with climate but it allows soil organic matter to equilibrate. Note that these simulations are performed by J. O. Kaplan.

2.3 Regional Climate Simulations

In this thesis, 438 years are simulated with WRF to build 11 experiments in total. These experiments consist of several WRF simulations driven by five CCSM4 simulations. Each CCSM4 simulations covered 33 years with a 3-year spin-up. The spin-up period is not used to drive any WRF simulation. Two of these CCSM4 simulations are performed under perpetual conditions of 1990 CE (present day or PD) and the Last Glacial Maximum (LGM), respectively. Other three of these CCSM4 simulations are run using perpetual conditions of the Marine Isotope 4 stage (MIS4) period. Each MIS4 simulation is performed with a different northern hemispheric ice-sheet thickness: 66, 100 and 125 % of the LGM ice-sheet thickness, respectively. More detailed information on the simulations and their settings are presented in Hofer et al.

Table 2.2: External forcing used in Hofer et al. (2012a,b) for 1990 CE, LGM and MIS4 conditions.

Parameter name	1990 AD	LGM	MIS4
TSI (W m^{-2})	1361.77	1360.89	1360.89
Eccentricity (10^{-2})	1.6708	1.8994	0.020713
Obliquity (°)	23.441	22.949	22.564
Angular precession (°)	102.72	114.43	15.22
CO2 (ppm)	353.9	185	205
CH4 (ppb)	1693.6	350	460
N2O (ppb)	310.1	200	210

(2012a,b) and Merz et al. (2013, 2014a,b, 2015). Perpetual conditions, i.e., orbital forcing and atmospheric composition, are enlisted in Table 2.2. The 11 experiments are split in two groups: two-domain and four-domain simulations. They are in detail explained in the following.

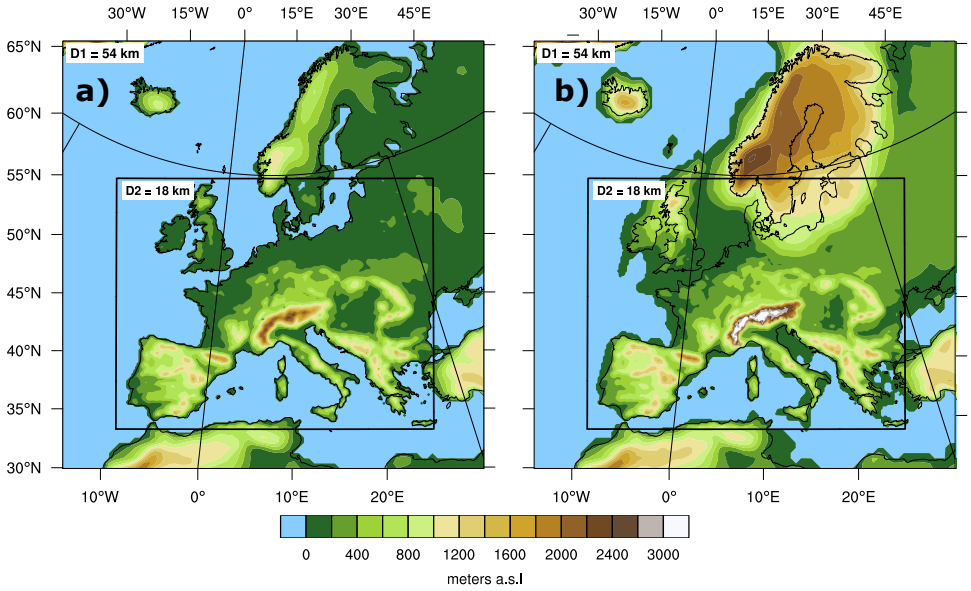

Figure 2.5: WRF domains and topography for the two-domain experiments. (a) illustrates the present-day topography and the two domains at 54 and 18 km horizontal resolution, (b) as (a) but for the LGM.

2.3.1 Two-domain Experiments

The first group encompasses three experiments that are used to gain insights in the role of the land cover on the European climate. These experiments consist of WRF simulations with 40 vertical eta levels and two domains at 54 and 18 km horizontal resolutions, respectively (domains in Fig. 2.5). Each WRF simulation is run for 30 years and split up into two single 15-year simulations. Each 15-year simulation is performed with a 2-month spin-up to account for the time required for the land surface to come into equilibrium. Tests show that the

Table 2.3: Variables passed between GCM/WRF and LPJ-LMfire.

GCM/WRF to LPJ-LMfire	
30-year monthly values	
mean temperature at 2 m	convective available potential energy
daily max. temperature at 2 m	horizontal wind velocity at 10 m
daily min. temperature at 2 m	precipitation (liquid and solid)
total cloud cover fraction	

LPJ-LMfire to WRF	
30-year monthly values	climatological value
vegetation cover fraction	land cover fraction (category)
leaf area index	dominant land cover type (category)
	soil temperature

WRF land surface scheme reaches a quasi-equilibrium after approximately 15 days. Further information about these tests is presented in the second paragraph of the next section (Sect. 2.3.2).

The first experiment (two-domain LGM_{LGM}) is driven by the CCSM4 simulation with LGM perpetual conditions (Hofer et al., 2012a). Reduced sea level and increased ice sheets are used for LGM conditions as specified in the PMIP3 protocol (for more details see: Hofer et al., 2012a; Ludwig et al., 2017). The LGM glaciation over the Alpine region is obtained from Seguinot et al. (2018) and additional LGM glaciated areas (e.g., Pyrenees, Carpathians) are from Ehlers et al. (2011). The following variables are accordingly modified in WPS: The present-day topography is subtracted from the PMIP3 topography. This difference is added to the WRF topography (HGT_M). Similarly, the other LGM glaciated areas (e.g., Pyrenees, Carpathians) are included in the the WRF topography (HGT_M). Due to the lowering sea level, the land surface coverage (LANDMASK) is increased, which leads to missing land cover information over the new land surface that was covered by water during present day. Comparing Fig. 2.5a to Fig. 2.5b illustrates the changes in the topography and surface coverage between present day and LGM conditions. This LGM land cover information is provided by this experiment (two-domain LGM_{LGM}), particularly by the LPJ-LMfire model. It is important to highlight that this experiment (two-domain LGM_{LGM}) is the final product of an iterative asynchronous coupling design that is used to create the best possible estimate of European land cover for the LGM (chapter 3; Velasquez et al., 2021). The coupling design combines CCSM4/WRF with LPJ-LMfire model and consists of four steps: (i) CCSM4 provides atmospheric variables to generate the first approximation of land cover with LPJ-LMfire at a horizontal resolution of 1.25 ° × 0.9 ° (longitude × latitude). (ii) WRF is driven by the CCSM4 with LGM perpetual conditions and the first approximation of land cover created in step (i) to generate the first downscaled atmospheric variables at 54 and 18 km resolution. (iii)

LPJ-LMfire is run with the downscaled atmospheric variables (from step ii) to regenerate the land cover at the WRF resolution. (iv) Same as in (ii) but WRF uses the land surface boundary conditions simulated at 54 and 18 km. Step (iii) and (iv) are carried out asynchronously over six iterations to achieve a quasi-equilibrium between the climate and land cover. Parts (i) and (ii) are considered as the first iteration and the iterations of (iii) and (iv) were considered as the second-to-seventh iterations. The variables that are passed between the climate and vegetation models are summarised in Table 2.3. A simple scheme is used to classify the vegetation cover fraction of LPJ-LMfire PFTs into the land cover categories that are required by WRF (according to NOAH-MP MODIS; Niu et al., 2011). The code for the classification is presented in Kaplan et al. (2018).

The second experiment (two-domain PD_{PD}) is a WRF simulation that is driven by the CCSM4 simulation with 1990 CE perpetual conditions (Hofer et al., 2012a). It uses the default present-day MODIS-based land cover dataset from WRF as the land surface boundary condition (Skamarock and Klemp, 2008).

The third experiment (two-domain LGM_{PD}) uses the CCSM4 simulation with LGM perpetual conditions (Hofer et al., 2012a), but with the default present-day MODIS-based land cover dataset from WRF as for the land surface.

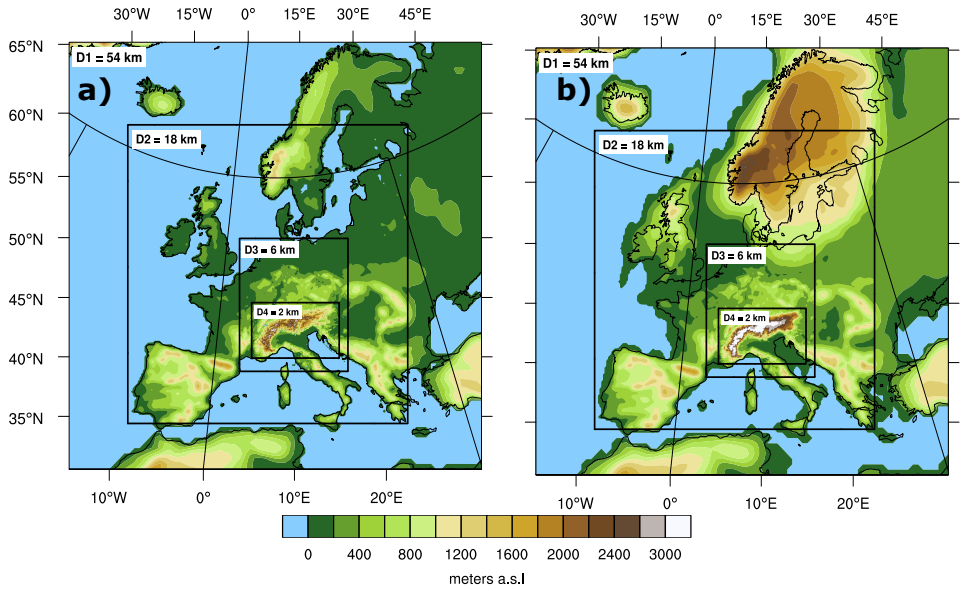

Figure 2.6: WRF domains and topography for the four-domain experiments. (a) illustrates the present-day topography and the four domains at 54, 18, 6 and 2 km horizontal resolution, (b) as (a) but for the LGM.

Comparing two-domain LGM_{PD} with two-domain PD_{PD} illustrates the atmospheric response to changes only in the atmospheric forcing, i.e., without changes in land cover. The comparison of two-domain LGM_{LGM} and the two-domain LGM_{PD} allows to investigate the influence of land cover on the atmosphere, i.e., without changes in atmospheric boundary conditions. These three experiments are summarised in Table 2.4. The results of this first group of experiments are presented in chapter 3 and in (Velasquez et al., 2021).

2.3.2 Four-domain Experiments

The second group encompassed eight experiments that are used to gain insights into the influence of the ice-sheet topography on the Alpine climate. These experiments consist of WRF simulations with 40 vertical eta levels and four domains at 54, 18, 6 and 2 km horizontal resolutions, respectively (domains in Fig. 2.6). The resolution in the two innermost domains (6 and 2 km) permits the explicit resolution of convective processes. Thus, no parameterisation for convection is used in these two domains and precipitation is described by microphysical processes (Table 2.1). Moreover, the innermost domain (2 km) covers the highly complex terrain of the Alps. Each WRF simulation was split up into single 3-year simulations.

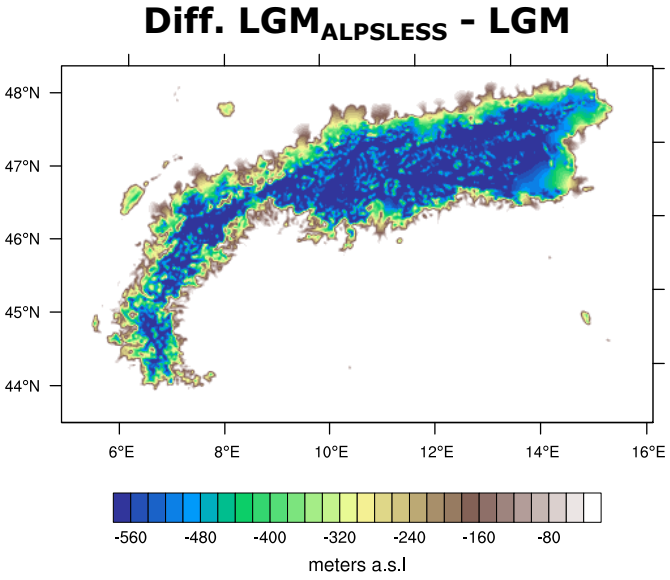

Figure 2.7: Innermost domain used by WRF. It shows the difference between LGM$_{ALPSLESS}$ and LGM topography.

Each 3-year simulation is performed with a spin-up period to account for the time required for the land surface to come into equilibrium. Many studies suggest different spin-up periods ranging from days to several months mostly depending on the variables that are analysed afterwards (e.g., Christensen, 1999; Giorgi and Bi, 2000; Jankov et al., 2007; Jerez et al., 2010, 2012, 2013; Argüeso et al., 2011; Angevine et al., 2014; Montavez et al., 2017; Zheng et al., 2017; González-Rojí et al., 2018; Li et al., 2020). For instance, Bonekamp et al. (2018) found that precipitation has the best performance with 24 hours of spin-up; however, it does not show a clear trend with increasing spin-up time over 24 hours. This allows to set a spin-up more flexible. To determine this spin-up, tests are done with the focus on the 1-year soil response after initialisation and on the four parameterised soil layers of the WRF land-surface scheme, i.e., down to 2 m. The climatological annual cycle is first subtracted in each 3-years simulation, i.e., one obtains daily soil moisture anomalies (Fig. 2.8, grey lines). Note that the climatological annual cycle is calculated from the ten simulations without the spin-up periods, and that the anomalies are divided by the climatological annual cycle to be presented in percentages. To reduce the noise of the internal variability, the anomalies are averaged (Fig. 2.8, dark lines).

Note that each 3-year simulation represents the present-day climate state. Additionally, we carry out the Mann-Kendall test (Mann, 1945; Kendall, 1948; Gilbert, 1987) combined with the Theil-Sen trend estimation method (Theil, 1950; Sen, 1968) to identify any trend and its probability of occurrence. Figure 2.8 shows no significant trend after 10 days in the four layers, which initially suggests that the spin-up period could be set at around 15 days. To ensure that the mode is in quasi-equilibrium, a longer spin-up is defined covering 61 days, i.e., 2 months.

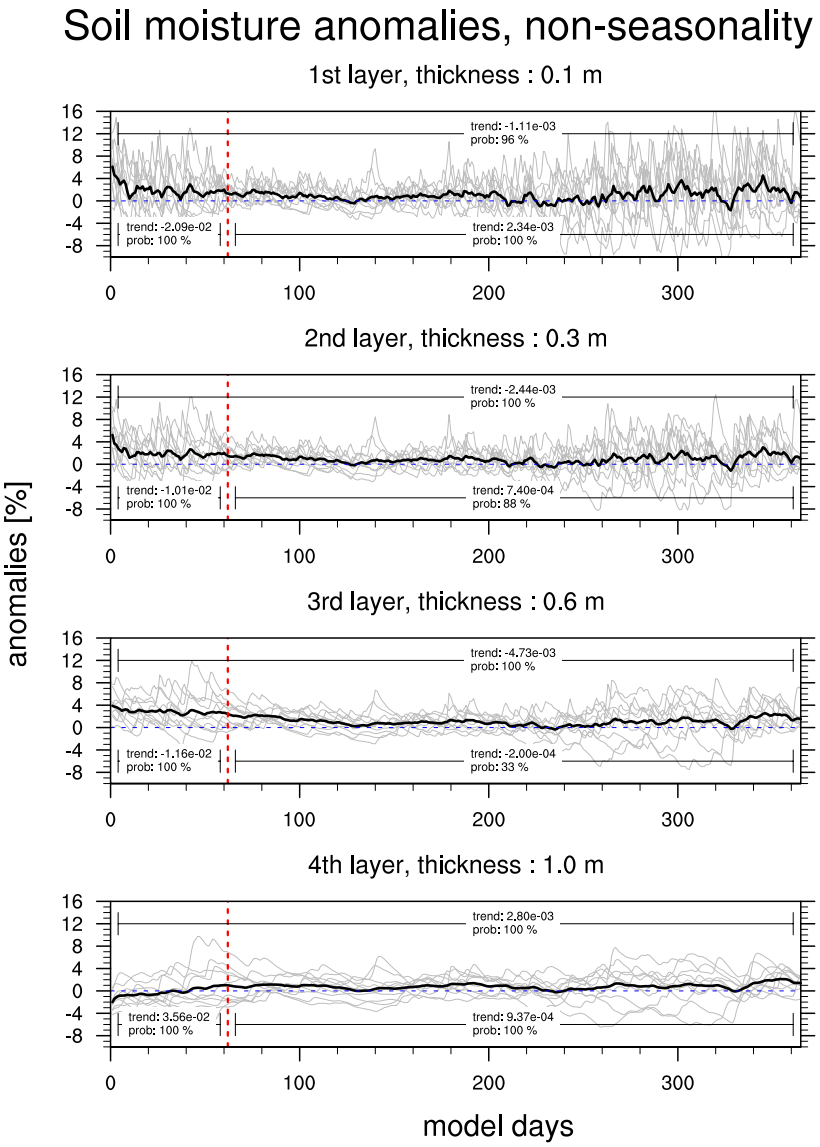

Figure 2.8: Soil moisture over the fourth layers of the WRF soil scheme. (a) represents the first layer with a thickness of 0.1 m, (b) the second layer with a thickness of 0.3 m, (c) the third layer with a thickness of 0.6 m, and (d) the fourth layer with a thickness of 1.0 m. Grey lines represent non-seasonality anomalies, black lines the average of the anomalies, blue dashed lines anomaly zero, and red dashed lines the 61-day spin-up. Trend and probability of occurrence for three periods after applying the Mann-Kendall test combined with the Theil-Sen trend estimation method: 61 days, 1 year with and without spin-up, separately.

The first (four-domain PD_{PD}) and second experiment (four-domain LGM_{LGM}) are WRF simulations that run for 30 years using 1990 CE and LGM perpetual conditions,

Table 2.4: Set of experiments carried out in this study. The first column indicates the name of the experiment (WRF simulation), the second column the perpetual conditions, the third column the northern hemispheric ice-sheets (this includes the modifications in the driving global model), the fourth column the FIS, the fifth column the Alpine glaciers, the sixth column the land cover, and the seventh column the length of the simulation.

Name	Perpetual conditions	North Hemis. ice sheets	Fennoscandian ice sheet	Alpine glaciers	Land cover	Sim. length
Two-domain experiments at 54 and 18 km horizontal resolution						
PD_{PD}	1990	1990	1990	1990	1990	30 yr
LGM_{PD}	LGM	LGM	LGM	LGM	1990	30 yr
LGM_{LGM}	LGM	LGM	LGM	LGM	LGM	30 yr
Four-domain experiments at 54, 18, 6 and 2 km horizontal resolution						
PD_{PD}	1990	1990	1990	1990	1990	30 yr
LGM_{LGM}	LGM	LGM	LGM	LGM	LGM	30 yr
$LGM_{ALPSLESS}$	LGM	LGM	LGM	reduced LGM	LGM	21 yr
$LGM_{FENNO50}$	LGM	LGM	50 % LGM	LGM	LGM	12 yr
$LGM_{FENNO150}$	LGM	LGM	150 % LGM	LGM	LGM	12 yr
$MIS4_{LGM66}$	MIS4	66 % LGM	LGM	LGM	LGM	21 yr
$MIS4_{LGM}$	MIS4	100 % LGM	LGM	LGM	LGM	21 yr
$MIS4_{LGM125}$	MIS4	125 % LGM	LGM	LGM	LGM	21 yr

respectively (Table 2.2). Similar to two-domain PD_{PD}, the four-domain PD_{PD} also uses the default present-day MODIS-based land cover dataset from WRF as the land-surface boundary conditions (Skamarock and Klemp, 2008). Similar to the two-domain LGM_{LGM}, the surface conditions also need some further adjustments for the four-domain LGM_{LGM}. These include the reduced sea level and the Fennoscandian ice sheets as specified in the PMIP3 protocol (Fig. 2.6b; for more details see: Hofer et al., 2012a; Ludwig et al., 2017). The LGM glaciation over the Alpine region is included in the regional climate model using estimates from Seguinot et al. (2018) and additional LGM glaciated areas (e.g., Pyrenees, Carpathians) from Ehlers et al. (2011). Figure 2.6a shows the present-day topography and surface coverage used in the four-domain PD_{PD}. Figure 2.6b illustrates the LGM topography and surface coverage used in the four-domain LGM_{LGM}. Additionally, the land cover is altered to comply with LGM conditions. To that end, the land cover is obtained from two-domain LGM_{LGM}, i.e., from the final product of an iterative asynchronous coupling design (Sect. 2.3.1; Velasquez et al., 2021). Results of these two experiments (four-domain PD_{PD} and LGM_{LGM}) are described in chapter 5, where they are used to develop a new bias correction suitable for climate states with strongly changed topography.

The third to fifth experiments ($LGM_{ALPSLESS}$, $LGM_{FENNO50}$ and $LGM_{FENNO150}$, respectively) are WRF simulations that are performed similar as the four-domain LGM_{LGM} but with a shorter temporal extent and a modified European ice-sheet topography. $LGM_{ALPSLESS}$ is run for 21 years and with a reduced Alpine glacier thickness. This reduction becomes stronger with height; namely, the Alpine ice sheet is strongly reduced over mountain peaks and slightly over the low lands. Figure 2.7 shows the changes in the Alpine glacier thickness between four-domain LGM_{LGM} and the $LGM_{ALPSLESS}$. $LGM_{FENNO50}$ is performed for 12 years with a Fennoscandian glacier thickness reduced by 50 %. $LGM_{FENNO150}$ is also run for 12 years but the Fennoscandian glacier thickness is increased by 150 %.

The sixth to eighth experiment ($MIS4_{LGM66}$, $MIS4_{LGM}$ and $MIS4_{LGM125}$, respectively) are WRF simulations that are run for 21 years using MIS4 perpetual conditions and using the LGM land cover from two-domain LGM_{LGM}. Following their driving CCSM4 simulations, each WRF simulation is performed with a different European ice-sheet thickness: 66, 100 and 125 % of the LGM ice-sheet thickness, respectively. Note that the Alpine ice sheet is not modified in these sixth-to-eighth experiments. These eight experiments are summarised in Table 2.4.

Bibliography

American Meteorological Society: Glossary of meteorology, URL http://glossary.ametsoc.org/wiki/Main_Page, 2019.

Angevine, W. M., Bazile, E., Legain, D., and Pino, D.: Land surface spinup for episodic modeling, Atmospheric Chemistry and Physics, 14, 8165–8172, doi:10.5194/acp-14-8165-2014, publisher: Copernicus GmbH, 2014.

Argüeso, D., Hidalgo-Muñoz, J. M., Gámiz-Fortis, S. R., Esteban-Parra, M. J., Dudhia, J., and Castro-Díez, Y.: Evaluation of WRF parameterizations for climate studies over southern Spain using a multistep regionalization, Journal of Climate, 24, 5633–5651, doi:10.1175/JCLI-D-11-00073.1, 2011.

Armstrong, E., Hopcroft, P. O., and Valdes, P. J.: Reassessing the value of regional climate modeling using paleoclimate simulations, Geophysical Research Letters, 46, 12 464–12 475, doi:10.1029/2019GL085127, 2019.

Ban, N., Schmidli, J., and Schär, C.: Evaluation of the convection-resolving regional climate modeling approach in decade-long simulations, Journal of Geophysical Research: Atmospheres, 119, 7889–7907, doi:10.1002/2014JD021478, 2014.

Berthou, S., Kendon, E. J., Chan, S. C., Ban, N., Leutwyler, D., Schär, C., and Fosser, G.: Pan-European climate at convection-permitting scale: a model intercomparison study, Climate Dynamics, doi:10.1007/s00382-018-4114-6, 2018.

Bonekamp, P. N. J., Collier, E., and Immerzeel, W. W.: The impact of spatial resolution, land use, and spinup time on resolving spatial precipitation patterns in the Himalayas, Journal of Hydrometeorology, 19, 1565–1581, doi:10.1175/JHM-D-17-0212.1, 2018.

Bozkurt, D., Rojas, M., Boisier, J. P., Rondanelli, R., Garreaud, R., and Gallardo, L.: Dynamical downscaling over the complex terrain of southwest South America: present climate conditions and added value analysis, Climate Dynamics, 53, 6745–6767, doi:10.1007/s00382-019-04959-y, 2019.

Christensen, O. B.: Relaxation of soil variables in a regional climate model, Tellus A, 51, 674–685, doi:10.1034/j.1600-0870.1999.00010.x, 1999.

Ciarlo‘, J. M., Coppola, E., Fantini, A., Giorgi, F., Gao, X., Tong, Y., Glazer, R. H., Torres Alavez, J. A., Sines, T., Pichelli, E., Raffaele, F., Das, S., Bukovsky, M., Ashfaq, M., Im, E.-S., Nguyen-Xuan, T., Teichmann, C., Remedio, A., Remke, T., Bülow, K., Weber, T., Buntemeyer, L., Sieck, K., Rechid, D., and Jacob, D.: A new spatially distributed added value index for regional climate models: the EURO-CORDEX and the CORDEX-CORE highest resolution ensembles, Climate Dynamics, doi:10.1007/s00382-020-05400-5, 2020.

Demory, M.-E., Berthou, S., Fernández, J., Sørland, S. L., Brogli, R., Roberts, M. J., Beyerle, U., Seddon, J., Haarsma, R., Schär, C., Buonomo, E., Christensen, O. B., Ciarlo ?, J. M., Fealy, R., Nikulin, G., Peano, D., Putrasahan, D., Roberts, C. D., Senan, R., Steger, C., Teichmann, C., and Vautard, R.: European daily precipitation according to EURO-CORDEX regional climate models (RCMs) and high-resolution global climate models (GCMs) from the High-Resolution Model Intercomparison Project (HighResMIP), Geoscientific Model Development, 13, 5485–5506, doi:10.5194/gmd-13-5485-2020, 2020.

Ehlers, J., Gibbard, P., and Hughes, P.: Quaternary glaciations-extent and chronology: a closer look, vol. 15, Elsevier, Amsterdam, Netherlands, 2011.

Finney, D. L., Marsham, J. H., Jackson, L. S., Kendon, E. J., Rowell, D. P., Boorman, P. M., Keane, R. J., Stratton, R. A., and Senior, C. A.: Implications of improved representation of convection for the East Africa water budget using a convection-permitting model, Journal of Climate, 32, 2109–2129, doi:10.1175/JCLI-D-18-0387.1, 2019.

Fiori, E., Ferraris, L., Molini, L., Siccardi, F., Kranzlmueller, D., and Parodi, A.: Triggering and evolution of a deep convective system in the Mediterranean Sea: modelling and observations at a very fine scale, Quarterly Journal of the Royal Meteorological Society, 143, 927–941, doi:10.1002/qj.2977, 2017.

Flato, G., Marotzke, J., Abiodun, B., Braconnot, P., Chou, S., Collins, W., Cox, P., Driouech, F., Emori, S., Eyring, V., and others: Evaluation of climate models, Climate change 2013: The physical science basis. Contribution of working group I to the fifth assessment report of the Intergovernmental Panel on Climate Change [Stocker, T.F., D. Qin, G.-K. Plattner, M. Tignor, S.K. Allen, J. Boschung, A. Nauels, Y. Xia, V. Bex and P.M. Midgley (eds.)] Cambridge University Press, Cambridge, United Kingdom and New York, NY, USA, pp. 741–866, 2013.

Gent, P. R., Danabasoglu, G., Donner, L. J., Holland, M. M., Hunke, E. C., Jayne, S. R., Lawrence, D. M., Neale, R. B., Rasch, P. J., Vertenstein, M., Worley, P. H., Yang, Z.-L., and Zhang, M.: The community climate system model version 4, Journal of Climate, 24, 4973–4991, doi:10.1175/2011JCLI4083.1, 2011.

Gilbert, R. O.: Statistical methods for environmental pollution monitoring, John Wiley & Sons, 1987.

Giorgi, F. and Bi, X.: A study of internal variability of a regional climate model, Journal of Geophysical Research: Atmospheres, 105, 29 503–29 521, doi:10.1029/2000JD900269, 2000.

Giorgi, F., Torma, C., Coppola, E., Ban, N., Schär, C., and Somot, S.: Enhanced summer convective rainfall at Alpine high elevations in response to climate warming, Nature Geoscience, 9, 584–589, doi:10.1038/ngeo2761, 2016.

Gómez-Navarro, J. J., Montávez, J. P., Jiménez-Guerrero, P., Jerez, S., Lorente-Plazas, R., González-Rouco, J. F., and Zorita, E.: Internal and external variability in regional simulations of the Iberian Peninsula climate over the last millennium, Climate of the Past, 8, 25–36, doi:10.5194/cp-8-25-2012, 2012.

Gómez-Navarro, J. J., Montávez, J. P., Wagner, S., and Zorita, E.: A regional climate palaeosimulation for Europe in the period 1500-1990 - Part 1: model validation, Climate of the Past, 9, 1667–1682, doi:10.5194/cp-9-1667-2013, 2013.

Gómez-Navarro, J. J., Raible, C. C., Bozhinova, D., Martius, O., García Valero, J. A., and Montávez, J. P.: A new region-aware bias-correction method for simulated precipitation in areas of complex orography, Geoscientific Model Development, 11, 2231–2247, doi:10.5194/gmd-11-2231-2018, 2018.

González-Rojí, S. J., Sáenz, J., Ibarra-Berastegi, G., and Díaz de Argandoña, J.: Moisture balance over the Iberian Peninsula according to a regional climate model: the impact of 3DVAR data assimilation, Journal of Geophysical Research: Atmospheres, 123, 708–729, doi:10.1002/2017JD027511, 2018.

Haxeltine, A. and Prentice, I. C.: BIOME3: an equilibrium terrestrial biosphere model based on ecophysiological constraints, resource availability, and competition among plant functional types, Global biogeochemical cycles, 10, 693–709, 1996.

Haxeltine, A., Prentice, I. C., and Creswell, I. D.: A coupled carbon and water flux model to predict vegetation structure, Journal of Vegetation Science, 7, 651–666, doi:10.2307/3236377, 1996.

Hofer, D., Raible, C. C., Dehnert, A., and Kuhlemann, J.: The impact of different glacial boundary conditions on atmospheric dynamics and precipitation in the North Atlantic region, Climate of the Past, 8, 935–949, doi:10.5194/cp-8-935-2012, 2012a.

Hofer, D., Raible, C. C., Merz, N., Dehnert, A., and Kuhlemann, J.: Simulated winter circulation types in the North Atlantic and European region for preindustrial and glacial conditions: glacial circulation types, Geophysical Research Letters, 39, L15 805, doi:10.1029/2012GL052296, 2012b.

Hunke, E. C. and Lipscomb, W. H.: CICE: the Los Alamos sea ice model documentation and software user's manual version 4.1 LA-CC-06-012, Tech. rep., Los Alamos National Laboratory, Los Alamos, NM, USA, 2010.

Hurrell, J. W., Holland, M. M., Gent, P. R., Ghan, S., Kay, J. E., Kushner, P. J., Lamarque, J.-F., Large, W. G., Lawrence, D., Lindsay, K., Lipscomb, W. H., Long, M. C., Mahowald, N., Marsh, D. R., Neale, R. B., Rasch, P., Vavrus, S., Vertenstein, M., Bader, D., Collins, W. D., Hack, J. J., Kiehl, J., and Marshall, S.: The community Earth system model: a framework for collaborative research, Bulletin of the American Meteorological Society, 94, 1339–1360, doi:10.1175/BAMS-D-12-00121.1, 2013.

Hutchinson, T. A.: An adaptive time-step for increased model efficiency, in: Extended abstracts, eighth WRF users' workshop, p. 4, 2007.

Jankov, I., Gallus, W. A., Segal, M., and Koch, S. E.: Influence of initial conditions on the WRF–ARW model QPF response to physical parameterization changes, Weather and Forecasting, 22, 501–519, doi:10.1175/WAF998.1, 2007.

Jerez, S., Montavez, J. P., Gomez-Navarro, J. J., Jimenez-Guerrero, P., Jimenez, J., and Gonzalez-Rouco, J. F.: Temperature sensitivity to the land-surface model in MM5 climate simulations over the Iberian Peninsula, Meteorologische Zeitschrift, pp. 363–374, doi:10.1127/0941-2948/2010/0473, publisher: Schweizerbart'sche Verlagsbuchhandlung, 2010.

Jerez, S., Montavez, J. P., Gomez-Navarro, J. J., Jimenez, P. A., Jimenez-Guerrero, P., Lorente, R., and Gonzalez-Rouco, J. F.: The role of the land-surface model for climate change projections over the Iberian Peninsula, Journal of Geophysical Research: Atmospheres, 117, doi:10.1029/2011JD016576, 2012.

Jerez, S., Montavez, J. P., Jimenez-Guerrero, P., Gomez-Navarro, J. J., Lorente-Plazas, R., and Zorita, E.: A multi-physics ensemble of present-day climate regional simulations over the Iberian Peninsula, Climate Dynamics, 40, 3023–3046, doi:10.1007/s00382-012-1539-1, 2013.

Kaplan, J. O.: Geophysical applications of vegetation modeling, Doctoral dissertation, Lund University, Lund, Sweden, iSBN: 9178740894, 2001.

Kaplan, J. O., Pfeiffer, M., Kolen, J. C. A., and Davis, B. A. S.: Large scale anthropogenic reduction of forest cover in Last Glacial Maximum Europe, PLOS ONE, 11, e0166 726, doi:10.1371/journal.pone.0166726, 2016.

Kaplan, J. O., Pfeiffer, M., and Chaste, E.: ARVE-Research/LPJ-LMfire: LPJ-LMfire, doi:10.5281/zenodo.1184589, 2018.

Kendall, M. G.: Rank correlation methods., tex.publisher: Griffin, 1948.

Kendon, E. J., Ban, N., Roberts, N. M., Fowler, H. J., Roberts, M. J., Chan, S. C., Evans, J. P., Fosser, G., and Wilkinson, J. M.: Do convection-permitting regional climate models improve projections of future precipitation change?, Bulletin of the American Meteorological Society, 98, 79–93, doi:10.1175/BAMS-D-15-0004.1, 2017.

Kjellström, E., Brandefelt, J., Näslund, J.-O., Smith, B., Strandberg, G., Voelker, A. H. L., and Wohlfarth, B.: Simulated climate conditions in Europe during the Marine Isotope Stage 3 stadial, Boreas, 39, 436–456, doi:10.1111/j.1502-3885.2010.00143.x, 2010.

Kochanski, A. K., Jenkins, M. A., Mandel, J., Beezley, J. D., Clements, C. B., and Krueger, S.: Evaluation of WRF-SFIRE performance with field observations from the FireFlux experiment, Geoscientific Model Development, 6, 1109–1126, doi:10.5194/gmd-6-1109-2013, 2013.

Leung, L. R., Mearns, L. O., Giorgi, F., and Wilby, R. L.: Regional climate research, Bulletin of the American Meteorological Society, 84, 89–95, doi:10.1175/BAMS-84-1-89, 2003.

Li, L., Pontoppidan, M., Sobolowski, S., and Senatore, A.: The impact of initial conditions on convection-permitting simulations of a flood event over complex mountainous terrain, Hydrology and Earth System Sciences, 24, 771–791, doi:10.5194/hess-24-771-2020, 2020.

Ludwig, P., Pinto, J. G., Raible, C. C., and Shao, Y.: Impacts of surface boundary conditions on regional climate model simulations of European climate during the Last Glacial Maximum, Geophysical Research Letters, 44, 5086–5095, doi:10.1002/2017GL073622, 2017.

Ludwig, P., Gómez-Navarro, J. J., Pinto, J. G., Raible, C. C., Wagner, S., and Zorita, E.: Perspectives of regional paleoclimate modeling, Annals of the New York Academy of Sciences, 1436, 54–69, doi:10.1111/nyas.13865, 2019.

Ludwig, P., Gavrilov, M. B., Markovic, S. B., Ujvari, G., and Lehmkuhl, F.: Simulated regional dust cycle in the Carpathian Basin and the Adriatic Sea region during the Last Glacial Maximum, Quaternary International, 581-582, 114–127, doi:10.1016/j.quaint.2020.09.048, 2020.

Mann, H. B.: Nonparametric tests against trend, Econometrica: Journal of the Econometric Society, pp. 245–259, tex.publisher: JSTOR, 1945.

Merz, N., Raible, C. C., Fischer, H., Varma, V., Prange, M., and Stocker, T. F.: Greenland accumulation and its connection to the large-scale atmospheric circulation in ERA-Interim and paleoclimate simulations, Climate of the Past, 9, 2433–2450, doi:10.5194/cp-9-2433-2013, 2013.

Merz, N., Born, A., Raible, C. C., Fischer, H., and Stocker, T. F.: Dependence of Eemian Greenland temperature reconstructions on the ice sheet topography, Climate of the Past, 10, 1221–1238, doi:10.5194/cp-10-1221-2014, 2014a.

Merz, N., Gfeller, G., Born, A., Raible, C. C., Stocker, T. F., and Fischer, H.: Influence of ice sheet topography on Greenland precipitation during the Eemian interglacial, Journal of Geophysical Research: Atmospheres, 119, 10,749–10,768, doi:10.1002/2014JD021940, 2014b.

Merz, N., Raible, C. C., and Woollings, T.: North Atlantic eddy-driven jet in interglacial and glacial winter climates, Journal of Climate, 28, 3977–3997, doi:10.1175/JCLI-D-14-00525.1, 2015.

Messmer, M., Gómez-Navarro, J. J., and Raible, C. C.: Sensitivity experiments on the response of Vb cyclones to sea surface temperature and soil moisture changes, Earth System Dynamics, 8, 477–493, doi:10.5194/esd-8-477-2017, 2017.

Montavez, J. P., Lopez-Romero, J. M., Jerez, S., Gomez-Navarro, J. J., Jimenez-Guerrero, P., and de Lisboa, U.: How much spin-up period is really necessary in regional climate simulations?, p. 1, 2017.

Neale, R. B., Richter, J. H., Conley, A. J., Park, S., Lauritzen, P. H., Gettelman, A., Rasch, P. J., and Vavrus, J.: Description of the NCAR community atmosphere model (CAM4), National Center for Atmospheric Research Tech. Rep. NCAR/TN+ STR, URL http://www.cesm.ucar.edu/models/ccsm4.0/cam/docs/description/cam4_desc.pdf, 2010.

Niu, G.-Y., Yang, Z.-L., Mitchell, K. E., Chen, F., Ek, M. B., Barlage, M., Kumar, A., Manning, K., Niyogi, D., Rosero, E., Tewari, M., and Xia, Y.: The community Noah land surface model with multiparameterization options (Noah-MP): 1. model description and evaluation with local-scale measurements, Journal of Geophysical Research: Atmospheres, 116, D12 109, doi:10.1029/2010JD015139, 2011.

Oleson, W., Lawrence, M., Bonan, B., Flanner, G., Kluzek, E., Lawrence, J., Levis, S., Swenson, C., Thornton, E., Dai, A., Decker, M., Dickinson, R., Feddema, J., Heald, L., Hoffman, F., Lamarque, J.-F., Mahowald, N., Niu, G.-Y., Qian, T., Randerson, J., Running, S., Sakaguchi, K., Slater, A., Stockli, R., Wang, A., Yang, Z.-L., Zeng, X., and Zeng, X.: Technical description of version 4.0 of the community land model (CLM), NCAR

Technical Note NCAR/TN-478+STR, National Center for Atmospheric Research, Boulder, CO, Boulder, CO, URL http://www.cesm.ucar.edu/models/cesm1.0/clm/CLM4_Tech_Note.pdf, 2010.

Pennelly, C., Reuter, G., and Flesch, T.: Verification of the WRF model for simulating heavy precipitation in Alberta, Atmospheric Research, 135-136, 172–192, doi:10.1016/j.atmosres.2013.09.004, 2014.

Pfeiffer, M., Spessa, A., and Kaplan, J. O.: A model for global biomass burning in preindustrial time: LPJ-LMfire (v1.0), Geoscientific Model Development, 6, 643–685, doi:10.5194/gmd-6-643-2013, 2013.

Prein, A. F., Gobiet, A., Suklitsch, M., Truhetz, H., Awan, N. K., Keuler, K., and Georgievski, G.: Added value of convection permitting seasonal simulations, Climate Dynamics, 41, 2655–2677, doi:10.1007/s00382-013-1744-6, 2013.

Prein, A. F., Langhans, W., Fosser, G., Ferrone, A., Ban, N., Goergen, K., Keller, M., Tölle, M., Gutjahr, O., Feser, F., Brisson, E., Kollet, S., Schmidli, J., Lipzig, N. P. M. v., and Leung, R.: A review on regional convection-permitting climate modeling: demonstrations, prospects, and challenges, Reviews of Geophysics, 53, 323–361, doi:10.1002/2014RG000475, 2015.

Prentice, I. C., Cramer, W., Harrison, S. P., Leemans, R., Monserud, R. A., and Solomon, A. M.: Special paper: a global biome model based on plant physiology and dominance, soil properties and climate, Journal of Biogeography, 19, 117–134, doi:10.2307/2845499, publisher: Wiley, 1992.

Seguinot, J., Ivy-Ochs, S., Jouvet, G., Huss, M., Funk, M., and Preusser, F.: Modelling last glacial cycle ice dynamics in the Alps, The Cryosphere, 12, 3265–3285, doi:10.5194/tc-12-3265-2018, 2018.

Sen, P. K.: Estimates of the regression coefficient based on Kendall's tau, Journal of the American statistical association, 63, 1379–1389, tex.publisher: Taylor & Francis Group, 1968.

Siewert, J. and Kroszczynski, K.: GIS data as a valuable source of information for increasing resolution of the WRF model for Warsaw, Remote Sensing, 12, 1881, doi:10.3390/rs12111881, 2020.

Sitch, S., Smith, B., Prentice, I. C., Arneth, A., Bondeau, A., Cramer, W., Kaplan, J. O., Levis, S., Lucht, W., Sykes, M. T., Thonicke, K., and Venevsky, S.: Evaluation of ecosystem dynamics, plant geography and terrestrial carbon cycling in the LPJ dynamic global vegetation model, Global Change Biology, 9, 161–185, doi:10.1046/j.1365-2486.2003.00569.x, 2003.

Skamarock, W. C. and Klemp, J. B.: A time-split nonhydrostatic atmospheric model for weather research and forecasting applications, Journal of Computational Physics, 227, 3465–3485, doi:10.1016/j.jcp.2007.01.037, 2008.

Skamarock, W. C., Klemp, J. B., Dudhia, J., Gill, O., Barker, D., Duda, G., Huang, X.-y., Wang, W., and Powers, G.: A description of the advanced research WRF version 3, doi:10.5065/D68S4MVH, 2008.

Skamarock, W. C., Klemp, J. B., Dudhia, J., Gill, D. O., Liu, Z., Berner, J., Wang, W., Powers, J. G., Duda, M. G., Barker, D. M., and Huang, X.-Y.: A Description of the Advanced Research WRF Model Version 4, Tech. rep., UCAR/NCAR, doi:10.5065/1DFH-6P97, 2019.

Smith, T. M., Shugart, H. H., Woodward, F. I., and Burton, P. J.: Plant functional types, in: Vegetation Dynamics & Global Change, edited by Solomon, A. M. and Shugart, H. H., pp. 272–292, Springer US, Boston, MA, doi:10.1007/978-1-4615-2816-6_14, 1993.

Solman, S. A. and Blázquez, J.: Multiscale precipitation variability over South America: analysis of the added value of CORDEX RCM simulations, Climate Dynamics, 53, 1547–1565, doi:10.1007/s00382-019-04689-1, 2019.

Strandberg, G., Brandefelt, J., Kjellstro M., E., and Smith, B.: High-resolution regional simulation of Last Glacial Maximum climate in Europe, Tellus A: Dynamic Meteorology and Oceanography, 63, 107–125, doi:10.1111/j.1600-0870.2010.00485.x, 2011.

Su, F., Duan, X., Chen, D., Hao, Z., and Cuo, L.: Evaluation of the global climate models in the CMIP5 over the Tibetan Plateau, Journal of Climate, 26, 3187–3208, doi:10.1175/JCLI-D-12-00321.1, 2012.

Theil, H.: A rank-invariant method of linear and polynomial regression analysis, 1-2; confidence regions for the parameters of linear regression equations in two, three and more variables, Indagationes Mathematicae, XII, URL https://ir.cwi.nl/pub/18445, number: SP 5/49/R, 1950.

Velasquez, P., Kaplan, J. O., Messmer, M., Ludwig, P., and Raible, C. C.: The role of land cover in the climate of glacial Europe, Climate of the Past, 17, 1161–1180, doi:10.5194/cp-17-1161-2021, 2021.

Wyszogrodzki, A. A., Miao, S., and Chen, F.: Evaluation of the coupling between mesoscale-WRF and LES-EULAG models for simulating fine-scale urban dispersion, Atmospheric Research, 118, 324–345, doi:10.1016/j.atmosres.2012.07.023, 2012.

Zhang, Y., Qian, Y., Dulière, V., Salathé, E. P., and Leung, L. R.: ENSO anomalies over the Western United States: present and future patterns in regional climate simulations, Climatic Change, 110, 315–346, doi:10.1007/s10584-011-0088-7, 2012.

Zheng, D., Velde, R. V. D., Su, Z., Wen, J., and Wang, X.: Assessment of Noah land surface model with various runoff parameterizations over a Tibetan river, Journal of Geophysical Research: Atmospheres, 122, 1488–1504, doi:10.1002/2016JD025572, 2017.

Chapter 3

The Role of Land Cover in the Climate of Glacial Europe

P. Velasquez, J. O. Kaplan, M. Messmer, P. Ludwig and C. C. Raible.

Published in *Climate of the Past*, Volume 17, pp. 1161–1180, 2021.

https://doi.org/10.5194/cp-17-1161-2021.

Clim. Past, 17, 1161–1180, 2021
https://doi.org/10.5194/cp-17-1161-2021

Climate of the Past
Open Access
EGU

The role of land cover in the climate of glacial Europe

Patricio Velasquez[1,2], Jed O. Kaplan[3], Martina Messmer[1,2,4], Patrick Ludwig[5], and Christoph C. Raible[1,2]

[1]Climate and Environmental Physics, Physics Institute, University of Bern, Bern, Switzerland
[2]Oeschger Center for Climate Change Research, University of Bern, Bern, Switzerland
[3]Department of Earth Sciences, The University of Hong Kong, Hong Kong SAR, China
[4]School of Earth Sciences, The University of Melbourne, Melbourne, Victoria, Australia
[5]Institute of Meteorology and Climate Research, Karlsruhe Institute of Technology, Karlsruhe, Germany

Correspondence: Patricio Velasquez (patricio.velasquez@climate.unibe.ch)

Received: 13 November 2020 – Discussion started: 21 November 2020
Revised: 4 May 2021 – Accepted: 17 May 2021 – Published: 14 June 2021

Abstract. Earth system models show wide disagreement when simulating the climate of the continents at the Last Glacial Maximum (LGM). This disagreement may be related to a variety of factors, including model resolution and an incomplete representation of Earth system processes. To assess the importance of resolution and land–atmosphere feedbacks on the climate of Europe, we performed an iterative asynchronously coupled land–atmosphere modelling experiment that combined a global climate model, a regional climate model, and a dynamic vegetation model. The regional climate and land cover models were run at high (18 km) resolution over a domain covering the ice-free regions of Europe. Asynchronous coupling between the regional climate model and the vegetation model showed that the land–atmosphere coupling achieves quasi-equilibrium after four iterations. Modelled climate and land cover agree reasonably well with independent reconstructions based on pollen and other paleoenvironmental proxies. To assess the importance of land cover on the LGM climate of Europe, we performed a sensitivity simulation where we used LGM climate but present-day (PD) land cover. Using LGM climate and land cover leads to colder and drier summer conditions around the Alps and warmer and drier climate in southeastern Europe compared to LGM climate determined by PD land cover. This finding demonstrates that LGM land cover plays an important role in regulating the regional climate. Therefore, realistic glacial land cover estimates are needed to accurately simulate regional glacial climate states in areas with interplays between complex topography, large ice sheets, and diverse land cover, as observed in Europe.

1 Introduction

The Last Glacial Maximum (LGM, 21 ka; Yokoyama et al., 2000; Clark et al., 2009; Van Meerbeeck et al., 2009) is a period of focus for Earth system modelling because it represents a time when boundary conditions were very different from the present and is therefore a good test bed of models' ability to faithfully reproduce a range of climate states (e.g. Mix et al., 2001; Janská et al., 2017; Cleator et al., 2020). In Europe, the LGM is also an interesting period in human history because small groups of highly mobile Upper Paleolithic hunter-gatherers persisted in the face of inhospitable climate, while Neanderthals disappeared (Finlayson, 2004; Finlayson et al., 2006; Finlayson, 2008; Burke et al., 2014; Maier et al., 2016; Baena Preysler et al., 2019; Klein et al., 2021). However, despite more than 3 decades of research, the LGM climate of the continents is only poorly understood. Global climate models (GCMs) show little agreement in LGM simulations for Europe (Braconnot et al., 2012; Kageyama et al., 2017; Ludwig et al., 2019; Kageyama et al., 2021). It has been suggested that a reason for the large uncertainty could be related to the spatial resolution in the climate models (Walsh et al., 2008; Jia et al., 2019b; Ludwig et al., 2019; Raible et al., 2020). Advances in regional climate models have led to the application of such models to the glacial climate of Europe on a high spatial resolution (e.g. Kjellström et al., 2010; Strandberg et al., 2011; Gómez-Navarro et al., 2012, 2013; Ludwig et al., 2017, 2020). Here, we further investigate the importance of land cover for climate during this period.

Published by Copernicus Publications on behalf of the European Geosciences Union.

Paleoclimate reconstructions suggest that the climate of Europe was 10 to 14 °C colder and around 200 mm yr^{-1} drier during the LGM compared to the present day (PD; Wu et al., 2007; Bartlein et al., 2011). However, uncertainties in the paleoclimate reconstructions are large, the few sites with samples dating to the LGM are not uniformly distributed in space (e.g. Wu et al., 2007), and in some regions, reconstructions are contradictory (e.g. de Vernal et al., 2006). For example, some LGM climate reconstructions suggest that the Iberian Peninsula was dry (Bartlein et al., 2011; Cleator et al., 2020), while others suggest wetter conditions were prevalent (Vegas et al., 2010; Moreno et al., 2012). Some of these discrepancies may result from the fact that many paleoclimate archives record a certain season, while the signal is frequently interpreted as an annual value (Beghin et al., 2016), or from the fact that even sites that are close together record strong climatic gradients. Whatever the case, generation of a spatially continuous map of climate and environmental conditions in the LGM Europe is currently not possible using a strictly proxy-driven approach. As an alternative, it should be possible to generate continuous maps using climate models.

GCM simulations are overall consistent with reconstructions in simulating an LGM climate that is largely colder and drier than PD (e.g. Ludwig et al., 2016; Hofer et al., 2012a). At the regional scale, however, GCMs show broad intermodel variety and partly disagree in comparison to proxy reconstructions, particularly concerning the magnitude and spatial patterning of temperature and precipitation (Harrison et al., 2015). For example, GCMs show a broad disagreement in the simulation of precipitation over the Iberian Peninsula, with some models suggesting it was wetter while in others the simulated climate is drier compared to PD (Beghin et al., 2016). One possible explanation for the disagreement is the coarse spatial resolution of the GCMs; at the continental scale, mountains, ice sheets, and water bodies have an important influence on regional circulation and climate that may not be represented appropriately at a typical GCM grid spacing of ca. 100 km (Rauscher et al., 2010; Gómez-Navarro et al., 2011, 2012, 2013; Di Luca et al., 2012; Prein et al., 2013; Demory et al., 2020; Iles et al., 2020).

To improve the representation of local and regional climate, GCMs can be dynamically downscaled using regional climate models (RCMs). Ludwig et al. (2019) found that downscaling using an RCM offers a clear benefit to answer paleoclimate research questions and to improve interpretation of climate modelling and proxy reconstructions. They also found that the regional climate models require appropriate surface boundary conditions to properly represent the lower troposphere. Studies have demonstrated that a realistic representation of surface conditions is essential for the accuracy of the simulated regional climate as they play a crucial role in regulating water and energy fluxes between the land surface and the atmosphere (e.g. Crowley and Baum, 1997; Kjellström et al., 2010; Strandberg et al., 2011, 2014; Gómez-Navarro et al., 2015; Jia et al., 2019a; Ludwig et al., 2017).

As noted above, the sparse distribution of paleoecological samples in Europe that are securely dated to the LGM precludes the development of a continuous map of land cover that can be used as a boundary condition for climate modelling and other purposes, e.g. archaeological and botanical research. Since climate affects land cover and land cover in turn affects climate, it is not sufficient to simply use climate model output to generate a vegetation map. To overcome this dichotomy, one may adopt a coupled modelling approach, where a climate model simulation is initialised with an estimate of land cover and the resulting climate output fields are used to simulate land cover. This process, which is called asynchronous coupling, is repeated between the climate and land cover models until the land–atmosphere system is in quasi-equilibrium. Asynchronous coupling is computationally inexpensive and has been successfully employed in several modelling studies to investigate problems in paleoclimate science (e.g. Texier et al., 1997; Noblet et al., 1996). For example, Kjellström et al. (2010) uses an iterative coupling of an RCM and a land cover model and found that asynchronous coupling produces a vegetation cover that is close to paleo-reconstructions. Also, Strandberg et al. (2011) and Ludwig et al. (2017) showed that fine-scale land cover is important for representing the climate and needs to be included in regional climate simulations.

Here, we perform an asynchronously coupled modelling study to simulate the climate and land cover of Europe at the LGM. The asynchronously coupled modelling starts with a GCM (Community Climate System Model version 4, CCSM4; Gent et al., 2011) which serves as input to drive a dynamic vegetation model (LPJ-LMfire; Pfeiffer et al., 2013). In a next step, the atmospheric boundary conditions from the GCM and the output of LPJ-LMfire are passed to an RCM (WRF; Skamarock and Klemp, 2008). The resulting RCM output is in turn used to drive LPJ-LMfire which again returns land cover to the RCM. The RCM simulation is then repeated with the new land cover as a boundary condition. We evaluate the results of our coupled model experiment using independent reconstructions of land cover and climate, and we perform a sensitivity test to better understand the importance of land cover for LGM climate in Europe by forcing the RCM with an alternative set of land-surface boundary conditions.

2 Models and methods

2.1 General circulation model: CCSM4

In this study, we dynamically downscaled one global climate simulation for PD conditions (1990 CE conditions) and another one for LGM. These global simulations were performed with the atmospheric and land component of CCSM (version 4; Gent et al., 2011). A horizontal grid spacing of

$1.25° \times 0.9°$ (longitude $\times$ latitude) was used in both components. The vertical dimension is discretised in 26 vertical hybrid sigma-pressure levels in the atmospheric component (CAM4; Neale et al., 2010) and 15 soil layers in the land component (CLM4; Oleson et al., 2010). CCSM4 was coupled to so-called data models for the ocean and sea ice. These surface boundary conditions were obtained from a fully coupled simulation with CCSM3 at lower resolution (see details in Hofer et al., 2012a). CCSM3 provided monthly mean time-varying sea-ice cover and sea-surface temperatures (SSTs). Furthermore, the Community Ice Code (version 4, CICE4; Hunke and Lipscomb, 2010) was set to its thermodynamic-only mode. This means that sea-ice cover was prescribed and surface fluxes through the ice were computed by considering snow depth, albedo, and surface temperature as simulated by CAM4 (Merz et al., 2015). Further details of the global model setting were presented in Hofer et al. (2012a, b) and Merz et al. (2015).

Each CCSM4 simulation was run for 33 years, from which only the last 30 years and 2 months were used in this study. PD boundary conditions were set to 1990 CE values, whereas LGM boundary conditions were modified as follows: lower concentrations of greenhouse gases ($CO_2 = 185$ ppm, $N_2O = 200$ ppb, and $CH_4 = 350$ ppb), change in Earth's orbital parameters (Berger, 1978), addition of major continental ice sheets (Peltier, 2004), and associated sea-level changes (120 m lower than today; Clark et al., 2009). Note that land cover was set to pre-industrial conditions in the LGM simulation. Additional land cells of the LGM simulation are filled with vegetation and soil types of the mean values of nearby cells, and in the ice-covered regions the model's standard values are used for such conditions. The simulations further provided 6-hourly data, which is necessary to drive regional climate models.

These PD and LGM CCSM4 simulations have been analysed in a variety of studies, including additional simulations for other glacial and interglacial states (e.g. Hofer et al., 2012a, b; Merz et al., 2013, 2014a, b, 2015, 2016; Landais et al., 2016). The focus of these studies was in particular on the model's ability to simulate LGM climate and atmospheric circulation changes during glacial times. Hofer et al. (2012a) showed that the model performs reasonably well under PD conditions, showing a cold bias in the global mean temperature of 0.3 °C. The reason for this bias is the rather coarse resolution of the ocean, which led to an underestimation of the northward heat transport in the North Atlantic and an overestimation in the horizontal extension of sea-ice cover (Hofer et al., 2012a). The LGM CCSM4 simulation agrees with models used in the second phase of the Paleoclimate Modelling Intercomparison Project (PMIP2; Braconnot et al., 2007) showing a global mean temperature response between LGM and pre-industrial conditions of -5.6 °C. However, the temperature response over Europe shows a better agreement with proxy data (Wu et al., 2007) than the multi-model mean response in Braconnot et al. (2007). The global mean precipitation response of the LGM simulation used in this study is similar to the multi-model mean response of Braconnot et al. (2007), although the regional pattern and seasonal behaviour show some deviations from proxy data over Europe (Wu et al., 2007; Hofer et al., 2012a). The LGM simulation further reveals a clear southward shift and a more zonal orientation of the storm track over the North Atlantic compared to PD conditions (Hofer et al., 2012a). This shift and substantial changes in the weather patterns (Hofer et al., 2012b) are able to explain precipitation anomalies over the Iberian Peninsula and the western part of the Mediterranean Sea. Sensitivity simulations in Merz et al. (2015) suggested that the shift can be traced back to the height of the Laurentide ice sheet and the effect of it on stationary and transient waves and the eddy-driven jet over the North Atlantic. Such a shift is also reported in several other modelling studies (see review of Raible et al., 2020). Overall, CCSM4 simulations of LGM climate were state of the art in 2012, and they still are today as their horizontal resolution is similar to models used in phase 4 of the Paleoclimate Model Intercomparison Project (PMIP4; Kageyama et al., 2017, 2021).

2.2 Regional climate model: WRF

To investigate the importance of model resolution and land cover on the climate of LGM Europe, we dynamically downscaled the global CCSM4 simulations using the Weather Research and Forecasting (WRF) model (version 3.8.1, Skamarock et al., 2008). This regional climate model was set up with two domains that are two-way nested. These domains have 40 vertical eta levels and a horizontal grid spacing of 54 and 18 km. The inner domain is centred on the Alpine region, and the outer domain includes an extended westward and northward area to capture the influence of the North Atlantic Ocean and the Fennoscandian ice sheet on the European climate (Fig. 1). The relevant parameterisation schemes chosen to run WRF are described in Velasquez et al. (2020).

The initial and boundary conditions for the WRF model were provided by CCSM4 simulations, including the Fennoscandian ice sheet and reduced sea levels during the LGM. Other external forcing functions followed the PMIP3 protocol (for more details, see Hofer et al., 2012a; Ludwig et al., 2017). Furthermore, no nudging was applied in the RCM simulations. LGM glaciation over the Alpine region was included in the regional climate model using estimates from Seguinot et al. (2018) and additional LGM glaciated areas (e.g. Pyrenees, Carpathians) from Ehlers et al. (2011). The LGM land cover is described in Sect. 2.4. These settings are used to produce the main simulation (LGM_{LGM}) which at the same time is the final product of the asynchronous coupling design (described in Sect. 2.4).

To perform the regional simulations in this study, we used the so-called adaptive time-step method as described in Skamarock et al. (2008); i.e. the integration time step can vary from time to time. For example, the model is stable with a

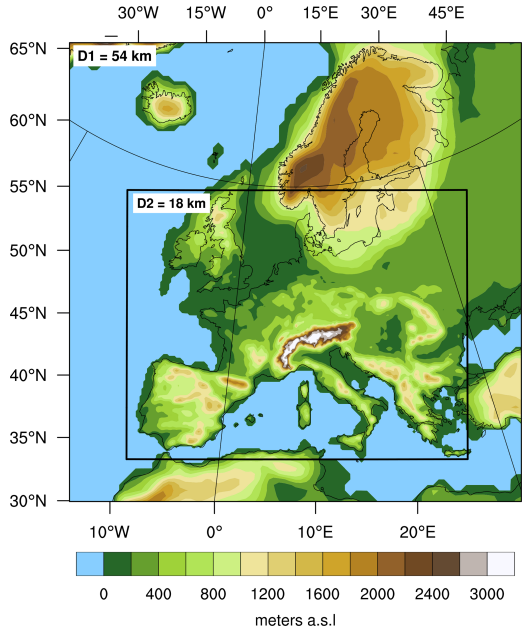

Figure 1. Topography and the two domains for the WRF LGM simulations.

time step of 160 s during most integration steps, but it might need a reduction to 60 s during convective situations to maintain stability. With a fixed time step, the entire simulation must be run with 60 s to overcome these convective situations, while the adaptive time-step method is able to make use of the larger time step 160 s during most of the simulation. The advantage of this approach is to substantially save computer resources. Furthermore, each simulation was driven by the 30 years of the corresponding GCM simulation (excluding the 3-year spin-up of the GCM simulation). These 30 years were split up into two single 15-year periods which are both preceded by a 2-month spin-up to account for the time required for land surface to come into quasi equilibrium. We used the last 2 months of the 3-year spin-up of the GCM simulation for the first 15 years. A spin-up of 2 months in the regional model is sufficient as soil moisture reaches a quasi equilibrium, i.e. no significant trend after 15 d in the four layers of the WRF land-surface scheme, i.e. down to 2 m.

We also carried out a control simulation under PD conditions (PD_{PD}) to assess the simulated LGM climate and land cover response compared to proxy data. PD_{PD} was driven by the GCM simulation with 1990 CE conditions (Hofer et al., 2012a) and used the default PD MODIS-based land cover dataset from WRF (Skamarock and Klemp, 2008).

Finally, we conducted a sensitivity simulation to quantify the importance of land cover for the LGM climate in Europe (LGM_{PD}). This simulation used the GCM simulation with LGM conditions (Hofer et al., 2012a) but with the default PD MODIS-based land cover dataset from WRF for the land surface (Skamarock and Klemp, 2008).

Comparing LGM_{PD} with PD_{PD} illustrates the atmospheric response to changes only in the atmospheric forcing, i.e. without changes in land cover. The comparison of LGM_{LGM} and the LGM_{PD} allows us to extract the influence of land cover on the atmosphere, i.e. without changes in atmospheric boundary conditions. These simulations are summarised in Table 1.

To assess the statistical significance of the responses, we use a bootstrapping technique (Wilks, 2011). This technique consists of randomly selecting elements from the original sample to generate a new sample. This is also called resampling whereby the number of elements remains unchanged. This procedure is repeated 1000 times. A new mean value is calculated from each resampling obtaining 1000 mean values that are used to build a probabilistic distribution function (PDF). We assess the significance of the mean value using a significance level of 0.01 for each PDF's tail. The bootstrapping technique is applied to the spatially averaged values using as elements the climatological mean values across Europe. We use one experiment to build the PDF on which we allocate the spatially averaged value of another experiment to assess the significance. Also, the bootstrapping technique is applied at each grid point using as elements the 30 yearly mean values. At each grid point, we obtain the PDF from one experiment on which we allocate the climatological mean value of another experiment to estimate the significance.

2.3 Dynamic global vegetation model: LPJ-LMfire

Land cover for the LGM is simulated by the LPJ-LMfire dynamic global vegetation model (Pfeiffer et al., 2013), which is an evolution of LPJ (Sitch et al., 2003). LPJ-LMfire is a processed-based, large-scale representation of vegetation dynamics and land–atmosphere water and carbon exchanges that simulates land cover patterns in response to climate, soils, and atmospheric CO_2 concentrations (Prentice et al., 1992; Haxeltine and Prentice, 1996; Haxeltine et al., 1996; Kaplan, 2001; Kaplan et al., 2016). LPJ-LMfire simulates land cover in the form of the fractional coverage of nine plant functional types (PFTs), including tropical, temperate, and boreal trees and tropical and extratropical herbaceous vegetation (Sitch et al., 2003).

In each of our simulations, we drove LPJ-LMfire for 1020 years with the climate and forcing (greenhouse gases: CO_2, N_2O, and CH_4) from the GCM and PD soil physical properties extrapolated out onto the continental shelves (Kaplan et al., 2016). Such a long simulation is not necessary to bring above-ground vegetation into quasi-equilibrium with climate, but it allows soil organic matter to equilibrate. Since the vegetation model is computationally inexpensive, we per-

Table 1. Set of simulations used in the asynchronous coupling and sensitivity experiments. First column indicates the name of the simulation, second and third columns the forcing used in the global and regional climate models, and fourth column the purpose of the comparison.

Name	GCM simulations	RCM simulations		Aim
	Hofer et al. 2012a	topography and other forcing	land cover	insights into the responses to changes in the
PD_{PD}	1990s	1990s	1990s	forcing
LGM_{PD}	LGM	LGM	1990s	land cover
LGM_{LGM}	LGM	LGM	LGM	

formed these millennium-long simulations so that they could be analysed for other purposes in the future.

2.4 Iterative asynchronous coupling design

To create the best possible estimate of European land cover for the LGM, we used an iterative asynchronous coupling design that combines CCSM4/WRF with the LPJ-LMfire model (resulting in the LGM_{LGM} climate simulation). This coupling design consists of four steps: (i) the fully coupled CCSM4 provides atmospheric variables for the LGM to generate the first approximation of LGM land cover with LPJ-LMfire at a horizontal grid spacing of $1.25° \times 0.9°$ (longitude $\times$ latitude); (ii) WRF is driven by the CCSM4 with LGM conditions and the first approximation of LGM land cover created in step (i) to generate the first downscaled atmospheric variables for the LGM at 54 and 18 km grid spacing; (iii) LPJ-LMfire is run with the downscaled LGM atmospheric variables (from step ii) to regenerate the LGM land cover at the RCM resolutions; and (iv) same as (ii) but WRF uses the land-surface boundary conditions simulated at 54 and 18 km. Steps (iii) and (iv) are carried out asynchronously over five additional iterations to achieve a quasi-equilibrium between the climate and land cover. Parts (i) and (ii) are regarded as the first iteration, and the iterations of (iii) and (iv) are regarded as the second to seventh iterations. The variables that are passed between the climate and vegetation models are summarised in Table 2. Vegetation cover fraction is defined as the fraction of ground covered by vegetation at each grid point, with values between 0 % and 100 %. Also, to classify vegetation cover fraction into the land cover categories required by WRF (according to NOAH-MP MODIS; Niu et al., 2011), we used a simple scheme based only on the cover fraction of the LPJ-LMfire PFTs. Note that we identified a problem with the land–sea mask and around glaciated areas which was fixed between the third and fourth iteration. To test whether the asynchronous coupling has reached a quasi-equilibrium state, we assess the statistical significance with a bootstrapping technique that is introduced at the end of Sect. 2.2.

Table 2. Variables passed between CCSM4/WRF and LPJ-LMfire.

CCSM4/WRF to LPJ-LMfire	
30-year monthly values	
Mean temperature at 2 m	Convective available potential energy
Daily max. temperature at 2 m	Horizontal wind velocity at 10 m
Daily min. temperature at 2 m	Precipitation (liquid and solid)
Total cloud cover fraction	
LPJ-LMfire to WRF	
30-year monthly values	Climatological value
Vegetation cover fraction	Land cover fraction (category)
Leaf area index	Dominant land cover type (category)
	Deep-soil temperature

3 Results of the iterative asynchronous coupling

The offline coupling design (Sect. 2.4) aims at generating a simulation of the LGM climate and land cover that is as realistic as possible. Thereby, it is important that the land cover and the climate is in quasi-equilibrium (Strandberg et al., 2011) in order to discard the source of uncertainty related to an unbalanced climate system. In this study, we determine the quasi-equilibrium in the land cover and the climate, first, through empirical observation and second, through a statistical test applied to a set of variables (see Sect. 2.4). To illustrate the differences between the iterations, we concentrate on climate and land cover changes over the ice-free land areas of Europe at LGM (in domain 2) using the following variables: the spatial climatology of total precipitation, temperature at 2 m, albedo, deep-soil temperature, cloud cover, leaf area index and vegetation cover fraction, and the number of grid points dominated by the following land cover categories: sparsely vegetated, tundra, forest, and shrublands (NOAH-MP MODIS categories, Niu et al., 2011). Land cover categories that are functionally similar are grouped together, e.g. wooded tundra, mixed tundra, and barren tundra are all combined into the category tundra. Some land cover categories are not considered in our analysis as they are poorly represented in both periods, e.g. savanna, grassland, and wetland, or are not relevant for the LGM, e.g. cropland and urban (Fig. 2a–b).

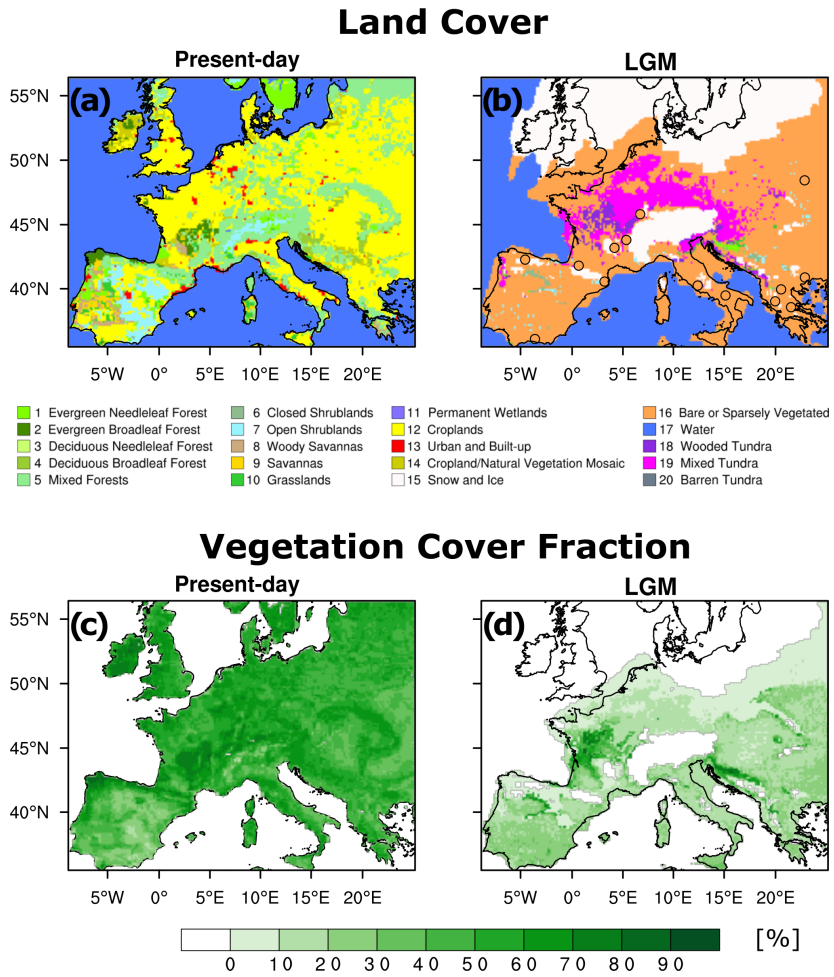

Figure 2. Land cover used by WRF. Panel **(a)** represents the dominant land cover category during PD. Panel **(b)** is the same as **(a)** but during the LGM. Panels **(c)** and **(d)** are the same as **(a)** and **(b)** but for vegetation cover fraction. Circles in **(b)** represent proxy evidence from Wu et al. (2007).

Results show that the most notable and statistically significant changes, from one iteration to the next, in the variables exchanged between land cover and atmosphere occur within the first four iterations (Fig. 3). Only albedo and leaf area index show significant changes also in the fifth iteration. The significance of the differences is assessed using a two-tailed bootstrapping technique with a significance level of 2 % (Sect. 2.2) and is marked in each panel of Fig. 3. Note that the significance for the land cover categories is not shown. The reason is that this significance can be summarised using the significance of the vegetation cover fraction. The variables level off from the fifth to the seventh iteration. In particular, we observe two sharp changes in all variables within the first five iterations. The first important change is found between the first and second iteration and is present in the atmospheric and land-surface variables. The reasoning is twofold: (i) there are significant changes in the land cover classes, e.g. forest fraction is reduced from 35 % to 2 %; (ii) the horizontal resolution of the land cover is increased from approximately 100 to 18 km (horizontal grid spacing of GCM and RCM, respectively). The higher spatial resolution of the RCM results in a better representation of the regional-to-local-scale processes and interactions with other components of the climate system compared to a GCM (Ludwig et al., 2019). The second change happens between the third and fourth iteration in precipitation and cloud cover (Fig. 3a and d) and between the fourth and fifth in albedo and leaf area index (Fig. 3c and d). Note that the improvements in the land–sea mask and around glaciated areas between the third and fourth iteration can partially explain the

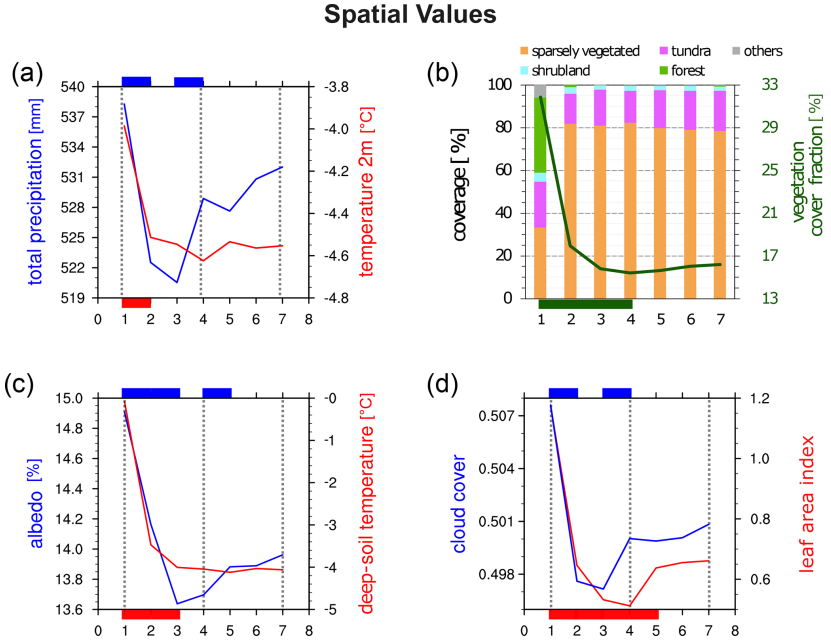

Figure 3. Thirty-year spatial climatology of annual mean values throughout the iterations. Panel **(a)** represents total precipitation (blue line) and temperature at 2 m (red line) and **(b)** the percentage spatial fraction of bare (orange), tundra (pink), shrubland (sky blue), forest (light green), others (grey), and the spatial mean value of vegetation cover fraction (dark green line); **(c)** is the same as **(a)** but for albedo and deep-soil temperature, and **(d)** is the same as **(a)** but for cloud cover and leaf area index. The grey dotted lines in **(a)**, **(c)**, and **(d)** represent the first, fourth, and seventh iterations. Blue, red, and green boxes represent statistically significant differences between iterations at a 2 % significance level (using a two-tailed bootstrapping technique).

significantly sharp change in precipitation and cloud cover between the third and fourth iteration. We consider the significant changes from the fourth to the fifth iteration in albedo and leaf area index as a delayed effect of the variation in cloud cover and precipitation and thus an effect of the improvement.

Spatially averaged total precipitation significantly decreases in the second iteration (drop of 15 mm) and significantly increases in the fourth iteration (increase of 9 mm) with small and no significant changes thereafter (blue line in Fig. 3a). A significant decrease in the spatially averaged temperature at 2 m is observed in the second iteration (cooling of around 0.5 °C), which turns into small and insignificant fluctuations in the range of a 10th of a degree afterwards (red line in Fig. 3a). Albedo significantly decreases until the third iteration (change of around 1.3 %) and significantly increases in the fifth iteration with small and insignificant changes afterwards (blue line Fig. 3c). A significant cooling is also observed in the spatially averaged deep-soil temperature from the first to the third iteration (red line in Fig. 3c). Deep-soil temperature stabilises from the fourth to the seventh iteration. Similar to total precipitation, we observe that the spatially averaged cloud cover fraction significantly decreases in the second iteration (change of 0.009) and significantly increases in the fourth iteration (change of 0.003) with very small and insignificant variations afterwards (blue line in Fig. 3d). Leaf area index significantly fluctuates till the fifth iteration (maximum change of 0.5) with minimal and insignificant changes thereafter (red line Fig. 3d). Additionally, changes in vegetation cover fraction are observed in the first four iterations (32 %, 18 %, 16 %, and 15 %). In the following iterations, the changes remain rather small and insignificant (Fig. 3b). The land cover categories change mostly between the first and second iteration. The category sparsely vegetated is strongly increased in the second iteration and at the same time forest is strongly reduced (Fig. 3b). Thus, the quasi-equilibrium state is achieved after the fourth to fifth iteration.

In the following, we analyse the spatial patterns of climate and land cover between the iterations that represent the transient progression towards quasi-equilibrium (fourth minus first iteration) and the quasi-equilibrium state (seventh minus fourth iteration). We consider temperature at 2 m, total precipitation, and vegetation cover fraction as variables that summarise the coupled land–atmosphere response. Note that temperature, precipitation, and vegetation cover fraction are displayed using absolute differences (Fig. 4a–f).

During the transient state (Fig. 4a, c, and e), the southwestern part of the Iberian Peninsula and some areas in Italy and

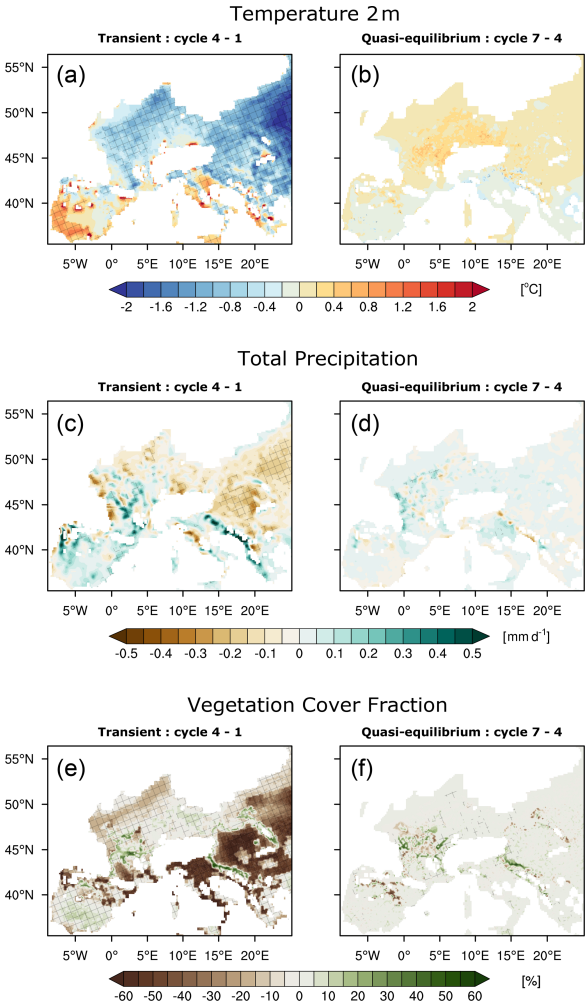

Figure 4. Differences in 30-year mean values. Panel **(a)** represents the difference in temperature at 2 m between the first and fourth iteration (transient); **(b)** is the same as **(a)** but between the fourth and seventh iteration (quasi-equilibrium). Panels **(c)**–**(d)** and **(e)**–**(f)** are the same as **(a)**–**(b)** but for total precipitation and vegetation cover fraction, respectively. Masked out areas are in white. Crosshatched areas indicate statistically significant differences using a two-tailed bootstrapping technique with a 2 % significance level.

Greece warm, but the rest of Europe experiences a cooling. In addition, precipitation reveals a wetting over the Iberian Peninsula, in parts of France, and in the Balkan Peninsula and a drying over eastern Europe, the north of the Alps, and some regions of France (Fig. 4c). The vegetation cover fraction shows a strong decrease during the transient state, particularly in the flat lands of eastern Europe (over 50 % reduction) and the Italian Peninsula, and an increase over the Iberian Peninsula (around 20 %) and northwest of the Alps (around 40 %; Fig. 4e). The vegetation response is related to changes in temperature and precipitation: many regions that experience a cooling are related to a reduction in vegetation. Drying and wetting are overall related to a reduction and an increase in vegetation cover, respectively. This is true except for a few areas in the north of the Alps and along the Mediterranean coast such as the eastern region of the Iberian Peninsula, southern Greece, and southern Italy. North of the Alps, the poor relation between precipitation and vegetation cover fraction could be explained by a lesser pronounced cooling. In the eastern part of the Iberian Peninsula and southern Greece, the reduction in vegetation seems to be related to an increase in temperature.

The changes between the seventh and fourth iterations, which illustrate the quasi-equilibrium state, are minimal for the three variables (Fig. 4b, d, and f). The remaining small differences are interpreted as a part of the internal climate variability and uncertainties predominantly caused by parameterisations in the models, e.g. cloud formation and microphysical processes (Casanueva et al., 2016; Rajczak and Schär, 2017; Shrestha et al., 2017; Knist et al., 2018; Yang et al., 2019).

4 Comparison and discussion of the modelled and reconstructed climate

To evaluate the $\mathrm{LGM}_{\mathrm{LGM}}$ climate simulation, we compared temperature and precipitation to pollen-based reconstructions. Wu et al. (2007) provided reconstructions of temperature and precipitation for the coldest and warmest months of the LGM at 14 sites in Europe. Thus, we considered 56 samples (14 sites $\times$ 2 variables $\times$ 2 months) in this comparison. For the model–proxy comparison, we use the nearest model grid point to the pollen site and consider the model and proxy reconstruction to agree when the model-based anomaly is within the 90 % confidence interval of the pollen-based anomaly (more details about the proxies in Wu et al., 2007). Note that the simulated temperature and precipitation are anomalies with respect to $\mathrm{PD}_{\mathrm{PD}}$ and that January and July values are selected to mimic the coldest and warmest months.

In general, cooler and drier anomalies are observed in the $\mathrm{LGM}_{\mathrm{LGM}}$ with especially pronounced cooling in January and drying in July (Fig. 5). This resembles the proxy evidence given by the pollen-based reconstruction of Wu et al. (2007). In January, we observe a positive precipitation anomaly of up to 7 mm d^{-1} over the Iberian Peninsula, northern Italy, and the Dinaric Alps (Fig. 5c). Overall, the $\mathrm{LGM}_{\mathrm{LGM}}$ climate agrees with the pollen-based paleoclimate reconstructions at three-quarters of the 56 samples.

Still, some samples, e.g. over the Iberian Peninsula, show considerable differences between the pollen-based and model-based climate anomalies, in line with similar findings mentioned in earlier studies (e.g. Beghin et al., 2016; Ludwig et al., 2016; Cleator et al., 2020). These differences can be associated with shortcomings within the GCM–RCM mod-

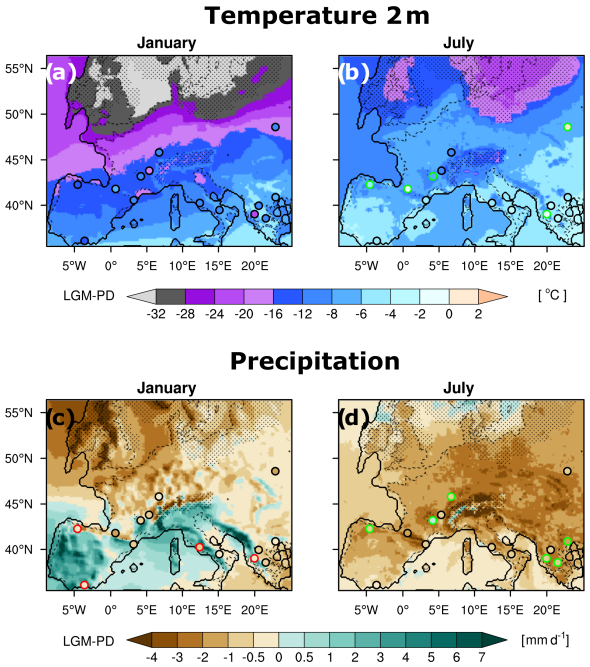

Figure 5. Changes in temperature and precipitation patterns. Panel **(a)** represents the differences in 30-year mean temperature between LGM and PD ($LGM_{LGM} - PD_{PD}$) for January. Panel **(b)** is the same as **(a)** but for July. Panels **(c)** and **(d)** are the same as **(a)** and **(b)** but for precipitation differences. Circles represent proxy evidence: a red (green) border indicates that the simulated value is significantly above (below) the proxy value at the closest grid cell of the model (outside the 90 % confidence interval, Wu et al., 2007). The solid line represents the LGM coastline, the dashed line the PD coastline, and dots the area covered by glaciers.

elling chain and/or uncertainties in the proxy reconstructions (Bartlein et al., 2011; Ludwig et al., 2019; Cleator et al., 2020). Kageyama et al. (2006) suggested that terrestrial paleoclimate proxies may be more sensitive to climatic extremes than to the climatological mean state, which could partly explain the discrepancies between pollen-based reconstructions and the model simulations. One important model–proxy disagreement is the precipitation anomaly over the Iberian Peninsula in January. Based on evidence for the presence of certain tree species in the northwestern part of the Iberian Peninsula, Roucoux et al. (2005) suggested that the LGM was not necessarily the period of the most severe, i.e. cold and dry, climatic conditions everywhere. Roucoux et al. (2005) and Ludwig et al. (2018) also suggested that this region during LGM sensu stricto was warmer and wetter than the end of Marine Isotope Stage 3 (MIS3, ca. 23 ka; Voelker et al., 1997; Kreveld et al., 2000) and the start of the Heinrich event 1 (H1, ca. 19 ka; Sanchez Goñi and Harrison, 2010; Álvarez-Solas et al., 2011; Stanford et al., 2011). This could be an indication that model–proxy comparison fails because the proxies refer to 21 ± 2 ka (Wu et al., 2007), i.e. either the end of MIS3 or the beginning of H1. Compared to the pre-industrial period, Beghin et al. (2016) found evidence in a model–proxy comparison that the interior and northwestern Iberian Peninsula experiences wetter conditions during the LGM. These wetter conditions can be explained by a southward shift in the North Atlantic storm track during the LGM compared to PD as suggested by many studies (e.g. Hofer et al., 2012a; Luetscher et al., 2015; Merz et al., 2015; Ludwig et al., 2016; Wang et al., 2018; Raible et al., 2020; Lofverstrom, 2020). Note further that we had only two pollen-based quantitative climate reconstructions from Iberia for the LGM; we therefore regard the model–proxy intercomparison in this region as equivocal.

5 Comparison and discussion of the modelled and reconstructed land cover

To evaluate the LGM_{LGM} and land cover simulation, we compare the simulated tree cover with pollen-based biome reconstructions from the BIOME6000 data product (Prentice and Jolly, 2000; Wu et al., 2007) and with a newer synthesis by Kaplan et al. (2016). For the purposes of this comparison, we define tree cover as the fraction of ground covered by trees at each grid point excluding herbaceous and grass, whose value varies between 0 % and 100 %.

The LGM_{LGM} simulation generally shows low values for vegetation cover fraction (Fig. 2d), which reflects lower temperatures, reduced precipitation, and lower global atmospheric CO_2 concentrations that were present at the LGM compared to the Holocene (Gerhart and Ward, 2010; Woillez et al., 2011; Chen et al., 2019; Lu et al., 2019). Our simulated LGM_{LGM} land cover is generally in good agreement with the pollen-based biome reconstructions (Fig. 2b). We interpret the pollen reconstructions of steppe vegetation as sparsely vegetated in the WRF land cover categories (Niu et al., 2011). Using the nine nearest 18 km grid points surrounding each pollen site to compare the model results with pollen-based reconstructions of the land cover categories, we define good model–proxy agreement when at least one of the grid points matches the proxy reconstruction. For example, the dominant land cover category northwest of the Alps (47.73° N, 6.5° E) reconstructed from pollen (steppe) agrees with the surrounding simulated land cover (sparse vegetation). For the Carpathian Basin, an area with few proxy reconstructions, the modelled LGM land cover categories are tundra and grassland, which is in agreement with results found by Magyari et al. (2014a, b). Additionally, we simulate an extended area of tundra categories (i.e. wooded and mixed tundra) between the Alps and the Fennoscandian ice sheet which can be regarded as the northernmost ice-free area of Europe. Similarly, Kjellström et al. (2010) simulated an extended area of tundra-like vegetation in the northernmost ice-free areas of Europe for MIS3.

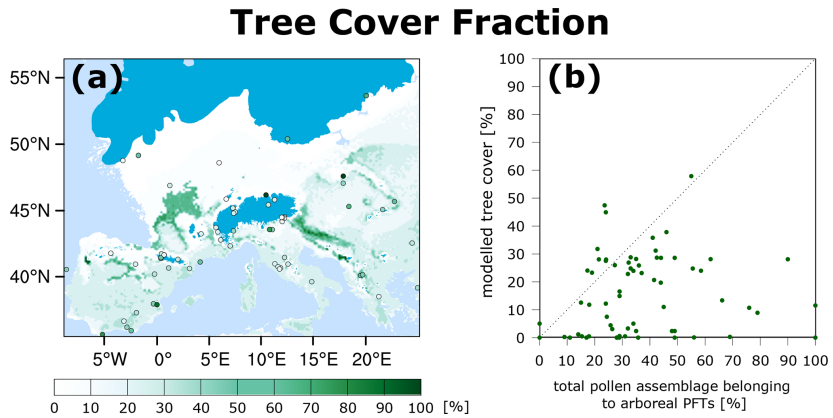

Figure 6. Comparison between modelled and reconstructed tree cover. Panel **(a)** shows the LPJ-LMfire-simulated tree cover fraction from LGM_{LGM}. Circles represent the 71 pollen samples securely dated to LGM from Kaplan et al. (2016). Panel **(b)** shows a scatter plot of reconstructed vs. modelled LGM tree cover.

We further compared tree cover fraction simulated by LPJ-LMfire with a reconstruction of relative landscape openness from 71 pollen sites across Europe containing samples securely dated to the LGM based on a compilation by Davis et al. (2015) and Kaplan et al. (2016). This compilation represents a substantial improvement in spatial coverage and dating precision compared to the 14 sites of BIOME6000 used by Wu et al. (2007). Comparison between modelled tree cover and relative landscape openness is shown in Fig. 6. Generally, LPJ-LMfire moderately underestimates tree cover compared with the pollen-based openness reconstructions. Modelled tree cover has a maximum value of about 60 %, while there are eight sites where the relative tree cover reconstruction is > 60 % and two samples with 100 % arboreal pollen percentage. As noted by Kaplan et al. (2016), these sites with very high reconstructed tree cover fraction should be treated with caution because they may represent locations with very little vegetation, e.g. at the edge of the Alpine ice sheet or at high-altitude in the Carpathian Mountains. In high mountain areas where we expect local vegetation to be very sparse if present at all, the pollen signal in sedimentary bodies may be dominated by the long-distance transport of tree pollen; this phenomenon is also observed in the analysis of pollen trapped in glacier ice (Brugger et al., 2019). At the bulk of the sites, LPJ-LMfire simulates 10 %–20 % lower tree cover than the relative tree cover inferred by the pollen. While this discrepancy is well within the uncertainty of both datasets and could be related to the calibration of arboreal pollen percentage with tree cover (Kaplan et al., 2016), it could also suggest that the modelled climate is too cold and/or too dry or that the LPJ-LMfire model is too sensitive to lower atmospheric CO_2 concentrations.

6 Influence of external forcing and land cover on climate

We assess the atmospheric response to changes in the entire climate system, in external forcing, and in land cover, separately, to better understand the importance of the land surface for the LGM climate in Europe. LGM_{LGM} is compared to PD_{PD} to determine the atmospheric response to complete LGM conditions. Then, we investigate the atmospheric response to changes in orbital forcing by comparing LGM_{PD} with PD_{PD}. Finally, the differences between LGM_{LGM} and LGM_{PD} determine the atmospheric response to changes in land cover. Our assessment considers the land areas without snow/ice that are shared by both LGM and PD climate, i.e. we discard glaciated areas and land areas on the continental shelves that were exposed at the LGM. Temperature and precipitation are selected as the main indicators of the atmospheric response, and latent and sensible heat fluxes as secondary indicators. Note that we use a two-tailed bootstrapping technique with a significance level of 2 % to assess the significance of the differences (Sect. 2.2), which is illustrated by bold numbers in Table 3.

Comparing LGM_{LGM} to PD_{PD} shows a statistically significant cooling of $-11.99\,°C$ in the annual value (Table 3). This cooling is significantly enhanced to $-15.34\,°C$ in DJF (December–January–February), remains similar to the annual mean in MAM and SON (March–April–May and September–October–November), and significantly weakens to $-7.24\,°C$ in JJA (June–July–August; Table 3). This clearly illustrates a seasonality in the temperature response to complete LGM conditions (LGM_{LGM} minus PD_{PD}). Broccoli and Manabe (1987) mentioned that one reason for the seasonality in the temperature response can be the fluctuations in the horizontal thermal advection from glaciers and ice sheets to ice-free regions, predominantly in winter. Additionally, we

Table 3. Assessment of the atmospheric response using 30 years of simulated precipitation and temperature data. First column indicates the simulations, second column the annual response, and the other columns the response in each season. Numbers in bold represent statistically significant differences using a two-tailed bootstrapping and a significance level of 2 %. Note that the assessment considers land areas without snow/ice that are shared by both LGM and PD climate and discards the continental shelves exposed at the LGM.

	Annual	DJF	MAM	JJA	SON
Temperature response (°C)					
$LGM_{LGM} - PD_{PD}$	**−11.99**	**−15.34**	**−13.85**	**−7.24**	**−11.53**
$LGM_{PD} - PD_{PD}$	**−12.06**	**−15.44**	**−13.19**	**−8.09**	**−11.52**
$LGM_{LGM} - LGM_{PD}$	0.07	0.10	**−0.66**	**0.85**	−0.01
Precipitation response (mm d^{-1})					
$LGM_{LGM} - PD_{PD}$	**−0.67**	0.09	**−0.86**	**−1.55**	**−0.37**
$LGM_{PD} - PD_{PD}$	**−0.53**	0.16	**−0.77**	**−1.15**	**−0.37**
$LGM_{LGM} - LGM_{PD}$	−0.14	−0.07	**−0.09**	−0.40	0
Latent heat response (W m^{-2})					
$LGM_{LGM} - PD_{PD}$	**−25.63**	**−6.09**	**−32.44**	**−52.47**	**−11.51**
$LGM_{PD} - PD_{PD}$	**−17.57**	**−5.34**	**−27.23**	**−28.14**	**−9.57**
$LGM_{LGM} - LGM_{PD}$	**−8.06**	**−0.75**	**−5.21**	**−24.33**	**−1.94**
Sensible heat response (W m^{-2})					
$LGM_{LGM} - PD_{PD}$	**7.48**	**−4.30**	**−2.44**	**33.97**	**2.69**
$LGM_{PD} - PD_{PD}$	**7.59**	0.10	**5.75**	**19.02**	**5.48**
$LGM_{LGM} - LGM_{PD}$	**−0.11**	**−4.40**	**−8.19**	**14.95**	**−2.79**

find a statistically significant dryness in the annual value of around $-0.67\,mm\,d^{-1}$ when comparing LGM_{LGM} to PD_{PD}. A significant drying is evident in most months, in particular in summer months, where precipitation is reduced by $-1.55\,mm\,d^{-1}$. Only in the winter months do we observe a marginal increase in precipitation (Table 3). Cao et al. (2019) on the one hand attributed the overall decrease in precipitation to the strong anticyclonic circulations over the ice sheets during LGM compared to PD, especially to the low-level divergent cold air (Schaffernicht et al., 2020). On the other hand, Luetscher et al. (2015) and Lofverstrom (2020) found wetter conditions in southern parts of Europe in LGM wintertime, and they attributed them to atmospheric rivers and Rossby-wave breaking, respectively. This together with the LGM southward shift of the storm track (found by Hofer et al., 2012a; Luetscher et al., 2015; Ludwig et al., 2016; Wang et al., 2018; Raible et al., 2020) could then compensate for an expected dryness in wintertime (i.e. LGM_{LGM} minus PD_{PD}), which would not only affect the statistical significance in wintertime, but also lead to the seasonality in the precipitation response to complete LGM conditions. The comparison (LGM_{LGM} minus PD_{PD}) also shows a statistically significant decrease in latent heat flux in the annual value ($-25.63\,W\,m^{-2}$), which is true for most months and particularly strong for JJA ($-52.47\,W\,m^{-2}$). Moreover, we observe a statistically significant increase in sensible heat flux of $7.48\,W\,m^{-2}$ (Table 3). This increase is strongest in JJA when it reaches an addition of $33.97\,W\,m^{-2}$ and weakest in SON as we find a small but still significant increase of $2.69\,W\,m^{-2}$. A statistically significant decrease in sensible heat flux of -4.30 and $-2.44\,W\,m^{-2}$ is simulated in DJF and MAM, respectively.

To further understand the atmospheric response, we investigate the role of the forcing (i.e. $LGM_{PD} - PD_{PD}$) and the land cover (i.e. $LGM_{LGM} - LGM_{PD}$), separately. The temperature response is clearly dominated by changes in the forcing. Changes in land cover can only slightly influence temperature by an additional cooling of 0.66 °C in MAM and a warming of 0.85 °C in JJA, both statistically significant (Table 3). Similarly, Jahn et al. (2005) found that the LGM-like vegetation cover produces colder temperatures (ca. −0.6 °C globally), especially in areas with the greatest decrease in tree cover. The precipitation anomalies are also dominated by changes in the forcing, whose values are statistically significant except in DJF, but changes in the land cover also contribute to a reduction in precipitation, especially in MAM (significant reduction of $0.09\,mm\,d^{-1}$) and JJA (reduction of $0.40\,mm\,d^{-1}$). The response of the latent heat flux is also dominated by changes in the forcing with statistically significant values. Changes in the land cover moderately influence the latent heat flux by an additional reduction of $8.06\,W\,m^{-2}$ in the annual mean, while changes in land cover account for almost half of the reduction in the latent heat flux in JJA ($-24.33\,W\,m^{-2}$). Moreover, the response of the sensible heat flux is dominated by changes in the orbital forcing in the annual mean, JJA, and SON. Modifications in land cover only dominate DJF and MAM by an additional significant reduction of 4.40 and $8.19\,W\,m^{-2}$, respectively. Still, changes in the land cover influence summer sensible heat by an additional increase of $14.95\,W\,m^{-2}$.

The analysis so far demonstrates that the seasonality of the atmospheric response is overall driven by changes in the forcing but its intensity can be modulated by changes in the land cover, in particular in the latent heat flux in JJA and sensible heat flux in DJF, MAM, and JJA. A possible reason for the modulated intensity in the response may be a modification of the stability in the lowest levels of the atmosphere that is produced by the changes in the land cover. A cooling (warming) in the lower layer may lead to an inversion (unstable) zone that therefore weakens (enhances) precipitation processes. Another reason is that the differences in land cover lead to modifications in available moisture coming from the surface, i.e. evapotranspiration or latent heat. A reduction in latent heat is interpreted as reduced availability of surface moisture, which leads to a reduction in precipitation. Ludwig et al. (2017) suggested that including LGM-like vegetation in regional climate models causes changes in heat fluxes that lead to impacts on temperature and precipitation. Based on a similar coupling design, Strandberg et al. (2011) found that the impact of a different land cover on LGM climate simulations is small compared to the uncertainties in

the proxy reconstructions. Even though this is also true in our study, our results and discussion suggest that modifications in land cover like deforestation could play an important role when other forcing agents marginally change, as is observed in some climate change scenarios such as RCP 2.6 and 4.5 (Strandberg and Kjellström, 2019; Davin et al., 2020; Jia et al., 2020).

To obtain a more detailed understanding of the atmospheric response to changes in land cover (LGM_{LGM} – LGM_{PD}), we further analyse the differences in the spatial patterns in January and July to be consistent with the evaluation done in Sect. 5. We focus on temperature at 2 m, precipitation and latent and sensible heat fluxes. We use a two-tailed bootstrapping technique with a significance level of 2 % to assess the significance of the differences at each grid point (Sect. 2.2), which is illustrated by crosshatched areas in Figs. 7 and 8.

The annual mean temperature shows a statistically significant cooling of around 2 °C in the vicinity of glaciers and in high-altitude regions; while a statistically significant warming is visible in lower-elevation areas including the southwestern part of the Iberian Peninsula, France, and the Carpathian Basin (Fig. 7a). A similar spatial pattern is observed for January and July temperatures: a significantly stronger warming is evident for the northern part of Italy in January (Fig. 7b), whereas the rest of the continent does not show significant changes. In July, the amplitude of the temperature anomaly becomes significantly stronger, especially where the positive temperature anomaly covers a large area, e.g. over eastern Europe (Fig. 7c). The precipitation response is moderate in the annual mean. A general and statistically significant decrease is observed over the rest of Europe. Changes in January precipitation are overall insignificant, except for some areas in eastern Europe where a significant dryness is observed. LGM land cover leads to a negative and statistically significant precipitation anomaly in July, which is especially strong around the Alps and in eastern Europe. The response of the latent heat flux is also moderate in the annual mean (Fig. 8a). We observe a general and statistically significant reduction, especially in eastern Europe. A similarly significant but weakened pattern is observed in January, which even shows a few small areas with an increase in latent heat flux (Fig. 8b). In July, a stronger reduction in the latent heat flux is observed with the largest reductions around the Alps and over eastern Europe (Fig. 8c). Note that some areas with strong increases in the latent heat flux (reddish) are associated with large PD urban areas. Moreover, the annual mean sensible heat flux shows a statistically significant reduction of about 30 $W m^{-2}$ around mountainous areas, i.e. the Pyrenees, Alps, and Carpathian Mountains (Fig. 8d), while a statistically significant increase in sensible heat is visible in lower-elevation areas, especially over France and some areas in eastern Europe (Fig. 8d). In January, the pattern of the sensible heat flux is overall moderately reduced (still statistically significant, Fig. 8e). In July, we find an enhanced amplitude of the sensible heat flux with small changes in the spatial pattern with respect to the annual one: there is an additional statistically significant decrease in sensible heat flux of around 60 $W m^{-2}$ around mountainous areas except for most of the Carpathian Mountains (Fig. 8f). A statistically significant increase in sensible heat flux dominates the rest of Europe, with values of up to 40 $W m^{-2}$ in some areas over central and eastern Europe.

Even though changes in land cover have a small-to-moderate effect on the response of temperature, precipitation, and the latent and sensible heat fluxes (Table 3), their spatial pattern changes strongly across Europe (Figs. 7, 8). Important spatial changes are statistically significant over eastern Europe in July. Strandberg et al. (2011) and Kjellström et al. (2010), in similar coupling designs, compared glacial simulations using two land cover settings and found that the simulated regional climate patterns in parts of Europe are sensitive to feedbacks from large differences in vegetation. Particularly, Kjellström et al. (2010) found that glacial-like vegetation leads to warmer conditions over eastern Europe compared to modern vegetation. Strandberg et al. (2014) showed in their RCM experiments for the Holocene that summer temperature and precipitation are sensitive to changes in land cover in eastern Europe due to evapotranspiration (in our results as latent heat) feedbacks (see Fig. 8 in Strandberg et al., 2014). They found that a reduction in tree cover leads to warmer and drier summers in eastern Europe, which is similar to our finding as we observe that a reduction in vegetation cover fraction is associated with a warmer and drier July in the same region. This suggests that the land–atmosphere coupling strength may be stronger in eastern Europe compared to other parts of Europe, especially during summer.

7 Conclusions

In this study, we investigated the importance of land–atmosphere feedbacks for the climate of Europe during the Last Glacial Maximum. To this end, we performed a series of high-resolution asynchronously coupled atmosphere–vegetation model simulations. We simulated the European climate and vegetation using the WRF regional climate model and LPJ-LMfire vegetation model with a 54 and an 18 km horizontal grid spacing.

Results of the asynchronous coupling show that quasi-equilibrium between climate and land cover is reached after the fourth to fifth iteration. Between the first and fourth iterations, the climate becomes progressively wetter in southern Europe, while it becomes drier in eastern Europe. Once the coupled model system reaches quasi-equilibrium (from fourth to seventh iterations), we identified only marginal spatial differences that can be attributed to internal variability in the climate and vegetation models. The final iteration of the asynchronous coupling represents our best estimate of

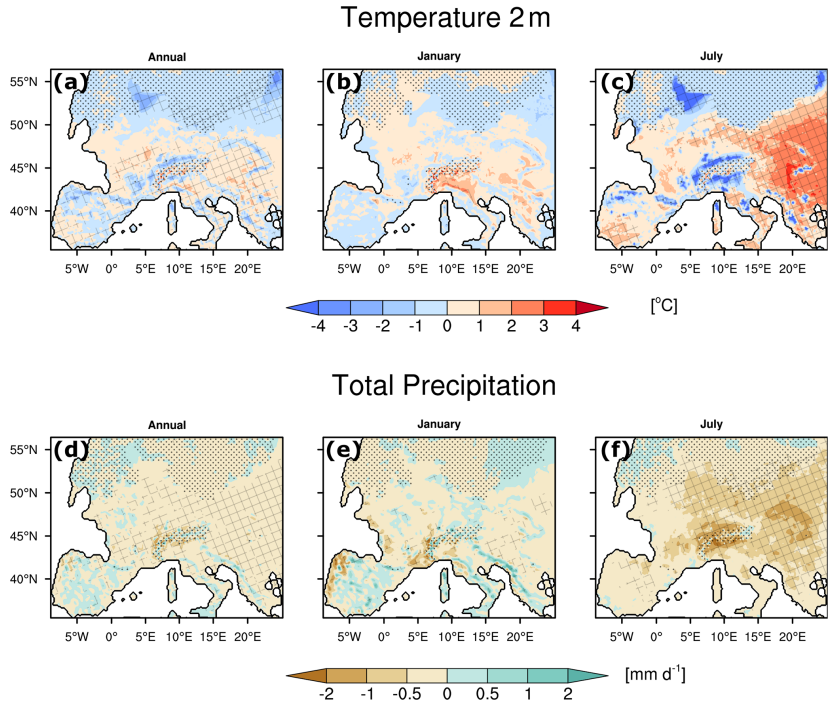

Figure 7. Atmospheric response to changes in the land cover. Panel **(a)** shows differences in the annual mean temperature between LGM_{LGM} – LGM_{PD}. Panels **(b)** and **(c)** are the same as **(a)** but for January and July, respectively. Panels **(d)**, **(e)**, and **(f)** are the same as **(a)**, **(b)**, and **(c)** but for precipitation. The solid line represents the coastline during the LGM, stippled areas are covered by glaciers, and crosshatched areas indicate statistically significant differences using a two-tailed bootstrapping technique with a 2 % significance level.

the atmospheric and land-surface conditions in Europe at the LGM. Consistent with many previous studies (e.g. Wu et al., 2007; Bartlein et al., 2011; Újvári et al., 2017; Cleator et al., 2020), we observe that the LGM climate of Europe was generally much colder and drier compared to PD. The LGM_{LGM} land cover was characterised by tundra and sparse vegetation, although open forest parkland (transition from grass to forest during the LGM) may have been common in many parts of central Europe, which is supported by comparisons with pollen-based vegetation reconstructions.

Using two additional sensitivity simulations – PD_{PD} and LGM_{PD} – we quantified the direct effects of external forcing and land cover on the LGM climate. Comparing LGM_{LGM}, i.e. the complete LGM conditions, to PD_{PD} shows not only a general cooling and drying but also a seasonality in the atmospheric response. Comparing LGM_{PD} to PD_{PD} illustrates that the seasonality is mainly driven by changes in forcing. The comparison between LGM_{LGM} to LGM_{PD} shows that, even in Europe where we would generally expect a weak land–atmosphere coupling compared, e.g. to the monsoon tropics, the atmosphere is sensitive to changes in land cover. The land–atmosphere response also has a seasonality which differs across Europe with a stronger coupling strength in eastern Europe. These features can be partially explained by the variable spatial and temporal influence of vegetation cover (albedo) and heat fluxes (sensible and latent heat fluxes) to the lower troposphere. Our results show that dry conditions in the LGM are partially attributed to LGM land cover as a reduction in vegetation overall led to stronger dryness compared to PD land cover. This is particularly true for central and eastern Europe during summer.

An evaluation of the modelled LGM_{LGM} climate should be performed with independent paleoclimate reconstructions from more sites than the 14 published points that are in the spatial domain of this study. Since the publication of Wu et al. (2007) and Bartlein et al. (2011), more than 70 well-dated pollen records from Europe that cover the LGM have become available (Kaplan et al., 2016). However, these data have not been transformed into paleoclimate reconstructions to date and such an effort would be beyond the scope of the current study. Additionally, as more paleoenvironmental reconstructions become available in the future, these simulations will be worthy of further evaluation and more detailed examination of specific areas. For instance, future work that improves pollen-based land cover reconstructions, e.g. using multi-proxy approaches that combine pollen data with presence–absence information from DNA (e.g. Alsos et al., 2020), will be very valuable for quantitative evaluation

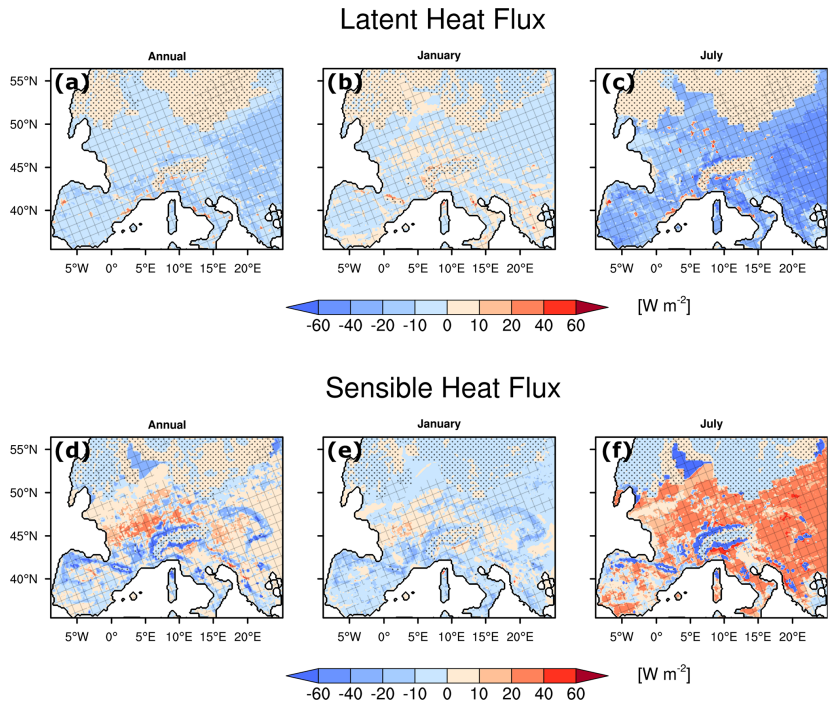

Figure 8. Atmospheric response to changes in the land cover. Panel **(a)** represents differences in the annual mean latent heat flux between $LGM_{LGM} - LGM_{PD}$. Panels **(b)** and **(c)** are the same as **(a)** but for January and July, respectively. Panels **(d)**, **(e)**, and **(f)** are the same as **(a)**, **(b)**, and **(c)** but for sensible heat flux. The solid line represents the coastline during the LGM, stippled areas are covered by glaciers, and crosshatched areas indicate statistically significant differences using a two-tailed bootstrappping technique with a 2 % significance level.

of model results using paleoenvironmental data. Although 18 km is a relatively high grid spacing for regional climate models, future studies will benefit from even more detailed climate simulations, particularly to better understand precipitation patterns in complex terrain such as Iberia, across the Mediterranean, and in the Carpathians. This is also true for studies on the local and regional paleobotany and archaeology of this important period in Europe's history.

Code and data availability. WRF is a community model that can be downloaded from its web page (http://www2.mmm.ucar.edu/wrf/users/code_admin.php, Skamarock and Klemp, 2008). The source code of LPJ-LMfire can be downloaded from Github (https://github.com/ARVE-Research/LPJ-LMfire/tree/v1.3, last access: 4 November 2020; https://doi.org/10.5281/zenodo.1184589, Kaplan et al., 2018). The climate simulations (global: CCSM4 and regional: WRF) and land cover simulations (LPJ-LMfire) occupy several terabytes and thus are not freely available. Nevertheless, they can be accessed upon request to the contributing authors. Simple calculations carried out at a grid point level are performed with Climate Data Operator (CDO; https://doi.org/10.5281/zenodo.2558193, Schulzweida, 2019) and NCAR Command Language (NCL; https://doi.org/10.5065/D6WD3XH5, UCAR/NCAR/CISL/TDD, 2019). The figures are performed with NCL (UCAR/NCAR/CISL/TDD, 2019). The source code of the program to classify vegetation cover fraction into the WRF land cover categories is archived on Github (https://github.com/ARVE-Research/lpj2wrf; https://doi.org/10.5281/zenodo.4922199, Kaplan, 2021).

Author contributions. PV, JOK, and CCR contributed to the design of the experiments. PV carried out the climate simulations and wrote the first draft. JOK carried out the land cover simulations. PL provided the guidelines for introducing new land cover and LGM boundary conditions into WRF. MM provided support in the application of these guidelines. All authors contributed to the writing and scientific discussion.

Competing interests. The authors declare that they have no conflict of interest.

Acknowledgements. This work was supported by the Swiss National Science Foundation (SNF) within the project "Modelling the ice flow in the western Alps during the last glacial cycle". Jed O. Kaplan is grateful for computing support from the School of Geography, University of Oxford. The simulations are performed on

the supercomputing architecture of the Swiss National Supercomputing Centre (CSCS). Patrick Ludwig thanks the Helmholtz initiative REKLIM for funding. Martina Messmer is supported by the SNF Early Postdoc.Mobility programme. Data are locally stored on the oschgerstore provided by the Oeschger Center for Climate Change Research (OCCR). This study contributes to the PALEOLINK project as part of the PAGES 2k Network.

Financial support. This research has been supported by the Schweizerischer Nationalfonds zur Förderung der Wissenschaftlichen Forschung (grant nos. 200021-162444 and P2BEP_181837).

Review statement. This paper was edited by Qiuzhen Yin and reviewed by two anonymous referees.

References

Alsos, I. G., Sjögren, P., Brown, A. G., Gielly, L., Merkel, M. K. F., Paus, A., Lammers, Y., Edwards, M. E., Alm, T., Leng, M., Goslar, T., Langdon, C. T., Bakke, J., and van der Bilt, W. G. M.: Last Glacial Maximum environmental conditions at Andøya, northern Norway; evidence for a northern ice-edge ecological "hotspot", Quaternary Sci. Rev., 239, 106364, https://doi.org/10.1016/j.quascirev.2020.106364, 2020.

Álvarez-Solas, J., Montoya, M., Ritz, C., Ramstein, G., Charbit, S., Dumas, C., Nisancioglu, K., Dokken, T., and Ganopolski, A.: Heinrich event 1: an example of dynamical ice-sheet reaction to oceanic changes, Clim. Past, 7, 1297–1306, https://doi.org/10.5194/cp-7-1297-2011, 2011.

Baena Preysler, J., Carrión Santafé, E., Torres Navas, C., and Vaquero Rodríguez, M.: Mousterian inside the upper Paleolithic? The last interval of El Esquilleu (Cantabria, Spain) sequence, Quatern. Int., 508, 153–163, https://doi.org/10.1016/j.quaint.2018.11.015, 2019.

Bartlein, P. J., Harrison, S. P., Brewer, S., Connor, S., Davis, B. A. S., Gajewski, K., Guiot, J., Harrison-Prentice, T. I., Henderson, A., Peyron, O., Prentice, I. C., Scholze, M., Seppä, H., Shuman, B., Sugita, S., Thompson, R. S., Viau, A. E., Williams, J., and Wu, H.: Pollen-based continental climate reconstructions at 6 and 21 ka: a global synthesis, Clim. Dynam., 37, 775–802, https://doi.org/10.1007/s00382-010-0904-1, 2011.

Beghin, P., Charbit, S., Kageyama, M., Combourieu-Nebout, N., Hatté, C., Dumas, C., and Peterschmitt, J.-Y.: What drives LGM precipitation over the western Mediterranean? A study focused on the Iberian Peninsula and northern Morocco, Clim. Dynam., 46, 2611–2631, https://doi.org/10.1007/s00382-015-2720-0, 2016.

Berger, A.: Long-Term Variations of Daily Insolation and Quaternary Climatic Changes, J. Atmos. Sci., 35, 2362–2367, https://doi.org/10.1175/1520-0469(1978)035<2362:LTVODI>2.0.CO;2, 1978.

Braconnot, P., Otto-Bliesner, B., Harrison, S., Joussaume, S., Peterchmitt, J.-Y., Abe-Ouchi, A., Crucifix, M., Driesschaert, E., Fichefet, Th., Hewitt, C. D., Kageyama, M., Kitoh, A., Laîné, A., Loutre, M.-F., Marti, O., Merkel, U., Ramstein, G., Valdes, P., Weber, S. L., Yu, Y., and Zhao, Y.: Results of PMIP2 coupled simulations of the Mid-Holocene and Last Glacial Maximum – Part 1: experiments and large-scale features, Clim. Past, 3, 261–277, https://doi.org/10.5194/cp-3-261-2007, 2007.

Braconnot, P., Harrison, S. P., Kageyama, M., Bartlein, P. J., Masson-Delmotte, V., Abe-Ouchi, A., Otto-Bliesner, B., and Zhao, Y.: Evaluation of climate models using palaeoclimatic data, Nat. Clim. Change, 2, 417–424, https://doi.org/10.1038/nclimate1456, 2012.

Broccoli, A. J. and Manabe, S.: The influence of continental ice, atmospheric CO_2, and land albedo on the climate of the last glacial maximum, Clim. Dynam., 1, 87–99, https://doi.org/10.1007/BF01054478, 1987.

Brugger, S. O., Gobet, E., Blunier, T., Morales-Molino, C., Lotter, A. F., Fischer, H., Schwikowski, M., and Tinner, W.: Palynological insights into global change impacts on Arctic vegetation, fire, and pollution recorded in Central Greenland ice, Holocene, 29, 1189–1197, https://doi.org/10.1177/0959683619838039, 2019.

Burke, A., Levavasseur, G., James, P. M. A., Guiducci, D., Izquierdo, M. A., Bourgeon, L., Kageyama, M., Ramstein, G., and Vrac, M.: Exploring the impact of climate variability during the Last Glacial Maximum on the pattern of human occupation of Iberia, J. Hum. Evol., 73, 35–46, https://doi.org/10.1016/j.jhevol.2014.06.003, 2014.

Cao, J., Wang, B., and Liu, J.: Attribution of the Last Glacial Maximum climate formation, Clim. Dynam., 53, 1661–1679, https://doi.org/10.1007/s00382-019-04711-6, 2019.

Casanueva, A., Kotlarski, S., Herrera, S., Fernández, J., Gutiérrez, J. M., Boberg, F., Colette, A., Christensen, O. B., Goergen, K., Jacob, D., Keuler, K., Nikulin, G., Teichmann, C., and Vautard, R.: Daily precipitation statistics in a EURO-CORDEX RCM ensemble: Added value of raw and bias-corrected high-resolution simulations, Clim. Dynam., 47, 719–737, https://doi.org/10.1007/s00382-015-2865-x, 2016.

Chen, W., Zhu, D., Ciais, P., Huang, C., Viovy, N., and Kageyama, M.: Response of vegetation cover to CO_2 and climate changes between Last Glacial Maximum and pre-industrial period in a dynamic global vegetation model, Quaternary Sci. Rev., 218, 293–305, https://doi.org/10.1016/j.quascirev.2019.06.003, 2019.

Clark, P. U., Dyke, A. S., Shakun, J. D., Carlson, A. E., Clark, J., Wohlfarth, B., Mitrovica, J. X., Hostetler, S. W., and McCabe, A. M.: The Last Glacial Maximum, Science, 325, 710–714, https://doi.org/10.1126/science.1172873, 2009.

Cleator, S. F., Harrison, S. P., Nichols, N. K., Prentice, I. C., and Roulstone, I.: A new multivariable benchmark for Last Glacial Maximum climate simulations, Clim. Past, 16, 699–712, https://doi.org/10.5194/cp-16-699-2020, 2020.

Crowley, T. J. and Baum, S. K.: Effect of vegetation on an ice-age climate model simulation, J. Geophys. Res.-Atmos., 102, 16463–16480, https://doi.org/10.1029/97JD00536, 1997.

Davin, E. L., Rechid, D., Breil, M., Cardoso, R. M., Coppola, E., Hoffmann, P., Jach, L. L., Katragkou, E., de Noblet-Ducoudré, N., Radtke, K., Raffa, M., Soares, P. M. M., Sofiadis, G., Strada, S., Strandberg, G., Tölle, M. H., Warrach-Sagi, K., and Wulfmeyer, V.: Biogeophysical impacts of forestation in Europe: first results from the LUCAS (Land Use and Climate Across Scales) regional climate model intercomparison, Earth Syst. Dynam., 11, 183–200, https://doi.org/10.5194/esd-11-183-2020, 2020.

Davis, B. A. S., Collins, P. M., and Kaplan, J. O.: The age and post-glacial development of the modern European vegetation: a plant functional approach based on pollen data, Veg. Hist. Archaeobot., 24, 303–317, https://doi.org/10.1007/s00334-014-0476-9, 2015.

Demory, M.-E., Berthou, S., Fernández, J., Sørland, S. L., Brogli, R., Roberts, M. J., Beyerle, U., Seddon, J., Haarsma, R., Schär, C., Buonomo, E., Christensen, O. B., Ciarlo `, J. M., Fealy, R., Nikulin, G., Peano, D., Putrasahan, D., Roberts, C. D., Senan, R., Steger, C., Teichmann, C., and Vautard, R.: European daily precipitation according to EURO-CORDEX regional climate models (RCMs) and high-resolution global climate models (GCMs) from the High-Resolution Model Intercomparison Project (HighResMIP), Geosci. Model Dev., 13, 5485–5506, https://doi.org/10.5194/gmd-13-5485-2020, 2020.

de Vernal, A., Rosell-Melé, A., Kucera, M., Hillaire-Marcel, C., Eynaud, F., Weinelt, M., Dokken, T., and Kageyama, M.: Comparing proxies for the reconstruction of LGM sea-surface conditions in the northern North Atlantic, Quaternary Sci. Rev., 25, 2820–2834, https://doi.org/10.1016/j.quascirev.2006.06.006, 2006.

Di Luca, A., de Elía, R., and Laprise, R.: Potential for added value in precipitation simulated by high-resolution nested Regional Climate Models and observations, Clim. Dynam., 38, 1229–1247, https://doi.org/10.1007/s00382-011-1068-3, 2012.

Ehlers, J., Gibbard, P., and Hughes, P.: Quaternary glaciations-extent and chronology: a closer look, vol. 15, Elsevier, Amsterdam, the Netherlands, 2011.

Finlayson, C.: Neanderthals and modern humans: an ecological and evolutionary perspective, vol. 38, Cambridge University Press, Cambridge, UK, https://doi.org/10.1017/CBO9780511542374, 2004.

Finlayson, C.: On the importance of coastal areas in the survival of Neanderthal populations during the Late Pleistocene, Quaternary Sci. Rev., 27, 2246–2252, https://doi.org/10.1016/j.quascirev.2008.08.033, 2008.

Finlayson, C., Giles Pacheco, F., Rodríguez-Vidal, J., Fa, D. A., María Gutierrez López, J., Santiago Pérez, A., Finlayson, G., Allue, E., Baena Preysler, J., Cáceres, I., Carrión, J. S., Fernández Jalvo, Y., Gleed-Owen, C. P., Jimenez Espejo, F. J., López, P., Antonio López Sáez, J., Antonio Riquelme Cantal, J., Sánchez Marco, A., Giles Guzman, F., Brown, K., Fuentes, N., Valarino, C. A., Villalpando, A., Stringer, C. B., Martinez Ruiz, F., and Sakamoto, T.: Late survival of Neanderthals at the southernmost extreme of Europe, Nature, 443, 850–853, https://doi.org/10.1038/nature05195, 2006.

Gent, P. R., Danabasoglu, G., Donner, L. J., Holland, M. M., Hunke, E. C., Jayne, S. R., Lawrence, D. M., Neale, R. B., Rasch, P. J., Vertenstein, M., Worley, P. H., Yang, Z.-L., and Zhang, M.: The Community Climate System Model Version 4, J. Climate, 24, 4973–4991, https://doi.org/10.1175/2011JCLI4083.1, 2011.

Gerhart, L. M. and Ward, J. K.: Plant responses to low [CO_2] of the past, New Phytol., 188, 674–695, https://doi.org/10.1111/j.1469-8137.2010.03441.x, 2010.

Gómez-Navarro, J. J., Montávez, J. P., Jerez, S., Jiménez-Guerrero, P., Lorente-Plazas, R., González-Rouco, J. F., and Zorita, E.: A regional climate simulation over the Iberian Peninsula for the last millennium, Clim. Past, 7, 451–472, https://doi.org/10.5194/cp-7-451-2011, 2011.

Gómez-Navarro, J. J., Montávez, J. P., Jiménez-Guerrero, P., Jerez, S., Lorente-Plazas, R., González-Rouco, J. F., and Zorita, E.: Internal and external variability in regional simulations of the Iberian Peninsula climate over the last millennium, Clim. Past, 8, 25–36, https://doi.org/10.5194/cp-8-25-2012, 2012.

Gómez-Navarro, J. J., Montávez, J. P., Wagner, S., and Zorita, E.: A regional climate palaeosimulation for Europe in the period 1500–1990 – Part 1: Model validation, Clim. Past, 9, 1667–1682, https://doi.org/10.5194/cp-9-1667-2013, 2013.

Gómez-Navarro, J. J., Bothe, O., Wagner, S., Zorita, E., Werner, J. P., Luterbacher, J., Raible, C. C., and Montávez, J. P.: A regional climate palaeosimulation for Europe in the period 1500–1990 – Part 2: Shortcomings and strengths of models and reconstructions, Clim. Past, 11, 1077–1095, https://doi.org/10.5194/cp-11-1077-2015, 2015.

Harrison, S. P., Bartlein, P. J., Izumi, K., Li, G., Annan, J., Hargreaves, J., Braconnot, P., and Kageyama, M.: Evaluation of CMIP5 palaeo-simulations to improve climate projections, Nat. Clim. Change, 5, 735–743, https://doi.org/10.1038/nclimate2649, 2015.

Haxeltine, A. and Prentice, I. C.: BIOME3: An equilibrium terrestrial biosphere model based on ecophysiological constraints, resource availability, and competition among plant functional types, Global Biogeochem. Cy., 10, 693–709, 1996.

Haxeltine, A., Prentice, I. C., and Creswell, I. D.: A coupled carbon and water flux model to predict vegetation structure, J. Veg. Sci., 7, 651–666, https://doi.org/10.2307/3236377, 1996.

Hofer, D., Raible, C. C., Dehnert, A., and Kuhlemann, J.: The impact of different glacial boundary conditions on atmospheric dynamics and precipitation in the North Atlantic region, Clim. Past, 8, 935–949, https://doi.org/10.5194/cp-8-935-2012, 2012a.

Hofer, D., Raible, C. C., Merz, N., Dehnert, A., and Kuhlemann, J.: Simulated winter circulation types in the North Atlantic and European region for preindustrial and glacial conditions: Glacial circulation types, Geophys. Res. Lett., 39, L15805, https://doi.org/10.1029/2012GL052296, 2012b.

Hunke, E. C. and Lipscomb, W. H.: CICE: the Los Alamos Sea Ice Model Documentation and Software User's Manual Version 4.1 LA-CC-06-012, Tech. rep., Los Alamos National Laboratory, Los Alamos, NM, USA, 2010.

Iles, C. E., Vautard, R., Strachan, J., Joussaume, S., Eggen, B. R., and Hewitt, C. D.: The benefits of increasing resolution in global and regional climate simulations for European climate extremes, Geosci. Model Dev., 13, 5583–5607, https://doi.org/10.5194/gmd-13-5583-2020, 2020.

Jahn, A., Claussen, M., Ganopolski, A., and Brovkin, V.: Quantifying the effect of vegetation dynamics on the climate of the Last Glacial Maximum, Clim. Past, 1, 1–7, https://doi.org/10.5194/cp-1-1-2005, 2005.

Janská, V., Jiménez-Alfaro, B., Chytrý, M., Divíšek, J., Anenkhonov, O., Korolyuk, A., Lashchinskyi, N., and Culek, M.: Palaeodistribution modelling of European vegetation types at the Last Glacial Maximum using modern analogues from Siberia: Prospects and limitations, Quaternary Sci. Rev., 159, 103–115, https://doi.org/10.1016/j.quascirev.2017.01.011, 2017.

Jia, G., Shevliakova, E., Artaxo, P., Noblet-Ducoudré, N. D., Houghton, R., House, J., Kitajima, K., Lennard, C., Popp, A., Sirin, A., Sukumar, R., and Verchot, L.: Land–climate interactions, in: Climate Change and Land: an IPCC special report

on climate change, desertification, land degradation, sustainable land management, food security, and greenhouse gas fluxes in terrestrial ecosystems, edited by: Shukla, P. R., Skea, J., Calvo Buendia, E., Masson-Delmotte, V., Pörtner, H.-O., Roberts, D. C., Zhai, P., Slade, R., Connors, S., van Diemen, R., Ferrat, M., Haughey, E., Luz, S., Neogi, S., Pathak, M., Petzold, J., Portugal Pereira, J., Vyas, P., Huntley, E., Kissick, K., Belkacemi, M., and Malley, J., in press, 2019a.

Jia, K., Ruan, Y., Yang, Y., and Zhang, C.: Assessing the Performance of CMIP5 Global Climate Models for Simulating Future Precipitation Change in the Tibetan Plateau, Water, 11, 1771, https://doi.org/10.3390/w11091771, 2019b.

Jia, K.-H., Zhao, W., Maier, P. A., Hu, X.-G., Jin, Y., Zhou, S.-S., Jiao, S.-Q., El-Kassaby, Y. A., Wang, T., Wang, X.-R., and Mao, J.-F.: Landscape genomics predicts climate change-related genetic offset for the widespread Platycladus orientalis (Cupressaceae), Evol. Appl., 13, 665–676, 2020.

Kageyama, M., Laîné, A., Abe-Ouchi, A., Braconnot, P., Cortijo, E., Crucifix, M., de Vernal, A., Guiot, J., Hewitt, C. D., Kitoh, A., Kucera, M., Marti, O., Ohgaito, R., Otto-Bliesner, B., Peltier, W. R., Rosell-Melé, A., Vettoretti, G., Weber, S. L., and Yu, Y.: Last Glacial Maximum temperatures over the North Atlantic, Europe and western Siberia: a comparison between PMIP models, MARGO sea–surface temperatures and pollen-based reconstructions, Quaternary Sci. Rev., 25, 2082–2102, https://doi.org/10.1016/j.quascirev.2006.02.010, 2006.

Kageyama, M., Albani, S., Braconnot, P., Harrison, S. P., Hopcroft, P. O., Ivanovic, R. F., Lambert, F., Marti, O., Peltier, W. R., Peterschmitt, J.-Y., Roche, D. M., Tarasov, L., Zhang, X., Brady, E. C., Haywood, A. M., LeGrande, A. N., Lunt, D. J., Mahowald, N. M., Mikolajewicz, U., Nisancioglu, K. H., Otto-Bliesner, B. L., Renssen, H., Tomas, R. A., Zhang, Q., Abe-Ouchi, A., Bartlein, P. J., Cao, J., Li, Q., Lohmann, G., Ohgaito, R., Shi, X., Volodin, E., Yoshida, K., Zhang, X., and Zheng, W.: The PMIP4 contribution to CMIP6 – Part 4: Scientific objectives and experimental design of the PMIP4-CMIP6 Last Glacial Maximum experiments and PMIP4 sensitivity experiments, Geosci. Model Dev., 10, 4035–4055, https://doi.org/10.5194/gmd-10-4035-2017, 2017.

Kageyama, M., Harrison, S. P., Kapsch, M.-L., Lofverstrom, M., Lora, J. M., Mikolajewicz, U., Sherriff-Tadano, S., Vadsaria, T., Abe-Ouchi, A., Bouttes, N., Chandan, D., Gregoire, L. J., Ivanovic, R. F., Izumi, K., LeGrande, A. N., Lhardy, F., Lohmann, G., Morozova, P. A., Ohgaito, R., Paul, A., Peltier, W. R., Poulsen, C. J., Quiquet, A., Roche, D. M., Shi, X., Tierney, J. E., Valdes, P. J., Volodin, E., and Zhu, J.: The PMIP4 Last Glacial Maximum experiments: preliminary results and comparison with the PMIP3 simulations, Clim. Past, 17, 1065–1089, https://doi.org/10.5194/cp-17-1065-2021, 2021.

Kaplan, J. O.: Geophysical Applications of Vegetation Modeling, Doctoral dissertation, Lund University, Lund, Sweden, 2001.

Kaplan, J. O.: ARVE-Research/lpj2wrf: first release (Version v1.0.0), Zenodo [code], https://doi.org/10.5281/zenodo.4922199, 2021.

Kaplan, J. O., Pfeiffer, M., Kolen, J. C. A., and Davis, B. A. S.: Large scale anthropogenic reduction of forest cover in Last Glacial Maximum Europe, PLOS ONE, 11, e0166726, https://doi.org/10.1371/journal.pone.0166726, 2016.

Kaplan, J. O., Pfeiffer, M., and Chaste, E.: ARVE-Research/LPJ-LMfire: LPJ-LMfire, Zenodo [code], https://doi.org/10.5281/zenodo.1184589, 2018.

Kjellström, E., Brandefelt, J., Näslund, J.-O., Smith, B., Strandberg, G., Voelker, A. H. L., and Wohlfarth, B.: Simulated climate conditions in Europe during the Marine Isotope Stage 3 stadial, Boreas, 39, 436–456, https://doi.org/10.1111/j.1502-3885.2010.00143.x, 2010.

Klein, K., Wegener, C., Schmidt, I., Rostami, M., Ludwig, P., Ulbrich, S., Richter, J., Weniger, G.-C., and Shao, Y.: Human existence potential in Europe during the Last Glacial Maximum, Quatern. Int., 581–582, 7–27, https://doi.org/10.1016/j.quaint.2020.07.046, 2021.

Knist, S., Goergen, K., and Simmer, C.: Evaluation and projected changes of precipitation statistics in convection-permitting WRF climate simulations over Central Europe, Clim. Dynam., https://doi.org/10.1007/s00382-018-4147-x, 2018.

Kreveld, S. v., Sarnthein, M., Erlenkeuser, H., Grootes, P., Jung, S., Nadeau, M. J., Pflaumann, U., and Voelker, A.: Potential links between surging ice sheets, circulation changes, and the Dansgaard-Oeschger Cycles in the Irminger Sea, 60–18 Kyr, Paleoceanography, 15, 425–442, https://doi.org/10.1029/1999PA000464, 2000.

Landais, A., Masson-Delmotte, V., Capron, E., Langebroek, P. M., Bakker, P., Stone, E. J., Merz, N., Raible, C. C., Fischer, H., Orsi, A., Prié, F., Vinther, B., and Dahl-Jensen, D.: How warm was Greenland during the last interglacial period?, Clim. Past, 12, 1933–1948, https://doi.org/10.5194/cp-12-1933-2016, 2016.

Lofverstrom, M.: A dynamic link between high-intensity precipitation events in southwestern North America and Europe at the Last Glacial Maximum, Earth Planet. Sc. Lett., 534, 116081, https://doi.org/10.1016/j.epsl.2020.116081, 2020.

Lu, Z., Miller, P. A., Zhang, Q., Wårlind, D., Nieradzik, L., Sjolte, J., Li, Q., and Smith, B.: Vegetation pattern and terrestrial carbon variation in past warm and cold climates, Geophys. Res. Lett., 46, 8133–8143, https://doi.org/10.1029/2019GL083729, 2019.

Ludwig, P., Schaffernicht, E. J., Shao, Y., and Pinto, J. G.: Regional atmospheric circulation over Europe during the Last Glacial Maximum and its links to precipitation, J. Geophys. Res.-Atmos., 121, 2130–2145, https://doi.org/10.1002/2015JD024444, 2016.

Ludwig, P., Pinto, J. G., Raible, C. C., and Shao, Y.: Impacts of surface boundary conditions on regional climate model simulations of European climate during the Last Glacial Maximum, Geophys. Res. Lett., 44, 5086–5095, https://doi.org/10.1002/2017GL073622, 2017.

Ludwig, P., Shao, Y., Kehl, M., and Weniger, G.-C.: The Last Glacial Maximum and Heinrich event I on the Iberian Peninsula: A regional climate modelling study for understanding human settlement patterns, Global Planet. Chang., 170, 34–47, https://doi.org/10.1016/j.gloplacha.2018.08.006, 2018.

Ludwig, P., Gómez-Navarro, J. J., Pinto, J. G., Raible, C. C., Wagner, S., and Zorita, E.: Perspectives of regional paleoclimate modeling, Ann. NY Acad. Sci., 1436, 54–69, https://doi.org/10.1111/nyas.13865, 2019.

Ludwig, P., Gavrilov, M. B., Markovic, S. B., Ujvari, G., and Lehmkuhl, F.: Simulated regional dust cycle in the Carpathian Basin and the Adriatic Sea region during the

Last Glacial Maximum, Quatern. Int., 581–582, 114–127, https://doi.org/10.1016/j.quaint.2020.09.048, 2020.

Luetscher, M., Boch, R., Sodemann, H., Spötl, C., Cheng, H., Edwards, R. L., Frisia, S., Hof, F., and Müller, W.: North Atlantic storm track changes during the Last Glacial Maximum recorded by Alpine speleothems, Nat. Commun., 6, 6344, https://doi.org/10.1038/ncomms7344, 2015.

Magyari, E. K., Kuneš, P., Jakab, G., Sümegi, P., Pelánková, B., Schäbitz, F., Braun, M., and Chytrý, M.: Late Pleniglacial vegetation in eastern-central Europe: are there modern analogues in Siberia?, Quaternary Sci. Rev., 95, 60–79, https://doi.org/10.1016/j.quascirev.2014.04.020, 2014a.

Magyari, E. K., Veres, D., Wennrich, V., Wagner, B., Braun, M., Jakab, G., Karátson, D., Pál, Z., Ferenczy, G., St-Onge, G., Rethemeyer, J., Francois, J. P., von Reumont, F., and Schäbitz, F.: Vegetation and environmental responses to climate forcing during the Last Glacial Maximum and deglaciation in the East Carpathians: attenuated response to maximum cooling and increased biomass burning, Quaternary Sci. Rev., 106, 278–298, https://doi.org/10.1016/j.quascirev.2014.09.015, 2014b.

Maier, A., Lehmkuhl, F., Ludwig, P., Melles, M., Schmidt, I., Shao, Y., Zeeden, C., and Zimmermann, A.: Demographic estimates of hunter–gatherers during the Last Glacial Maximum in Europe against the background of palaeoenvironmental data, Quatern. Int., 425, 49–61, https://doi.org/10.1016/j.quaint.2016.04.009, 2016.

Merz, N., Raible, C. C., Fischer, H., Varma, V., Prange, M., and Stocker, T. F.: Greenland accumulation and its connection to the large-scale atmospheric circulation in ERA-Interim and paleoclimate simulations, Clim. Past, 9, 2433–2450, https://doi.org/10.5194/cp-9-2433-2013, 2013.

Merz, N., Born, A., Raible, C. C., Fischer, H., and Stocker, T. F.: Dependence of Eemian Greenland temperature reconstructions on the ice sheet topography, Clim. Past, 10, 1221–1238, https://doi.org/10.5194/cp-10-1221-2014, 2014a.

Merz, N., Gfeller, G., Born, A., Raible, C. C., Stocker, T. F., and Fischer, H.: Influence of ice sheet topography on Greenland precipitation during the Eemian interglacial, J. Geophys. Res.-Atmos., 119, 10749–10768, https://doi.org/10.1002/2014JD021940, 2014b.

Merz, N., Raible, C. C., and Woollings, T.: North Atlantic Eddy-Driven jet in interglacial and glacial winter climates, J. Climate, 28, 3977–3997, https://doi.org/10.1175/JCLI-D-14-00525.1, 2015.

Merz, N., Born, A., Raible, C. C., and Stocker, T. F.: Warm Greenland during the last interglacial: the role of regional changes in sea ice cover, Clim. Past, 12, 2011–2031, https://doi.org/10.5194/cp-12-2011-2016, 2016.

Mix, A. C., Bard, E., and Schneider, R.: Environmental processes of the ice age: land, oceans, glaciers (EPILOG), Quaternary Sci. Rev., 20, 627–657, https://doi.org/10.1016/S0277-3791(00)00145-1, 2001.

Moreno, A., González-Sampériz, P., Morellón, M., Valero-Garcés, B. L., and Fletcher, W. J.: Northern Iberian abrupt climate change dynamics during the last glacial cycle: A view from lacustrine sediments, Quaternary Sci. Rev., 36, 139–153, https://doi.org/10.1016/j.quascirev.2010.06.031, 2012.

Neale, R. B., Richter, J. H., Conley, A. J., Park, S., Lauritzen, P. H., Gettelman, A., Rasch, P. J., and Vavrus, J.: Description of the NCAR community atmosphere model (CAM4), National Center for Atmospheric Research Tech. Rep. NCAR/TN+STR, available at: http://www.cesm.ucar.edu/models/ccsm4.0/cam/docs/description/cam4_desc.pdf (last access: 9 June 2021), 2010.

Niu, G.-Y., Yang, Z.-L., Mitchell, K. E., Chen, F., Ek, M. B., Barlage, M., Kumar, A., Manning, K., Niyogi, D., Rosero, E., Tewari, M., and Xia, Y.: The community Noah land surface model with multiparameterization options (Noah-MP): 1. Model description and evaluation with local-scale measurements, J. Geophys. Res.-Atmos., 116, D12109, https://doi.org/10.1029/2010JD015139, 2011.

Noblet, N. I. d., Prentice, I. C., Joussaume, S., Texier, D., Botta, A., and Haxeltine, A.: Possible role of atmosphere-biosphere interactions in triggering the Last Glaciation, Geophys. Res. Lett., 23, 3191–3194, https://doi.org/10.1029/96GL03004, 1996.

Oleson, W., Lawrence, M., Bonan, B., Flanner, G., Kluzek, E., Lawrence, J., Levis, S., Swenson, C., Thornton, E., Dai, A., Decker, M., Dickinson, R., Feddema, J., Heald, L., Hoffman, F., Lamarque, J.-F., Mahowald, N., Niu, G.-Y., Qian, T., Randerson, J., Running, S., Sakaguchi, K., Slater, A., Stockli, R., Wang, A., Yang, Z.-L., Zeng, X., and Zeng, X.: Technical description of version 4.0 of the community land model (CLM), NCAR Technical Note NCAR/TN-478+STR, National Center for Atmospheric Research, Boulder, CO, USA, available at: http://www.cesm.ucar.edu/models/cesm1.0/clm/CLM4_Tech_Note.pdf (last access: 9 June 2021), 2010.

Peltier, W.: Global glacial isostasy and the surface of the ice-age Earth: The ICE-5G (VM2) model and grace, Annu. Rev. Earth Pl. Sc., 32, 111–149, https://doi.org/10.1146/annurev.earth.32.082503.144359, 2004.

Pfeiffer, M., Spessa, A., and Kaplan, J. O.: A model for global biomass burning in preindustrial time: LPJ-LMfire (v1.0), Geosci. Model Dev., 6, 643–685, https://doi.org/10.5194/gmd-6-643-2013, 2013.

Prein, A. F., Holland, G. J., Rasmussen, R. M., Done, J., Ikeda, K., Clark, M. P., and Liu, C. H.: Importance of Regional Climate Model Grid Spacing for the Simulation of Heavy Precipitation in the Colorado Headwaters, J. Climate, 26, 4848–4857, https://doi.org/10.1175/JCLI-D-12-00727.1, 2013.

Prentice, I. C. and Jolly, D.: Mid-Holocene and glacial-maximum vegetation geography of the northern continents and Africa, J. Biogeogr., 27, 507–519, https://doi.org/10.1046/j.1365-2699.2000.00425.x, 2000.

Prentice, I. C., Cramer, W., Harrison, S. P., Leemans, R., Monserud, R. A., and Solomon, A. M.: Special Paper: A Global Biome Model Based on Plant Physiology and Dominance, Soil Properties and Climate, J. Biogeogr., 19, 117–134, https://doi.org/10.2307/2845499, 1992.

Raible, C. C., Pinto, J. G., Ludwig, P., and Messmer, M.: A review of past changes in extratropical cyclones in the northern hemisphere and what can be learned for the future, WIRES Clim. Change, 12, e680, https://doi.org/10.1002/wcc.680, 2020.

Rajczak, J. and Schär, C.: Projections of future precipitation extremes over Europe: A multimodel assessment of climate simulations, J. Geophys. Res.-Atmos., 122, 10773–10800, https://doi.org/10.1002/2017JD027176, 2017.

Rauscher, S. A., Coppola, E., Piani, C., and Giorgi, F.: Resolution effects on regional climate model simulations of sea-

sonal precipitation over Europe, Clim. Dynam., 35, 685–711, https://doi.org/10.1007/s00382-009-0607-7, 2010.

Roucoux, K. H., de Abreu, L., Shackleton, N. J., and Tzedakis, P. C.: The response of NW Iberian vegetation to North Atlantic climate oscillations during the last 65 kyr, Quaternary Sci. Rev., 24, 1637–1653, https://doi.org/10.1016/j.quascirev.2004.08.022, 2005.

Sanchez Goñi, M. F. and Harrison, S. P.: Millennial-scale climate variability and vegetation changes during the Last Glacial: Concepts and terminology, Quaternary Sci. Rev., 29, 2823–2827, https://doi.org/10.1016/j.quascirev.2009.11.014, 2010.

Schaffernicht, E. J., Ludwig, P., and Shao, Y.: Linkage between dust cycle and loess of the Last Glacial Maximum in Europe, Atmos. Chem. Phys., 20, 4969–4986, https://doi.org/10.5194/acp-20-4969-2020, 2020.

Schulzweida, U.: CDO User Guide (Version 1.9.6), Zenodo, https://doi.org/10.5281/zenodo.2558193, 2019.

Seguinot, J., Ivy-Ochs, S., Jouvet, G., Huss, M., Funk, M., and Preusser, F.: Modelling last glacial cycle ice dynamics in the Alps, The Cryosphere, 12, 3265–3285, https://doi.org/10.5194/tc-12-3265-2018, 2018.

Shrestha, R. K., Connolly, P. J., and Gallagher, M. W.: Sensitivity of WRF Cloud Microphysics to Simulations of a Convective Storm Over the Nepal Himalayas, The Open Atmospheric Science Journal, 11, 29–43, https://doi.org/10.2174/1874282301711010029, 2017.

Sitch, S., Smith, B., Prentice, I. C., Arneth, A., Bondeau, A., Cramer, W., Kaplan, J. O., Levis, S., Lucht, W., Sykes, M. T., Thonicke, K., and Venevsky, S.: Evaluation of ecosystem dynamics, plant geography and terrestrial carbon cycling in the LPJ dynamic global vegetation model, Glob. Change Biol., 9, 161–185, https://doi.org/10.1046/j.1365-2486.2003.00569.x, 2003.

Skamarock, W. C. and Klemp, J. B.: A time-split nonhydrostatic atmospheric model for weather research and forecasting applications, J. Comput. Phys., 227, 3465–3485, https://doi.org/10.1016/j.jcp.2007.01.037, 2008 (data available at: http://www2.mmm.ucar.edu/wrf/users/code_admin.php, last access: 12 October 2020).

Skamarock, W. C., Klemp, J. B., Dudhia, J., Gill, O., Barker, D., Duda, G., Huang, X.-y., Wang, W., and Powers, G.: A description of the advanced research WRF version 3, (No. NCAR/TN-475+STR), University Corporation for Atmospheric Research, https://doi.org/10.5065/D68S4MVH, 2008.

Stanford, J. D., Rohling, E. J., Bacon, S., Roberts, A. P., Grousset, F. E., and Bolshaw, M.: A new concept for the paleoceanographic evolution of Heinrich event 1 in the North Atlantic, Quaternary Sci. Rev., 30, 1047–1066, https://doi.org/10.1016/j.quascirev.2011.02.003, 2011.

Strandberg, G. and Kjellström, E.: Climate impacts from afforestation and deforestation in Europe, Earth Interact., 23, 1–27, https://doi.org/10.1175/EI-D-17-0033.1, 2019.

Strandberg, G., Brandefelt, J., Kjellstro M., E., and Smith, B.: High-resolution regional simulation of Last Glacial Maximum climate in Europe, Tellus A, 63, 107–125, https://doi.org/10.1111/j.1600-0870.2010.00485.x, 2011.

Strandberg, G., Kjellström, E., Poska, A., Wagner, S., Gaillard, M.-J., Trondman, A.-K., Mauri, A., Davis, B. A. S., Kaplan, J. O., Birks, H. J. B., Bjune, A. E., Fyfe, R., Giesecke, T., Kalnina, L., Kangur, M., van der Knaap, W. O., Kokfelt, U., Kuneš, P., Latałowa, M., Marquer, L., Mazier, F., Nielsen, A. B., Smith, B., Seppä, H., and Sugita, S.: Regional climate model simulations for Europe at 6 and 0.2 k BP: sensitivity to changes in anthropogenic deforestation, Clim. Past, 10, 661–680, https://doi.org/10.5194/cp-10-661-2014, 2014.

Texier, D., de Noblet, N., Harrison, S. P., Haxeltine, A., Jolly, D., Joussaume, S., Laarif, F., Prentice, I. C., and Tarasov, P.: Quantifying the role of biosphere-atmosphere feedbacks in climate change: coupled model simulations for 6000 years BP and comparison with palaeodata for northern Eurasia and northern Africa, Clim. Dynam., 13, 865–881, https://doi.org/10.1007/s003820050202, 1997.

UCAR/NCAR/CISL/TDD: The NCAR Command Language (Version 6.6.2) [Software], https://doi.org/10.5065/D6WD3XH5, 2019.

Újvári, G., Stevens, T., Molnár, M., Demény, A., Lambert, F., Varga, G., Jull, A. J. T., Páll-Gergely, B., Buylaert, J.-P., and Kovács, J.: Coupled European and Greenland last glacial dust activity driven by North Atlantic climate, P. Natl. Acad. Sci. USA, 114, E10632–E10638, https://doi.org/10.1073/pnas.1712651114, 2017.

Van Meerbeeck, C. J., Renssen, H., and Roche, D. M.: How did Marine Isotope Stage 3 and Last Glacial Maximum climates differ? – Perspectives from equilibrium simulations, Clim. Past, 5, 33–51, https://doi.org/10.5194/cp-5-33-2009, 2009.

Vegas, J., Ruiz-Zapata, B., Ortiz, J. E., Galán, L., Torres, T., García-Cortés, Á., Gil-García, M. J., Pérez-González, A., and Gallardo-Millán, J. L.: Identification of arid phases during the last 50 cal. ka BP from the Fuentillejo maar-lacustrine record (Campo de Calatrava Volcanic Field, Spain), J. Quaternary Sci., 25, 1051–1062, https://doi.org/10.1002/jqs.1262, 2010.

Velasquez, P., Messmer, M., and Raible, C. C.: A new bias-correction method for precipitation over complex terrain suitable for different climate states: a case study using WRF (version 3.8.1), Geosci. Model Dev., 13, 5007–5027, https://doi.org/10.5194/gmd-13-5007-2020, 2020.

Voelker, A. H. L., Sarnthein, M., Grootes, P. M., Erlenkeuser, H., Laj, C., Mazaud, A., Nadeau, M.-J., and Schleicher, M.: Correlation of Marine ^{14}C Ages from the Nordic Seas with the GISP2 Isotope Record: Implications for 14C Calibration Beyond 25 ka BP, Radiocarbon, 40, 517–534, https://doi.org/10.1017/S0033822200018397, 1997.

Walsh, J. E., Chapman, W. L., Romanovsky, V., Christensen, J. H., and Stendel, M.: Global Climate Model Performance over Alaska and Greenland, J. Climate, 21, 6156–6174, https://doi.org/10.1175/2008JCLI2163.1, 2008.

Wang, N., Jiang, D., and Lang, X.: Northern Westerlies during the Last Glacial Maximum: Results from CMIP5 Simulations, J. Climate, 31, 1135–1153, https://doi.org/10.1175/JCLI-D-17-0314.1, 2018.

Wilks, D. S.: Statistical methods in the atmospheric sciences, Academic Press, Burlington, MA, USA, San Diego, California, USA, London, UK, google-Books-ID: IJuCVtQ0ySIC, 2011.

Woillez, M.-N., Kageyama, M., Krinner, G., de Noblet-Ducoudré, N., Viovy, N., and Mancip, M.: Impact of CO2 and climate on the Last Glacial Maximum vegetation: results from the ORCHIDEE/IPSL models, Clim. Past, 7, 557–577, https://doi.org/10.5194/cp-7-557-2011, 2011.

Wu, H., Guiot, J., Brewer, S., and Guo, Z.: Climatic changes in Eurasia and Africa at the last glacial maximum and mid-Holocene: reconstruction from pollen data using inverse vegetation modelling, Clim. Dynam., 29, 211–229, https://doi.org/10.1007/s00382-007-0231-3, 2007.

Yang, Q., Dai, Q., Han, D., Chen, Y., and Zhang, S.: Sensitivity analysis of raindrop size distribution parameterizations in WRF rainfall simulation, Atmos. Res., 228, 1–13, https://doi.org/10.1016/j.atmosres.2019.05.019, 2019.

Yokoyama, Y., Lambeck, K., De Deckker, P., Johnston, P., and Fifield, L. K.: Timing of the Last Glacial Maximum from observed sea-level minima, Nature, 406, 713–716, https://doi.org/10.1038/35021035, 2000.

Chapter 4

The Role of Ice-Sheet Topography in the Alpine Hydro-Climate at Glacial Times

P. Velasquez, M. Messmer and C. C. Raible.

In review for *Climate of the Past*. Published in *Climate of the Past Discussions* (preprint), pp. 1-34, 2021

https://doi.org/10.5194/cp-2021-67

Abstract

In this study, we investigate the sensitivity of the glacial Alpine hydro-climate to northern hemispheric and local ice-sheet changes. Bridging the scale gap by using a chain of global and regional climate models, we perform sensitivity simulations of up to 2 km horizontal resolution over the Alps for the Last Glacial Maximum (LGM) and the Marine Isotope Stage 4 (MIS4). In winter, we find wetter conditions in the southern part of the Alps during LGM compared to present day, to which dynamical processes, i.e., changes in the wind speed and direction, substantially contribute. During summer, we find the expected drier conditions in most of the Alpine region during LGM, as thermodynamics suggests drier conditions under lower temperatures. The MIS4 climate shows enhanced winter precipitation compared to the LGM, which is explain by its warmer climate compared to the LGM — thus, again explained by thermodynamics. The sensitivity simulations of the northern hemispheric ice-sheet changes show that an increase of the ice-sheet thickness leads to a significant intensification of glacial Alpine hydro-climate conditions, which is mainly explained by dynamical processes. Changing only the Fennoscandian ice sheet is less influential on the Alpine precipitation, whereas modifications in the local Alpine ice-sheet topography significantly alter the Alpine precipitation, in particular we find a reduction of summer precipitation at the southern face of the Alps when lowering the Alpine ice sheet. The findings demonstrate that the northern hemispheric and local ice-sheet topography play an important role in regulating the Alpine hydro-climate and thus permits a better understanding of the precipitation patterns in the complex Alpine terrain at glacial times.

4.1 Introduction

Glacial times are characterised by very different boundary conditions than today, leading to cold conditions, substantial sea-level drops and a strong increase in land ice sheets (Mix et al., 2001). This different climate behaviour of glacial times have attracted the scientific community, since they are an ideal test bed to challenge state-of-the-art climate models in their ability to simulate changes in climate (e.g. Kageyama et al., 2021). Further, glacial times are also suitable to identify relevant mechanisms such as feedback processes in the climate system (e.g. Stocker and Johnsen, 2003) and to investigate response behaviour to external forcing (e.g. Ganopolski and Calov, 2011). Thereby, the hydrological cycle is an important ingredient in the Earth's climate system due to its transport and redistribution of mass and energy (e.g. Mayewski et al., 2004). To understand the climate during glacial times and to validate climate models proxy data are a prerequisite. Besides proxy data for atmospheric characteristics, also the extent and height of the ice sheet must be known, since these have an influence on the atmospheric circulation (Monegato et al., 2017). Still, large uncertainties remain, in particular in land ice-sheet extent and height reconstructions prior to the Last Glacial Maximum (LGM, 21 ka; e.g. Peltier, 1994, 1998; Angelis and Kleman, 2005; Ehlers et al., 2011; Tarasov et al., 2012; Ullman et al., 2014; Batchelor et al., 2019; Gowan et al.,

2021), but also the ice-sheet height during the LGM is still debated in literature (e.g. Peltier, 2004; Peltier et al., 2015; Ganopolski and Brovkin, 2017; Batchelor et al., 2019).

Thus, the purpose of this study is to investigate the role of the global and local ice-sheet topography in the regional hydro-climate over the European Alps with a focus on two glacial states, the LGM and the Marine Isotope Stage 4 (MIS4, 65 ka). In this study, we investigate to which extent changes in the dynamics are responsible for precipitation changes over the European Alps, based on eight high-resolution regional climate model (RCM) simulations.

So far, many proxy and global modelling studies have focused on the LGM (e.g. Yokoyama et al., 2000; Clark et al., 2009; Van Meerbeeck et al., 2009; Hughes et al., 2013) as LGM is also a focal period of the Paleoclimate Modelling Intercomparsion Projects (PMIP) (Abe-Ouchi et al., 2015; Kageyama et al., 2017). Globally, the reconstructed temperature at LGM is reduced by 5 to 6.5 °C compared to present day (PD; Otto-Bliesner et al., 2006). This led to the building up of large ice sheets, in particular over the Northern Hemisphere (Peltier et al., 2015), a strong reduction in the sea level by approximately 115 to 130 m (Lambeck et al., 2014) and changes in vegetation and land surfaces (e.g. Annan and Hargreaves, 2013; Bartlein et al., 2011; Cleator et al., 2020), inducing higher atmospheric dust loadings during the LGM (Lambert et al., 2008). Paleoclimate reconstructions of Europe based on pollen data show, depending on the region, a temperature decrease of 10 to 14 °C (Wu et al., 2007; Bartlein et al., 2011). The same data is also used to reconstruct the hydro-climatic response over Europe at LGM showing mainly drier conditions (reduction in precipitation of around 200 mm year^{-1}) compared to PD (Wu et al., 2007; Bartlein et al., 2011). Other climate reconstructions suggest also circulation-induced changes in the moisture transport (Florineth and Schlüchter, 2000). In this case, the atmospheric circulation is changed so that the Alpine area receives more moisture from the south which results in wet conditions in the southern part of the Alps and dry conditions north of the Alps. This is confirmed by reconstructions based on speleothems in the Alpine region (Luetscher et al., 2015). Still, the interpretation of sparse paleo-proxy data remains a challenge due to the inherent uncertainties of proxy reconstructions, spatial coverage, uncertain seasonality of the proxy sensitivity, and contradicting signals recorded by different proxy archives (e.g. Wu et al., 2007; de Vernal et al., 2006; Beghin et al., 2016). MIS4 climate is less understood compared to LGM as proxy data availability is further reduced. Available paleoclimate reconstructions characterise MIS4 to be warmer than the LGM (e.g. Eggleston et al., 2016; Newnham et al., 2017; De Deckker et al., 2019) with a global sea level drop of roughly 80 m compared to PD (e.g. Cutler et al., 2003; Siddall et al., 2008, 2010; De Deckker et al., 2019).

Global climate model (GCM) simulations offer an alternative view on glacial climate conditions. With respect to the global mean climate response under LGM conditions, they are overall consistent with reconstructions (e.g. Braconnot et al., 2012; Hofer et al., 2012a; Kageyama et al., 2021). On the regional scale, GCM results show stronger deviations to reconstructions, e.g. they tend to underestimate the amplitude of European temperature between LGM and PD or partly disagree in the European precipitation pattern (Braconnot

et al., 2012; Kageyama et al., 2017, 2021; Harrison et al., 2015). Besides, GCM simulations are used to deduce relevant processes and assess sensitivity of uncertain components, like the reconstruction of major ice-sheets (e.g. Angelis and Kleman, 2005; Tarasov et al., 2012; Ullman et al., 2014; Peltier et al., 2015; Batchelor et al., 2019). Several studies demonstrated a strong sensitivity of glacial climate to the extent and height of ice sheets (e.g. Kageyama and Valdes, 2000; Rivière et al., 2010; Hofer et al., 2012a,a; Merz et al., 2015). This is particularly true for the Laurentide ice sheet (LIS) as it drives major changes in the glacial atmospheric circulation and its variability compared to PD (Kageyama and Valdes, 2000; Rivière et al., 2010; Pausata et al., 2011; Hofer et al., 2012a; Merz et al., 2015; Harrison et al., 2016). For example, Hofer et al. (2012a) and Merz et al. (2015) found that an increase in the elevation of the LIS causes an enhancement and a southward displacement of the jet stream and the storm track over the North Atlantic. This has a strong impact on the precipitation pattern over Europe, in particular during winter. Still, GCMs operate on relatively coarse resolutions and thus poorly represent the effect of the topography at finer scales such as the complex Alpine terrain. Additionally, GCMs use parameterisations for processes that govern regional-to-local scale precipitation (Leung et al., 2003; Su et al., 2012).

Regional downscaling provides a way to overcome some of the shortcomings of GCM simulations. Latombe et al. (2018) proposed a statistical downscaling method to increase the spatial resolution of LGM simulations in a computationally efficient way. Another approach is dynamical downscaling by employing an RCM (e.g. Strandberg et al., 2011; Rummukainen, 2016; Ludwig et al., 2019). Among others, Ludwig et al. (2016) showed that the application of RCMs substantially improves the simulated LGM climate over Europe compared to the driving GCM, although biases from the GCM simulation may still impact the regional output. For instance, Ludwig et al. (2017) found that RCMs are sensitive to boundary conditions provided by GCM such as sea surface temperature. Thus, regional climate modelling is beneficial for answering paleoclimate research questions (Ludwig et al., 2019). Pinto and Ludwig (2020) and Raible et al. (2020) showed that extratropical cyclones are characterised by enhanced wind speeds over Europe during the LGM compared to PD, which helps to understand the reallocation and build-up of thick loess deposits in Europe (e.g. Römer et al., 2016; Krauß et al., 2016). Recently, the horizontal resolution of RCMs in the paleoclimate context is increased to a level that convection is explicitly resolved (e.g. Velasquez et al., 2020). This study shows the benefit of higher spatial resolution in particular over areas with complex terrain such as the Alps. An accompanying study shows that also land surface conditions play an important role and need to be considered to realistically simulate the LGM climate state (Velasquez et al., 2021), which is similar to earlier findings obtained with coarser resolved RCM simulations for LGM and MIS3 (Kjellström et al., 2010; Strandberg et al., 2011; Ludwig et al., 2017). Nevertheless, a detailed analysis of the sensitivity of the global and local ice-sheet topography on the regional hydro-climate over the European Alps — the purpose of this study — is missing. Hence, we employ eight high-resolution RCM simulations with the Weather Research and Forecasting (WRF) model (Skamarock and Klemp, 2008) driven by simulations under constant climate conditions using the Community Climate System Model version 4 (CCSM4,

Table 4.1: External forcing used in Hofer et al. (2012a,b) for 1990 CE, LGM and MIS4 conditions.

Parameter name	**1990 CE**	**LGM**	**MIS4**
TSI (W m^{-2})	1361.77	1360.89	1360.89
Eccentricity (10^{-2})	1.6708	1.8994	2.0713
Obliquity (°)	23.441	22.949	22.564
Angular precession (°)	102.72	114.43	15.22
CO_2 (ppm)	353.9	185	205
CH_4 (ppb)	1693.6	350	460
N_2O (ppb)	310.1	200	210

Gent et al., 2011). Thereby, we modify either the height of the northern hemispheric ice sheets, i.e. LIS, the Fennoscandian and Greenland ice-sheet in both CCSM4 and WRF, or the height of the Fennoscandian ice sheets (FIS) in the regional model or solely the height of the Alpine ice sheet in the regional model.

The study is structured as follows. Section 4.2 describes the models and experiments carried out in this study. Section 4.3 introduces methods used for analysing the role of the ice-sheet topography on the Alpine hydro-climate. In Sect. 4.4, we first characterise the two glacial states LGM and MIS4. Secondly, we investigate how the Alpine hydro-climate reacts to changes in the northern hemispheric and the FIS, separately. In a third step, we assess the sensitivity of the Alpine hydro-climate to local (Alpine) ice-sheet changes. Finally, a discussion and conclusive remarks are given in Sect. 4.5.

4.2 Models and experiments

The study is based on eight experiments using PD and glacial climate conditions to assess the role of the large-scale (LIS and FIS) and local (Alpine) ice-sheet topography on the Alpine climate. The focus on the European Alps necessitates to employ a model chain that consists of a GCM and RCM. Thereby, the GCM provides the initial and boundary conditions for the RCM. The models' configuration and the experiments are explained in the following.

The Community Climate System Model is used as GCM in the model chain (version 4, CCSM4; Gent et al., 2011). We use the atmosphere-land-only setting of CCSM4, i.e., the components of the atmosphere (CAM4, Neale et al., 2010) and land (CLM4, Oleson et al., 2010) are dynamical models whereas the ocean and sea ice components are so-called *data models* obtained from a coarsely resolved fully coupled simulation performed with CCSM3 (Hofer et al., 2012a). Thus, the two data models force the atmospheric component by time-varying sea-surface temperatures and sea-ice cover. The atmosphere-land-only model is run for 33 years with 6-hourly output, a horizontal resolution of 1.25° × 0.9° (longitude × latitude) and 26 vertical hybrid sigma-pressure levels in the atmosphere and 15 layers in the land component.

In this study, we use the first 21 or 12 years of the GCM simulation that follow after the first 3 years of spin-up.

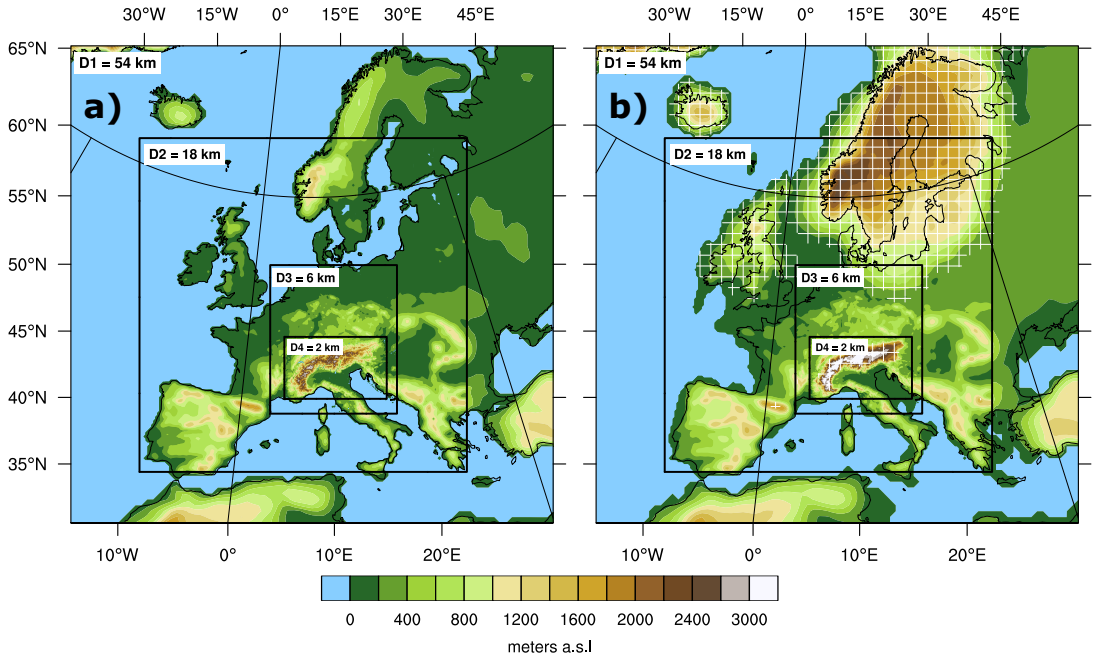

Figure 4.1: Domains and topography used by WRF. (a) represents the four domains at 54, 18, 6 and 2 km horizontal resolution and the shading indicates present-day topography, (b) as (a) but for the LGM topography, crosshatched areas are covered by glaciers.

Five global climate simulations provide the RCM with initial and boundary conditions. Two of these CCSM4 simulations are performed under PD 1990 CE conditions and LGM conditions, respectively. The other three simulations are performed under MIS4 conditions. The orbital forcing and atmospheric composition are adjusted to the respective period (Table 4.1). The MIS4 simulations differ in their northern hemispheric ice-sheet elevation: 66, 100 and 125 % of the LGM ice-sheet elevation, respectively. Note that glaciers and small ice caps such as the ones over the Alps and Pyrenees are not included in these simulations due to the coarse resolution of approximately 100 km in the GCM. More detailed information on these simulations and their settings are presented in Hofer et al. (2012a,b) and Merz et al. (2013, 2014a,b, 2015).

The global CCSM4 simulations are dynamically downscaled with the RCM Weather Research and Forecasting (WRF) model (version 3.8.1, Skamarock et al., 2008). This RCM solves the basic non-hydrostatic equations with an Eulerian mass-coordinate solver and employs a terrain-following eta-coordinate system in the vertical. We use an adaptive time-step, 40 vertical eta levels and four domains that are two-way nested. The horizontal resolution of these four domains is 54, 18, 6 and 2 km, respectively. The domains focus on the Alpine region; the outermost domain includes Europe and part of the North Atlantic to capture the influence of the North Atlantic Ocean and the FIS on the European climate (Fig. 4.1). Furthermore, we use the same setting as in Velasquez et al. (2020), thus we refer to this publication on the details of the relevant parameterisation schemes used. Still, we highlight that the horizontal

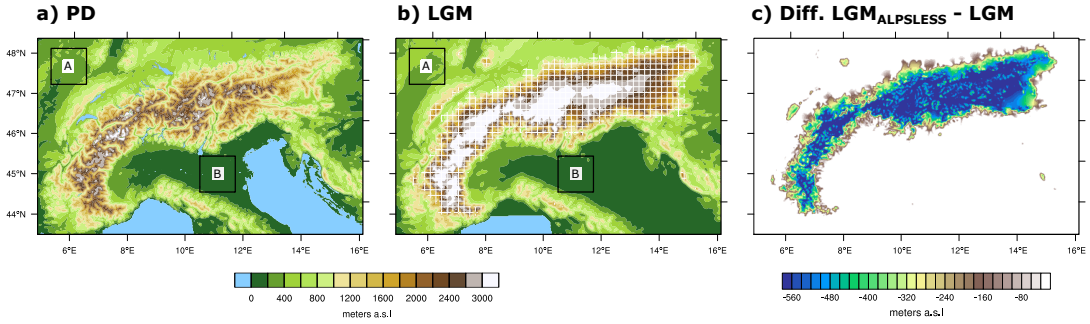

Figure 4.2: Innermost domain and topography used by WRF. (a) represents the domain at 2 km horizontal resolution and the shading indicates PD topography, (b) as (a) but for the LGM topography, crosshatched areas are covered by glaciers. (c) shows the difference between $\mathrm{LGM_{ALPSLESS}}$ and LGM topography. The boxes in (a) and (b) are the two regions used for the Skew–T diagrams: Site A represents the north-western and site B the central-southern region.

resolutions in the two innermost domains (6 and 2 km) are convection permitting, i.e., we omit the use of parameterisation for convection in these two domains. WRF uses 21 or 12 years (compare Table 4.2 for more details) of the corresponding GCM simulation as initial and boundary conditions, but WRF is not nudged to the GCM output. These 21 and 12 years are further split up into 7 and 4 individual 3-year simulation segments, respectively, to efficiently use the available computer facilities. For each segment, a 2-month spin-up is needed in order to allow the land surface to come into quasi-equilibrium. Tests suggest that a 2-month spin-up is sufficient to obtain a quasi-equilibrium of the upper meter of the land surface (Velasquez et al., 2020, 2021).

The first experiment ($\mathrm{PD_{PD}}$) is a reference simulation under PD conditions (1990 CE conditions). We run WRF for 21 years using 1990 CE conditions and initial and boundary conditions of the corresponding CCSM4 simulation (Table 4.1). $\mathrm{PD_{PD}}$ uses the default PD MODIS-based land cover dataset from WRF as land surface boundary conditions (Skamarock et al., 2008).

The second experiment ($\mathrm{LGM_{LGM}}$) uses the external forcing of the LGM (Table 4.1), except for eccentricity and precession. The reason is that in the radiative routine of WRF only the obliquity parameter is processed. We realised this problem after the simulations have been performed. We expect that this problem is of minor importance as the driving CCSM4 uses all orbital parameters and thus the orbital signal is at least partly included in the simulations. Some preliminary results with a model version, which fixes this bug, shows no strong dependence on this error under LGM conditions (Emmanuele Russo pers. comm.). Additionally, the $\mathrm{LGM_{LGM}}$ surface conditions need some further adjustments. These include the lowering of the sea level and ice sheets as specified in the PMIP3 protocol (Fig. 4.1b; for more details see: Ludwig et al., 2017). The glaciation over the Alpine region (obtained from Seguinot et al., 2018) and other glaciated areas (e.g. Pyrenees, from Ehlers et al., 2011) are modified according to LGM conditions (Fig. 4.1b). Additionally, the land cover is altered to comply with LGM conditions, as described in Velasquez et al. (2021). Comparing $\mathrm{LGM_{LGM}}$ with $\mathrm{PD_{PD}}$ illustrates the entire effect of changes in the external forcing and in the surface

Table 4.2: Set of experiments carried out in this study. The first column indicates the name of the WRF simulation, the second column the perpetual conditions, the third column the northern hemispheric ice sheets (this includes the modifications in the driving global model), the fourth column the FIS, the fifth column the Alpine glaciers, the sixth column the land cover, and the seventh column the length of the simulation.

Name	Perpetual conditions	North Hemis. ice sheets	Fennoscandian ice sheet	Alpine glaciers	Land cover	Sim. length
PD_{PD}	1990	1990	1990	1990	1990	21 years
LGM_{LGM}	LGM	LGM	LGM	LGM	LGM	21 years
$MIS4_{LGM66}$	MIS4	66 % LGM	66 % LGM	LGM	LGM	21 years
$MIS4_{LGM}$	MIS4	100 % LGM	100 % LGM	LGM	LGM	21 years
$MIS4_{LGM125}$	MIS4	125 % LGM	125 % LGM	LGM	LGM	21 years
LGM_{FIS50}	LGM	LGM	50 % LGM	LGM	LGM	12 years
LGM_{FIS150}	LGM	LGM	150 % LGM	LGM	LGM	12 years
$LGM_{ALPSLESS}$	LGM	LGM	LGM	reduced LGM	LGM	21 years

conditions (sea level drop, land cover and northern hemispheric ice sheets). Note that the LGM_{LGM} simulation is evaluated against proxy evidence (Prentice and Jolly, 2000; Wu et al., 2007; Kaplan et al., 2016) showing an improved LGM climate state in the WRF simulation (Velasquez et al., 2020, 2021) compared to the driving CCSM4 simulations (Hofer et al., 2012a).

The third to seventh experiments assess the sensitivity of the Alpine climate to changes in the northern hemispheric ice-sheet configuration. Thereby, the MIS4 simulations of CCSM4 are dynamically downscaled with WRF resulting in $MIS4_{LGM66}$, $MIS4_{LGM}$ and $MIS4_{LGM125}$. These three WRF simulations are run for 21 years using MIS4 conditions and using the LGM_{LGM} land cover (described in Velasquez et al., 2021). Note further that the Alpine ice sheet is always set to LGM conditions (Fig. 4.2b). Following their driving CCSM4 simulations, we perform each WRF simulation with a different Fennoscandian ice-sheet thickness: 66, 100 and 125 % of the LGM ice-sheet thickness, respectively. $MIS4_{LGM}$ serves as reference for $MIS4_{LGM66}$ and $MIS4_{LGM125}$.

To investigate the effect of the FIS on the Alpine climate, we perform two additional sensitivity simulations: LGM_{FIS50} and LGM_{FIS150}. For both simulations, the initial and boundary conditions are from the LGM CCSM4 simulation. Note that this CCSM4 simulation uses 100 % LGM ice-sheet configurations. To assess the influence of the FIS, we reduce or increase FIS thickness to 50 % and 150 %, but only in the WRF model. Both simulations are run for 12 years.

With the eighth experiment, we investigate the influence of local modifications of the Alpine ice sheet on the Alpine climate. One sensitivity simulation is performed: $LGM_{ALPSLESS}$. This simulation is based on the LGM_{LGM} (which serves as reference) but with a modified Alpine topography (Fig. 4.2c). $LGM_{ALPSLESS}$ is run for 21 years and with a reduced Alpine

glacier thickness. This reduction becomes stronger with height; namely, the Alpine ice sheet is strongly reduced over mountain peaks and slightly over the low lands. All eight experiments are summarised in Table 4.2.

4.3 Methods

The analysis of the past hydro-climate and its response to different forcing factors is based on climatological means of precipitation, their differences between the experiments and some of the driving factors for these differences, e.g. changes in humidity or wind. We assess the statistical significance with a bootstrapping technique (Wilks, 2011). This technique randomly selects elements from the original sample to generate a new sample, also called resampling, whereby the number of elements remains unchanged. This procedure is repeated 1000 times. A new mean value is calculated from each resampling leading to 1000 mean values that are used to build a probabilistic distribution function (PDF). We assess the significance of the mean value using a significance level of 0.05 (0.025 for each PDF's tail). The bootstrapping technique is applied at each grid point using as elements the 30 annual mean values.

Additionally, we analyse vertical atmospheric profiles using the SkewT–Log P diagram (AWC, 1969, 1990; NOAA, 2021) to gain insights into the atmospheric drivers of precipitation changes. The SkewT–LogP or Skew–T diagram is a thermodynamic diagram that is widely used in atmospheric science, particularly by meteorologists for weather forecasts (e.g. Duarte and Gomes, 2017; Morsy et al., 2017; da Silva et al., 2019; Chen et al., 2020). It illustrates the vertical atmospheric state by several meteorological variables such as air temperature, humidity, wind speed and wind direction. The x-axis indicates temperature and the y-axis pressure levels in a logarithmic scale (thus the name LogP). There are usually five isolines on the diagram: isotherms, isohumes (or mixing ratio lines), dry adiabatic lines (or lines of equal potential temperature θ), isobars, and moist adiabatic lines. In this study, we use a simplified diagram that only contains the first three variables for the analysis as we focus on changes in temperature, humidity and wind. For instance, an unsaturated air panel follows a dry adiabatic line when ascending without changes of state, i.e., there is no loss or gain of latent heat. These lines are used in this study to qualitatively estimate the stability of the atmosphere. A stable atmosphere is characterised by an increase of potential temperature with height.

Two vertical profiles are included in the Skew–T diagram: temperature (solid lines) and dew-point temperatures (dashed lines). The latter simply indicate temperatures at which the air becomes saturated and is used to deduce the mixing ratio with height, i.e., the amount of water vapour in the air where the dew point temperature line crosses the mixing ratio line. Both temperatures are used to investigate the relative humidity, i.e., the level of saturation at a certain pressure and temperature. This is done by qualitatively estimating the distance between both temperatures. A short distance indicates a high relative humidity and, inversely, a large distance a low relative humidity. Wind speed and direction are illustrated by wind bars in km h^{-1}.

The Skew–T diagram is built with climatological means of the atmospheric variables above surface at the following pressure levels: 1000, 925, 900, 850, 800, 750, 700, 600, 500, 400, 300, 250, 200 and 100 hPa. We consider the lowest pressure level above surface as the best representation of the near-surface atmosphere. Two additional vertically integrated quantities are given at the top of the diagram: precipitable water (PW) and convective available potential energy (CAPE). CAPE quantitatively represents the energy available for convective processes, the higher it is the stronger these processes could be (for more information see chapter 8 of Wallace and Hobbs, 2006). In this study, we use the climatological mean values to calculate the PW and CAPE values; the later are only shown at the top of the diagram when it is different from zero.

4.4 Results

In the following, the glacial Alpine hydro-climate is characterised for two glacial states the LGM and MIS4. Then, we investigate the sensitivity of the hydro-climate to northern hemispheric ice-sheet changes for MIS4 and the sensitivity to the FIS for LGM. We assess the Alpine hydro-climate response to changes in the Alpine ice sheet by one simulation using LGM conditions. For the analysis, we select winter (DJF, December-January-February) and summer (JJA, June-July-August) as these two seasons summarise the changes in spatial precipitation patterns over the Alpine region. The other two transition seasons (MAM, March-April-May and SON, September-October-November) show either similarities to winter (for MAM) or summer (for SON). The analysis is based on the innermost domain of the WRF simulations (Fig. 4.2).

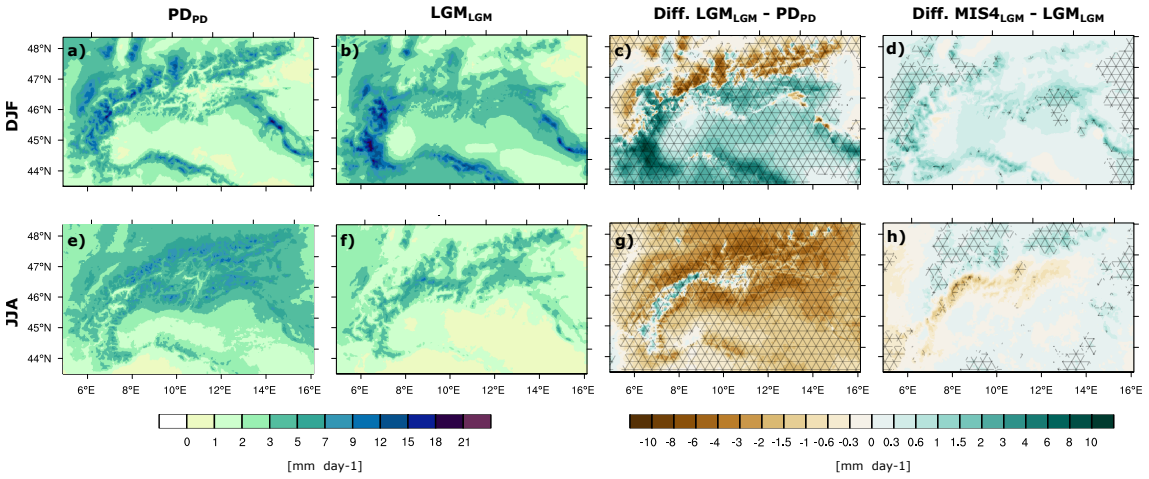

Figure 4.3: Climatological mean values of daily precipitation intensity over the Alps for (a, b, c and d) winter (DJF) and (e, f, g, and h) summer (JJA): (a, e) the mean PD precipitation, (b, f) the mean LGM precipitation, (c, g) the difference between LGM and PD and (d, h) the difference between MIS4 and LGM. Crosshatched areas represent statistically significant differences with a significance level of 0.05 (using a two-tailed bootstrapping technique).

4.4.1 Characterisation of the glacial hydro-climate of the Alps

Present-day hydro-climate over the Alpine area is characterised by the large scale atmospheric circulation with its dominant westerlies, influences from the Mediterranean (Messmer et al., 2015, 2017, 2020) and convective processes (Ban et al., 2014; Gómez-Navarro et al., 2018). In winter, the westerlies are enhanced, so that we observe high precipitation amounts in the north-western area of the domain and at the northern face of the Alps, whereas the southern and the eastern parts receive less precipitation (Fig. 4.3a). Due to the orographic barrier of the Alps the flow is uplifted leading to a higher precipitation intensity over mountain tops and lower intensity in valleys. In summer, the precipitation pattern is more uniform over the Alps, showing high intensities also on the southern face of the Alps and in the east (Fig. 4.3e). This suggests that the topographically triggered convection is an important process in summer under PD climate.

The LGM shows a completely different precipitation behaviour over the Alps (Fig. 4.3). In winter, precipitation is mostly concentrated on the south-western Alps (Fig. 4.3b and c) with a statistically significant increase of more than 8 mm day^{-1} compared to PD (Fig. 4.3c). The southern face of the Alps generally shows a statistically significant increase of winter precipitation of about 3 mm day^{-1} during LGM compared to PD, whereas the northern face experiences a statistically significant decrease of more than 6 mm day^{-1} (Fig. 4.3c). During summer, precipitation is significantly reduced at LGM compared to PD (Fig. 4.3e, f and g), which suggests that convective processes, typically observed in PD summer, are less active during the LGM. Still, few areas show wetter conditions during the LGM compared to PD, particularly over mountains peaks in the western Alps (Fig. 4.3g). The increase in precipitation observed over mountain peaks indicates precipitation induced by orographic lifting. As the surroundings are drier it is assumed that the higher elevation of the Alps during LGM triggers precipitation only at the highest points.

To further understand the precipitation changes between LGM and PD, we use the Skew–T diagram, as introduced in Sect. 4.3. The vertical profiles are estimated for two sites: upstream to the Alpine region (site A, north-western region) and downstream (site B, central-southern region) according to the general westerlies of the mid latitudes (Fig. 4.2). Note that these two sites are over rather flat terrain and therefore experience less influence from local orographic-induced atmospheric dynamics such as the mountain-valley breeze.

Starting with the Skew–T diagrams in winter (Fig. 4.4a and c), we find the expected strong reduction of LGM temperatures compared to PD at both sites. The mixing ratios are also reduced in the LGM compared to PD resulting in less precipitable water under LGM conditions at both sites. Interestingly, the relative humidity, measured by the distance between dew-point temperature and temperature remains unchanged when comparing LGM and PD. However, we find a clear structural change in the vertical profiles of the temperatures, as illustrated by the different slopes between LGM and PD. Both sites show that potential temperature values (comparing the temperature profile with the dashed brown lines) overall increase with height indicating a stable atmosphere. This increase is stronger in the LGM

indicating a more stable atmosphere at both sites compared to PD. Particularly, the stability is higher in site A (north-western part) than in site B (central-southern region) in winter, which is a first hint that both regions show different behaviours in their winter precipitation. Another hint is given by the wind speed and direction, since we find an increase in wind speed

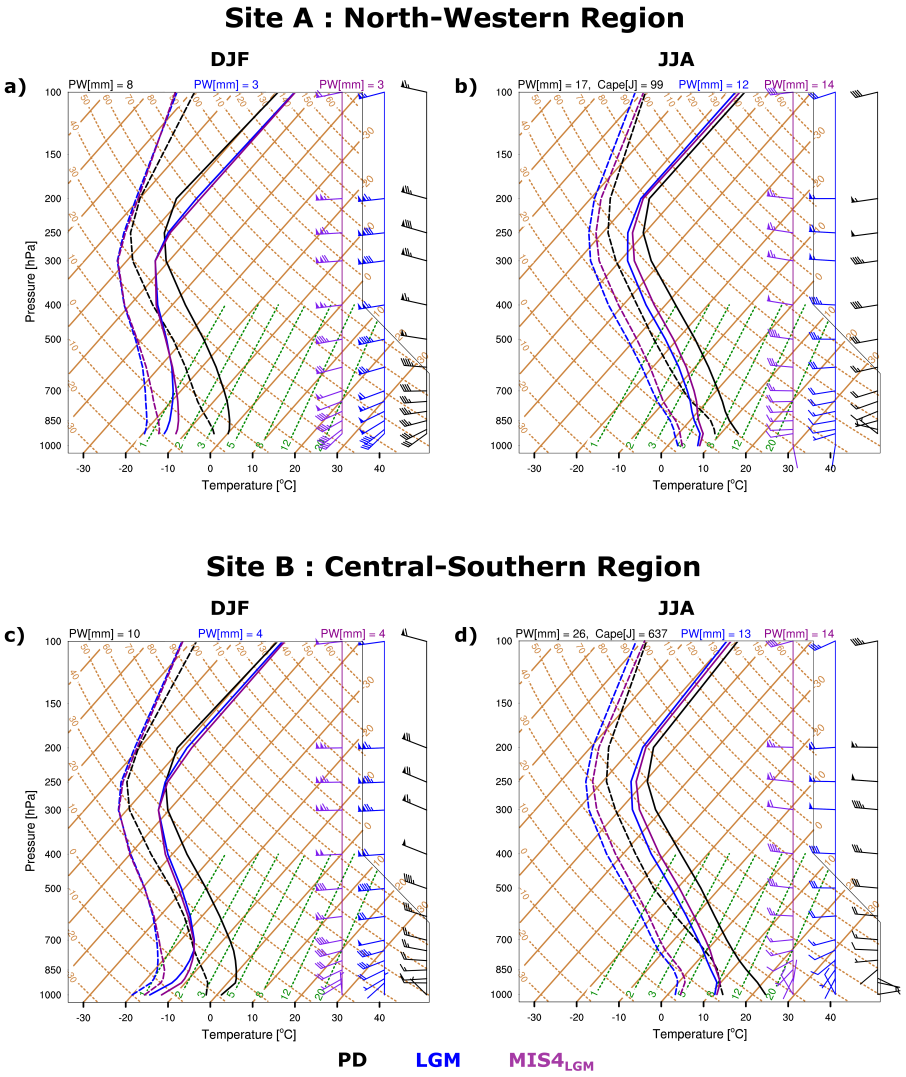

Figure 4.4: Skew–T diagram for site A (north-western region; a and b) and site B (central-southern region; c and d). Sites' locations are shown in Fig. 4.2. (a and c) represent climatological vertical profiles for DJF and (b and d) for JJA. PD climate is illustrated by black, LGM climate by blue and $\mathrm{MIS4_{LGM}}$ climate by purple lines. Skewed straight dashed green lines represent isohumes labelled on the bottom of the diagram. The mixing ratio increases to the right at a constant pressure level. Solid brown lines are isotherms. Dry adiabatic lines (lines of equal potential temperature θ) are slightly curved dashed brown lines. In the wind bars, the triangle, line and half-size line represent 50, 10, 5 km $\mathrm{h^{-1}}$, respectively. Furthermore vertically integrated precipitable water (PW) and CAPE are given at the top of each panel. Note that CAPE is only displayed if it is different from zero. Please see Sect. 4.3 for a in-detail description of the Skew–T diagram.

and an anticlockwise rotation of the LGM compared to PD. This is evident at both sites but the rotation is more pronounced in the central-southern region. The boundary layer is thicker in the LGM than in PD, in particular for the central-southern region. Both sites show the expected lowering of the tropopause during the LGM due to colder conditions compared to PD.

Summer shows a rather similar behaviour as winter, but with a few exceptions related with the season (Fig. 4.4b and d). CAPE is only observed during PD summer at both sites. Additionally, we find a development of a small boundary layer under LGM conditions, which is not present under PD conditions. Furthermore, the wind is rotated slightly clockwise at site A (north-western region), whereas site B (central-southern region) shows an anticlockwise rotation. Again, at both sites, the wind speed is increased in the LGM, but not as clearly as in winter.

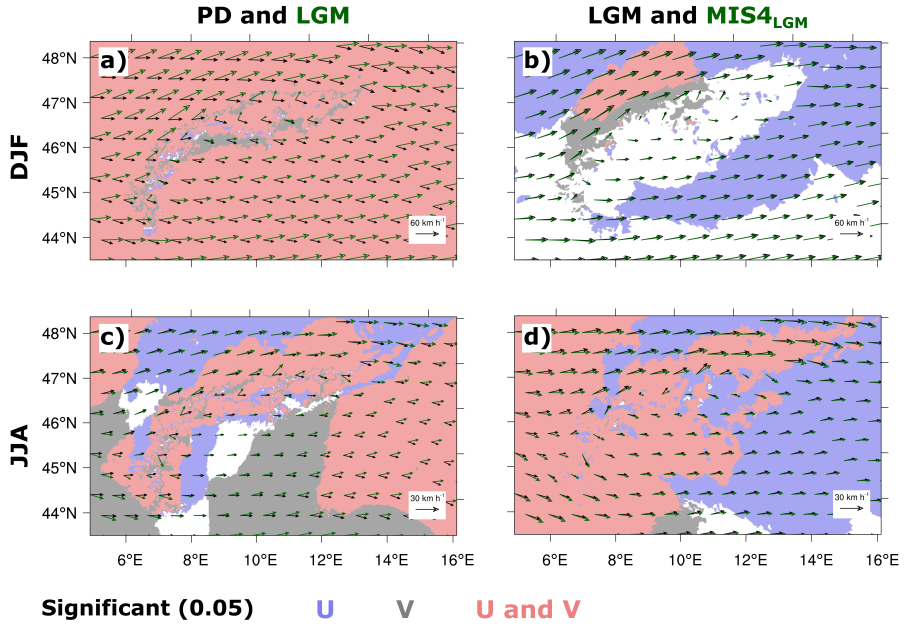

Figure 4.5: Climatological mean wind vectors over the Alps for (a and b) DJF and (c and d) JJA: (a and c) black and green wind vectors correspond to PD and LGM, respectively, (b and d) black and green wind vectors correspond to LGM and MIS4, respectively. Red shading illustrates statistically significant differences in zonal (U) and meridional (V) wind components with a significance level of 0.05 (two-tailed bootstrapping technique), blue and grey shading indicate significance either in the U or V wind component, respectively. Please note that the reference wind vectors differ for DJF and JJA.

To gain further insights in the advection of moisture, we exhibit the wind vectors at 700 hPa. This level summarises winds in the low-to-mid troposphere. Note that this pressure level could also represent near-surface winds over mountain peaks in certain regions. Compared to PD wind vectors, LGM winds are significantly stronger and rotated anticlockwise during winter (Fig. 4.5a), confirming the finding of the Skew–T diagrams (Fig. 4.4 a and c). Almost the entire domain shows significant changes in both wind components (red shading in Fig. 4.5a). Stronger winds are also observed during summer but with slightly different rotation patterns across the domain (Fig. 4.5c). These winds are generally rotated anticlockwise except for the southwestern region of the domain where it is clockwise. The increase in speed covers approximately half of the domain, which is attributed to either significant changes in the zonal component (U) only or both wind components (i.e., blue or red shading, respectively; Fig. 4.5c). Similarly, the wind rotation also covers about half of the domain, which is associated to either significant changes in the meridional component (V) only or both wind components (i.e., areas in grey or red, respectively; Fig. 4.5c).

MIS4 is the second glacial state considered here. Figure 4.3d shows that winter precipitation intensities of $MIS4_{LGM}$ are higher than LGM ones, especially over some areas such as the western area of the domain with a significant increase of about 3 mm day^{-1}. This is expected as $MIS4_{LGM}$ climate is warmer than LGM, thus the ability of the atmosphere to hold more moisture is increased due to the Clausius–Clapeyron equation (e.g. third chapter of Wallace and Hobbs, 2006). In summer, the precipitation difference between MIS4 and LGM shows a significant north-south dipole pattern (Fig. 4.3h). There are slightly wetter conditions of about 1.5 mm day^{-1} on the northern face of the Alps during $MIS4_{LGM}$ compared to LGM. On the southern face of the Alps precipitation is reduced by around 2 mm day^{-1}.

To understand these differences, we again investigate the atmospheric vertical profiles at both sites. Overall, the MIS4 profiles look very similar to LGM ones during winter. The expected shift towards warmer conditions under MIS4 conditions is visible at both sites (Fig. 4.4a and c), in particular in the lower part of the troposphere (mainly in the boundary layer), leading to higher mixing ratios in MIS4 compared to LGM. The comparison of MIS4 and LGM further shows that the stability is slightly reduced under MIS4 conditions in the lower part of the troposphere (up to 600 hPa; Fig. 4.4a). This reduction is more evident in the north-western region (site A), whereas the stability in the central-southern region (site B) is slightly reduced in the mid layer of the troposphere (between 800 and 400 hPa; Fig. 4.4c). The wind directions seem to be unchanged with slightly lower wind speeds under MIS4 than LGM conditions. Thus, thermodynamic changes are the major processes in explaining the increased winter precipitation during MIS4 (Fig. 4.3d). In summer, the temperature profiles agree between the two glacial states at both sites, except for a shift towards higher temperatures leading again to higher mixing ratios. The only deviation is that the boundary layer shows a slightly stronger inversion during MIS4 than LGM at both sites. The shift to warmer temperature and higher mixing ratios suggest a general moistening under MIS4 compared to LGM conditions, which can explain the increase in summer precipitation in the northern part but not the decrease in the southern part of the domain.

Therefore, we assess the wind fields in more detail. Figure 4.5b shows that MIS4 winds become weaker during winter compared to LGM, but a rotation is almost absent. During summer, MIS4 winds become stronger with a slight clockwise rotation compared to LGM (Fig. 4.5d). Both, the increase in speed and the rotation, enhances the wind shear in the low-to-mid troposphere (Fig. 4.4) resulting in more convective-related precipitation in the northern part of the Alps, whereas the clockwise rotation over the southern face of the Alps in MIS4 leads to reduced moisture availability as the flow dries out when crossing the Alps and reaching the Po valley (Foehn process).

In summary, we find that both thermodynamic and dynamical changes are responsible to generate precipitation changes in winter and summer when comparing LGM and PD conditions and MIS4 and LGM, respectively. Interestingly, the changes in winter precipitation between LGM and PD is explained by a combination of thermodynamic and dynamic processes, whereas the summer reduction is mainly explained by thermodynamics and reduced convection.

The comparison of MIS4 and LGM shows that the winter changes are mainly driven by thermodynamics, whereas in summer also dynamical changes are important.

4.4.2 Sensitivity of the Alpine hydro-climate to northern hemispheric ice-sheet changes

Here, we investigate the role of the northern hemispheric ice-sheet topography in the Alpine climate. Two sets of sensitivity simulations are used. The uncertainty in the thickness of the northern hemispheric ice sheets is assessed by comparing two simulations with 66 and 125 % to the one with 100 % LGM ice-sheet thickness under MIS4 conditions. The second set of simulations uses the LGM climate state as a reference and only the FIS thickness is changed by 50 and 150 %.

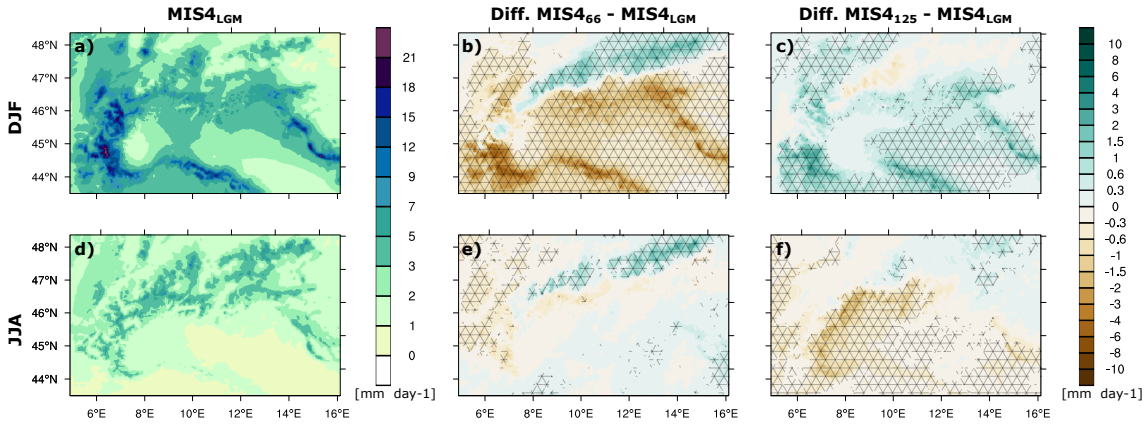

Figure 4.6: Climatological mean values of daily precipitation intensity over the Alps. (a) represents $MIS4_{LGM}$ precipitation for DJF, (b) the differences between $MIS4_{LGM66}$ and $MIS4_{LGM}$, (c) as (b) but between $MIS4_{LGM125}$ and $MIS4_{LGM}$. (d), (e) and (f) as (a), (b) and (c) but for JJA. Crosshatched areas indicate statistically significant differences at a significance level of 0.05 (using a two-tailed bootstrapping technique).

We first focus on the precipitation response to these changes in ice-sheet thickness. The comparison of $MIS4_{LGM66}$ with $MIS4_{LGM}$ shows that lowering the northern hemispheric ice sheets by 66 % significantly increases the winter precipitation by about 3 mm day^{-1} on the northern face of the Alps and leads to significantly drier conditions in the rest of the domain (Fig. 4.6b). In particular, winter precipitation is reduced by up to 8 mm day^{-1} in the south-western Alps (Fig. 4.6b). Comparing these patterns to the difference between PD and LGM, we find a north-south winter pattern inversely to the one of PD and LGM. This suggests that decreasing ice-sheet thickness (i.e., $MIS4_{LGM66}$) leads to more PD-like conditions during glacial climates. Summer precipitation differences between the two experiments resembles the winter pattern, but the amplitudes are reduced, i.e., precipitation is increased by about 2 mm day^{-1} on the northern face of the Alps and reduced by about 1 mm day^{-1} in the western part of the domain (Fig. 4.6e). The southern part shows no significant changes. This pattern of precipitation is only partly similar to the difference pattern of the LGM and PD.

An increased ice-sheet thickness as in $MIS4_{LGM125}$ shows a different influence on precipitation patterns (Fig. 4.6c and f). In winter, the difference pattern in precipitation between $MIS4_{LGM125}$ and $MIS4_{LGM}$ is similar to the one found between LGM and $MIS4_{LGM}$ with overall wetter conditions. Especially, we find significantly high precipitation intensities up to 3 mm day^{-1} on the north western and southern regions of the domain (Fig. 4.6c). The northern face of the Alps shows a decrease in the precipitation intensities. Thus, we interpret that the response of winter precipitation is linear with respect to the northern hemispheric ice-sheet thickness changes. In summer, we generally find drier conditions in the $MIS4_{LGM125}$ than in $MIS4_{LGM}$, in particular significantly lower precipitation of up to -3 mm day^{-1} on the central to southern part of the domain (Fig. 4.6f). This indicates that increasing northern hemispheric ice-sheet thickness (such as in $MIS4_{LGM125}$) enhances glacial climate conditions.

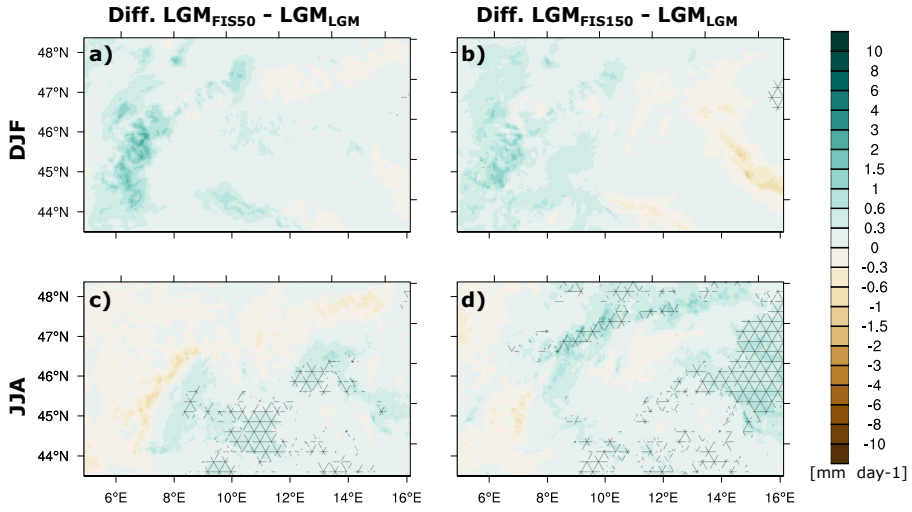

Figure 4.7: Differences in climatological mean values of daily precipitation intensity over the Alps for (a and b) winter (DJF) and (c and d) summer (JJA): (a and c) LGM_{FIS50} minus LGM_{LGM} and (b and d) LGM_{FIS150} minus LGM_{LGM}. Crosshatched areas indicate statistically significant differences at a significance level of 0.05 (using a two-tailed bootstrapping technique).

Secondly, we focus on the other set of sensitivity simulations under LGM conditions, where only the FIS thickness is varied. These simulations show a rather weak response of the precipitation within the domain (Fig. 4.7). In winter, increasing or decreasing the FIS thickness does not lead to significant changes in precipitation (Fig. 4.7a and b). In summer, we find an increase in the southern part of the domain for both sensitivity simulations (Fig. 4.7c and d) and a small but significant increase in the northeast of the domain in the LGM_{FIS150} simulation.

Again, the Skew–T diagram is used to understand the role of the vertical behaviour of the atmosphere on precipitation changes at the two sites (Fig. 4.2). The sensitivity simulations of the northern hemispheric ice-sheet height shows that at both sites the wind speed in winter is enhanced and anticlockwise rotated with increasing ice-sheet thickness (Fig. 4.8a and c). While decreasing northern hemispheric ice-sheet thickness leads to slightly weaker and clockwise rotated winds and a slightly warmer atmosphere. The latter results in a small increase of

moisture availability (dashed green lines), especially in the central-southern region (site B) where there is more precipitable water (Fig. 4.8a and c). In summer, only small wind changes are found at both sites (Fig. 4.8b and d) and changes in the other variables of the Skew–T diagram are mainly restricted to the lower troposphere and the boundary layer (Fig. 4.8b and d). We find a reduced relative humidity at site A (north-western region), measured by the distance between the dew-point temperature and temperature, and lower mixing ratios (dashed green lines) at site B (central-southern region) with increasing ice-sheet thickness. This

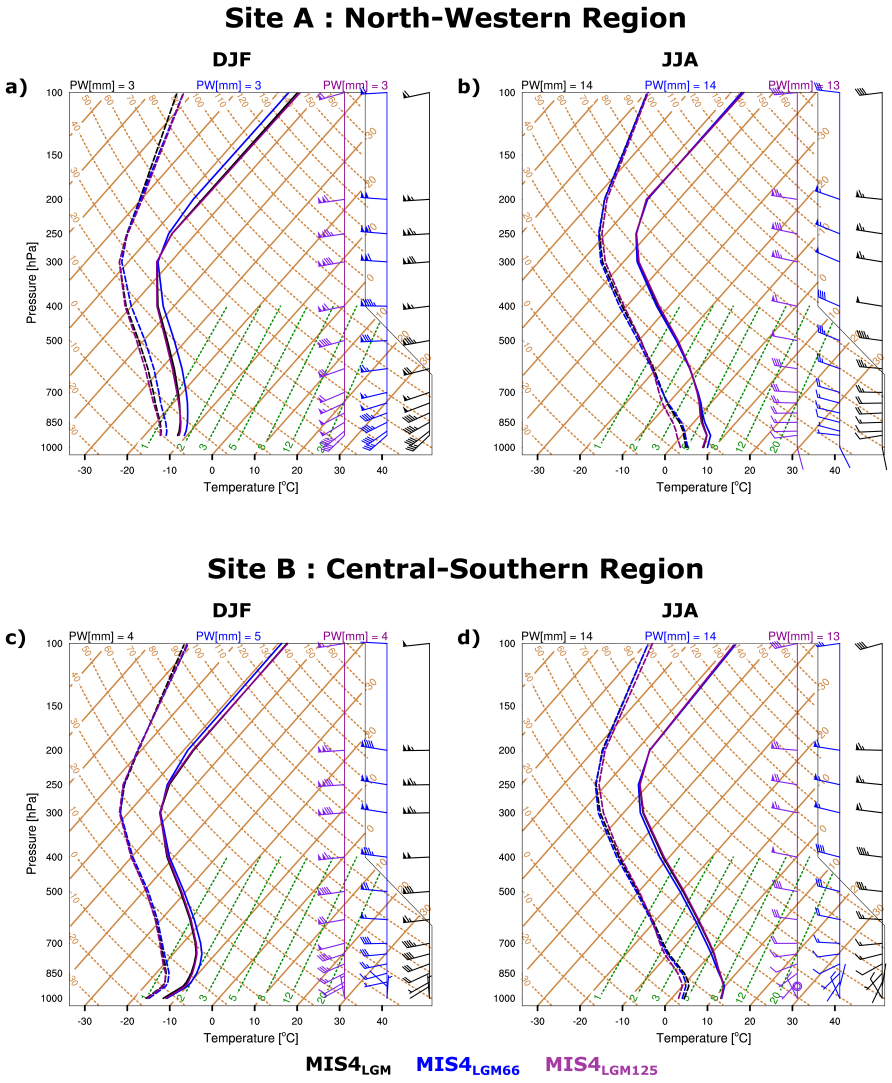

Figure 4.8: As Fig. 4.4, but for $\mathrm{MIS4_{LGM100}}$ (black), $\mathrm{MIS4_{LGM66}}$ (blue), and $\mathrm{MIS4_{LGM125}}$ (purple).

suggests dryer conditions at both sites in the case of $\mathrm{MIS4_{LGM125}}$. The Skew–T diagrams for the sensitivity of the FIS do not show strong differences (therefore not shown). Thus, the Skew–T analysis confirms that an increase in northern hemispheric ice-sheet thickness enhances glacial climate conditions. It further suggests that similar processes as discussed in the comparison between LGM and PD are responsible for precipitation changes, whereas only changing the FIS does not seem to have strong implications.

The Skew–T diagrams already give some hints to wind alterations with respect to changes in the northern hemispheric ice-sheet topography. Thus, we further assess the role of the northern hemispheric ice-sheet topography on the Alpine winds by showing the 700 hPa wind fields. In general, we observe that wind speed is weaker with decreasing ice-sheet thickness. In winter, we find a clockwise rotation of the wind vectors over the entire domain with decreasing northern hemispheric ice-sheet thickness (Fig. 4.9a and b). These modifications are generally associated with either significant changes in the meridional component (V) only or both wind components (i.e., grey or red shading, respectively; Fig. 4.9a and b). In summer, we find that winds rotate clockwise with decreasing ice-sheet height (Fig. 4.9c and d). The alterations in summer are related to either significant changes in the zonal and meridional component (U and V) only or both wind components (i.e., blue, grey or red shading, respectively; Fig. 4.9c and d). Thus, the winter and summer wind fields react similar to the comparison between LGM and PD suggesting that northern hemispheric ice-sheet thickness is an important driver of the advection processes over the Alps. Again, the sensitivity simulations with changed FIS thickness do not show significant changes in the wind field (therefore not shown), which again confirms the findings that the thickness of the FIS seems to have limited influence on Alpine precipitation.

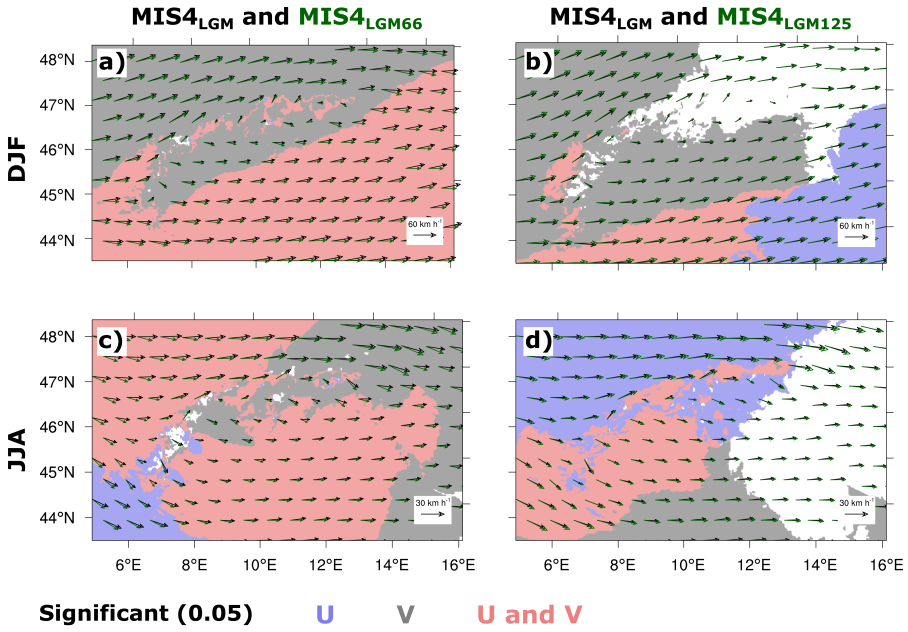

Figure 4.9: Climatological mean wind vectors over the Alps. (a) represents wind vectors for DJF, black and green vectors correspond to $MIS4_{LGM}$ and $MIS4_{LGM66}$, respectively, (b) as (a) but green vectors to $MIS4_{LGM125}$. (c) and (d) as (a) and (b) but for JJA. Red shading indicates statistically significant differences in zonal (U) and meridional (V) wind components at a significance level of 0.05 (two-tailed bootstrapping technique), blue and grey shading as the red one but only in U and V wind components, respectively. Please note that the reference wind vectors differ for DJF and JJA.

In summary, the analysis shows that winter and summer seasons react differently to northern hemispheric ice-sheet thickness changes, but resemble the processes already found in the comparison between LGM and PD: Increasing northern hemispheric ice-sheet thickness

generally leads to enhanced glacial conditions, i.e., a moistening during winter due to dynamic processes and a drying in summer mainly explained by thermodynamics. The sensitivity of precipitation to the FIS thickness is rather weak and the simulations suggest that its thickness has only a negligible influence on the Alpine precipitation.

4.4.3 Sensitivity of the Alpine hydro-climate to Alpine ice-sheet changes

Besides changes in the northern hemispheric ice sheet, modifications in the Alpine ice sheet might also influence Alpine precipitation. Therefore, we investigate the precipitation pattern of the sensitivity simulation $\mathrm{LGM_{ALPSLESS}}$ in comparison to $\mathrm{LGM_{LGM}}$. Then, we assess the processes explaining these changes using again the Skew–T diagram and the wind field at 700 hPa.

In winter, the $\mathrm{LGM_{ALPSLESS}}$ experiment shows some areas with significantly drier conditions over the Alps compared to $\mathrm{LGM_{LGM}}$ (Fig. 4.10a), especially in the western Alps with some significant precipitation reductions of up to 6 mm day^{-1}. This dryness generally coincides with the reduced Alpine ice-sheet thickness (Fig. 4.2c). Interestingly, the reduction in precipitation is higher in the western part than in the central to eastern part of the Alps, although the Alpine ice-sheet thickness is reduced more strongly in the east than in the west (Fig. 4.2c). In summer, changes of the Alpine ice sheet go along with a significant north-south precipitation pattern (Fig. 4.10b). Most of the significant precipitation changes are found in the central to eastern Alps, whereas only a small reduction in precipitation is evident in the western part. Thus, this modification in summer follows the west east gradient of the Alpine ice-sheet thickness reduction (Fig. 4.2c). Overall, both seasons demonstrate that locally heterogeneous changes in the topography significantly influence local precipitation patterns over the Alps.

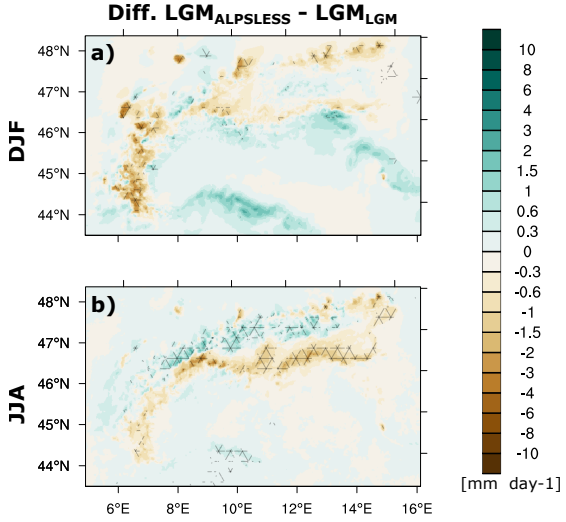

Figure 4.10: Differences in climatological mean values of daily precipitation intensity over the Alps between $\mathrm{LGM_{ALPSLESS}}$ and $\mathrm{LGM_{LGM}}$ for (a) winter (DJF) and (b) summer (JJA). Crosshatched areas indicate statistically significant differences at a significance level of 0.05 (using a two-tailed bootstrapping technique).

To further understand these precipitation changes, we investigate the vertical profiles at the two sites (Fig. 4.2) and the wind field at 700 hPa. The Skew–T diagrams of both sites and both seasons show no structural change in the temperature, moisture, and thus the stability of the atmosphere when comparing the $LGM_{ALPSLESS}$ with the LGM_{LGM} simulation (therefore not shown). This is somehow expected, since the two sites are located in areas where the Alpine ice sheet is not present. Nevertheless, we interpret this result that precipitation changes are restricted to the area where the ice sheet is changed, i.e., no downstream effects are found in the temperature and moisture profiles and thus in the stability. This is in contrast to wind, where some changes are evident at both sites. These changes are better illustrated in the wind field at 700 hPa (Fig. 4.11). In winter, the wind field of the $LGM_{ALPSLESS}$ experiment only changes significantly over the central to western Alps and in some areas south of the Alps (Fig. 4.11a). The $LGM_{ALPSLESS}$ winds are stronger and rotate clockwise compared to LGM_{LGM}. The rotation is associated with significant changes in V at the northern face of the Alps, in both wind components over the Alpine axis and in U in the south of the Alps (Fig. 4.11a). During summer, we overall observe a similar behaviour as in winter but with an eastward extension of the changes.

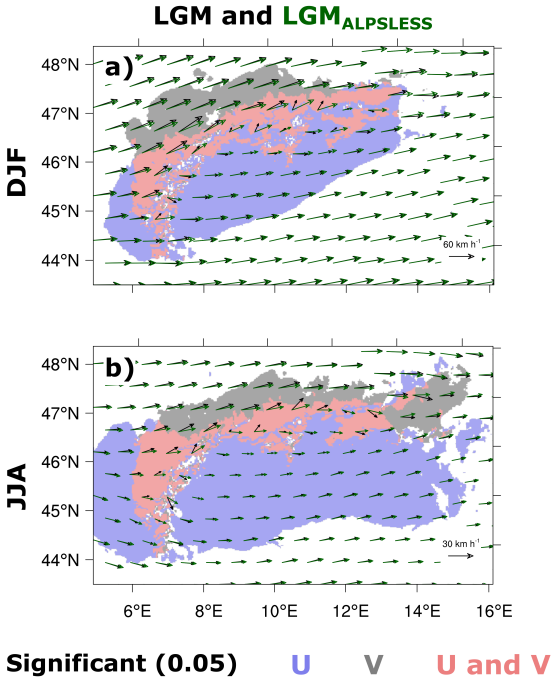

Figure 4.11: Climatological mean wind vectors over the Alps. (a) represents wind vectors for DJF, black and green vectors correspond to LGM_{LGM} and $LGM_{ALPSLESS}$, (b) as (a) but for JJA. Red shading indicates statistically significant differences in zonal (U) and meridional (V) wind components at a significance level of 0.05 (two-tailed bootstrapping technique), blue and grey shading as the red one but only in U and V wind components, respectively. Please note that the reference wind vectors differ for DJF and JJA.

In summary, precipitation changes in both seasons are associated with the fact that the wind field faces a lower orographic barrier due to a reduction of the Alpine ice sheet. This effect results in reduced (increased) precipitation at the northern face of the Alps in winter

(summer). Additionally, this leads to drying the south-western Alps in winter and the southern face of the Alps in summer.

4.5 Discussion and conclusions

In this study, we investigate the sensitivity of the glacial Alpine hydro-climate to northern hemispheric and local ice-sheet changes. To that end, we employ a GCM-RCM model chain to perform sensitivity simulations for two glacial periods, the LGM and MIS4. The LGM is compared to the PD and MIS4 climate simulation in order to characterise these glacial states. Then, we assess the impact of northern hemispheric ice-sheet thickness on the Alpine hydro-climate under MIS4 and LGM conditions. The second sensitivity test uses LGM conditions as base line and assesses the hydro-climatic response to changes in the Alpine ice sheet.

The LGM is known to be a period of generally drier and colder conditions than today (Otto-Bliesner et al., 2006). Earlier studies using the same LGM WRF simulation (e.g. Velasquez et al., 2020, 2021) showed that an application of the GCM-RCM model chain is beneficial with respect to temperature and precipitation over Europe compared to the driving GCM (Hofer et al., 2012a,b; Merz et al., 2013, 2014a,b, 2015, 2016) and other global model simulations (e.g. Kageyama et al., 2017, 2021), since the last ones underestimate the temperature amplitude between PD and LGM.

Here, we focus the analysis on the hydro-climate over the Alps. In winter, we find wetter conditions in the southern part of the Alps during LGM compared to PD (Frei and Schär, 1998; Schwarb et al., 2001). The northern part, however, is dryer under LGM conditions, which is expected due to the general colder conditions of the LGM (as the Clausius–Clapeyron equation suggests). This enhanced north-south precipitation gradient resembles finding of Becker et al. (2016) showing that such a gradient is a prerequisite to explain the extent of the Alpine glacier during the LGM. Even though LGM climate was colder with lower mixing ratios, our analysis shows that changes in the wind speed and direction substantially contribute to the north-south precipitation pattern. Winds are significantly stronger and anticlockwise rotated over the Alpine region during LGM suggesting an increase of intensity or frequency of the moisture advection from the south to the Alps. This is in line with proxy evidence (Florineth and Schlüchter, 2000; Luetscher et al., 2015). These authors similarly found a circulation change from dominant westerlies during PD to a more southern atmospheric circulation during the LGM. To explain these changes, global modelling studies suggested a southward shift of the North Atlantic storm track during the LGM compared to PD (e.g. Hofer et al., 2012a; Luetscher et al., 2015; Merz et al., 2015; Raible et al., 2020) and a change in the weather patterns (e.g. Hofer et al., 2012b; Ludwig et al., 2016; Wang et al., 2018). Thus, our analysis shows that changes in the atmospheric dynamics on the regional to local scale are also relevant to explain precipitation changes, in particular the moistening of the southern face of the Alps. During summer, we find drier conditions in most of the Alpine domain. This is expected, as

the LGM is generally colder than PD (Clausius–Clapeyron equation). Additionally, we find a strong reduction in convective activity, which can be traced back to a colder atmospheric state and an increase in stability during the LGM compared to PD.

The MIS4 climate shows enhanced winter precipitation compared to the LGM. The reason is that the MIS4 climate state is warmer (Hofer et al., 2012a,b; Merz et al., 2013, 2014a,b, 2015, 2016) and thus more moisture is available. Wind changes do not contribute to these wetter conditions as they become weaker and therefore reduce the moisture transport and orographically forced uplifts. Thus, we interpret the winter changes between MIS4 and LGM to be purely thermodynamically driven (Clausius–Clapeyron equation). In summer, $\mathrm{MIS4_{LGM}}$ shows slightly wetter conditions at the northern face and drier conditions at the southern side of the Alps during $\mathrm{MIS4_{LGM}}$. The wetter conditions are induced by an increase in the tropospheric vertical wind shear enhancing convection processes. The drier conditions at the southern face of the Alps are explained by slightly clockwise rotated winds, which enhance the Foehn effect. Thus, for summer also dynamical processes are relevant to explain the precipitation changes between MIS4 and LGM.

The northern hemispheric ice-sheet topography strongly influences the precipitation over the Alpine region. In both seasons, the precipitation patterns and the related thermodynamic and dynamic processes are similar to the ones found in the comparison between the LGM and PD. Namely, an increase of the northern hemispheric ice sheet leads to an intensification of glacial conditions over the Alps. Changes in the FIS do only weakly alter the precipitation patterns over the Alpine region. One potential reason of this weak precipitation response may also be the design of the Fennoscandian sensitivity experiment as the driving GCM has not experienced the changes of the FIS. However, we introduced rather strong changes in the RCM; thus, we expect only a minor impact of the experimental design on the conclusion that the FIS is less influential on the Alpine precipitation. We further conclude that changes in the Laurentide ice sheet needs to be considered in the estimation of Alpine precipitation. Moreover, the analysis shows that the northern hemispheric ice-sheet thickness is mainly responsible for the dynamical processes explaining the precipitation changes. This is suggested by the similarity of the processes found in the sensitivity experiments of northern hemispheric ice-sheet thickness and in the comparison between the LGM and PD.

In the assessment of the role of the Alpine ice-sheet topography, we found significant changes mainly over the area where the ice sheet was altered and south to this area, e.g. south to the Alps during summer. These changes are not as strong as the ones identified for changes in the northern hemispheric ice sheet or between LGM and PD. Nevertheless, they are responsible for a redistribution of precipitation over the Alps, e.g. a stronger reduction in the western part than in the central and eastern part during winter. These changes are relevant for glacier modelling (e.g. Jouvet et al., 2017; Seguinot et al., 2018). Thus, the analysis presented here suggests that future modelling efforts should ideally involve coupled glacier regional climate models. At the moment, this is not possible due to the long calculation time needed for glacier models and the high computational cost of RCMs. An intermediate step is to use the

output of different sensitivity simulations, as presented here, in ice-sheet modelling studies (e.g. Jouvet et al., 2017; Seguinot et al., 2018).

Moreover, future studies will benefit from even more detailed climate simulations over the Alpine region, particularly to better understand precipitation patterns in complex terrain. Both, the climate variables but also a better understanding of the ice-sheet dynamics would be beneficial for studies on the local and regional paleobotany (Kaplan et al., 2016), archaeology (Burke et al., 2017; Wren and Burke, 2019) and anthropology (e.g. Finlayson, 2004; Finlayson et al., 2006; Finlayson, 2008; Burke et al., 2014; Maier et al., 2016; Baena Preysler et al., 2019).

Acknowledgements

This work was supported by the Swiss National Science Foundation (SNF) within the project 'Modelling the ice flow in the western Alps during the last glacial cycle' (grant: 200021-162444). MM is supported by the SNF Early Postdoc Mobility programme (grant: P2BEP_181837). The simulations are performed on the super computing architecture of the Swiss National Supercomputing Centre (CSCS). Data is locally stored on the oschgerstore provided by the Oeschger Center for Climate Change Research (OCCR).

Bibliography

Abe-Ouchi, A., Saito, F., Kageyama, M., Braconnot, P., Harrison, S. P., Lambeck, K., Otto-Bliesner, B. L., Peltier, W. R., Tarasov, L., Peterschmitt, J.-Y., and Takahashi, K.: Ice-sheet configuration in the CMIP5/PMIP3 Last Glacial Maximum experiments, Geoscientific Model Development, 8, 3621–3637, doi:10.5194/gmd-8-3621-2015, 2015.

Angelis, H. D. and Kleman, J.: Palaeo-ice streams in the northern Keewatin sector of the Laurentide ice sheet, Annals of Glaciology, 42, 135–144, doi:10.3189/172756405781812925, 2005.

Annan, J. D. and Hargreaves, J. C.: A new global reconstruction of temperature changes at the Last Glacial Maximum, Climate of the Past, 9, 367–376, doi:10.5194/cp-9-367-2013, 2013.

AWC: The use of the Skew T, Log P diagram in analysis and forecasting. Manual 105-124, Tech. rep., Air Weather Service, Department of the Air Force, Illinois, USA, 1969.

AWC: The use of the Skew T, Log P diagram in analysis and forecasting. Technical report TR-79/006 (1979), revised, Tech. rep., Air Weather Service, Department of the Air Force, Illinois, USA, 1990.

Baena Preysler, J., Carrión Santafé, E., Torres Navas, C., and Vaquero Rodríguez, M.: Mousterian inside the upper Paleolithic? The last interval of El Esquilleu (Cantabria, Spain) sequence, Quaternary International, 508, 153–163, doi:10.1016/j.quaint.2018.11.015, 2019.

Ban, N., Schmidli, J., and Schär, C.: Evaluation of the convection-resolving regional climate modeling approach in decade-long simulations, Journal of Geophysical Research: Atmospheres, 119, 7889–7907, doi:10.1002/2014JD021478, 2014.

Bartlein, P. J., Harrison, S. P., Brewer, S., Connor, S., Davis, B. A. S., Gajewski, K., Guiot, J., Harrison-Prentice, T. I., Henderson, A., Peyron, O., Prentice, I. C., Scholze, M., Seppä, H., Shuman, B., Sugita, S., Thompson, R. S., Viau, A. E., Williams, J., and Wu, H.: Pollen-based continental climate reconstructions at 6 and 21 ka: a global synthesis, Climate Dynamics, 37, 775–802, doi:10.1007/s00382-010-0904-1, 2011.

Batchelor, C. L., Margold, M., Krapp, M., Murton, D. K., Dalton, A. S., Gibbard, P. L., Stokes, C. R., Murton, J. B., and Manica, A.: The configuration of Northern Hemisphere ice sheets through the Quaternary, Nature Communications, 10, 3713, doi:10.1038/s41467-019-11601-2, 2019.

Becker, P., Seguinot, J., Jouvet, G., and Funk, M.: Last Glacial Maximum precipitation pattern in the Alps inferred from glacier modelling, Geographica Helvetica, 71, 173–187, doi:10.5194/gh-71-173-2016, 2016.

Beghin, P., Charbit, S., Kageyama, M., Combourieu-Nebout, N., Hatté, C., Dumas, C., and Peterschmitt, J.-Y.: What drives LGM precipitation over the western Mediterranean? A study focused on the Iberian Peninsula and northern Morocco, Climate Dynamics, 46, 2611–2631, doi:10.1007/s00382-015-2720-0, 2016.

Braconnot, P., Harrison, S. P., Kageyama, M., Bartlein, P. J., Masson-Delmotte, V., Abe-Ouchi, A., Otto-Bliesner, B., and Zhao, Y.: Evaluation of climate models using palaeoclimatic data, Nature Climate Change, 2, 417–424, doi:10.1038/nclimate1456, 2012.

Burke, A., Levavasseur, G., James, P. M. A., Guiducci, D., Izquierdo, M. A., Bourgeon, L., Kageyama, M., Ramstein, G., and Vrac, M.: Exploring the impact of climate variability during the Last Glacial Maximum on the pattern of human occupation of Iberia, Journal of Human Evolution, 73, 35–46, doi:10.1016/j.jhevol.2014.06.003, 2014.

Burke, A., Kageyama, M., Latombe, G., Fasel, M., Vrac, M., Ramstein, G., and James, P. M. A.: Risky business: the impact of climate and climate variability on human population dynamics in Western Europe during the Last Glacial Maximum, Quaternary Science Reviews, 164, 217–229, doi:10.1016/j.quascirev.2017.04.001, 2017.

Chen, J., Dai, A., Zhang, Y., and Rasmussen, K. L.: Changes in convective available potential energy and convective inhibition under global warming, Journal of Climate, 33, 2025–2050, doi:10.1175/JCLI-D-19-0461.1, 2020.

Clark, P. U., Dyke, A. S., Shakun, J. D., Carlson, A. E., Clark, J., Wohlfarth, B., Mitrovica, J. X., Hostetler, S. W., and McCabe, A. M.: The Last Glacial Maximum, Science, 325, 710–714, doi:10.1126/science.1172873, 2009.

Cleator, S. F., Harrison, S. P., Nichols, N. K., Prentice, I. C., and Roulstone, I.: A new multivariable benchmark for Last Glacial Maximum climate simulations, Climate of the Past, 16, 699–712, doi:10.5194/cp-16-699-2020, 2020.

Cutler, K. B., Edwards, R. L., Taylor, F. W., Cheng, H., Adkins, J., Gallup, C. D., Cutler, P. M., Burr, G. S., and Bloom, A. L.: Rapid sea-level fall and deep-ocean temperature change since the last interglacial period, Earth and Planetary Science Letters, 206, 253–271, doi:10.1016/S0012-821X(02)01107-X, 2003.

da Silva, F. P., Rotunno Filho, O. C., Sampaio, R. J., Dragaud, I. C. D. V., de Araújo, A. A. M., Justi da Silva, M. G. A., and Pires, G. D.: Evaluation of atmospheric thermodynamics and dynamics during heavy-rainfall and no-rainfall events in the metropolitan area of Rio de Janeiro, Brazil, Meteorology and Atmospheric Physics, 131, 299–311, doi:10.1007/s00703-017-0570-5, 2019.

De Deckker, P., Arnold, L. J., van der Kaars, S., Bayon, G., Stuut, J.-B. W., Perner, K., Lopes dos Santos, R., Uemura, R., and Demuro, M.: Marine Isotope Stage 4 in Australasia: a full glacial culminating 65,000 years ago – global connections and implications for human dispersal, Quaternary Science Reviews, 204, 187–207, doi:10.1016/j.quascirev.2018.11.017, 2019.

de Vernal, A., Rosell-Melé, A., Kucera, M., Hillaire-Marcel, C., Eynaud, F., Weinelt, M., Dokken, T., and Kageyama, M.: Comparing proxies for the reconstruction of LGM sea-surface conditions in the northern North Atlantic, Quaternary Science Reviews, 25, 2820–2834, doi:10.1016/j.quascirev.2006.06.006, 2006.

Duarte, R. P. and Gomes, A. J.: Real-time simulation of cumulus clouds through SkewT/LogP diagrams, Computers and Graphics, 67, 103–114, doi:10.1016/j.cag.2017.06.005, 2017.

Eggleston, S., Schmitt, J., Bereiter, B., Schneider, R., and Fischer, H.: Evolution of the stable carbon isotope composition of atmospheric CO2 over the last glacial cycle, Paleoceanography, 31, 434–452, doi:10.1002/2015PA002874, 2016.

Ehlers, J., Gibbard, P., and Hughes, P.: Quaternary glaciations-extent and chronology: a closer look, vol. 15, Elsevier, Amsterdam, Netherlands, 2011.

Finlayson, C.: Neanderthals and modern humans: an ecological and evolutionary perspective, vol. 38, Cambridge University Press, 2004.

Finlayson, C.: On the importance of coastal areas in the survival of Neanderthal populations during the Late Pleistocene, Quaternary Science Reviews, 27, 2246–2252, doi:10.1016/j.quascirev.2008.08.033, 2008.

Finlayson, C., Giles Pacheco, F., Rodríguez-Vidal, J., Fa, D. A., María Gutierrez López, J., Santiago Pérez, A., Finlayson, G., Allue, E., Baena Preysler, J., Cáceres, I., Carrión, J. S., Fernández Jalvo, Y., Gleed-Owen, C. P., Jimenez Espejo, F. J., López, P., Antonio López Sáez, J., Antonio Riquelme Cantal, J., Sánchez Marco, A., Giles Guzman, F., Brown, K., Fuentes, N., Valarino, C. A., Villalpando, A., Stringer, C. B., Martinez Ruiz, F., and Sakamoto, T.: Late survival of Neanderthals at the southernmost extreme of Europe, Nature, 443, 850–853, doi:10.1038/nature05195, 2006.

Florineth, D. and Schlüchter, C.: Alpine evidence for atmospheric circulation patterns in Europe during the Last Glacial Maximum, Quaternary Research, 54, 295–308, doi:10.1006/qres.2000.2169, 2000.

Frei, C. and Schär, C.: A precipitation climatology of the Alps from high-resolution rain-gauge observations, International Journal of Climatology, 18, 873–900, doi:10.1002/(SICI)1097-0088(19980630)18:8⟨873::AID-JOC255⟩3.0.CO;2-9, 1998.

Ganopolski, A. and Brovkin, V.: Simulation of climate, ice sheets and CO_2 evolution during the last four glacial cycles with an Earth system model of intermediate complexity, Climate of the Past, 13, 1695–1716, doi:10.5194/cp-13-1695-2017, 2017.

Ganopolski, A. and Calov, R.: The role of orbital forcing, carbon dioxide and regolith in 100 kyr glacial cycles, Climate of the Past, 7, 1415–1425, doi:10.5194/cp-7-1415-2011, 2011.

Gent, P. R., Danabasoglu, G., Donner, L. J., Holland, M. M., Hunke, E. C., Jayne, S. R., Lawrence, D. M., Neale, R. B., Rasch, P. J., Vertenstein, M., Worley, P. H., Yang, Z.-L., and Zhang, M.: The community climate system model version 4, Journal of Climate, 24, 4973–4991, doi:10.1175/2011JCLI4083.1, 2011.

Gómez-Navarro, J. J., Raible, C. C., Bozhinova, D., Martius, O., García Valero, J. A., and Montávez, J. P.: A new region-aware bias-correction method for simulated precipitation in areas of complex orography, Geoscientific Model Development, 11, 2231–2247, doi:10.5194/gmd-11-2231-2018, 2018.

Gowan, E. J., Zhang, X., Khosravi, S., Rovere, A., Stocchi, P., Hughes, A. L. C., Gyllencreutz, R., Mangerud, J., Svendsen, J.-I., and Lohmann, G.: A new global ice sheet reconstruction for the past 80 000 years, Nature Communications, 12, 1199, doi:10.1038/s41467-021-21469-w, 2021.

Harrison, S. P., Bartlein, P. J., Izumi, K., Li, G., Annan, J., Hargreaves, J., Braconnot, P., and Kageyama, M.: Evaluation of CMIP5 palaeo-simulations to improve climate projections, Nature Climate Change, 5, 735–743, doi:10.1038/nclimate2649, 2015.

Harrison, S. P., Bartlein, P. J., and Prentice, I. C.: What have we learnt from palaeoclimate simulations?, Journal of Quaternary Science, 31, 363–385, doi:10.1002/jqs.2842, 2016.

Hofer, D., Raible, C. C., Dehnert, A., and Kuhlemann, J.: The impact of different glacial boundary conditions on atmospheric dynamics and precipitation in the North Atlantic region, Climate of the Past, 8, 935–949, doi:10.5194/cp-8-935-2012, 2012a.

Hofer, D., Raible, C. C., Merz, N., Dehnert, A., and Kuhlemann, J.: Simulated winter circulation types in the North Atlantic and European region for preindustrial and glacial conditions: glacial circulation types, Geophysical Research Letters, 39, L15 805, doi:10.1029/2012GL052296, 2012b.

Hughes, P. D., Gibbard, P. L., and Ehlers, J.: Timing of glaciation during the last glacial cycle: evaluating the concept of a global 'Last Glacial Maximum' (LGM), Earth-Science Reviews, 125, 171–198, doi:10.1016/j.earscirev.2013.07.003, 2013.

Jouvet, G., Seguinot, J., Ivy-Ochs, S., and Funk, M.: Modelling the diversion of erratic boulders by the Valais Glacier during the last glacial maximum, Journal of Glaciology, 63, 487–498, doi:10.1017/jog.2017.7, 2017.

Kageyama, M. and Valdes, P. J.: Impact of the North American ice-sheet orography on the Last Glacial Maximum eddies and snowfall, Geophysical Research Letters, 27, 1515–1518, doi:10.1029/1999GL011274, 2000.

Kageyama, M., Albani, S., Braconnot, P., Harrison, S. P., Hopcroft, P. O., Ivanovic, R. F., Lambert, F., Marti, O., Peltier, W. R., Peterschmitt, J.-Y., Roche, D. M., Tarasov, L., Zhang, X., Brady, E. C., Haywood, A. M., LeGrande, A. N., Lunt, D. J., Mahowald, N. M., Mikolajewicz, U., Nisancioglu, K. H., Otto-Bliesner, B. L., Renssen, H., Tomas, R. A., Zhang, Q., Abe-Ouchi, A., Bartlein, P. J., Cao, J., Li, Q., Lohmann, G., Ohgaito, R., Shi, X., Volodin, E., Yoshida, K., Zhang, X., and Zheng, W.: The PMIP4 contribution to CMIP6 – Part 4: Scientific objectives and experimental design of the PMIP4-CMIP6 Last Glacial

Maximum experiments and PMIP4 sensitivity experiments, Geoscientific Model Development, 10, 4035–4055, doi:10.5194/gmd-10-4035-2017, 2017.

Kageyama, M., Harrison, S. P., Kapsch, M.-L., Lofverstrom, M., Lora, J. M., Mikolajewicz, U., Sherriff-Tadano, S., Vadsaria, T., Abe-Ouchi, A., Bouttes, N., Chandan, D., Gregoire, L. J., Ivanovic, R. F., Izumi, K., LeGrande, A. N., Lhardy, F., Lohmann, G., Morozova, P. A., Ohgaito, R., Paul, A., Peltier, W. R., Poulsen, C. J., Quiquet, A., Roche, D. M., Shi, X., Tierney, J. E., Valdes, P. J., Volodin, E., and Zhu, J.: The PMIP4 Last Glacial Maximum experiments: preliminary results and comparison with the PMIP3 simulations, Climate of the Past, 17, 1065–1089, doi:10.5194/cp-17-1065-2021, publisher: Copernicus GmbH, 2021.

Kaplan, J. O., Pfeiffer, M., Kolen, J. C. A., and Davis, B. A. S.: Large scale anthropogenic reduction of forest cover in Last Glacial Maximum Europe, PLOS ONE, 11, e0166 726, doi:10.1371/journal.pone.0166726, 2016.

Kjellström, E., Brandefelt, J., Näslund, J.-O., Smith, B., Strandberg, G., Voelker, A. H. L., and Wohlfarth, B.: Simulated climate conditions in Europe during the Marine Isotope Stage 3 stadial, Boreas, 39, 436–456, doi:10.1111/j.1502-3885.2010.00143.x, 2010.

Krauß, L., Zens, J., Zeeden, C., Schulte, P., Eckmeier, E., and Lehmkuhl, F.: A multi-proxy analysis of two loess-paleosol sequences in the Northern Harz Foreland, Germany, Palaeogeography, Palaeoclimatology, Palaeoecology, 461, 401–417, doi:10.1016/j.palaeo.2016.09.001, 2016.

Lambeck, K., Rouby, H., Purcell, A., Sun, Y., and Sambridge, M.: Sea level and global ice volumes from the Last Glacial Maximum to the Holocene, Proceedings of the National Academy of Sciences, 111, 15 296–15 303, doi:10.1073/pnas.1411762111, 2014.

Lambert, F., Delmonte, B., Petit, J. R., Bigler, M., Kaufmann, P. R., Hutterli, M. A., Stocker, T. F., Ruth, U., Steffensen, J. P., and Maggi, V.: Dust-climate couplings over the past 800,000 years from the EPICA Dome C ice core, Nature, 452, 616–619, doi:10.1038/nature06763, 2008.

Latombe, G., Burke, A., Vrac, M., Levavasseur, G., Dumas, C., Kageyama, M., and Ramstein, G.: Comparison of spatial downscaling methods of general circulation model results to study climate variability during the Last Glacial Maximum, Geoscientific Model Development, 11, 2563–2579, doi:10.5194/gmd-11-2563-2018, 2018.

Leung, L. R., Mearns, L. O., Giorgi, F., and Wilby, R. L.: Regional climate research, Bulletin of the American Meteorological Society, 84, 89–95, doi:10.1175/BAMS-84-1-89, 2003.

Ludwig, P., Schaffernicht, E. J., Shao, Y., and Pinto, J. G.: Regional atmospheric circulation over Europe during the Last Glacial Maximum and its links to precipitation, Journal of Geophysical Research: Atmospheres, 121, 2130–2145, doi:10.1002/2015JD024444, 2016.

Ludwig, P., Pinto, J. G., Raible, C. C., and Shao, Y.: Impacts of surface boundary conditions on regional climate model simulations of European climate during the Last Glacial Maximum, Geophysical Research Letters, 44, 5086–5095, doi:10.1002/2017GL073622, 2017.

Ludwig, P., Gómez-Navarro, J. J., Pinto, J. G., Raible, C. C., Wagner, S., and Zorita, E.: Perspectives of regional paleoclimate modeling, Annals of the New York Academy of Sciences, 1436, 54–69, doi:10.1111/nyas.13865, 2019.

Luetscher, M., Boch, R., Sodemann, H., Spötl, C., Cheng, H., Edwards, R. L., Frisia, S., Hof, F., and Müller, W.: North Atlantic storm track changes during the Last Glacial Maximum recorded by Alpine speleothems, Nature Communications, 6, 6344, doi:10.1038/ncomms7344, number: 1 Publisher: Nature Publishing Group, 2015.

Maier, A., Lehmkuhl, F., Ludwig, P., Melles, M., Schmidt, I., Shao, Y., Zeeden, C., and Zimmermann, A.: Demographic estimates of hunter–gatherers during the Last Glacial Maximum in Europe against the background of palaeoenvironmental data, Quaternary International, 425, 49–61, doi:10.1016/j.quaint.2016.04.009, 2016.

Mayewski, P. A., Rohling, E. E., Stager, J. C., Karlén, W., Maasch, K. A., Meeker, L. D., Meyerson, E. A., Gasse, F., Kreveld, S. v., Holmgren, K., Lee-Thorp, J., Rosqvist, G., Rack, F., Staubwasser, M., Schneider, R. R., and Steig, E. J.: Holocene climate variability, Quaternary Research, 62, 243–255, doi:10.1016/j.yqres.2004.07.001, 2004.

Merz, N., Raible, C. C., Fischer, H., Varma, V., Prange, M., and Stocker, T. F.: Greenland accumulation and its connection to the large-scale atmospheric circulation in ERA-Interim and paleoclimate simulations, Climate of the Past, 9, 2433–2450, doi:10.5194/cp-9-2433-2013, 2013.

Merz, N., Born, A., Raible, C. C., Fischer, H., and Stocker, T. F.: Dependence of Eemian Greenland temperature reconstructions on the ice sheet topography, Climate of the Past, 10, 1221–1238, doi:10.5194/cp-10-1221-2014, 2014a.

Merz, N., Gfeller, G., Born, A., Raible, C. C., Stocker, T. F., and Fischer, H.: Influence of ice sheet topography on Greenland precipitation during the Eemian interglacial, Journal of Geophysical Research: Atmospheres, 119, 10,749–10,768, doi:10.1002/2014JD021940, 2014b.

Merz, N., Raible, C. C., and Woollings, T.: North Atlantic eddy-driven jet in interglacial and glacial winter climates, Journal of Climate, 28, 3977–3997, doi:10.1175/JCLI-D-14-00525.1, 2015.

Merz, N., Born, A., Raible, C. C., and Stocker, T. F.: Warm Greenland during the last interglacial: the role of regional changes in sea ice cover, Climate of the Past, 12, 2011–2031, doi:10.5194/cp-12-2011-2016, 2016.

Messmer, M., Gómez-Navarro, J. J., and Raible, C. C.: Climatology of Vb cyclones, physical mechanisms and their impact on extreme precipitation over Central Europe, Earth System Dynamics, 6, 541–553, doi:10.5194/esd-6-541-2015, 2015.

Messmer, M., Gómez-Navarro, J. J., and Raible, C. C.: Sensitivity experiments on the response of Vb cyclones to sea surface temperature and soil moisture changes, Earth System Dynamics, 8, 477–493, doi:10.5194/esd-8-477-2017, 2017.

Messmer, M., Raible, C. C., and Gómez-Navarro, J. J.: Impact of climate change on the climatology of Vb cyclones, Tellus A: Dynamic Meteorology and Oceanography, 72, 1–18, doi:10.1080/16000870.2020.1724021, 2020.

Mix, A. C., Bard, E., and Schneider, R.: Environmental processes of the ice age: land, oceans, glaciers (EPILOG), Quaternary Science Reviews, 20, 627–657, doi:10.1016/S0277-3791(00)00145-1, 2001.

Monegato, G., Scardia, G., Hajdas, I., Rizzini, F., and Piccin, A.: The Alpine LGM in the boreal ice-sheets game, Scientific Reports, 7, 2078, doi:10.1038/s41598-017-02148-7, 2017.

Morsy, M., Sayad, T., Khamees, A., and Ibrahim, M. M.: Stability study of severe weather event over Eastern Mediterranean, Al Azhar Bulletin of Science Vol. 9th, Conference, Tech. rep., Egypt, 2017.

Neale, R. B., Richter, J. H., Conley, A. J., Park, S., Lauritzen, P. H., Gettelman, A., Rasch, P. J., and Vavrus, J.: Description of the NCAR community atmosphere model (CAM4), National Center for Atmospheric Research Tech. Rep. NCAR/TN+ STR, URL http://www.cesm.ucar.edu/models/ccsm4.0/cam/docs/description/cam4_desc.pdf, 2010.

Newnham, R. M., Alloway, B. V., Holt, K. A., Butler, K., Rees, A. B. H., Wilmshurst, J. M., Dunbar, G., and Hajdas, I.: Last Glacial pollen–climate reconstructions from Northland, New Zealand, Journal of Quaternary Science, 32, 685–703, doi:10.1002/jqs.2955, 2017.

NOAA: Skew-T parameters and indices, National Weather Service, National Oceanic and Atmospheric Administration (NOAA), US Department of Commerce, URL https://www.weather.gov/source/zhu/ZHU_Training_Page/convective_parameters/skewt/skewtinfo.html, 2021.

Oleson, W., Lawrence, M., Bonan, B., Flanner, G., Kluzek, E., Lawrence, J., Levis, S., Swenson, C., Thornton, E., Dai, A., Decker, M., Dickinson, R., Feddema, J., Heald, L., Hoffman, F., Lamarque, J.-F., Mahowald, N., Niu, G.-Y., Qian, T., Randerson, J., Running, S., Sakaguchi, K., Slater, A., Stockli, R., Wang, A., Yang, Z.-L., Zeng, X., and Zeng, X.: Technical description of version 4.0 of the community land model (CLM), NCAR Technical Note NCAR/TN-478+STR, National Center for Atmospheric Research, Boulder, CO, Boulder, CO, URL http://www.cesm.ucar.edu/models/cesm1.0/clm/CLM4_Tech_Note.pdf, 2010.

Otto-Bliesner, B. L., Brady, E. C., Clauzet, G., Tomas, R., Levis, S., and Kothavala, Z.: Last Glacial Maximum and Holocene climate in CCSM3, Journal of Climate, 19, 2526–2544, doi:10.1175/JCLI3748.1, 2006.

Pausata, F. S. R., Li, C., Wettstein, J., Kageyama, M., and Nisancioglu, K. H.: The key role of topography in altering North Atlantic atmospheric circulation during the last glacial period, Climate of the Past, doi:10.5194/cp-7-1089-2011, 2011.

Peltier, W.: Global glacial isostasy and the surface of the ice-age Earth: the ICE-5G (VM2) model and grace, Annual Review of Earth and Planetary Sciences, 32, 111–149, doi:10.1146/annurev.earth.32.082503.144359, 2004.

Peltier, W. R.: Ice age paleotopography, Science, 265, 195–201, doi:10.1126/science.265.5169.195, 1994.

Peltier, W. R.: Postglacial variations in the level of the sea: Implications for climate dynamics and solid-Earth geophysics, Reviews of Geophysics, 36, 603–689, doi:10.1029/98RG02638, 1998.

Peltier, W. R., Argus, D. F., and Drummond, R.: Space geodesy constrains ice age terminal deglaciation: the global ICE-6G_C (VM5a) model, Journal of Geophysical Research: Solid Earth, 120, 450–487, doi:10.1002/2014JB011176, 2015.

Pinto, J. G. and Ludwig, P.: Extratropical cyclones over the North Atlantic and western Europe during the Last Glacial Maximum and implications for proxy interpretation, Climate of the Past, 16, 611–626, doi:10.5194/cp-16-611-2020, 2020.

Prentice, I. C. and Jolly, D.: Mid-Holocene and glacial-maximum vegetation geography of the northern continents and Africa, Journal of Biogeography, 27, 507–519, doi:10.1046/j.1365-2699.2000.00425.x, 2000.

Raible, C. C., Pinto, J. G., Ludwig, P., and Messmer, M.: A review of past changes in extratropical cyclones in the northern hemisphere and what can be learned for the future, Wiley Interdisciplinary Reviews: Climate Change, 12, e680, doi:10.1002/wcc.680, 2020.

Rivière, G., Laîné, A., Lapeyre, G., Salas-Mélia, D., and Kageyama, M.: Links between Rossby wave breaking and the North Atlantic Oscillation–Arctic Oscillation in present-day and Last Glacial Maximum climate simulations, Journal of Climate, 23, 2987–3008, doi:10.1175/2010JCLI3372.1, 2010.

Römer, W., Lehmkuhl, F., and Sirocko, F.: Late Pleistocene aeolian dust provenances and wind direction changes reconstructed by heavy mineral analysis of the sediments of the Dehner dry maar (Eifel, Germany), Global and Planetary Change, 147, 25–39, doi:10.1016/j.gloplacha.2016.10.012, 2016.

Rummukainen, M.: Added value in regional climate modeling, WIREs Climate Change, 7, 145–159, doi:10.1002/wcc.378, 2016.

Schwarb, M., Daly, C., Frei, C., and Schär, C.: Mean annual and seasonal precipitation in the European Alps 1971–1990, Hydrological Atlas of Switzerland, Landeshydrologie und Geologie, Bern, Switzerland, 2001.

Seguinot, J., Ivy-Ochs, S., Jouvet, G., Huss, M., Funk, M., and Preusser, F.: Modelling last glacial cycle ice dynamics in the Alps, The Cryosphere, 12, 3265–3285, doi:10.5194/tc-12-3265-2018, 2018.

Siddall, M., Rohling, E. J., Thompson, W. G., and Waelbroeck, C.: Marine isotope stage 3 sea level fluctuations: data synthesis and new outlook, Reviews of Geophysics, 46, doi:10.1029/2007RG000226, 2008.

Siddall, M., Kaplan, M. R., Schaefer, J. M., Putnam, A., Kelly, M. A., and Goehring, B.: Changing influence of Antarctic and Greenlandic temperature records on sea-level over the last glacial cycle, Quaternary Science Reviews, 29, 410–423, doi:10.1016/j.quascirev.2009.11.007, 2010.

Skamarock, W. C. and Klemp, J. B.: A time-split nonhydrostatic atmospheric model for weather research and forecasting applications, Journal of Computational Physics, 227, 3465–3485, doi:10.1016/j.jcp.2007.01.037, 2008.

Skamarock, W. C., Klemp, J. B., Dudhia, J., Gill, O., Barker, D., Duda, G., Huang, X.-y., Wang, W., and Powers, G.: A description of the advanced research WRF version 3, doi:10.5065/D68S4MVH, 2008.

Stocker, T. F. and Johnsen, S. J.: A minimum thermodynamic model for the bipolar seesaw, Paleoceanography, 18, doi:10.1029/2003PA000920, 2003.

Strandberg, G., Brandefelt, J., Kjellstro M., E., and Smith, B.: High-resolution regional simulation of Last Glacial Maximum climate in Europe, Tellus A: Dynamic Meteorology and Oceanography, 63, 107–125, doi:10.1111/j.1600-0870.2010.00485.x, 2011.

Su, F., Duan, X., Chen, D., Hao, Z., and Cuo, L.: Evaluation of the global climate models in the CMIP5 over the Tibetan Plateau, Journal of Climate, 26, 3187–3208, doi:10.1175/JCLI-D-12-00321.1, 2012.

Tarasov, L., Dyke, A. S., Neal, R. M., and Peltier, W. R.: A data-calibrated distribution of deglacial chronologies for the North American ice complex from glaciological modeling, Earth and Planetary Science Letters, 315-316, 30–40, doi:10.1016/j.epsl.2011.09.010, 2012.

Ullman, D. J., LeGrande, A. N., Carlson, A. E., Anslow, F. S., and Licciardi, J. M.: Assessing the impact of Laurentide Ice Sheet topography on glacial climate, Climate of the Past, 10, 487–507, doi:10.5194/cp-10-487-2014, 2014.

Van Meerbeeck, C. J., Renssen, H., and Roche, D. M.: How did Marine Isotope Stage 3 and Last Glacial Maximum climates differ? – Perspectives from equilibrium simulations, Climate of the Past, 5, 33–51, doi:10.5194/cp-5-33-2009, 2009.

Velasquez, P., Messmer, M., and Raible, C. C.: A new bias-correction method for precipitation over complex terrain suitable for different climate states: a case study using WRF (version 3.8.1), Geoscientific Model Development, 13, 5007–5027, doi:10.5194/gmd-13-5007-2020, 2020.

Velasquez, P., Kaplan, J. O., Messmer, M., Ludwig, P., and Raible, C. C.: The role of land cover in the climate of glacial Europe, Climate of the Past, 17, 1161–1180, doi:10.5194/cp-17-1161-2021, 2021.

Wallace, J. M. and Hobbs, P. V.: Atmospheric science: an introductory survey, vol. 92, Elsevier, 2006.

Wang, N., Jiang, D., and Lang, X.: Northern westerlies during the Last Glacial Maximum: Results from CMIP5 simulations, Journal of Climate, 31, 1135–1153, doi:10.1175/JCLI-D-17-0314.1, 2018.

Wilks, D. S.: Statistical methods in the atmospheric sciences, Academic Press, Burlington, MA and San Diego, California, USA, and London, UK, google-Books-ID: IJuCVtQ0ySIC, 2011.

Wren, C. D. and Burke, A.: Habitat suitability and the genetic structure of human populations during the Last Glacial Maximum (LGM) in Western Europe, PLOS ONE, 14, e0217 996, doi:10.1371/journal.pone.0217996, 2019.

Wu, H., Guiot, J., Brewer, S., and Guo, Z.: Climatic changes in Eurasia and Africa at the last glacial maximum and mid-Holocene: reconstruction from pollen data using inverse vegetation modelling, Climate Dynamics, 29, 211–229, doi:10.1007/s00382-007-0231-3, 2007.

Yokoyama, Y., Lambeck, K., De Deckker, P., Johnston, P., and Fifield, L. K.: Timing of the Last Glacial Maximum from observed sea-level minima, Nature, 406, 713–716, doi:10.1038/35021035, 2000.

Chapter 5

A New Bias-Correction Method for Precipitation over Complex Terrain Suitable for Different Climate States: A Case Study Using WRF (version 3.8.1)

P. Velasquez, M. Messmer and C. C. Raible.

Published in *Geoscientific Model Development*, Volume 13, pp. 5007–5027, 2020.

https://doi.org/10.5194/gmd-13-5007-2020.

Geosci. Model Dev., 13, 5007–5027, 2020
https://doi.org/10.5194/gmd-13-5007-2020

Geoscientific Model Development
Open Access
EGU

A new bias-correction method for precipitation over complex terrain suitable for different climate states: a case study using WRF (version 3.8.1)

Patricio Velasquez[1,2], **Martina Messmer**[1,2,3], **and Christoph C. Raible**[1,2]

[1]Climate and Environmental Physics Institute, University of Bern, Bern, Switzerland
[2]Oeschger Centre for Climate Change Research, University of Bern, Bern, Switzerland
[3]School of Earth Sciences, University of Melbourne, Melbourne, Victoria, Australia

Correspondence: Patricio Velasquez (patricio.velasquez@climate.unibe.ch)

Received: 10 May 2019 – Discussion started: 1 July 2019
Revised: 12 August 2020 – Accepted: 24 August 2020 – Published: 26 October 2020

Abstract. This work presents a new bias-correction method for precipitation over complex terrain that explicitly considers orographic characteristics. This consideration offers a good alternative to the standard empirical quantile mapping (EQM) method during colder climate states in which the orography strongly deviates from the present-day state, e.g. during glacial conditions such as the Last Glacial Maximum (LGM). Such a method is needed in the event that absolute precipitation fields are used, e.g. as input for glacier modelling or to assess potential human occupation and according migration routes in past climate states. The new bias correction and its performance are presented for Switzerland using regional climate model simulations at 2 km resolution driven by global climate model outputs obtained under perpetual 1990 and LGM conditions. Comparing the present-day regional climate model simulation with observations, we find a strong seasonality and, especially during colder months, a height dependence of the bias in precipitation. Thus, we suggest a three-step correction method consisting of (i) a separation into different orographic characteristics, (ii) correction of very low intensity precipitation, and (iii) the application of an EQM, which is applied to each month separately. We find that separating the orography into 400 m height intervals provides the overall most reasonable correction of the biases in precipitation. The new method is able to fully correct the seasonal precipitation bias induced by the global climate model. At the same time, some regional biases remain, in particular positive biases over high elevated areas in winter and negative biases in deep valleys and Ticino in winter and summer. A rigorous temporal and spatial cross-validation with independent data exhibits robust results. The new bias-correction method certainly leaves some drawbacks under present-day conditions. However, the application to the LGM demonstrates that it is a more appropriate correction compared to the standard EQM under highly different climate conditions as the latter imprints present-day orographic features into the LGM climate.

1 Introduction

The hydrological cycle is an important component in the Earth's climate system because of its capability to transport and redistribute mass and energy around the world. Changes in the hydrological cycle can lead to droughts or floods and thus impact the ecosystem services. Moreover, it plays an important role in shaping the Earth's climate history (Mayewski et al., 2004). The latter is because the hydrological cycle shows a strong response to different external forcing functions and to changes in atmospheric compositions (Ganopolski and Calov, 2011; Stocker et al., 2013). Namely, hydrology and water resources are strongly influenced by changes in precipitation patterns (Stocker et al., 2013; Raible et al., 2016).

Cold periods, i.e. glacial periods, offer a unique testbed to better understand how the hydrological cycle responds to climate conditions highly different compared to today's climate. The Last Glacial Maximum (LGM) is the most recent

glacial period and dates back to around 21 ka (Yokoyama et al., 2000; Clark et al., 2009). The LGM is characterised by large ice sheets in the Northern Hemisphere, a global mean temperature roughly 5 to 6.5 °C colder than today (Otto-Bliesner et al., 2006), and a global sea level of 115 to 130 m below the present-day one (Lambeck et al., 2014; Peltier and Fairbanks, 2006). Proxy records for Europe show that the climate was 10 to 14 °C colder and around 200 mm yr^{-1} drier during the LGM compared to recent climate conditions (Wu et al., 2007; Bartlein et al., 2011). These climatic conditions have strong implications not only for nature but also for humans. For instance, Burke et al. (2017) and Wren and Burke (2019) demonstrated the importance of climate conditions and its variability as drivers of human behaviour during the LGM, e.g. the spatial distribution of populations and influence on the cultural and biological evolution (Kaplan et al., 2016). Important modelling tools, e.g. global atmospheric climate models and hydrological models, have been used to describe the Earth's system in the LGM. Compared to the sparse and local climate information from the proxies, these tools provide physically consistent and spatially gridded three-dimensional information on various meteorological variables. Thus, they offer valuable information to improve the understanding of the responses and feedbacks to internal and external forcing on timescales longer than some centuries (e.g. Xu, 2000; Andréasson et al., 2004; Xu et al., 2005; Fowler et al., 2007a; Yang et al., 2010; Chen et al., 2012). Global climate models are generally in line with the proxy evidence and depict a European climate that was largely colder and drier than today. However, they underestimate the amplitudes of the changes compared to proxy evidence and poorly represent areas with complex terrain (e.g. Hofer et al., 2012a; Ludwig et al., 2016).

The modelling tools also show other uncertainties, in particular in the hydrological cycle, as not all relevant processes are explicitly simulated by the models (e.g. Ban et al., 2014; Giorgi et al., 2016). This is especially true for global models, which have a comparably coarse spatial resolution. Hence, most processes governing regional- to local-scale precipitation are not resolved and need to be parameterised (Leung et al., 2003; Su et al., 2012), resulting in a strong parameter dependence when simulating regional-scale precipitation (Rougier et al., 2009). To overcome some of the uncertainties, regional climate models (RCMs) are used to dynamically downscale global climate models. Many RCM simulations are carried out within the framework of the Coordinated Regional Downscaling Experiment (CORDEX), which defines one of the premier goals to better understand relevant phenomena at finer scales (Moss et al., 2010). Even though regional climate models can solve atmospheric equations on a much finer scale than global models, the simulated precipitation patterns still show large biases for present-day climate when comparing them to observations. This has, for example, been illustrated by the CORDEX simulations analysed by Casanueva et al. (2016) and Rajczak and Schär (2017). Not only are these biases produced by initial and boundary conditions provided by global climate models (GCMs), but they are also related to regions characterised by complex topography and to processes that correspond to a finer scale, such as cloud microphysical processes. These processes need to be parameterised as they cannot be explicitly resolved because of the RCM resolution used in CORDEX (Boer, 1993; Zhang and McFarlane, 1995; Fu, 1996; Haslinger et al., 2013; Yang et al., 2013; Warrach-Sagi et al., 2013; Maraun and Widmann, 2015; Hui et al., 2016). To overcome these shortcomings, RCMs need to be run at a resolution where they can explicitly resolve some of the relevant processes, such as convection (e.g. Giorgi et al., 2016; Messmer et al., 2017). Even though the convection-resolving RCMs can describe precipitation much more precisely, biases are still evident (e.g. Ban et al., 2014; Gómez-Navarro et al., 2018). These inconsistencies and uncertainties may, for example, impact the results obtained through hydrological and glacier modelling that follow next in the modelling chain (Allen and Ingram, 2002; Seguinot et al., 2014; Felder et al., 2018).

Some climate change studies try to correct parts of these errors in precipitation patterns and intensities by so-called bias-correction methods (Maraun et al., 2010). These bias-correction methods are needed in the event that absolute values matter, e.g. for the forcing of impact models like glaciers or ice sheets (Jouvet et al., 2017; Jouvet and Huss, 2019), when temperature thresholds are important as limiting factor, e.g. for vegetation coverage, freezing of water, snowfall vs. rainfall, or when precipitation thresholds are essential (Liu et al., 2006; Zhao et al., 2017; Liu et al., 2018; Chen et al., 2019; Wang et al., 2020). So far, several correction methods have been suggested in the literature, e.g. linear scaling, local intensity scaling, or power transformation (e.g. Berg et al., 2012; Fang et al., 2015; Lafon et al., 2013). An overview of different methods and their limitations is given in Maraun (2016) and Maraun and Widmann (2018b). Another important bias-correction method is the empirical quantile mapping (EQM), which is known as one of the best techniques to correct precipitation biases in the present-day climate (e.g. Lafon et al., 2013; Teutschbein and Seibert, 2012, 2013; Teng et al., 2015). If the method is applied to a climate state different from the present one, all these methods suffer basically from the assumption of stationarity in the biases, since they are trained with a climate that does not correspond to the simulated climate that is afterwards bias corrected. Statistical relationships between observations and model output are used to estimate transfer functions in the observed period and are then applied to different climate states, e.g. past and future climate change scenarios. These statistical relationships and the bias structure can be altered by changes in the precipitation processes in the different climate states. Focusing on the LGM climate, an important process is related to changes in the albedo due to differences in vegetation and land cover (Kaplan et al., 2016; Velasquez et al., 2020). Also, changes in near-surface condensation processes may play an important

role, i.e. freezing of near-surface moisture over areas covered by ice. These processes can influence the temperature and moisture profiles and thus also precipitation processes. Other important processes are linked to modifications in the general atmospheric circulation and in the water availability (Hofer et al., 2012b; Kageyama et al., 2020; Pinto and Ludwig, 2020). This can also regulate the water transport and thus also the precipitation patterns.

Hence, these changes amongst others may violate the stationarity assumption of bias-correction methods. Besides the assumption of stationarity of the transfer functions, these correction methods only implicitly consider orographic features that strongly affect precipitation and its biases (e.g. Piani et al., 2010b; Amengual et al., 2011; Berg et al., 2012; Chen et al., 2013; Cannon et al., 2015; Fang et al., 2015). Note that this implicit consideration relies on the orography where the method is trained. Hence, the applicability of bias corrections may not be justified to different climate states where the topography strongly changes, such as in the LGM.

This calls for a flexible method that can ameliorate the assumption of stationarity in the biases when correcting precipitation errors. One possibility is to apply a cluster analysis to precipitation and its biases to identify classes with similar bias behaviour. An example for Switzerland of such an approach is presented by Gómez-Navarro et al. (2018). The drawback of such an approach for our purpose is that the cluster analysis still relies on the characteristics and circulation of the current climate. To be as independent from current climates as possible and to provide a correction that includes important characteristics of the Alpine climate, we came up with "static" characteristics, i.e. topography height and slope orientation, and the assumption that relationships to these static characteristics remain unchanged in different climate states. Thus, our work aims at presenting a new bias-correction method that fills this gap by using orographic features as variables for the correction. Such a correction avoids the explicit usage of current atmospheric circulation and provides a new alternative to the standard EQM for areas with complex topography during highly different climate states, i.e. glacial times.

The new method is based on EQM (Lafon et al., 2013; Teutschbein and Seibert, 2012, 2013; Teng et al., 2015) explicitly combined with orographic characteristics and attempts to correct wet or dry biases that are introduced by parameterisations and numerical formulations in global, regional, or a combination of both models. Such biases include especially those that are associated with orographic effects, namely, vertical motion leading to precipitation. Observations or proxy reconstructions are limited over the Alps during glacial times. Thus, the method is directly evaluated under present-day climate conditions and its performance compared to the standard EQM is assessed in an LGM climate simulation. The data to be corrected stem from climate simulation performed with the high-resolution Weather Research and Forecasting (WRF) RCM (Skamarock and Klemp, 2008) driven by simulations under perpetual climate conditions using the Community Climate System Model version 4 (CCSM4; Gent et al., 2011). To estimate the transfer functions of the EQM we use two observation data sets separately: one for Switzerland (MeteoSwiss, 2013) and one for the Alpine region (Isotta et al., 2014). The focus of the presented study is on the method itself and its evaluation. The latter consists of assessing the performance over the Alps, the temporal and spatial transferability, and the comparison of the new method and standard EQM method (Lafon et al., 2013) under LGM conditions.

The paper is structured as follows. Section 2 describes the models and data sets used to construct the method. Section 3 presents the new bias-correction method. Section 4 evaluates the new method. Finally, a summary and conclusive remarks are given in Sect. 5.

2 Models and data

We use a present-day and an LGM simulation to create and evaluate the new bias correction. Thereby, we employ a model chain that consists of a global climate model and a regional climate model, where the global climate model provides the boundary conditions for the regional climate model.

The global climate model is the Community Climate System Model (version 4; CCSM4; Gent et al., 2011). The model's atmospheric component is calculated by the Community Atmosphere Model version 4 (CAM4; Neale et al., 2010) and the land component by the Community Land Model version 4 (CLM4; Oleson et al., 2010). Only two components, the so-called data models, are used for the ocean and sea ice; i.e. the atmospheric component is forced by time-varying sea surface temperatures and sea ice cover obtained from a coarser-resolved fully coupled 1990 AD and LGM simulation with CCSM3, respectively (Hofer et al., 2012a). The atmosphere land-only model was run with a horizontal resolution of $1.25° \times 0.9°$ (longitude $\times$ latitude) and with 26 vertical hybrid sigma-pressure levels. Two global climate simulations are performed each covering 31 years: (i) under perpetual 1990 AD and (ii) under LGM conditions, respectively. The orbital forcing and atmospheric composition are adjusted to the respective period (Table 1). The temporal resolution of the output is 6-hourly. More detailed information on these simulations and their settings is presented in Hofer et al. (2012a, b) and Merz et al. (2013); Merz et al. (2014a, b); Merz et al. (2015).

To investigate the climate over central Europe and in particular over Switzerland in more detail, an RCM is used for the dynamical downscaling. Note that Switzerland is only covered by 12 grid points and the Alps are represented with a maximum height of approximately 1400 m a.s.l. in CCSM4. We use WRF model version 3.8.1 for the dynamical downscaling (Skamarock and Klemp, 2008). The model is set up with four two-way nested domains with a nest ratio of 1 : 3.

Table 1. External forcing used in Hofer et al. (2012a, b) for 1990 AD and LGM conditions.

Parameter name	1990 AD	LGM
TSI ($W\,m^{-2}$)	1361.77	1360.89
Eccentricity (10^{-2})	1.6708	1.8994
Obliquity (°)	23.441	22.949
Angular precession (°)	102.72	114.43
CO_2 (ppm)	353.9	185
CH_4 (ppb)	1693.6	350
N_2O (ppb)	310.1	200

The domains have horizontal resolutions of 56, 18, 6, and 2 km, respectively, and 40 vertical eta levels. The outermost domain includes an extended westward and northward area that takes the Alpine region as the midpoint (Fig. 1). Moreover, the innermost domain focuses on the Alpine region. The fine resolution of 2 km over this area is important as it covers a highly complex terrain. The resolution in the two innermost domains permits the explicit resolution of convective processes. Thus, no parameterisation for convection is used in these two domains and precipitation is described by microphysical processes (Table 2). Convection-permitting model resolutions are in general preferred as many recent studies show better performance in simulating precipitation (e.g. Ban et al., 2014; Prein et al., 2015; Kendon et al., 2017; Berthou et al., 2018; Finney et al., 2019). However, we shall keep in mind that some biases in temperature and cloud formation may be produced by this setup, which may lead to additional biases in precipitation as shown in Ban et al. (2014). Table 2 lists the relevant parameterisation schemes chosen to run WRF with.

WRF is driven by, but not nudged to, the corresponding global simulation and is run for 30 years using perpetual 1990 AD and LGM conditions, respectively (Table 1). For the LGM simulation, the surface conditions need some further adjustments. These include the lowering of the sea level and extended ice sheets as specified in the PMIP3 protocol (Fig. 3; for more details, see Ludwig et al., 2017). The glaciation over the Alpine region (obtained from Seguinot et al., 2018) and other glaciated areas (e.g. Pyrenees, from Ehlers et al., 2011) are modified according to LGM conditions (Fig. 3b). Additionally, the land cover and land use are altered to comply with LGM conditions, as described in Velasquez et al. (2020). Each 30-year simulation is split up into 10 individual 3-year simulations and carried out with adaptive time step in order to increase the throughput on the available computer facilities. For each of the 3-year simulations, a 2-month spin-up time is considered to account for the longer equilibrium times of the land surface scheme of WRF. Tests show that the WRF land scheme reaches a quasi-equilibrium after approximately 15 d.

Two gridded observational data sets for daily precipitation are used: RhiresD (MeteoSwiss, 2013) and the Alpine Precipitation Grid Dataset (APGD; Isotta et al., 2014). Both data sets cover more than 35 years. In this study, we use only the 30-year period (1979–2008). Note that we carry out a bilinear interpolation using the Climate Data Operators (CDO; Schulzweida, 2019) to convert both observational data sets into the corresponding grid of WRF. The RhiresD has a spatial resolution of approximately 2×2 km and covers only Switzerland (MeteoSwiss, 2013). This data set is based on rain gauge measurements distributed across Switzerland (for more details, see Isotta et al., 2014; Güttler et al., 2015). These point measurements are spatially interpolated to obtain a gridded data set, which is described in more detail in Frei and Schär (1998), Shepard (1984) and Schwarb et al. (2001). The APGD encompasses the entire Alpine region with a spatial resolution of 5×5 km (Isotta et al., 2014). It was developed in the framework of EURO4M (European Reanalysis and Observations for Monitoring) by using a distance-angular weighting scheme that integrates climatological precipitation using the local orography and the rain gauge measurements (Isotta et al., 2014). For our analysis, the Alpine areas of Italy and Slovenia are excluded from APGD because of their poor station density covering the period 1979–2008 compared to RhiresD, especially over complex topography and at high altitudes. Note that all data sets consider daily precipitation as total precipitation, i.e. both solid and liquid precipitation, and convective and non-convective precipitation. Moreover, days without precipitation are treated as censored values, i.e. not considered in the analysis, when daily precipitation is equal to 0 mm, although in the case of observations this is equivalent to $0.1\,mm\,d^{-1}$ due to gauge precision.

The observational gridded data sets provide valuable insights. However, they also contain some discrepancies and uncertainties due to interpolation and extrapolation methods; e.g. high precipitation intensities are systematically underestimated and low intensities overestimated, especially in areas where observations are not available, i.e. on high elevated areas, such as mountain peaks. The magnitude of these errors depends on the season and the altitude. In regions above 1500 m a.s.l., the error can be higher than 30 % because of a "gauge undercatch" induced by strong winds and the applied interpolation method carried out with a distance-angular weighting scheme (Frei and Schär, 1998; Nešpor and Sevruk, 1999; Auer et al., 2001; Ungersböck et al., 2001; Schmidli et al., 2002; Frei et al., 2003; MeteoSwiss, 2013; Isotta et al., 2014). Note that the limitations of the observational data sets are not included in the analysis of this study; i.e. we consider the observational gridded data sets as truth. Nevertheless, one shall keep the limitations of the observational data in mind, in particular when discussing the remaining biases in areas and seasons where the observational data sets also have problems.

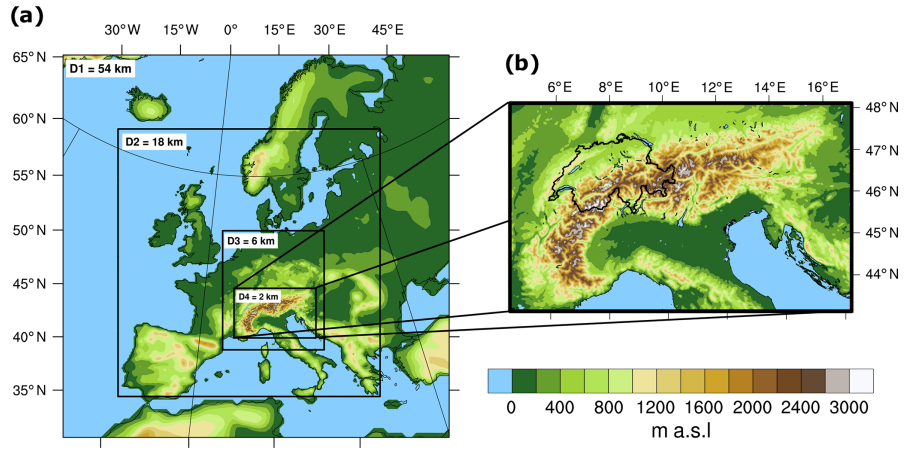

Figure 1. WRF domains and present-day topography. Panel **(a)** illustrates the present-day topography and the four domains used by WRF. Panel **(b)** shows the fourth domain including the area of interest (Switzerland) outlined by a black line.

Table 2. Important parameterisations used to run WRF.

Parameterisation	Parameter name	Chosen parameterisation	Applied to
Microphysics	mp_physics	WRF single-moment six-class scheme	Domains 1–4
Longwave radiation	ra_lw_physics	RRTM scheme	Domains 1–4
Shortwave radiation	ra_sw_physics	Dudhia scheme	Domains 1–4
Surface layer	sf_sfclay_physics	MM5 similarity	Domains 1–4
Land–water surface	sf_surface_physics	Noah – multi-parameterisation land surface model	Domains 1–4
Planetary boundary layer	bl_pbl_physics	Yonsei University scheme	Domains 1–4
Cumulus	cu_physics	Kain–Fritsch scheme	Domains 1–2
		No parameterisation	Domains 3–4

3 Bias correction

The correction method, developed in this study, consists of three steps: (i) separation with respect to different orographic characteristics, (ii) adjustment of daily precipitation with very low intensity, and (iii) application of the EQM. Each of these three steps is described in more detail in the following paragraphs.

In a first step, three orographic characteristics are used to separate the region of interest into several groups. These characteristics are height, slope orientations, and a combination of both. The height ranges from approximately 200 m a.s.l. to a maximal value of 3800 m a.s.l. over the area of interest. Thus, the groups are selected by height intervals, which cover the range from 400 to 3200 m a.s.l. Two height intervals are tested separately: 100 and 400 m (e.g. height intervals of 400 m are shown in Fig. 2). The heights below 400 and above 3200 m a.s.l. are considered as two additional height intervals. The second characteristic, used to group the region of interest, is four slope orientations: north ($315° \leq$ slope orientation $< 45°$), east ($45° \leq$ slope orientation $< 135°$), south ($135° \leq$ slope orientation $< 225°$) and west ($225° \leq$ slope orientations $< 315°$). Note that this characteristic is obtained by summing the two slope vectors that are directly provided by the RCM. Combining both characteristics, the groups are selected by height intervals and then separated into subgroups by the slope orientations.

In a second step, we correct the daily simulated precipitation with very low intensity in each group (or subgroup) and each month of the year separately. The reason for this is that the frequency of precipitation with very low intensity is often strongly overestimated due to the drizzle effect produced by the RCM (Murphy, 1999; Fowler et al., 2007b; Maraun et al., 2010).This overestimation can distort the precipitation distribution substantially, i.e. shifting the quantiles, producing inappropriate corrections in the third step when EQM is applied (Teutschbein and Seibert, 2012; Lafon et al., 2013).

To correct precipitation with very low intensity, simulated precipitation values are censored by setting them to zero when they are below a specific threshold. Many studies use a static threshold for the entire simulated data set which is between 0.01 and 1 mm d^{-1} (Piani et al., 2010a; Lafon et al., 2013; Maraun, 2013). To be consistent with the different biases' treatment across the groups, we calculate a static

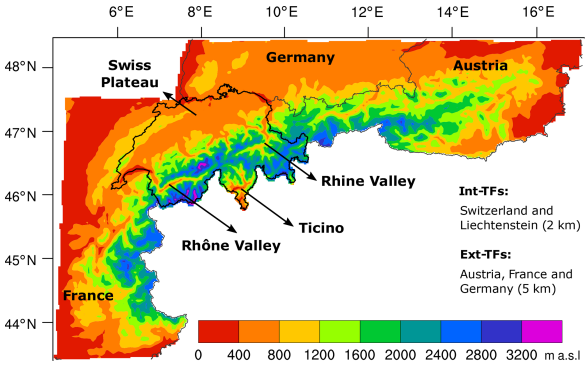

Figure 2. WRF innermost domain indicates the present-day height classes used for the correction method (400 m interval) for the Int-TFs at 2 km resolution (Switzerland, black outline) and for the Ext-TFs at 5 km resolution (other shaded areas). Additionally, some labels are added to identify some specific areas in Switzerland that are used throughout the paper.

threshold for each group (or subgroup) and each month of the year. Thus, we carry out the first part of the local intensity scaling method (Schmidli et al., 2006; Teutschbein and Seibert, 2012) before applying the quantile mapping technique. This method consists of choosing the threshold in a way such that the number of days with precipitation in the simulation coincides with the precipitation-day occurrence from the observations. In our work, the threshold can vary from group to group and from month to month between 0.001 and 1 mm d^{-1}.

In a third step, we correct the daily precipitation rate using an EQM method (Themessl et al., 2011; Lafon et al., 2013; Fang et al., 2015; Teng et al., 2015). Note that censored values are excluded from this step. EQM is based on the assumption that all probability distribution functions are unknown, i.e. non-parametric (Wilks, 2011). The method consists of adjusting the quantile values from a simulation (Q_{sim}) to those from the observations (Q_{obs}) through a transfer function (TF; Fig. 4). The method is implemented by splitting each cumulative distribution function, i.e. observed and modelled, into 100 discrete quantiles. For each quantile value, the adjustment is carried out with a linear correction (Lafon et al., 2013), where Q_{sim} is transformed into ${Q_{sim}}^*$ (corrected quantile; Eq. 1).

$$ {Q_{sim}}^* = \mathrm{TF} \times Q_{sim}, \text{ where } \mathrm{TF} = \frac{Q_{obs}}{Q_{sim}} \quad (1) $$

This linear correction is akin to the factor of change or delta change used in Hay et al. (2000). For values that are between quantiles, the same linear correction is used, but the TF is approximated by using a linear interpolation between the TFs related to the two nearest quantiles. In cases where values are below (above) the first (last) quantile, the TF related to the first (last) quantile is used for the adjustment. Similar methods were successfully applied to correct biases in precipitation simulated by RCMs (e.g. Sun et al., 2011; Themessl et al., 2012; Rajczak et al., 2016; Gómez-Navarro et al., 2018).

To combine all steps, the first part of the local intensity scaling method and the EQM are applied to each (sub)group defined in the first step and to each month of the year, separately, by pooling all grid points that belong to each group and handling them as a single distribution of daily precipitation. This results in a set of TFs for each (sub)group and each month of the year. For instance, it results in nine TFs for each month and in total 108 TFs throughout the year when the correction is carried out using height classes of 400 m. Moreover, the correction is afterwards applied to the daily precipitation at every grid point using the TFs that are common to all elements within the same group (or subgroup) and month. Thus, the new correction method guarantees that seasonality and height are taken into account.

To come up with a final method for the Alpine region, we first evaluate the influence of the different orographic characteristics (step 1). To be consistent with former studies (e.g. Sun et al., 2011; Themessl et al., 2012; Wilcke et al., 2013; Rajczak et al., 2016), the evaluation uses the same region where the TFs are estimated. This means that the Swiss region in the WRF output (at 2 km resolution) is defined as the area to be corrected and RhiresD (at 2 km resolution) is used to obtain the TFs and to evaluate the different correction methods. These TFs are called internal TFs (Int-TFs) during the cross-validation process later on.

Once the final method is determined, we apply two cross-validations to test the method more rigorously, as suggested by Bennett et al. (2014). First, a temporal cross-validation is applied. Thereby, the 30-year period is split into a 15-year training period and an independent 15-year verification period. New sets of TFs are calculated from the first and last 15 years of the 30-year period, separately. Each set of TFs is then applied to the first and last 15 years, which results in four newly corrected precipitation data sets, namely, two dependent and two independent ones. Second, we apply a spatial cross-validation. Thereby, Switzerland is defined as the area to be corrected (WRF output at 2 km resolution). For the spatial cross-validation, an additional set of TFs is then estimated from the corresponding Alpine region of Germany, France, and Austria excluding Switzerland (called the external TFs; Ext-TFs) using APGD (at 5 km resolution; Fig. 1c). Ext-TFs are carried out at 5 km horizontal resolution and applied to Switzerland at 2 km resolution. This guarantees that no additional uncertainty is introduced by a spatial interpolation when comparing the results of Ext-TF and Int-TF. To see that the coarser resolution of APGD has no influence on the result, the performance of the correction method is also evaluated when using Ext-TFs trained at 5 km and then applied to the Swiss region at 5 km resolution. Note that these results only show small differences to the 2 km results and are therefore not shown. To determine the improvement of

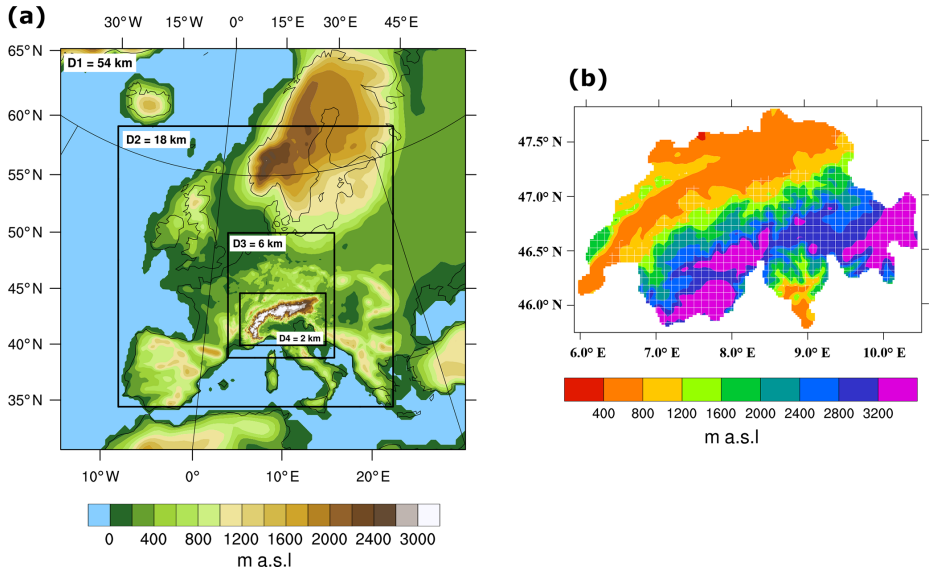

Figure 3. WRF domains and LGM topography. Panel **(a)** illustrates the LGM topography, LGM sea level, and the four domains used by WRF. Panel **(b)** indicates the height classes for the correction method (400 m interval) using the LGM topography over Switzerland at 2 km resolution; crosshatched areas are covered by glaciers.

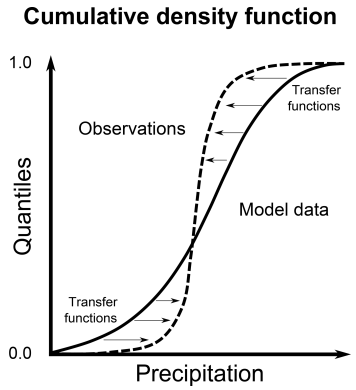

Figure 4. Diagram of the EQM technique. The solid (dashed) line shows a schematic simulated (observed) cumulative distribution.

the new method, we compare it to a simple method that is carried out without orographic features using one EQM for the entire region in each month (12 EQM in total, referred to as one EQM-TF hereinafter).

4 Validation of the method

4.1 Biases of WRF and their seasonality

To obtain insights into the performance of the RCM over complex topography, we compare the spatial and temporal representation of the simulated precipitation (the raw model output) with RhiresD. Focusing on monthly mean precipitation intensity across Switzerland, the box plots illustrate biases in the climatological annual mean cycle (Fig. 5a). The climatological mean values are slightly overestimated during colder months, i.e. between November and March, and are underestimated during warmer months, i.e. between April and October but especially in September. In addition to the climatological mean values, Fig. 5a also shows the distributions of monthly mean precipitation intensity and their interquartile ranges. In colder months, the simulated distributions are wider and shifted to higher values than the observed distributions, whereas a clear shift to less precipitation is found compared to the observed ones during warmer months. Overall, the interquartile ranges are reasonably simulated, which means that WRF realistically represents the variability of monthly mean precipitation intensity. Extreme precipitation, however, is strongly underestimated.

The annual cycle and the distributions of monthly mean precipitation intensities are estimated for different height classes to get additional understanding of the behaviour of the simulated precipitation and also to explicitly illustrate the relation of the precipitation biases to the topography. This is summarised in Fig. 5b and c for the height classes of 400–800 and 2800–3200 m which mostly represent the low and high altitudes, respectively. The climatological monthly means of the colder months, i.e. from November to March, are generally underestimated in the lower height classes but overestimated at high altitudes. Additionally, we assess the

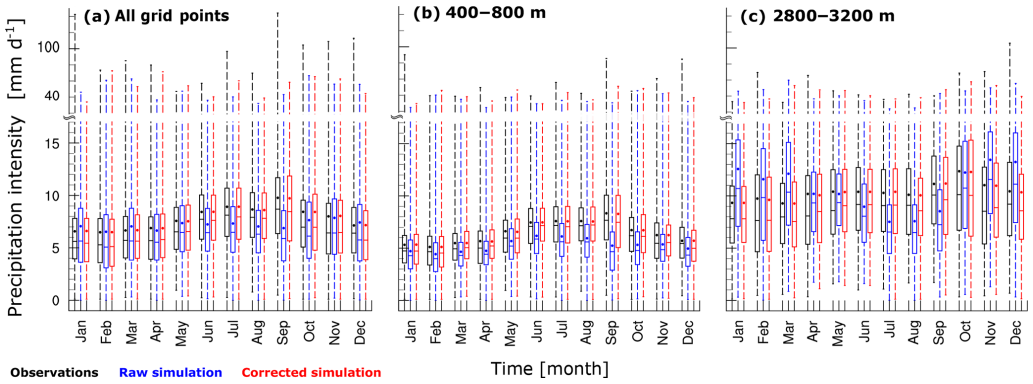

Figure 5. Boxplots illustrate the spatial distribution of monthly mean values of precipitation intensity across a specific area within 30 years: **(a)** the area covers all grid points over entire Switzerland, **(b)** the grid points in the height class of 400–800 m, and **(c)** the grid points in the height class of 2800–3200 m. Black box plots represent the observations (RhiresD); blue and red ones the raw and corrected simulations, respectively. Top and bottom ends of the dashed lines represent the maximum and minimum values, respectively. Dots represent the spatial climatological mean value.

biases at each grid point in a scatter plot. To that end, we select two months that mainly represent colder and warmer months, namely, January and July, respectively. We find a clear positive correlation between the biases and altitudes in January (Fig. 6a). In warmer months, i.e. April to October, both height classes (400–800 and 2800–3200 m) reveal an underestimation in the climatological monthly means compared to the observations. This is again confirmed by scatter plots between biases at grid points and altitude, where only a mean shift is found in July (Fig. 6b). Overall, the simulated annual cycle changes from a weak cycle at low altitudes, in agreement with the one of the observations, to a strong and inverse seasonal cycle at high altitudes (Fig. 5b and c). An inverse annual cycle is also identified by Gómez-Navarro et al. (2018), who used a similar model chain compared to the one in this study. These authors found that the inversed annual cycle in precipitation is caused by the driving global climate model. Furthermore, we observe positive biases in the interquartile ranges during colder months and a slight underestimation during warmer months (Fig. 5b and c). So far, the analysis of the biases suggests that including the height dependence can help in improving correction methods.

To better describe the spatial biases related to colder and warmer months, we select two months that mainly represent each period, namely, January and July. For these example months, we present the spatial patterns of the biases in the monthly mean precipitation intensity, in the variability illustrated by the interquartile range, and in the wet-day frequency. Note that the observational data sets are generally considered reliable and represent orographic features well, although at high altitudes fewer observations are available (Isotta et al., 2014). Furthermore, these spatial patterns implicitly illustrate the relation between the precipitation biases and the topography considering an uncertainty of around 30 % acceptable in the simulated precipitation due to the uncertainty in the observational data sets (Sect. 2).

The biases in the climatological mean precipitation intensity at each grid point (Fig. 7a and d) confirm the height dependence and seasonality already shown in Fig. 5. The strongest positive biases are mainly observed over mountains and during colder months, whereas the Swiss Plateau seems to be reasonably well simulated (Fig. 7a). Note that also the observations tend to underestimate precipitation in mountain regions, so that a part of the strong positive bias is related to observational uncertainties (Isotta et al., 2014). In warmer months, the strongest negative biases are found in the northwestern part of Switzerland, Ticino, and in the steep valleys, where the Rhône Valley is marked by the strongest biases. In high mountain regions, smaller positive biases are identified during warmer months than during colder months (Fig. 7d). The strongest biases over mountains and in steep valleys seem to be induced by an amplification of different observed precipitation climatologies that govern those areas; namely, the mountains are known as wet regions and the steep valleys as dry areas (for more details, see Frei and Schär, 1998; Schwarb et al., 2001). This gives a first hint that different processes may lead to the biases. The positive precipitation bias over mountains in colder months may be mainly related to wet bias of the global simulation and synoptic transport, which is also overestimated in the global simulation (Hofer et al., 2012a, b). The resolution of the RCM seems to be important as this affects the representation of steep valleys, especially during convective processes in warmer months. The same is also true for colder months but to a lesser extent, as convective processes only play a minor role in these months.

The interquartile ranges of the distribution of monthly mean precipitation intensity at each grid point (Fig. 8a and d) are strongly overestimated over the Alps during colder

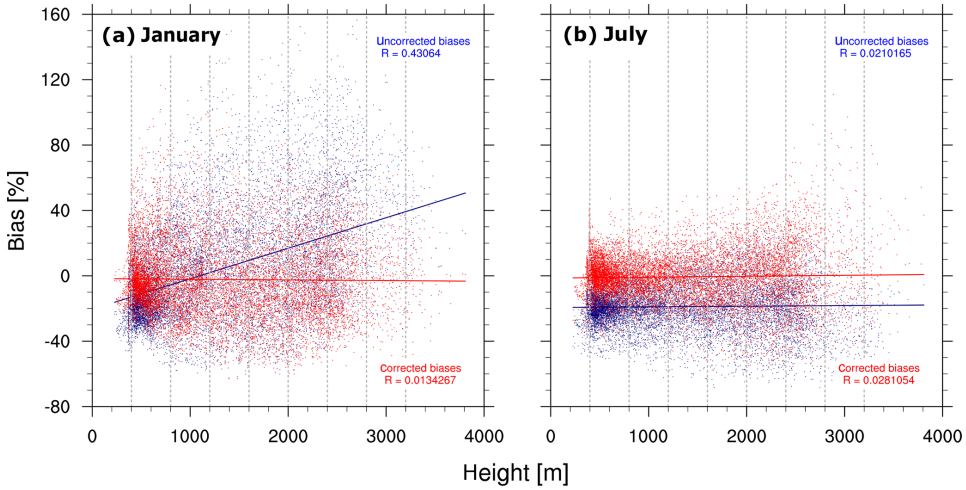

Figure 6. Biases over Switzerland. Blue (red) indicates the original (corrected) biases. Panel **(a)** illustrates the bias versus height at each grid point during January; panel **(b)** is the same as **(a)** but for July. Solid lines represent the linear regressions, *R* the correlation between biases and height, and vertical dashed grey lines the boundaries of the height classes.

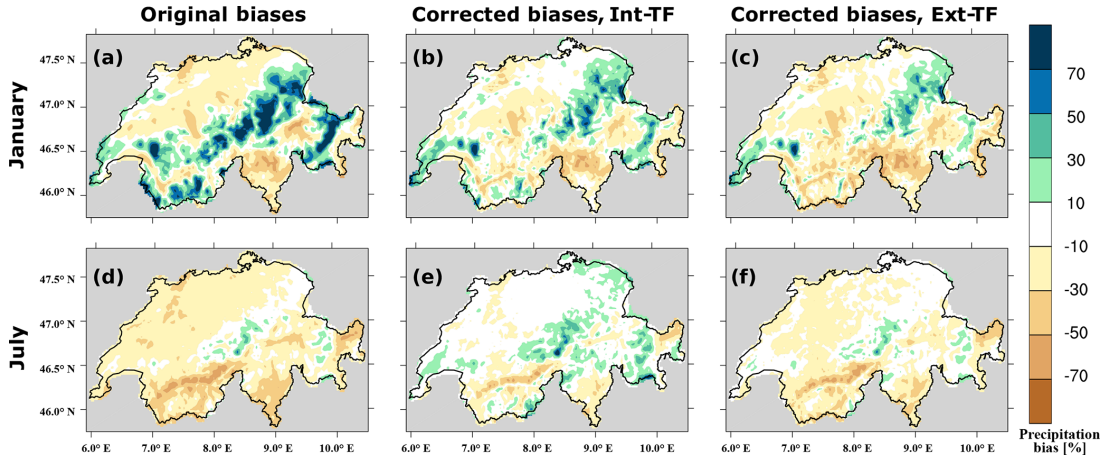

Figure 7. Biases in the climatological mean value of precipitation intensity over Switzerland. Panel **(a)** represents the original biases in January, **(b)** the biases after being corrected using Int-TFs in January, and **(c)** the biases after being corrected using Ext-TFs in January; panels **(d)**, **(e)**, and **(f)** are the same as **(a)**, **(b)**, and **(c)** but in July, respectively.

months, whereas they are generally smaller compared to the observations during warmer months. The biases are stronger than the ones observed in the climatological mean value (Fig. 7a and d), which means that the variability simulated by WRF is strongly season-dependent (Fig. 8a and d). The increase in variability during colder months is a hint that processes common during winter, e.g. the synoptic atmospheric systems, may be too efficient in producing precipitation compared to the observations. The reduced variability in warmer months hints at remaining problems in convective processes as these are more relevant during summer. Also, observations do not perfectly estimate the range due to their uncertainty that fluctuates from 5 % over the flatland regions to more than 30 % at high altitudes (Isotta et al., 2014).

Another important measure to characterise precipitation is the occurrence of precipitation at each grid point, defined by the wet-day frequency (the number of days with precipitation rate of at least 1 mm d^{-1}). The wet-day frequency is strongly overestimated during colder months but shows only a slight overestimation during warmer months (Fig. 9a and d). This overestimation can be also related to the well-known problem in regional climate modelling, i.e. the simulation of a higher frequency in precipitation but at the same time with a lower intensity than observed (Murphy, 1999; Fowler et al.,

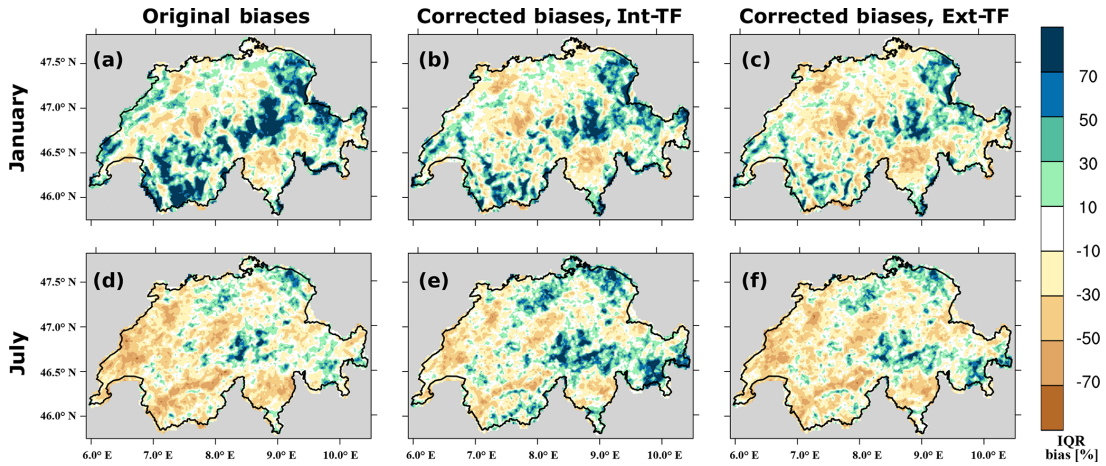

Figure 8. Biases in the interquartile range of monthly mean precipitation intensity over Switzerland. Panel **(a)** represents the original biases in January, **(b)** the biases after being corrected using Int-TFs in January, and **(c)** the biases after being corrected using Ext-TFs in January; panels **(d)**, **(e)**, and **(f)** are the same as **(a)**, **(b)**, and **(c)** but in July, respectively.

2007b; Maraun, 2013). The overestimation in wet-day frequency, the so-called drizzle effect, can be mainly related to the occurrence of synoptic atmospheric systems commonly observed during colder months and not to local convective processes that are frequently observed during summer (for climatology, see Frei and Schär, 1998; Isotta et al., 2014). Furthermore, the positive bias in the wet-day frequency may slightly contribute to the underestimation of the extreme precipitation (Fig. 5) as precipitable water, which is necessary for extreme precipitation events, is removed via the drizzle effect. Namely, the precipitable water available for a daily extreme precipitation event is distributed over several days due to problems in the parameterisations of the cloud microphysical and precipitation processes as found in Knist et al. (2018).

4.2 Influence of different orographic characteristics on the performance of the bias-correction method

Different orographic characteristics are suggested to be used as classification in the new bias-correction method (step 1 in Sect. 3): the height intervals (100 and 400 m), the slope orientations, and a combination of both using the height interval of 400 m (combined features). Note that the results are not affected by interchanges in the order of the orographic characteristics in the combined features (therefore not shown). We assess, in the following, which of these characteristics are necessary to improve a simple approach of applying one EQM-TF to the entire domain, where orographic features are not considered. An improvement compared to one EQM-TF for the entire domain would certainly support the height dependence of the biases. Note that we do not compare our results to the standard EQM as the latter would outperform the here-described method by definition. Note that the standard EQM removes the mean bias on a grid-point level as it is a statistical downscaling at the same time. We use Taylor diagrams (Fig. 10) for four months, namely, January, April, July, and September, as the biases show a strong seasonality (see previous section). The evaluation is carried out with three statistics: the spatial correlation, the spatial root-mean-square error, and the spatial standard deviation.

Figure 10a shows that the correction methods using height intervals of both 100 and 400 m, and the combined features have better performance during the colder months than the other methods, i.e. using just orientation or one TF for the entire domain: the standard deviation is better adjusted, especially when using height intervals of 100 m, the root-mean-square error is reduced by roughly 32 %, and the correlation is slightly increased (Fig. 10b). During the cold-to-warm transition months (here illustrated by April), the correction using height intervals of 400 m and the combined features have better performance than the other settings. This is because the standard deviation is fully adjusted, the root-mean-square error is reduced by 17 %, and the correlation is increased to $r = 0.75$ (Fig. 10b). During the warmer months, all correction methods except the one using height intervals of 100 m show similar good performance; i.e. the standard deviation is fully adjusted, the root-mean-square error is slightly reduced, and the correlation is slightly increased (Fig. 10c). The similar good correction in the warm months can be explained by a reduced height dependence of the biases in these months. During the warm-to-cold transition months (September; Fig. 10d), all correction methods show a similar performance increase compared to the observations; correlation and root-mean-square error are only slightly improved. The method using height intervals of 100 m often reduces the standard deviation. This can be explained by a

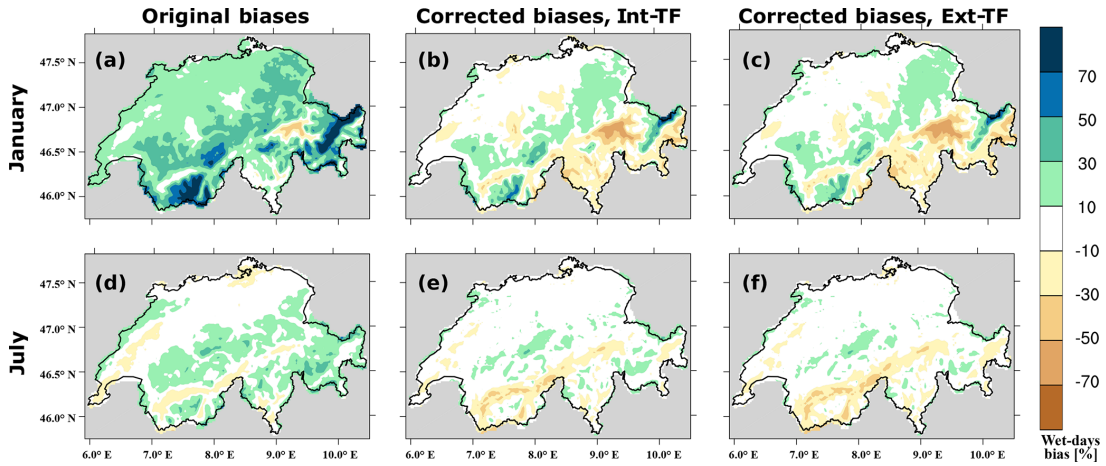

Figure 9. Biases in the wet-day frequency within the 30-year period over Switzerland. Panel **(a)** represents the original biases in January, **(b)** the biases after being corrected using Int-TFs in January, and **(c)** the biases after being corrected using Ext-TFs in January; panels **(d)**, **(e)**, and **(f)** are the same as **(a)**, **(b)**, and **(c)** but in July, respectively.

reduced data coverage which means less variability within some height classes as a smaller climatological range is encompassed by each height interval.

Even though all the settings mostly show good performance, the one using height intervals of 400 m outperforms in most measures and months. In addition, the correction method using the height intervals of 400 m needs less computational time compared to the similarly good correction method using height intervals of 400 m and slope orientations. Therefore, the method using height intervals of 400 m seems to be the most appropriate setting and is used in the following analysis.

4.3 Application of the bias-correction method and cross-validation under present-day conditions

The bias-correction method using height intervals of 400 m is now assessed in more detail. First, we focus on results where the TFs are estimated in the domain of Switzerland using 30 years (Int-TFs). Second, we discuss the results obtained by a temporal and spatial cross-validation technique, i.e. the TFs trained on another period and the TFs estimated with the surrounding Alpine region, excluding Switzerland (Ext-TFs). As in Sect. 4.2, a comparison to the standard EQM (Lafon et al., 2013) is not presented, since the standard EQM outperforms the new method under present-day conditions. A priori, this comparison is based on different prerequisites, as the standard EQM corrects at a grid-point level, and thus it removes the mean biases as in statistical downscaling methods. Instead, we again compare the new method to a simple one EQM-TF used for all of Switzerland. A similar approach is sometimes used in other studies as well to assess the added value of their proposed methods (e.g. Gómez-Navarro et al., 2018; Casanueva et al., 2016).

To illustrate the improvement by the correction method using Int-TFs, we compare the spatial and temporal representation of the corrected precipitation with RhiresD. Focusing on the monthly mean precipitation intensity across Switzerland, we find that the climatological annual cycle of mean precipitation intensity fully coincides with the one of the observations (Fig. 5a). Also, the distributions of monthly mean precipitation intensity are fully adjusted and the corresponding interquartile ranges mainly correspond to the ones of the observations when using the new bias-correction method. Still, the extreme precipitation events are underestimated with the new method, which is expected as the TF of the extreme values is poorly constrained in the EQM approach (e.g. Themessl et al., 2011). The segregation into the height classes (Fig. 5b and c) shows that the climatological monthly means and the distributions of monthly mean precipitation intensity are also well adjusted compared to the observations. This illustrates that the bias-correction method using height intervals of 400 m is appropriate.

To further describe the spatial improvements of the new bias-correction method, we select here, as in Sect. 4.1, two months that mainly represent the colder and warmer months, e.g. January and July, respectively. We again focus on biases in the monthly mean precipitation intensity, in the variability illustrated by the interquartile range, and in the wet-day frequency.

A comparison of Fig. 7a and d with b and e shows that the biases in the climatological mean precipitation intensity are substantially reduced, especially the overestimation over high mountain regions during colder months and the general underestimation during warmer months. Still, regions with positive and negative biases remain over the eastern part of the mountains in colder months and in the steep valleys like

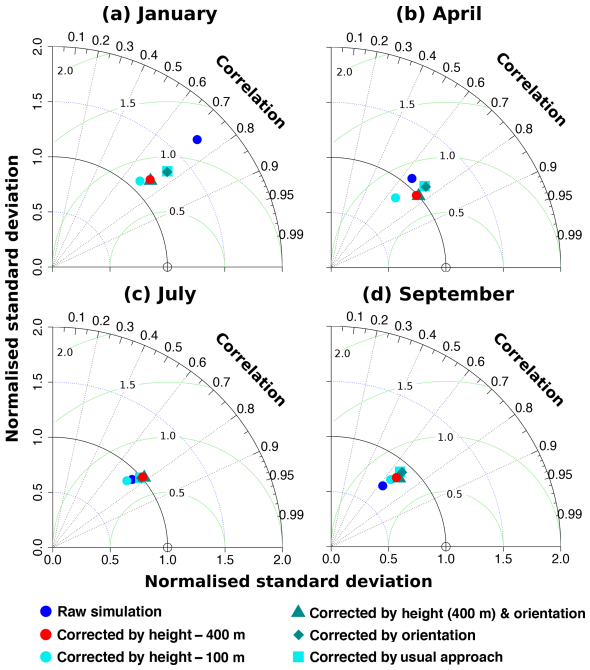

Figure 10. Performance of bias correction with different settings. Panel **(a)** shows a Taylor diagram for January, **(b)** for April, **(c)** for July, and **(d)** for September. Blue dots represent the raw simulation, red dots the simulation corrected by using height intervals of 400 m, cyan dots the simulation corrected by using height intervals of 100 m, petrol triangles the simulation corrected by using height intervals of 400 m and slope orientations, petrol diamonds the simulation corrected by slope orientations, and cyan squares the simulation corrected by the simple approach (the entire Swiss region). Note that in the Taylor diagram the spatial correlation, spatial root-mean-square error, and spatial standard deviation are shown.

the Rhône Valley in warmer months. Also, the negative bias in Ticino during colder months remains, albeit it is slightly ameliorated. The rather moderate performance in these regions can be traced back to the fact that some height classes sample over regions with different biases. Hence, biases of one area are diminished by the biases that are shared by the other areas. For instance, the strong negative biases observed in the Rhône Valley and Ticino are not fully decreased because the slight underestimation from the Swiss Plateau dominates this height class (Fig. 7b and e).

To assess the improvements with respect to precipitation variability, we focus on the interquartile range of the distribution of monthly mean precipitation intensity at each grid point (Fig. 8b and e compared to a and d). The biases of the interquartile range improve only moderately; i.e. the strong overestimation over the mountains is partly corrected during colder months but not during warmer months. The underestimation over the flatlands and steep valleys is corrected during warmer months and poorly during colder months.

For the wet-day frequency, we find that the positive biases are mostly reduced, especially the strong overestimation over the mountains during colder months (Fig. 9b and e). However, the regions of the Rhône Valley and Ticino, which show no biases in the raw model output, are slightly underestimated during colder months. The negative biases observed in the region of Grisons become stronger during colder months and in the region of the Rhône Valley during warmer months (Fig. 9b and e). This effect is again caused by sampling different regions with different biases in the height classes.

Recent studies by Maraun et al. (2017) and Maraun and Widmann (2018b) showed that the observational and simulated data sets do not have a synchronised internal climate variability, and thus this may be one of the sources of the remaining biases in free-running models. To assess these remaining biases, we perform a temporal cross-validation. An option could be to carry out a leave-one-out verification method to hold back most of the years for calibration; however, different lengths between calibration and the independent verification periods can lead to more uncertainties (Lafon et al., 2013; Maraun, 2016; Maraun et al., 2017; Maraun and Widmann, 2018b). Therefore, our temporal cross-validation consists of using different same-length periods for the calibration and the verification (see Sect. 3). Overall, the bias-correction method performs similarly in the independent 15 years and shows similar remaining biases compared to using the entire 30 years for training and verification. Still, some differences between dependent and independent periods are evident. During January, the method trained on the first 15 years and verified in the second 15 years shows lower biases over high altitudes and slightly higher biases in the flatlands and in Ticino (not shown). Inversely, the method trained with the second 15 years and verified in the first 15 years shows reduced biases in the flatlands and in Ticino but not over the mountains (not shown). During July, similar small differences are identified in the independent verification periods (therefore not shown). Thus, there is a potential that a different internal climate variability affects the bias-correction method (Maraun et al., 2017; Maraun and Widmann, 2018b). However, these differences can be considered minimal as the accuracy of bias-correction methods is sensitive to the length of the period the methods are trained on (a shorter training period results in less accurate performance; Lafon et al., 2013).

To further check the robustness of the new bias-correction method, a spatial cross-validation is performed (see Sect. 3). Thereby, we apply the TFs estimated from an independent data set of the Alpine region (at 5 km resolution), excluding Switzerland (Ext-TFs), to the Swiss region (at 2 km resolution). To have insights into the effects of the correction method using Ext-TFs, we compare the spatial and temporal representation of the corrected precipitation with the results obtained by the Int-TFs. Note that the RhiresD is always used as observations for the bias calculation. Again, to describe the spatial effects, we select here two months that

mainly represent the colder and warmer months, i.e. January and July, respectively.

A comparison of Fig. 7b with c shows almost the same pattern; i.e. the improvement in mean precipitation achieved by using Ext-TFs is similar to that using the Int-TFs during colder months. Still, some positive biases over the mountains seem to be smaller when using Ext-TFs than Int-TFs, whereas the remaining negative biases are slightly stronger than the ones after using Int-TFs (Fig. 7b and c). The reason for the latter could lie in the inclusion of larger regions in the north and west of the Alps mixing different climate conditions and thus bias behaviours. The slightly better performance in the mountain regions is probably related to more data being available in these height classes, i.e. more grid points at high altitudes (Fig. 2), and thus it is possible to better constrain the TFs. In the warmer months, we find that the method using Ext-TFs shows slightly more negative biases than with Int-TFs, in particular over the Swiss Plateau. Again, we hypothesise that the inclusion of larger regions in the north and west of the Alps is responsible for this bias behaviour.

The interquartile ranges of the distribution of monthly mean precipitation intensity are similar when using either Ext-TFs or Int-TFs for the colder months (Fig. 8c compared to b). During warmer months, the negative biases in the western part of Switzerland are less improved using Ext-TFs than Int-TFs, which is again a hint that the inclusion of larger regions in the north and west of the Alps in the lower height classes plays a role in the bias of the interquartile range.

The wet-day frequencies are very similarly corrected as in the approach using Ext-TFs compared to Int-TFs (Fig. 9c and f compared to b and e). Thus, the wet-day frequency seems to be insensitive to the region where the TFs are estimated.

Additionally, to further assess the local improvements of adding topographic features into the correction, we analyse the remaining biases of the simple method using TFs deduced for the Swiss region (Int-TFs), as described in Sect. 4.2, and for the corresponding Alpine region (Ext-TFs) separately. Overall, the comparison between the simple method and the new method shows small differences (therefore not shown). The new method shows better performance than the simple method in January but similar performance in July. Furthermore, the simple method increases the original biases over the flatlands, which are reduced by the new bias correction. This confirms the results of the Taylor diagram illustrated in the Fig. 10, i.e. the better performance of the method using height intervals of 400 m.

In summary, the new correction method reasonably well corrects biases in the monthly mean precipitation intensity, in the variability illustrated by the interquartile range, and in the wet-day frequency. The two cross-validations show that the improvements achieved by the new method are almost independent of the time period and region used to estimate the TFs. Additionally, the new method outperforms the simple method (one EQM-TF) in the present-day climate.

4.4 Application of bias-correction methods on the simulated LGM climate

To further examine the performance and applicability of the new bias-correction method, we apply it to the simulated LGM climate. Similarly, the standard EQM (e.g. Lafon et al., 2013; Teutschbein and Seibert, 2012, 2013; Teng et al., 2015) is applied and precipitation fields resulting from its correction are compared to the one of the new method. The reason is that the strength of the standard EQM (correction at grid-point level) under present-day climate might be a weakness under highly different climate states, since local-related biases might not exist. To that end, we again focus on the monthly mean precipitation intensity over Switzerland in January and July, i.e. the two months that represent the cold and warm seasons, respectively.

Focusing on the raw LGM simulation first, we find wetter conditions in the southern part of the Swiss Alps (Fig. 11a and d) rather than at the north-facing slopes, as is the case in present-day conditions (more details about present-day conditions are available in Frei and Schär, 1998; Schwarb et al., 2001). Becker et al. (2016) indicated a strong precipitation gradient between the north- and the south-facing slopes in order to obtain a reasonable extent of the Alpine glacier during the LGM. This suggests an increase of intensity or frequency of the southerly moisture advection over the Alps. Also, Florineth and Schlüchter (2000) and Luetscher et al. (2015) indicated a circulation change from dominant westerlies in the present day to a more southerly atmospheric circulation during the LGM. From this brief qualitative analysis, we can conclude that WRF reasonably simulates the precipitation patterns during the LGM, even if the total amount might present some uncertainties.

Before assessing the performance of the two bias-correction methods, it is worthwhile to shortly focus on the changes in the topography. The topography is differently lifted across Switzerland during the LGM (Fig. 3b) compared to the present-day climate (Fig. 2). While the mountainous areas become larger, the height of their peaks hardly changes. The present-day valleys are filled by ice during the LGM, and thus the deep valleys almost disappear. For instance, the Rhône Valley exhibits a continuous slope towards its spring (Fig. 3b), while it is a narrow and deep valley with almost a constant elevation in the present-day topography (Fig. 2). Since the Alps were covered by ice, the fine and complex present-day topography is lacking during the LGM.

We apply the standard EQM and the new method to not only assess their performance but also to identify the strength and weakness of each method. Comparing Fig. 11b and e to c and f illustrates that the corrections do not modify the north–south precipitation gradient observed in the raw simulation (Fig. 11a and d). The standard EQM method (Fig. 12b and d) shows that the shape of the valleys and the mountain peaks of the present-day topography are imprinted on the raw LGM climate (Fig. 12a and c). The standard EQM seems to add a

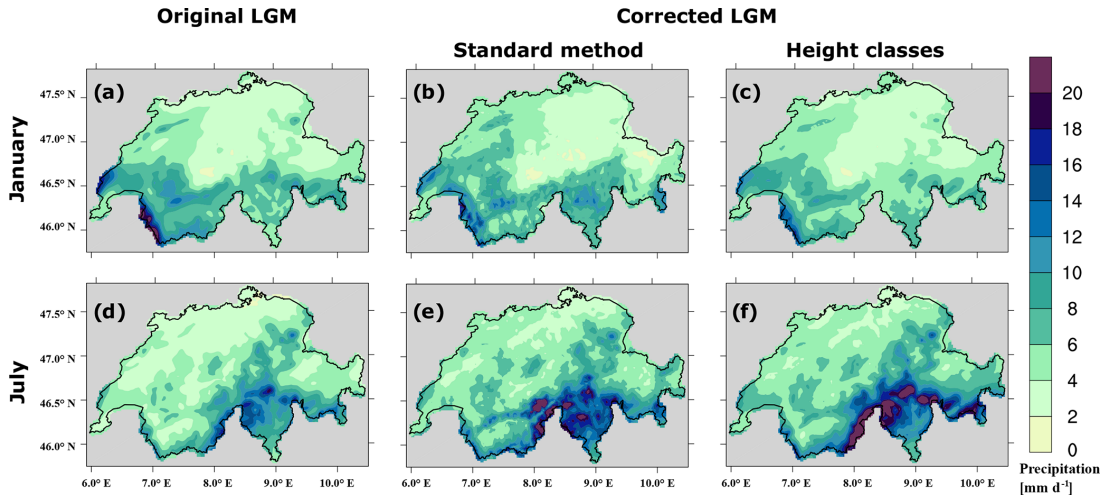

Figure 11. Monthly climatology of 30-year precipitation over Switzerland during the LGM. Panel **(a)** represents uncorrected precipitation intensity in January; panel **(b)** is the same as **(a)** but corrected using the standard EQM; panel **(c)** is the same as **(b)** but using the new method; panels **(d)**, **(e)**, and **(f)** are the same as **(a)**, **(b)**, and **(c)** but for July, respectively.

fine and complex structure to the precipitation pattern. This complexity is hardly justified over the Alps during the LGM, as stated before, which suggests that adding this structure is unnecessary. The imprint of the present-day topography is related to the nature of the standard EQM that trains the TFs point-wise assuming static orographic features. The new correction method follows by definition the LGM topography showing a smoother correction for the LGM climate, which provides precipitation patterns that more appropriately represent the LGM situation. Proxy records could give an idea on the LGM precipitation amounts but there is a very limited number of them in Switzerland; thus, a more rigorous analysis of the application of the two methods to the LGM climate is not possible. However, the difference between the two methods demonstrates that the application of the new bias correction is better suited than the standard EQM. Therefore, we consider it as more appropriate for climate states with strongly altered topography compared to today.

5 Summary and conclusions

In this study, we present a new bias-correction method for precipitation over complex topography, which takes orographic characteristics into account. This method is mainly designed for climate states where the topography is distinctively different to the present-day one, i.e. glacial times. This is particularly important for studies where absolute values of precipitation are essential, such as glacier and ice sheet modelling (Seguinot et al., 2014; Jouvet et al., 2017; Jouvet and Huss, 2019), and the assessment of human behaviour during glacial times (Burke et al., 2017; Wren and Burke, 2019). To illustrate the performance of the new method, two regional climate model simulations are performed with WRF at 2 km resolution over the Alpine region. We particularly focus on the performance over Switzerland.

The comparison between the WRF simulation and the observations over Switzerland shows that the biases are season dependent and related to the complexity of the topography, especially in colder months (November to March). These months exhibit positive biases over mountains and negative biases in steep valleys, whereas negative biases dominate during the warmer months (April to October), especially in the Rhône Valley and Ticino. Parts of the biases are introduced by the driving global climate model, in particular the seasonal biases (Gómez-Navarro et al., 2018). Moreover, the large-scale atmospheric circulation of the global climate model is too zonal – a known problem in many models (e.g. Raible et al., 2005; Raible et al., 2014; Hofer et al., 2012a, b; Mitchell et al., 2017) – which cannot be fully compensated for by the RCM. Thus, the wet bias present in the global simulation (Hofer et al., 2012a, b) may be transported into the regional model domain, rendering especially the colder months with more precipitation. Still, observations are also not perfect and underestimate precipitation in particular at high altitudes by up to 30 % (Isotta et al., 2014). Other biases are potentially induced by the RCM; e.g. a WRF simulation using a similar setting but driven by ERA-Interim (Gómez-Navarro et al., 2018) shows also a comparable overestimation of precipitation over mountain regions as the simulation used in this study. In addition, we find that the extreme precipitation values are underestimated. This is due to the drizzle effect (Murphy, 1999; Fowler et al., 2007b) that can remove moisture needed for the extreme precipitation, which mainly comes from physical parameterisations of the model itself

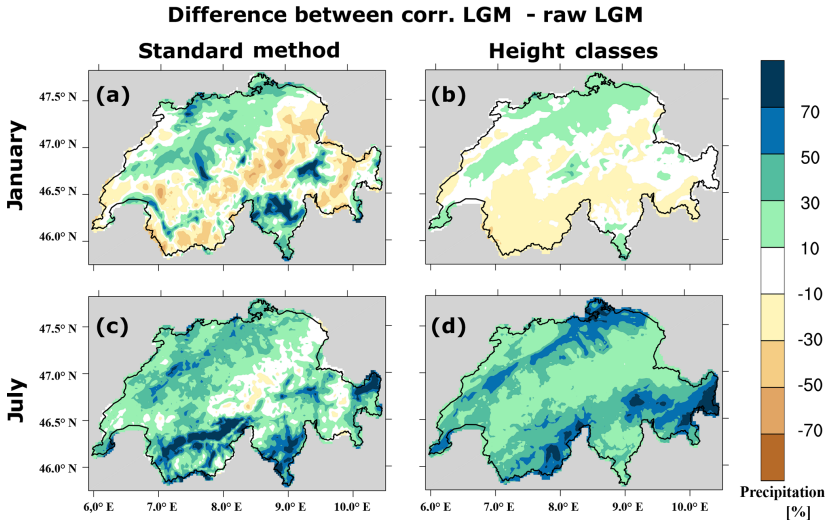

Figure 12. Performance of the correction for the monthly climatology of 30-year precipitation over Switzerland during the LGM. Panel **(a)** represents the differences in January between corrected precipitation using the standard EQM and uncorrected precipitation; panel **(b)** is the same as **(a)** but using the new method; panels **(c)** and **(d)** are the same as **(a)** and **(b)** but in July, respectively.

(Solman et al., 2008; Menéndez et al., 2010; Gianotti et al., 2011; Carril et al., 2012; Jerez et al., 2013). A hint for this is given by the fact that the wet-day frequency in the simulation is enhanced compared to the observations.

Numerous approaches to correct biases exist (e.g. Maraun, 2013; Teng et al., 2015; Casanueva et al., 2016; Ivanov et al., 2018); nevertheless, they assume stationary orographic features that are then imprinted onto the other climate state when applying the correction. Hence, an alternative method is needed, which reduces this assumption so that it adds value to especially colder climate states characterised by a strongly changed topography, such as the LGM. The new method consists of three steps: the orographic characteristics differentiation, the adjustment of very low precipitation intensities, and the EQM. Different orographic characteristics, i.e. the height intervals, the slope orientations, and the combination of both, are tested showing that the method using height intervals of 400 m is generally the most skilful correction compared to other orographic characteristics and at the same time it is computationally the most efficient one. In the colder months, the new method outperforms the simple method of applying one EQM-TF that is deduced for the entire region of interest and does not consider any orographic features.

Applying the new bias-correction method to the Swiss region exclusively shows that the biases are mostly corrected. In particular, the distribution of the monthly precipitation across Switzerland is mainly adjusted, the mean precipitation biases are substantially reduced, and the biases in the wet-day frequency are mostly reduced. The method better corrects the positive biases during colder than warmer months, and conversely, the negative biases during warmer than colder months. However, some biases are still observed, which is explained by the fact that some height classes sample over regions with different biases. Also, the deficient constraint of the TFs in outermost quantiles poorly corrects extreme values, i.e. below the first quantile and above the last quantile. Furthermore, part of the remaining biases may also be interpreted as possible error propagation, which initially comes from the interpolation methods and "gauge undercatch" in the gridded observational data sets, especially at high altitudes where less data are available (for more details, see Sevruk, 1985; Richter, 1995; Isotta et al., 2014).

The new method is temporally and spatially cross-validated. The 30-year period is split in a 15-year training and a 15-year independent temporal verification part. The results are similar to the case when the TFs are trained on and applied to the 30-year period. Still, such a cross-validation might be problematic as the method's accomplishment relies on the biases caught during the period the method is trained on, i.e. the asynchronism in the internal climate variability of the data sets (Maraun et al., 2017; Maraun and Widmann, 2018a). Maraun and Widmann (2018a) argued that cross-validation methods shall compare the correction with the observations on different climate states, i.e. the future or past climate state; otherwise, they can produce false positive or true negative results. To overcome some of these possible limitations, we apply a spatial cross-validation that checks the transferability of the bias-correction method to a different climate state. We use an independent data set of the Alpine region (APGD) excluding Switzerland when estimating the transfer functions (Ext-TFs). This shows a similar improve-

ment compared to the correction performed with data over the Swiss region exclusively (Int-TFs).

The applicability of the new method is further assessed under LGM climate conditions. There is a very limited amount of proxy evidence in Switzerland for a rigorous evaluation. Thus, we compare the performance of the new bias-correction method and the standard EQM when they are applied to LGM climate conditions. The standard EQM adds features to the precipitation that can hardly be justified in the LGM, whereas the performance of the new method suits it better. This indicates that the new method is safer and therefore more appropriate than the standard EQM under LGM climate conditions. In a similar manner, the new method may also be better suited in some regions for future climate scenarios. This is especially true for areas that are currently covered by ice, such as the Himalayas, since possible melting of glaciers can change the shape of the already complex terrain in the future.

Finally, a common drawback of all bias-correction methods (including the one presented in this study) is that they ignore a potential modification of the bias structure due to the handling of rainfall and snowfall in the model's microphysics. This is certainly important when the bias-correction method shall be used in cold climate states, like the LGM. Currently, there are no gridded and homogenised observations available for snowfall, which is needed for a rigorous analysis of this effect. Still, our seasonally separated and height-dependent method implicitly includes some aspects of the handling of rainfall and snowfall, since one can expect that most of the precipitation is snow at high altitudes and in colder months. Clearly, future work is needed on this aspect as soon as reliable observations of snowfall are available. Additionally, other variables of the Earth's system need to be assessed in future studies on bias-correction methods, especially the response of soil moisture and snow albedo to the corrected precipitation patterns. In the meantime, glaciologists can benefit from a better accuracy of precipitation data obtained by the new method for, e.g. LGM conditions. Glacier modelling (Seguinot et al., 2014; Jouvet et al., 2017; Jouvet and Huss, 2019) results may provide an alternative method for the validation when evaluating the prediction and proxy data of the glacier extents.

Code and data availability. WRF is a community model that can be downloaded from its web page (https://www2.mmm.ucar.edu/wrf/users/index.html, last access: 12 October 2020) (Skamarock et al., 2005). The two climate simulations (global: CCSM4 and regional: WRF) occupy several terabytes and thus are not freely available. Nevertheless, they can be accessed upon request to the contributing authors. The post-processed daily precipitation that is used to perform the bias correction is archived on Zenodo at https://doi.org/10.5281/zenodo.4009101 (Velasquez et al., 2019). The RhiresD and APGD data sets can be requested from MeteoSwiss. Simple calculations carried out at a grid-point level are performed with Climate Data Operators (CDO; https://doi.org/10.5281/zenodo.2558193; Schulzweida, 2019) and NCAR Command Language (NCL; https://doi.org/10.5065/D6WD3XH5; UCAR/NCAR/CISL/TDD, 2019). The data in the figures are obtained with NCL (UCAR/NCAR/CISL/TDD, 2019) and RStudio (RStudio Team, 2015). The codes to perform the bias correction, the simple calculations, and the figures are archived on Zenodo (https://doi.org/10.5281/zenodo.4009101; Velasquez et al., 2019).

Author contributions. PV, MM, and CCR contributed to the design of the experiments. PV carried out the simulations and wrote the first draft. All authors contributed to the internal review of the text prior to the submission.

Competing interests. The authors declare that they have no conflict of interest.

Acknowledgements. Martina Messmer acknowledges support by the SNF (Early Postdoc.Mobility). The CCSM4 and WRF simulations were performed on the supercomputing architecture of the Swiss National Supercomputing Centre (CSCS). Thanks are due to European Reanalysis and Observations for Monitoring for providing APGD.

Financial support. This research has been supported by the Swiss National Science Foundation (grant no. 200021_162444).

Review statement. This paper was edited by Fabien Maussion and reviewed by three anonymous referees.

References

Allen, M. R. and Ingram, W. J.: Constraints on future changes in climate and the hydrologic cycle, Nature, 419, 228–232, https://doi.org/10.1038/nature01092, 2002.

Amengual, A., Homar, V., Romero, R., Alonso, S., and Ramis, C.: A statistical adjustment of regional climate model outputs to local scales: Application to Platja de Palma, Spain, J. Climate, 25, 939–957, https://doi.org/10.1175/JCLI-D-10-05024.1, 2011.

Andréasson, J., Bergström, S., Carlsson, B., Graham, L. P., and Lindström, G.: Hydrological change – climate change impact simulations for Sweden, Ambio, 33, 228–234, https://doi.org/10.1579/0044-7447-33.4.228, 2004.

Auer, I., Böhm, R., and Schöner, W.: Austrian long-term climate 1767–2000, Osterreichische Beiträge zu Meteorologie und Geophysik, 25, 147, ISSN 1016-6254, 2001.

Ban, N., Schmidli, J., and Schär, C.: Evaluation of the convection-resolving regional climate modeling approach in decade-long simulations, J. Geophys. Res.-Atmos., 119, 7889–7907, https://doi.org/10.1002/2014JD021478, 2014.

Bartlein, P. J., Harrison, S. P., Brewer, S., Connor, S., Davis, B. A. S., Gajewski, K., Guiot, J., Harrison-Prentice, T. I., Hender-

son, A., Peyron, O., Prentice, I. C., Scholze, M., Seppä, H., Shuman, B., Sugita, S., Thompson, R. S., Viau, A. E., Williams, J., and Wu, H.: Pollen-based continental climate reconstructions at 6 and 21 ka: a global synthesis, Clim. Dynam., 37, 775–802, https://doi.org/10.1007/s00382-010-0904-1, 2011.

Becker, P., Seguinot, J., Jouvet, G., and Funk, M.: Last Glacial Maximum precipitation pattern in the Alps inferred from glacier modelling, Geogr. Helv., 71, 173–187, https://doi.org/10.5194/gh-71-173-2016, 2016.

Bennett, J. C., Grose, M. R., Corney, S. P., White, C. J., Holz, G. K., Katzfey, J. J., Post, D. A., and Bindoff, N. L.: Performance of an empirical bias-correction of a high-resolution climate dataset, Int. J. Climatol., 34, 2189–2204, https://doi.org/10.1002/joc.3830, 2014.

Berg, P., Feldmann, H., and Panitz, H. J.: Bias correction of high resolution regional climate model data, J. Hydrol., 448-449, 80–92, https://doi.org/10.1016/j.jhydrol.2012.04.026, 2012.

Berthou, S., Kendon, E. J., Chan, S. C., Ban, N., Leutwyler, D., Schär, C., and Fosser, G.: Pan-European climate at convection-permitting scale: a model intercomparison study, Clim. Dynam., 55, 35–59, https://doi.org/10.1007/s00382-018-4114-6, 2018.

Boer, G. J.: Climate change and the regulation of the surface moisture and energy budgets, Clim. Dynam., 8, 225–239, https://doi.org/10.1007/BF00198617, 1993.

Burke, A., Kageyama, M., Latombe, G., Fasel, M., Vrac, M., Ramstein, G., and James, P. M. A.: Risky business: The impact of climate and climate variability on human population dynamics in Western Europe during the Last Glacial Maximum, Quaternary Sci. Rev., 164, 217–229, https://doi.org/10.1016/j.quascirev.2017.04.001, 2017.

Cannon, A. J., Sobie, S. R., and Murdock, T. Q.: Bias correction of GCM precipitation by quantile mapping: How well do methods preserve changes in quantiles and extremes?, J. Climate, 28, 6938–6959, https://doi.org/10.1175/JCLI-D-14-00754.1, 2015.

Carril, A. F., Menéndez, C. G., Remedio, A. R. C., Robledo, F., Sörensson, A., Tencer, B., Boulanger, J.-P., de Castro, M., Jacob, D., Le Treut, H., Li, L. Z. X., Penalba, O., Pfeifer, S., Rusticucci, M., Salio, P., Samuelsson, P., Sanchez, E., and Zaninelli, P.: Performance of a multi-RCM ensemble for south eastern South America, Clim. Dynam., 39, 2747–2768, https://doi.org/10.1007/s00382-012-1573-z, 2012.

Casanueva, A., Kotlarski, S., Herrera, S., Fernández, J., Gutiérrez, J. M., Boberg, F., Colette, A., Christensen, O. B., Goergen, K., Jacob, D., Keuler, K., Nikulin, G., Teichmann, C., and Vautard, R.: Daily precipitation statistics in a EURO-CORDEX RCM ensemble: Added value of raw and bias-corrected high-resolution simulations, Clim. Dynam., 47, 719–737, https://doi.org/10.1007/s00382-015-2865-x, 2016.

Chen, H., Xu, C.-Y., and Guo, S.: Comparison and evaluation of multiple GCMs, statistical downscaling and hydrological models in the study of climate change impacts on runoff, J. Hydrol., 434–435, 36–45, https://doi.org/10.1016/j.jhydrol.2012.02.040, 2012.

Chen, J., Brissette, F. P., Chaumont, D., and Braun, M.: Finding appropriate bias correction methods in downscaling precipitation for hydrologic impact studies over North America, Water Resour. Res., 49, 4187–4205, https://doi.org/10.1002/wrcr.20331, 2013.

Chen, W., Zhu, D., Ciais, P., Huang, C., Viovy, N., and Kageyama, M.: Response of vegetation cover to CO2 and climate changes between Last Glacial Maximum and pre-industrial period in a dynamic global vegetation model, Quaternary Sci. Rev., 218, 293–305, https://doi.org/10.1016/j.quascirev.2019.06.003, 2019.

Clark, P. U., Dyke, A. S., Shakun, J. D., Carlson, A. E., Clark, J., Wohlfarth, B., Mitrovica, J. X., Hostetler, S. W., and McCabe, A. M.: The Last Glacial Maximum, Science, 325, 710–714, https://doi.org/10.1126/science.1172873, 2009.

Ehlers, J., Gibbard, P., and Hughes, P.: Quaternary glaciations-extent and chronology: a closer look, 15, Elsevier, Amsterdam, the Netherlands, 2011.

Fang, G. H., Yang, J., Chen, Y. N., and Zammit, C.: Comparing bias correction methods in downscaling meteorological variables for a hydrologic impact study in an arid area in China, Hydrol. Earth Syst. Sci., 19, 2547–2559, https://doi.org/10.5194/hess-19-2547-2015, 2015.

Felder, G., Gómez-Navarro, J. J., Zischg, A. P., Raible, C. C., Röthlisberger, V., Bozhinova, D., Martius, O., and Weingartner, R.: From global circulation to local flood loss: Coupling models across the scales, Sci. Total Environ., 635, 1225–1239, https://doi.org/10.1016/j.scitotenv.2018.04.170, 2018.

Finney, D. L., Marsham, J. H., Jackson, L. S., Kendon, E. J., Rowell, D. P., Boorman, P. M., Keane, R. J., Stratton, R. A., and Senior, C. A.: Implications of improved representation of convection for the East Africa water budget using a convection-permitting model, J. Climate, 32, 2109–2129, https://doi.org/10.1175/JCLI-D-18-0387.1, 2019.

Florineth, D. and Schlüchter, C.: Alpine Evidence for Atmospheric Circulation Patterns in Europe during the Last Glacial Maximum, Quaternary Res., 54, 295–308, https://doi.org/10.1006/qres.2000.2169, 2000.

Fowler, H. J., Blenkinsop, S., and Tebaldi, C.: Linking climate change modelling to impacts studies: Recent advances in downscaling techniques for hydrological modelling, Int. J. Climatol., 27, 1547–1578, https://doi.org/10.1002/joc.1556, 2007a.

Fowler, H. J., Ekström, M., Blenkinsop, S., and Smith, A. P.: Estimating change in extreme European precipitation using a multimodel ensemble, J. Geophys. Res.-Atmos., 112, D18 104, https://doi.org/10.1029/2007JD008619, 2007b.

Frei, C. and Schär, C.: A precipitation climatology of the Alps from high-resolution rain-gauge observations, Int. J. Climatol., 18, 873–900, https://doi.org/10.1002/(SICI)1097-0088(19980630)18:8<873::AID-JOC255>3.0.CO;2-9, 1998.

Frei, C., Christensen, J. H., Déqué, M., Jacob, D., Jones, R. G., and Vidale, P. L.: Daily precipitation statistics in regional climate models: Evaluation and intercomparison for the European Alps, J. Geophys. Res.-Atmos., 108, 4124, https://doi.org/10.1029/2002JD002287, 2003.

Fu, Q.: An accurate parameterization of the solar radiative properties of cirrus clouds for climate models, J. Climate, 9, 2058–2082, https://doi.org/10.1175/1520-0442(1996)009<2058:AAPOTS>2.0.CO;2, 1996.

Ganopolski, A. and Calov, R.: The role of orbital forcing, carbon dioxide and regolith in 100 kyr glacial cycles, Clim. Past, 7, 1415–1425, https://doi.org/10.5194/cp-7-1415-2011, 2011.

Gent, P. R., Danabasoglu, G., Donner, L. J., Holland, M. M., Hunke, E. C., Jayne, S. R., Lawrence, D. M., Neale, R. B., Rasch, P. J., Vertenstein, M., Worley, P. H., Yang, Z.-L., and Zhang, M.: The Community Climate System Model Version 4, J. Climate, 24, 4973–4991, https://doi.org/10.1175/2011JCLI4083.1, 2011.

Gianotti, R. L., Zhang, D., and Eltahir, E. A. B.: Assessment of the regional climate model version 3 over the maritime continent using different cumulus parameterization and land surface schemes, J. Climate, 25, 638–656, https://doi.org/10.1175/JCLI-D-11-00025.1, 2011.

Giorgi, F., Torma, C., Coppola, E., Ban, N., Schär, C., and Somot, S.: Enhanced summer convective rainfall at Alpine high elevations in response to climate warming, Nat. Geosci., 9, 584–589, https://doi.org/10.1038/ngeo2761, 2016.

Gómez-Navarro, J. J., Raible, C. C., Bozhinova, D., Martius, O., García Valero, J. A., and Montávez, J. P.: A new region-aware bias-correction method for simulated precipitation in areas of complex orography, Geosci. Model Dev., 11, 2231–2247, https://doi.org/10.5194/gmd-11-2231-2018, 2018.

Güttler, I., Stepanov, I., Branković, Č., Nikulin, G., and Jones, C.: Impact of horizontal resolution on precipitation in complex orography simulated by the regional climate model RCA3, Mon. Weather Rev., 143, 3610–3627, https://doi.org/10.1175/MWR-D-14-00302.1, 2015.

Haslinger, K., Anders, I., and Hofstätter, M.: Regional climate modelling over complex terrain: An evaluation study of COSMO-CLM hindcast model runs for the greater Alpine region, Clim. Dynam., 40, 511–529, https://doi.org/10.1007/s00382-012-1452-7, 2013.

Hay, L. E., Wilby, R. L., and Leavesley, G. H.: A Comparison of delta change and downscaled GCM scenarios for three mountainous basins in the United States, J. Am. Water Resour. As., 36, 387–397, https://doi.org/10.1111/j.1752-1688.2000.tb04276.x, 2000.

Hofer, D., Raible, C. C., Dehnert, A., and Kuhlemann, J.: The impact of different glacial boundary conditions on atmospheric dynamics and precipitation in the North Atlantic region, Clim. Past, 8, 935–949, https://doi.org/10.5194/cp-8-935-2012, 2012a.

Hofer, D., Raible, C. C., Merz, N., Dehnert, A., and Kuhlemann, J.: Simulated winter circulation types in the North Atlantic and European region for preindustrial and glacial conditions: Glacial circulation types, Geophys. Res. Lett., 39, L15805, https://doi.org/10.1029/2012GL052296, 2012b.

Hui, P., Tang, J., Wang, S., Wu, J., Niu, X., and Kang, Y.: Impact of resolution on regional climate modeling in the source region of Yellow River with complex terrain using RegCM3, Theor. Appl. Climatol., 125, 365–380, https://doi.org/10.1007/s00704-015-1514-y, 2016.

Isotta, F. A., Frei, C., Weilguni, V., Perčec Tadić, M., Lassègues, P., Rudolf, B., Pavan, V., Cacciamani, C., Antolini, G., Ratto, S. M., Munari, M., Micheletti, S., Bonati, V., Lussana, C., Ronchi, C., Panettieri, E., Marigo, G., and Vertačnik, G.: The climate of daily precipitation in the Alps: Development and analysis of a high-resolution grid dataset from pan-Alpine rain-gauge data, Int. J. Climatol., 34, 1657–1675, https://doi.org/10.1002/joc.3794, 2014.

Ivanov, M. A., Luterbacher, J., and Kotlarski, S.: Climate model biases and modification of the climate change signal by intensity-dependent bias correction, J. Climate, 31, 6591–6610, https://doi.org/10.1175/JCLI-D-17-0765.1, 2018.

Jerez, S., Montavez, J. P., Jimenez-Guerrero, P., Gomez-Navarro, J. J., Lorente-Plazas, R., and Zorita, E.: A multi-physics ensemble of present-day climate regional simulations over the Iberian Peninsula, Clim. Dynam., 40, 3023–3046, https://doi.org/10.1007/s00382-012-1539-1, 2013.

Jouvet, G. and Huss, M.: Future retreat of Great Aletsch Glacier, J. Glaciol., 65, 869–872, https://doi.org/10.1017/jog.2019.52, 2019.

Jouvet, G., Seguinot, J., Ivy-Ochs, S., and Funk, M.: Modelling the diversion of erratic boulders by the Valais Glacier during the last glacial maximum, J. Glaciol., 63, 487–498, https://doi.org/10.1017/jog.2017.7, 2017.

Kageyama, M., Harrison, S. P., Kapsch, M.-L., Löfverström, M., Lora, J. M., Mikolajewicz, U., Sherriff-Tadano, S., Vadsaria, T., Abe-Ouchi, A., Bouttes, N., Chandan, D., LeGrande, A. N., Lhardy, F., Lohmann, G., Morozova, P. A., Ohgaito, R., Peltier, W. R., Quiquet, A., Roche, D. M., Shi, X., Schmittner, A., Tierney, J. E., and Volodin, E.: The PMIP4-CMIP6 Last Glacial Maximum experiments: preliminary results and comparison with the PMIP3-CMIP5 simulations, Clim. Past Discuss., https://doi.org/10.5194/cp-2019-169, in review, 2020.

Kaplan, J. O., Pfeiffer, M., Kolen, J. C. A., and Davis, B. A. S.: Large scale anthropogenic reduction of forest cover in Last Glacial Maximum Europe, PLoS One, 11, e0166 726, https://doi.org/10.1371/journal.pone.0166726, 2016.

Kendon, E. J., Ban, N., Roberts, N. M., Fowler, H. J., Roberts, M. J., Chan, S. C., Evans, J. P., Fosser, G., and Wilkinson, J. M.: Do convection-permitting regional climate models improve projections of future precipitation change?, B. Am. Meteorol. Soc., 98, 79–93, https://doi.org/10.1175/BAMS-D-15-0004.1, 2017.

Knist, S., Goergen, K., and Simmer, C.: Evaluation and projected changes of precipitation statistics in convection-permitting WRF climate simulations over Central Europe, Clim. Dynam., 55, 325–341, https://doi.org/10.1007/s00382-018-4147-x, 2018.

Lafon, T., Dadson, S., Buys, G., and Prudhomme, C.: Bias correction of daily precipitation simulated by a regional climate model: A comparison of methods, Int. J. Climatol., 33, 1367–1381, https://doi.org/10.1002/joc.3518, 2013.

Lambeck, K., Rouby, H., Purcell, A., Sun, Y., and Sambridge, M.: Sea level and global ice volumes from the Last Glacial Maximum to the Holocene, P. Natl. Acad. Sci. USA, 111, 15 296–15 303, https://doi.org/10.1073/pnas.1411762111, 2014.

Leung, L. R., Mearns, L. O., Giorgi, F., and Wilby, R. L.: Regional climate research, B. Am. Meteorol. Soc., 84, 89–95, https://doi.org/10.1175/BAMS-84-1-89, 2003.

Liu, Z., Wang, Y., Gallimore, R., Notaro, M., and Prentice, I. C.: On the cause of abrupt vegetation collapse in North Africa during the Holocene: Climate variability vs. vegetation feedback, Geophys. Res. Lett., 33, L22709, https://doi.org/10.1029/2006GL028062, 2006.

Liu, Z., Ballantyne, A. P., Poulter, B., Anderegg, W. R. L., Li, W., Bastos, A., and Ciais, P.: Precipitation thresholds regulate net carbon exchange at the continental scale, Nat. Commun., 9, 3596, https://doi.org/10.1038/s41467-018-05948-1, 2018.

Ludwig, P., Schaffernicht, E. J., Shao, Y., and Pinto, J. G.: Regional atmospheric circulation over Europe during the Last Glacial Maximum and its links to precipitation, J. Geophys. Res.-Atmos., 121, 2130–2145, https://doi.org/10.1002/2015JD024444, 2016.

Ludwig, P., Pinto, J. G., Raible, C. C., and Shao, Y.: Impacts of surface boundary conditions on regional climate model simulations of European climate during the Last

Glacial Maximum, Geophys. Res. Lett., 44, 5086–5095, https://doi.org/10.1002/2017GL073622, 2017.

Luetscher, M., Boch, R., Sodemann, H., Spötl, C., Cheng, H., Edwards, R. L., Frisia, S., Hof, F., and Müller, W.: North Atlantic storm track changes during the Last Glacial Maximum recorded by Alpine speleothems, Nat. Commun., 6, 6344, https://doi.org/10.1038/ncomms7344, 2015.

Maraun, D.: Bias correction, quantile mapping, and downscaling: Revisiting the inflation issue, J. Climate, 26, 2137–2143, https://doi.org/10.1175/JCLI-D-12-00821.1, 2013.

Maraun, D.: Bias correcting climate change simulations - a critical review, Curr. Clim. Change Rep., 2, 211–220, https://doi.org/10.1007/s40641-016-0050-x, 2016.

Maraun, D. and Widmann, M.: The representation of location by a regional climate model in complex terrain, Hydrol. Earth Syst. Sci., 19, 3449–3456, https://doi.org/10.5194/hess-19-3449-2015, 2015.

Maraun, D. and Widmann, M.: Cross-validation of bias-corrected climate simulations is misleading, Hydrol. Earth Syst. Sci., 22, 4867–4873, https://doi.org/10.5194/hess-22-4867-2018, 2018a.

Maraun, D. and Widmann, M.: Statistical downscaling and bias correction for climate research, Cambridge University Press, Cambridge, UK and New York, NY, USA, 2018b.

Maraun, D., Wetterhall, F., Ireson, A. M., Chandler, R. E., Kendon, E. J., Widmann, M., Brienen, S., Rust, H. W., Sauter, T., Themeßl, M., Venema, V. K. C., Chun, K. P., Goodess, C. M., Jones, R. G., Onof, C., Vrac, M., and Thiele-Eich, I.: Precipitation downscaling under climate change: Recent developments to bridge the gap between dynamical models and the end user, Rev. Geophys., 48, RG3003, https://doi.org/10.1029/2009RG000314, 2010.

Maraun, D., Shepherd, T. G., Widmann, M., Zappa, G., Walton, D., Gutiérrez, J. M., Hagemann, S., Richter, I., Soares, P. M. M., Hall, A., and Mearns, L. O.: Towards process-informed bias correction of climate change simulations, Nat. Clim. Change, 7, 764–773, https://doi.org/10.1038/nclimate3418, 2017.

Mayewski, P. A., Rohling, E. E., Stager, J. C., Karlén, W., Maasch, K. A., Meeker, L. D., Meyerson, E. A., Gasse, F., Kreveld, S. v., Holmgren, K., Lee-Thorp, J., Rosqvist, G., Rack, F., Staubwasser, M., Schneider, R. R., and Steig, E. J.: Holocene climate variability, Quaternary Res., 62, 243–255, https://doi.org/10.1016/j.yqres.2004.07.001, 2004.

Menéndez, C. G., de Castro, M., Boulanger, J.-P., D'Onofrio, A., Sanchez, E., Sörensson, A. A., Blazquez, J., Elizalde, A., Jacob, D., Le Treut, H., Li, Z. X., Núñez, M. N., Pessacg, N., Pfeiffer, S., Rojas, M., Rolla, A., Samuelsson, P., Solman, S. A., and Teichmann, C.: Downscaling extreme month-long anomalies in southern South America, Climatic Change, 98, 379–403, https://doi.org/10.1007/s10584-009-9739-3, 2010.

Merz, N., Raible, C. C., Fischer, H., Varma, V., Prange, M., and Stocker, T. F.: Greenland accumulation and its connection to the large-scale atmospheric circulation in ERA-Interim and paleoclimate simulations, Clim. Past, 9, 2433–2450, https://doi.org/10.5194/cp-9-2433-2013, 2013.

Merz, N., Born, A., Raible, C. C., Fischer, H., and Stocker, T. F.: Dependence of Eemian Greenland temperature reconstructions on the ice sheet topography, Clim. Past, 10, 1221–1238, https://doi.org/10.5194/cp-10-1221-2014, 2014a.

Merz, N., Gfeller, G., Born, A., Raible, C. C., Stocker, T. F., and Fischer, H.: Influence of ice sheet topography on Greenland precipitation during the Eemian interglacial, J. Geophys. Res.-Atmos., 119, 10,749–10,768, https://doi.org/10.1002/2014JD021940, 2014b.

Merz, N., Raible, C. C., and Woollings, T.: North Atlantic Eddy-Driven jet in interglacial and glacial winter climates, J. Climate, 28, 3977–3997, https://doi.org/10.1175/JCLI-D-14-00525.1, 2015.

Messmer, M., Gómez-Navarro, J. J., and Raible, C. C.: Sensitivity experiments on the response of Vb cyclones to sea surface temperature and soil moisture changes, Earth Syst. Dynam., 8, 477–493, https://doi.org/10.5194/esd-8-477-2017, 2017.

MeteoSwiss: Documentation of MeteoSwiss gridded data product, daily precipitation: RhiresD, available at: http://www.meteoschweiz.admin.ch/content/dam/meteoswiss/de/service-und-publikationen/produkt/raeumliche-daten-niederschlag/doc/ProdDoc_RhiresD.pdf (last access: 12 October 2020), 2013.

Mitchell, D., Davini, P., Harvey, B., Massey, N., Haustein, K., Woollings, T., Jones, R., Otto, F., Guillod, B., Sparrow, S., Wallom, D., and Allen, M.: Assessing mid-latitude dynamics in extreme event attribution systems, Clim. Dynam., 48, 3889–3901, https://doi.org/10.1007/s00382-016-3308-z, 2017.

Moss, R. H., Edmonds, J. A., Hibbard, K. A., Manning, M. R., Rose, S. K., van Vuuren, D. P., Carter, T. R., Emori, S., Kainuma, M., Kram, T., Meehl, G. A., Mitchell, J. F. B., Nakicenovic, N., Riahi, K., Smith, S. J., Stouffer, R. J., Thomson, A. M., Weyant, J. P., and Wilbanks, T. J.: The next generation of scenarios for climate change research and assessment, Nature, 463, 747–756, https://doi.org/10.1038/nature08823, 2010.

Murphy, J.: An evaluation of statistical and dynamical techniques for downscaling local climate, J. Climate, 12, 2256–2284, https://doi.org/10.1175/1520-0442(1999)012<2256:AEOSAD>2.0.CO;2, 1999.

Neale, R. B., Richter, J. H., Conley, A. J., Park, S., Lauritzen, P. H., Gettelman, A., Rasch, P. J., and Vavrus, J.: Description of the NCAR community atmosphere model (CAM4), National Center for Atmospheric Research Tech. Rep. NCAR/TN+STR, available at: http://www.cesm.ucar.edu/models/ccsm4.0/cam/docs/description/cam4_desc.pdf (last access: 12 October 2020), 2010.

Nešpor, V. and Sevruk, B.: Estimation of wind-induced error of rainfall gauge measurements using a numerical simulation, J. Atmos. Ocean. Tech., 16, 450–464, https://doi.org/10.1175/1520-0426(1999)016<0450:EOWIEO>2.0.CO;2, 1999.

Oleson, W., Lawrence, M., Bonan, B., Flanner, G., Kluzek, E., Lawrence, J., Levis, S., Swenson, C., Thornton, E., Dai, A., Decker, M., Dickinson, R., Feddema, J., Heald, L., Hoffman, F., Lamarque, J.-F., Mahowald, N., Niu, G.-Y., Qian, T., Randerson, J., Running, S., Sakaguchi, K., Slater, A., Stockli, R., Wang, A., Yang, Z.-L., Zeng, X., and Zeng, X.: Technical description of version 4.0 of the community land model (CLM), NCAR Technical Note NCAR/TN-478+STR, National Center for Atmospheric Research, National Center for Atmospheric Research, Boulder, CO, ISSN 2153-2397, available at: http://www.cesm.ucar.edu/models/cesm1.0/clm/CLM4_Tech_Note.pdf (last access: 12 October 2020), 2010.

Otto-Bliesner, B. L., Brady, E. C., Clauzet, G., Tomas, R., Levis, S., and Kothavala, Z.: Last Glacial Maximum and Holocene Climate in CCSM3, J. Climate, 19, 2526–2544, https://doi.org/10.1175/JCLI3748.1, 2006.

Peltier, W. R. and Fairbanks, R. G.: Global glacial ice volume and Last Glacial Maximum duration from an extended Barbados sea level record, Quaternary Sci. Rev., 25, 3322–3337, https://doi.org/10.1016/j.quascirev.2006.04.010, 2006.

Piani, C., Haerter, J. O., and Coppola, E.: Statistical bias correction for daily precipitation in regional climate models over Europe, Theor. Appl. Climatol., 99, 187–192, https://doi.org/10.1007/s00704-009-0134-9, 2010a.

Piani, C., Weedon, G. P., Best, M., Gomes, S. M., Viterbo, P., Hagemann, S., and Haerter, J. O.: Statistical bias correction of global simulated daily precipitation and temperature for the application of hydrological models, J. Hydrol., 395, 199–215, https://doi.org/10.1016/j.jhydrol.2010.10.024, 2010b.

Pinto, J. G. and Ludwig, P.: Extratropical cyclones over the North Atlantic and western Europe during the Last Glacial Maximum and implications for proxy interpretation, Clim. Past, 16, 611–626, https://doi.org/10.5194/cp-16-611-2020, 2020.

Prein, A. F., Langhans, W., Fosser, G., Ferrone, A., Ban, N., Goergen, K., Keller, M., Tölle, M., Gutjahr, O., Feser, F., Brisson, E., Kollet, S., Schmidli, J., Lipzig, N. P. M. v., and Leung, R.: A review on regional convection-permitting climate modeling: Demonstrations, prospects, and challenges, Rev. Geophys., 53, 323–361, https://doi.org/10.1002/2014RG000475, 2015.

Raible, C. C., Stocker, T. F., Yoshimori, M., Renold, M., Beyerle, U., Casty, C., and Luterbacher, J.: Northern hemispheric trends of pressure indices and atmospheric circulation patterns in observations, reconstructions, and coupled GCM simulations, J. Climate, 18, 3968–3982, https://doi.org/10.1175/JCLI3511.1, 2005.

Raible, C. C., Lehner, F., González-Rouco, J. F., and Fernández-Donado, L.: Changing correlation structures of the Northern Hemisphere atmospheric circulation from 1000 to 2100 AD, Clim. Past, 10, 537–550, https://doi.org/10.5194/cp-10-537-2014, 2014.

Raible, C. C., Brönnimann, S., Auchmann, R., Brohan, P., Frölicher, T. L., Graf, H.-F., Jones, P., Luterbacher, J., Muthers, S., Neukom, R., Robock, A., Self, S., Sudrajat, A., Timmreck, C., and Wegmann, M.: Tambora 1815 as a test case for high impact volcanic eruptions: Earth system effects, Wiley Interdiscip. Rev. Clim. Change, 7, 569–589, https://doi.org/10.1002/wcc.407, 2016.

Rajczak, J. and Schär, C.: Projections of future precipitation extremes over Europe: A multimodel assessment of climate simulations, J. Geophys. Res.-Atmos., 122, 10 773–10 800, https://doi.org/10.1002/2017JD027176, 2017.

Rajczak, J., Kotlarski, S., and Schär, C.: Does quantile mapping of simulated precipitation correct for biases in transition probabilities and spell lengths?, J. Climate, 29, 1605–1615, https://doi.org/10.1175/JCLI-D-15-0162.1, 2016.

Richter, D.: Ergebnisse methodischer untersuchungen zur korrektur des systematischen messfehlers des hellmann-niederschlagsmessers, Deutscher Wetterdienst, Offenbach, 1995.

Rougier, J., Sexton, D. M. H., Murphy, J. M., and Stainforth, D.: Analyzing the climate sensitivity of the HadSM3 climate model using ensembles from different but related experiments, J. Climate, 22, 3540–3557, https://doi.org/10.1175/2008JCLI2533.1, 2009.

RStudio Team: RStudio: Integrated Development Environment for R, RStudio, Inc., Boston, MA, available at: http://www.rstudio.com/ (last access: 12 October 2020), 2015.

Schmidli, J., Schmutz, C., Frei, C., Wanner, H., and Schär, C.: Mesoscale precipitation variability in the region of the European Alps during the 20th century, Int. J. Climatol., 22, 1049–1074, https://doi.org/10.1002/joc.769, 2002.

Schmidli, J., Frei, C., and Vidale, P. L.: Downscaling from GCM precipitation: A benchmark for dynamical and statistical downscaling methods, Int. J. Climatol., 26, 679–689, https://doi.org/10.1002/joc.1287, 2006.

Schulzweida, U.: CDO User Guide (Version 1.9.6), Zenodo, https://doi.org/10.5281/zenodo.2558193, 2019.

Schwarb, M., Daly, C., Frei, C., and Schär, C.: Mean annual and seasonal precipitation in the European Alps 1971–1990, Hydrological Atlas of Switzerland, Landeshydrologie und Geologie, Bern, Switzerland, 2001.

Seguinot, J., Khroulev, C., Rogozhina, I., Stroeven, A. P., and Zhang, Q.: The effect of climate forcing on numerical simulations of the Cordilleran ice sheet at the Last Glacial Maximum, The Cryosphere, 8, 1087–1103, https://doi.org/10.5194/tc-8-1087-2014, 2014.

Seguinot, J., Ivy-Ochs, S., Jouvet, G., Huss, M., Funk, M., and Preusser, F.: Modelling last glacial cycle ice dynamics in the Alps, The Cryosphere, 12, 3265–3285, https://doi.org/10.5194/tc-12-3265-2018, 2018.

Sevruk, B.: Systematischer Niederschlagsmessfehler in der Schweiz, Der Niederschlag in der Schweiz. Beiträge zur Geologie der Schweiz – Hydrologie, 31, 65–75, 1985.

Shepard, D. S.: Computer mapping: The SYMAP interpolation algorithm, in: Spatial Statistics and Models, Theory and Decision Library, pp. 133–145, Springer, Dordrecht, https://doi.org/10.1007/978-94-017-3048-8_7, 1984.

Skamarock, W. C. and Klemp, J. B.: A time-split nonhydrostatic atmospheric model for weather research and forecasting applications, J. Comput. Physics, 227, 3465–3485, https://doi.org/10.1016/j.jcp.2007.01.037, 2008.

Skamarock, W. C., Klemp, J. B., Dudhia, J., Gill, D. O., Barker, D. M., Wang, W., and Powers, J. G.: A description of the advanced research WRF version 2, available at: https://www2.mmm.ucar.edu/wrf/users/index.html (last access: 12 October 2020), National center for atmospheric research, Boulder, CO, USA, 2005.

Solman, S. A., Nuñez, M. N., and Cabré, M. F.: Regional climate change experiments over southern South America. I: Present climate, Clim. Dynam., 30, 533–552, https://doi.org/10.1007/s00382-007-0304-3, 2008.

Stocker, T., Plattner, G.-K., Tignor, M., Allen, S., Boschung, J., Nauels, A., Xia, Y., Bex, V., and Midgley, P., eds.: Climate change 2013: The physical science basis. Contribution of working group I to the fifth assessment report of IPCC the Intergovernmental Panel on Climate Change, Cambridge University Press, Cambridge, United Kingdom and New York, NY, USA, https://doi.org/10.1017/CBO9781107415324, 2013.

Su, F., Duan, X., Chen, D., Hao, Z., and Cuo, L.: Evaluation of the global climate models in the CMIP5 over the Tibetan Plateau, J. Climate, 26, 3187–3208, https://doi.org/10.1175/JCLI-D-12-00321.1, 2012.

Sun, F., Roderick, M. L., Lim, W. H., and Farquhar, G. D.: Hydroclimatic projections for the Murray-Darling Basin based on an ensemble derived from Intergovernmental Panel on Climate Change AR4 climate models, Water Resour. Res., 47, W00G02, https://doi.org/10.1029/2010WR009829, 2011.

Teng, J., Potter, N. J., Chiew, F. H. S., Zhang, L., Wang, B., Vaze, J., and Evans, J. P.: How does bias correction of regional climate model precipitation affect modelled runoff?, Hydrol. Earth Syst. Sci., 19, 711–728, https://doi.org/10.5194/hess-19-711-2015, 2015.

Teutschbein, C. and Seibert, J.: Bias correction of regional climate model simulations for hydrological climate-change impact studies: Review and evaluation of different methods, J. Hydrol., 456-457, 12–29, https://doi.org/10.1016/j.jhydrol.2012.05.052, 2012.

Teutschbein, C. and Seibert, J.: Is bias correction of regional climate model (RCM) simulations possible for non-stationary conditions?, Hydrol. Earth Syst. Sci., 17, 5061–5077, https://doi.org/10.5194/hess-17-5061-2013, 2013.

Themessl, M. J., Gobiet, A., and Leuprecht, A.: Empirical-statistical downscaling and error correction of daily precipitation from regional climate models, Int. J. Climatol., 31, 1530–1544, https://doi.org/10.1002/joc.2168, 2011.

Themessl, M. J., Gobiet, A., and Heinrich, G.: Empirical-statistical downscaling and error correction of regional climate models and its impact on the climate change signal, Climatic Change, 112, 449–468, https://doi.org/10.1007/s10584-011-0224-4, 2012.

UCAR/NCAR/CISL/TDD: The NCAR Command Language (Version 6.6.2) [Software], https://doi.org/10.5065/D6WD3XH5, 2019.

Ungersböck, M., Auer, I., Rubel, F., Schöner, W., and Skomorowski, P.: Zur Korrektur des systematischen Fehlers bei der Niederschlagsmessung: Anwendung des Verfahrens für die ÖK-LIM Karten, 5, 2001.

Velasquez, P., Messmer, M., and Raible, C. C.: Code and Dataset, Zenodo, https://doi.org/10.5281/zenodo.4009101, 2019.

Velasquez, P., Kaplan, J. O., Messmer, M., Ludwig, P., and Raible, C. C.: Iterative asynchronous modeling of surface conditions over Europe during LGM, Quaternary Sci. Rev., in preparation, 2020.

Wang, Z., Wen, X., Lei, X., Tan, Q., Fang, G., and Zhang, X.: Effects of different statistical distribution and threshold criteria in extreme precipitation modelling over global land areas, Int. J. Climatol., 40, 1838–1850, https://doi.org/10.1002/joc.6305, 2020.

Warrach-Sagi, K., Schwitalla, T., Wulfmeyer, V., and Bauer, H.-S.: Evaluation of a climate simulation in Europe based on the WRF–NOAH model system: Precipitation in Germany, Clim. Dynam., 41, 755–774, https://doi.org/10.1007/s00382-013-1727-7, 2013.

Wilcke, R. A. I., Mendlik, T., and Gobiet, A.: Multi-variable error correction of regional climate models, Climatic Change, 120, 871–887, https://doi.org/10.1007/s10584-013-0845-x, 2013.

Wilks, D. S.: Statistical methods in the atmospheric sciences, Academic Press, 2011.

Wren, C. D. and Burke, A.: Habitat suitability and the genetic structure of human populations during the Last Glacial Maximum (LGM) in Western Europe, PLoS One, 14, e0217 996, https://doi.org/10.1371/journal.pone.0217996, 2019.

Wu, H., Guiot, J., Brewer, S., and Guo, Z.: Climatic changes in Eurasia and Africa at the last glacial maximum and mid-Holocene: reconstruction from pollen data using inverse vegetation modelling, Clim. Dynam., 29, 211–229, https://doi.org/10.1007/s00382-007-0231-3, 2007.

Xu, C.-y.: Modelling the effects of climate change on water resources in central sweden, Water Resources Management, 14, 177–189, https://doi.org/10.1023/A:1026502114663, 2000.

Xu, C.-y., Widén, E., and Halldin, S.: Modelling hydrological consequences of climate change – Progress and challenges, Advances in Atmospheric Sciences, 22, 789–797, https://doi.org/10.1007/BF02918679, 2005.

Yang, B., Qian, Y., Lin, G., Leung, L. R., Rasch, P. J., Zhang, G. J., McFarlane, S. A., Zhao, C., Zhang, Y., Wang, H., Wang, M., and Liu, X.: Uncertainty quantification and parameter tuning in the CAM5 Zhang-McFarlane convection scheme and impact of improved convection on the global circulation and climate, J. Geophys. Res.-Atmos., 118, 395–415, https://doi.org/10.1029/2012JD018213, 2013.

Yang, W., Andréasson, J., Graham, L. P., Olsson, J., Rosberg, J., and Wetterhall, F.: Distribution-based scaling to improve usability of regional climate model projections for hydrological climate change impacts studies, Hydrology Research, 41, 211–229, https://doi.org/10.2166/nh.2010.004, 2010.

Yokoyama, Y., Lambeck, K., De Deckker, P., Johnston, P., and Fifield, L. K.: Timing of the Last Glacial Maximum from observed sea-level minima, Nature, 406, 713–716, https://doi.org/10.1038/35021035, 2000.

Zhang, G. J. and McFarlane, N. A.: Sensitivity of climate simulations to the parameterization of cumulus convection in the Canadian climate centre general circulation model, Atmosphere-Ocean, 33, 407–446, https://doi.org/10.1080/07055900.1995.9649539, 1995.

Zhao, Y., Liu, Y., Guo, Z., Fang, K., Li, Q., and Cao, X.: Abrupt vegetation shifts caused by gradual climate changes in central Asia during the Holocene, Science China Earth Sciences, 60, 1317–1327, https://doi.org/10.1007/s11430-017-9047-7, 2017.

Chapter 6

Outlook

The goal of this thesis was to investigate the impact of glacial surface conditions on the European climate using climate model simulations at glacial times. Two studies conducted in the framework of this thesis demonstrated that surface conditions play an important role in regulating the regional glacial climate (Velasquez et al., 2021a,b). A third study (Velasquez et al., 2020) presented a new bias-correction method for precipitation whose application is more appropriate under highly different climate conditions such as glacial times than standard techniques commonly used under present day and future conditions (e.g, Maraun, 2013; Teng et al., 2015; Casanueva et al., 2016; Ivanov et al., 2018).

The first study (Velasquez et al., 2021a) assessed the role of the glacial land cover in the European glacial climate. The results show that dry conditions in the Last Glacial Maximum (LGM) are partially attributed to LGM land cover, i.e., to the reduction in vegetation compared to present-day land cover. This is particularly true for central and eastern Europe during summer. From this first study, future studies will benefit from even more detailed climate simulations, particularly to better understand precipitation patterns in complex terrain such as Iberia, across the Mediterranean, and in the Carpathians. This is also true for studies on the local and regional paleobotany and archaeology of this important period in Europe's history. Nevertheless, there is room for improvements, especially in a further evaluation of the modelled climate. An evaluation of the modelled LGM climate should be performed with independent paleoclimate reconstructions from more sites than the 14 published points that are in the spatial domain of this study. Since the publication of Wu et al. (2007) and Bartlein et al. (2011), more than 70 well-dated pollen records have become available for Europe at the LGM (Kaplan et al., 2016) but not transformed into paleoenvironmental reconstructions to-date yet. As soon as more paleoenvironmental reconstructions become available, futures studies will therefore be able to examine specific areas in more detail.

The second study (Velasquez et al., 2021b) determined the influence of the northern-hemispheric ice-sheet topography on the Alpine climate. Results show that an increase of the northern hemispheric ice sheet leads to an intensification of glacial conditions over the Alps. Especially, the Laurentide and Alpine ice-sheet topography strongly influence the climate over

the Alpine region. In a potential following-up work, only the Fennoscandian ice-sheet needs to be modified in the driving global climate model keeping the other northern-hemispheric ice sheet unchanged. This will reduce the uncertainties coming from the boundary conditions in the Fennoscandian experiment. Also, the current simulation length related to the Fennoscandian experiment might lead to uncertainties when comparing it with the baseline LGM climate. Additionally, the analysis presented in this study suggests that future modelling efforts shall ideally involve coupled glacier models. This is not possible at the moment due to the long calculation time needed for glacier models and the high computational cost of regional climate simulations. An intermediate step is to use the output of different sensitivity simulations in ice-sheet modelling studies (e.g., Jouvet et al., 2017; Seguinot et al., 2018). Also, future work will profit from even more detailed information about climate variables over the Alpine region, particularly to better understand precipitation patterns in complex terrain. Studies on the local and regional paleobotany, archaeology and anthropology will surely benefit from both the climate variables and the better understanding of the ice-sheet dynamics (e.g., Finlayson, 2004; Finlayson et al., 2006; Finlayson, 2008; Burke et al., 2014; Kaplan et al., 2016; Maier et al., 2016; Burke et al., 2017; Baena Preysler et al., 2019; Wren and Burke, 2019).

The third study (Velasquez et al., 2020) presents a new bias-correction method for precipitation over complex topography, which uses a quantile mapping technique that takes orographic characteristics into account. This method is mainly designed for climate states where the topography is distinctively different to the present-day one, i.e. glacial times. The evaluation of the method's performance does not only show robust results, but also that the new method substantially reduces the precipitation bias, especially the seasonal precipitation bias induced by the global climate model. Comparing the new method to the standard empirical quantile mapping (EQM) technique indicates that the new method is safer and therefore more appropriate under LGM climate conditions. However, a drawback is that the method ignores a potential modification of the bias structure due to the handling of rainfall and snowfall in the model's microphysics. Even though the new method includes some aspects of this handling, a future work is needed as soon as reliable observations of snowfall are available. A following-up work would be the assessment of other variables of the Earth's system on bias-correction methods, i.e., the response of soil-moisture and snow-albedo to the corrected precipitation patterns. Using this new method, glaciologists can benefit from a better accuracy of precipitation data that is used as an input for their glacier models.

Bibliography

Baena Preysler, J., Carrión Santafé, E., Torres Navas, C., and Vaquero Rodríguez, M.: Mousterian inside the upper Paleolithic? The last interval of El Esquilleu (Cantabria, Spain) sequence, Quaternary International, 508, 153–163, doi:10.1016/j.quaint.2018.11.015, 2019.

Bartlein, P. J., Harrison, S. P., Brewer, S., Connor, S., Davis, B. A. S., Gajewski, K., Guiot, J., Harrison-Prentice, T. I., Henderson, A., Peyron, O., Prentice, I. C., Scholze, M., Seppä, H., Shuman, B., Sugita, S., Thompson, R. S., Viau, A. E., Williams, J., and Wu, H.: Pollen-based continental climate reconstructions at 6 and 21 ka: a global synthesis, Climate Dynamics, 37, 775–802, doi:10.1007/s00382-010-0904-1, 2011.

Burke, A., Levavasseur, G., James, P. M. A., Guiducci, D., Izquierdo, M. A., Bourgeon, L., Kageyama, M., Ramstein, G., and Vrac, M.: Exploring the impact of climate variability during the Last Glacial Maximum on the pattern of human occupation of Iberia, Journal of Human Evolution, 73, 35–46, doi:10.1016/j.jhevol.2014.06.003, 2014.

Burke, A., Kageyama, M., Latombe, G., Fasel, M., Vrac, M., Ramstein, G., and James, P. M. A.: Risky business: the impact of climate and climate variability on human population dynamics in Western Europe during the Last Glacial Maximum, Quaternary Science Reviews, 164, 217–229, doi:10.1016/j.quascirev.2017.04.001, 2017.

Casanueva, A., Kotlarski, S., Herrera, S., Fernández, J., Gutiérrez, J. M., Boberg, F., Colette, A., Christensen, O. B., Goergen, K., Jacob, D., Keuler, K., Nikulin, G., Teichmann, C., and Vautard, R.: Daily precipitation statistics in a EURO-CORDEX RCM ensemble: added value of raw and bias-corrected high-resolution simulations, Climate Dynamics, 47, 719–737, doi:10.1007/s00382-015-2865-x, 2016.

Finlayson, C.: Neanderthals and modern humans: an ecological and evolutionary perspective, vol. 38, Cambridge University Press, 2004.

Finlayson, C.: On the importance of coastal areas in the survival of Neanderthal populations during the Late Pleistocene, Quaternary Science Reviews, 27, 2246–2252, doi:10.1016/j.quascirev.2008.08.033, 2008.

Finlayson, C., Giles Pacheco, F., Rodríguez-Vidal, J., Fa, D. A., María Gutierrez López, J., Santiago Pérez, A., Finlayson, G., Allue, E., Baena Preysler, J., Cáceres, I., Carrión, J. S., Fernández Jalvo, Y., Gleed-Owen, C. P., Jimenez Espejo, F. J., López, P., Antonio López Sáez, J., Antonio Riquelme Cantal, J., Sánchez Marco, A., Giles Guzman, F., Brown, K., Fuentes, N., Valarino, C. A., Villalpando, A., Stringer, C. B., Martinez Ruiz, F., and Sakamoto, T.: Late survival of Neanderthals at the southernmost extreme of Europe, Nature, 443, 850–853, doi:10.1038/nature05195, 2006.

Ivanov, M. A., Luterbacher, J., and Kotlarski, S.: Climate model biases and modification of the climate change signal by intensity-dependent bias correction, Journal of Climate, 31, 6591–6610, doi:10.1175/JCLI-D-17-0765.1, 2018.

Jouvet, G., Seguinot, J., Ivy-Ochs, S., and Funk, M.: Modelling the diversion of erratic boulders by the Valais Glacier during the last glacial maximum, Journal of Glaciology, 63, 487–498, doi:10.1017/jog.2017.7, 2017.

Kaplan, J. O., Pfeiffer, M., Kolen, J. C. A., and Davis, B. A. S.: Large scale anthropogenic reduction of forest cover in Last Glacial Maximum Europe, PLOS ONE, 11, e0166 726, doi:10.1371/journal.pone.0166726, 2016.

Maier, A., Lehmkuhl, F., Ludwig, P., Melles, M., Schmidt, I., Shao, Y., Zeeden, C., and Zimmermann, A.: Demographic estimates of hunter–gatherers during the Last Glacial Maximum in Europe against the background of palaeoenvironmental data, Quaternary International, 425, 49–61, doi:10.1016/j.quaint.2016.04.009, 2016.

Maraun, D.: Bias correction, quantile mapping, and downscaling: revisiting the inflation issue, Journal of Climate, 26, 2137–2143, doi:10.1175/JCLI-D-12-00821.1, 2013.

Seguinot, J., Ivy-Ochs, S., Jouvet, G., Huss, M., Funk, M., and Preusser, F.: Modelling last glacial cycle ice dynamics in the Alps, The Cryosphere, 12, 3265–3285, doi:10.5194/tc-12-3265-2018, 2018.

Teng, J., Potter, N. J., Chiew, F. H. S., Zhang, L., Wang, B., Vaze, J., and Evans, J. P.: How does bias correction of regional climate model precipitation affect modelled runoff?, Hydrology and Earth System Sciences, 19, 711–728, doi:10.5194/hess-19-711-2015, 2015.

Velasquez, P., Messmer, M., and Raible, C. C.: A new bias-correction method for precipitation over complex terrain suitable for different climate states: a case study using WRF (version 3.8.1), Geoscientific Model Development, 13, 5007–5027, doi:10.5194/gmd-13-5007-2020, 2020.

Velasquez, P., Kaplan, J. O., Messmer, M., Ludwig, P., and Raible, C. C.: The role of land cover in the climate of glacial Europe, Climate of the Past, 17, 1161–1180, doi:10.5194/cp-17-1161-2021, 2021a.

Velasquez, P., Messmer, M., and Raible, C. C.: The role of ice-sheet topography in the alpine hydro-climate at glacial times, Climate of the Past Discussions, pp. 1–34, doi:10.5194/cp-2021-67, 2021b.

Wren, C. D. and Burke, A.: Habitat suitability and the genetic structure of human populations during the Last Glacial Maximum (LGM) in Western Europe, PLOS ONE, 14, e0217 996, doi:10.1371/journal.pone.0217996, 2019.

Wu, H., Guiot, J., Brewer, S., and Guo, Z.: Climatic changes in Eurasia and Africa at the last glacial maximum and mid-Holocene: reconstruction from pollen data using inverse vegetation modelling, Climate Dynamics, 29, 211–229, doi:10.1007/s00382-007-0231-3, 2007.

Appendix A

NAMELIST.WPS

This appendix shows the file namelist.wps used in WPS.

&share
wrf_core = 'ARW',
max_dom = 4,
start_date = 'DATE1','DATE1','DATE1','DATE1',
end_date = 'DATE2','DATE2','DATE2','DATE2',
interval_seconds = 21600,
io_form_geogrid = 2,
/

&geogrid
parent_id = 1, 1, 2, 3,
parent_grid_ratio = 1, 3, 3, 3,
I_parent_start = 1, 13, 68, 23,
j_parent_start = 1, 10, 31, 24,
e_we = 84, 169, 196, 472,
e_sn = 83, 172, 229, 286,
geog_data_res = 'modis_30s+modis_lakes+5m','modis_30s+modis_lakes+2m', ...
...'modis_30s+modis_lakes+30s','modis_30s+modis_lakes+30s',
dx = 54000,
dy = 54000,
map_proj = 'lambert',
ref_lat = 52.848,
ref_lon = 7.892,
truelat1 = 52.848,
truelat2 = 52.848,
stand_lon = 7.892,

```
geog_data_path    = 'geog/'
ref_x             = 42.0,
ref_y             = 41.5,
/

&ungrib
out_format        = 'WPS',
prefix            = 'FILE',
/

&metgrid
fg_name           = 'FILE',
io_form_metgrid   = 2,
/
```

Appendix B

NAMELIST.INPUT

This appendix shows the file namelist.input used in WRF.

&time_control

run_days	= SIMDAY01,
run_hours	= 0,
run_minutes	= 0,
run_seconds	= 0,
start_year	= YEAR1, YEAR1, YEAR1, YEAR1,
start_month	= MONTH1, MONTH1, MONTH1, MONTH1,
start_day	= DAY1, DAY1, DAY1, DAY1,
start_hour	= HOUR1, HOUR1, HOUR1, HOUR1,
start_minute	= 00, 00, 00, 00,
start_second	= 00, 00, 00, 00,
end_year	= YEAR2, YEAR2, YEAR2, YEAR2,
end_month	= MONTH2, MONTH2, MONTH2, MONTH2,
end_day	= DAY2, DAY2, DAY2, DAY2,
end_hour	= 18, 18, 18, 18,
end_minute	= 00, 00, 00, 00,
end_second	= 00, 00, 00, 00,
interval_seconds	= 21600,
input_from_file	= .true.,.true.,.true.,.true.,
history_interval	= 360, 360, 360, 360,
frames_per_outfile	= 1460, 1460, 1460, 1460,
restart	= .BOOLEAN.,
restart_interval	= 1440,

io_form_history = 2,
io_form_restart = 2,
io_form_input = 2,
io_form_boundary = 2,
io_form_auxinput4 = 2,
auxinput4_inname = "wrflowinp_d<domain>",
auxinput4_interval = 360, 360, 360, 360,
output_diagnostics = 1,
io_form_auxhist3 = 2,
auxhist3_interval = 1440, 1440, 1440, 1440,
debug_level = 0,
adjust_output_times = .true.,
iofields_filename = T2_hourly_d01.txt, T2_hourly_d02.txt, T2_hourly_d03.txt, ...
... T2_hourly_d04.txt,
ignore_iofields_warning = .true.,
auxhist7_outname = T2_hourly_d<domain>_<date>,
auxhist7_interval = 60, 60, 60, 60,
frames_per_auxhist7 = 1460, 1460, 1460, 1460,
io_form_auxhist7 = 2
/

&domains
use_adaptive_time_step = .true.,
step_to_output_time = .true.,
adaptation_domain = 4,
target_cfl = 1.0, 1.0, 1.0, 1.0,
starting_time_step = 324, 108, 36, 12,
max_step_increase_pct = 5, 51, 51, 51,
max_time_step = -1, -1, -1, -1,
min_time_step = 108, 36, 12, 4,
time_step = 324,
time_step_fract_num = 0,
time_step_fract_den = 1,
max_dom = 4,
s_we = 1, 1, 1, 1,
e_we = 84, 169, 196, 472,
s_sn = 1, 1, 1, 1,
e_sn = 83, 172, 229, 286,

s_vert = 1, 1, 1, 1,
e_vert = 40, 40, 40, 40,
p_top_requested = 5000,
num_metgrid_levels = 15,
num_metgrid_soil_levels = 4,
dx = 54000, 18000, 6000, 2000,
dy = 54000, 18000, 6000, 2000,
grid_id = 1, 2, 3, 4,
parent_id = 1, 1, 2, 3,
i_parent_start = 1, 13, 68, 23,
j_parent_start = 1, 10, 31, 24,
parent_grid_ratio = 1, 3, 3, 3,
parent_time_step_ratio = 1, 3, 3, 3,
feedback = 1,
smooth_option = 0
/

&physics
mp_physics = 6, 6, 6, 6,
ra_lw_physics = 1, 1, 1, 1,
ra_sw_physics = 1, 1, 1, 1,
radt = 5, 5, 5, 5,
sf_sfclay_physics = 1, 1, 1, 1,
sf_surface_physics = 4, 4, 4, 4,
bl_pbl_physics = 1, 1, 1, 1,
bldt = 0, 0, 0, 0,
cu_physics = 1, 1, 0, 0,
cudt = 5, 5, 5, 5,
isfflx = 1,
ifsnow = 0,
icloud = 1,
surface_input_source = 1,
num_soil_layers = 4,
sf_urban_physics = 0, 0, 0, 0,
maxiens = 1,
maxens = 3,
maxens2 = 3,
maxens3 = 16,
ensdim = 144,
sst_update = 1,
topo_wind = 0, 0, 0, 1,
num_land_cat = 20
/

&fdda
/

&dynamics
w_damping = 0,
diff_opt = 1,
km_opt = 4,
diff_6th_opt = 0, 0, 0, 0,
diff_6th_factor = 0.12, 0.12, 0.12, 0.12,
base_temp = 290.,
damp_opt = 0,
zdamp = 5000., 5000., 5000., 5000.,
dampcoef = 0.2, 0.2, 0.2, 0.2,
khdif = 0, 0, 0, 0,
kvdif = 0, 0, 0, 0,
non_hydrostatic = .true., .true., .true., .true.,
moist_adv_opt = 1, 1, 1, 1,
scalar_adv_opt = 1, 1, 1, 1,
/

&bdy_control
spec_bdy_width = 5,
spec_zone = 1,
relax_zone = 4,
specified = .true., .false.,.false.,.false.,
nested = .false., .true., .true.,.true.,
/

&grib2
/

&namelist_quilt
nio_tasks_per_group = 0,
nio_groups = 1,
/

Appendix C

GEOGRID.TBL

This appendix shows part of the file Geogrid.tbl in WPS. An extra smoothing is applied as the domains cover an area of complex topography such as the Alps. This is necessary as the CFL criterion is violated.

```
===============================================================
  name                   = HGT_M
  priority               = 1
  dest_type              = continuous
  smooth_option          = 1-2-1; smooth_passes=1
  fill_missing           = 0.
  interp_option          = gmted2010_30s:average_gcell(4.0)+four_pt+average_4pt
  interp_option          = gtopo_30s:average_gcell(4.0)+four_pt+average_4pt
  interp_option          = gtopo_2m:four_pt
  interp_option          = gtopo_5m:four_pt
  interp_option          = gtopo_10m:four_pt
  interp_option          = default:average_gcell(4.0)+four_pt+average_4pt
  rel_path               = gmted2010_30s:topo_gmted2010_30s/
  rel_path               = gtopo_30s:topo_30s/
  rel_path               = gtopo_2m:topo_2m/
  rel_path               = gtopo_5m:topo_5m/
  rel_path               = gtopo_10m:topo_10m/
  rel_path               = default:topo_gmted2010_30s/
===============================================================
```

Appendix D

METGRID.TBL

This appendix shows part of the file Metgrid.tbl in WPS. This file needs some changes as different land-sea masks are used for different variables. Ignoring these changes produces hotspots along the coast. Note the modifications in this file are set to the default options after the compilation process and they therefore need to be modified afterwards. Accordingly, the options related to SSTs are modified. The option interp_mas is changed to LANDMASK(1) and the interpolation option (interp_option) is modified as shown below.

```
===========================================================
 name            = SST
 interp_option   = sixteen_pt+four_pt+wt_average_4pt+wt_average_16pt+search
 fill_missing    = 0.
 missing_value   = -1.E30
 flag_in_output  = FLAG_SST
 masked          = land
 interp_mask     = LANDMASK(1)
===========================================================
```

Acknowledgements

I would like to thank ....

... **Prof. Dr. Christoph C. Raible** for giving me the opportunity to write this Ph.D. thesis in your group and the support I received during my thesis. I greatly appreciate the scientific discussions and your continuous support.

... **Prof. Dr. Jed O. Kaplan** and **Dr. Patrik Ludwig** for your pleasantly scientific contribution to the first study of this this. Moreover, I greatly thank **Dr. Martina Messmer** for your valuable contribution in the three studies of this thesis. I highly appreciate the scientific discussions and your support during the first years of my Ph.D. Particularly, I thank you for the helpful advices and the motivating conversations that kept me engaged during crucial moments.

... **Prof. Dr. Joaquim Pinto** for the external review of the thesis.

... **the administrative staff** for the support in any administrative concern. Particularly, I thank **Doris Rätz** for your sympathy and for always having your door open at anytime.

... **Woon Mi Kim** for your sympathy and continuous support as a colleague and a friend. I enormously appreciate the time you dedicated to our lunchtime during the lockdown.

... **Dr. Bernhard Mani** for your love, constant encouragement and enormous patience. I immensely appreciate our scientific discussions and support at home. You showed me that the life outside the university can very positively impact the academic path.

... **my Chilean family** for your faith in me. I greatly thank **my mother** for your support, motivation and many advices that have strongly guided my personal evolution.

... **my family in Germany** for your always warm welcome and continuous encouragement. Since we met in December 2003 for the first time, you have positively impacted my life.

... **my Swiss family** for your motivation and constant interest in my work. I fully appreciate the opportunity of being part of your family. You make me feel at home every time.

Publications

Russo E., Buzan J., Lienert S., Jouvet G., **Velasquez, P.**, Davis B., Ludwig P., Joos F. and Raible, C. C.: High resolution reconstruction of LGM climate over1the Alpine region using WRF. In preparation.

Velasquez, P., Messmer, M., and Raible, C. C.: The role of ice-sheet topography in the alpine hydro-climate at glacial times, 1–34. In review for *Climate of the Past* (preprint), doi:10.5194/cp-2021-67, 2021.

Velasquez, P., Kaplan, J. O., Messmer, M., Ludwig, P., and Raible, C. C.: The role of land cover in the climate of glacial Europe. *Climate of the Past* , 17, 1161–1180, doi:10.5194/cp-17-1161-2021, 2021.

Laj, P., ... (many co-authors) ... , **Velasquez, P.**, et al.: A global analysis of climate-relevant aerosol properties retrieved from the network of Global Atmosphere Watch (GAW) near-surface observatories. *Atmospheric Measurement Techniques*, 13(8), 4353–4392, doi:10.5194/amt-13-4353-2020, 2020.

Velasquez, P., Messmer, M. and Raible, C. C.: A new bias-correction method for precipitation over complex terrain suitable for different climate states: a case study using WRF (version 3.8.1). *Geoscientific Model Development*, 13(10), 5007–5027, doi:10.5194/gmd-13-5007-2020, 2020.

Collaud Coen, M., ... (many co-authors) ..., **Velasquez, P.**, and Ruffieux, D.: Identification of topographic features influencing aerosol observations at high altitude stations. *Atmospheric Chemistry and Physics*, 18(16), 12289–12313, doi:10.5194/acp-18-12289-2018, 2018.

Fischer, H., ... (many co-authors) ..., **Velasquez, P.**, et al.: Palaeoclimate constraints on the impact of 2°C anthropogenic warming and beyond. *Nature Geoscience*, 11(7), 474–485, doi:10.1038/s41561-018-0146-0, 2018.

Anet, J. G., Steinbacher, M., Gallardo, L., **Velásquez Álvarez, P. A.**, Emmenegger, L. and Buchmann, B.: Surface ozone in the Southern Hemisphere: 20 years of data from a site with a unique setting in El Tololo, Chile. *Atmospheric Chemistry and Physics*, 17(10), 6477–6492, doi:10.5194/acp-17-6477-2017, 2017.

Gallardo, L., HenrÍquez, A., Thompson, A. M., Rondanelli, R., Carrasco, J., Orfanoz-Cheuquelaf, A. and **Velásquez, P.**: The first twenty years (1994–2014) of ozone soundings from Rapa Nui (27°S, 109°W, 51 m a.s.l.). *Tellus B: Chemical and Physical Meteorology*, 68(1), 29484, doi:10.3402/tellusb.v68.29484, 2016.

Erklärung

gemäss Art. 28 Abs. 2 RSL 05

Name/Vorname:	Velásquez Álvarez / Patricio Andrés
Matrikelnummer:	16-131-252
Studiengang:	Climate Sciences
	Bachelor ☐ Master ☐ Dissertation ☒
Titel der Arbeit:	Regional Climate Modelling over Europe at Glacial Times
Leiter der Arbeit:	Prof. Dr. Christoph C. Raible

Ich erkläre hiermit, dass ich diese Arbeit selbständig verfasst und keine anderen als die angegebenen Quellen benutzt habe. Alle Stellen, die wörtlich oder sinngemäss aus Quellen entnommen wurden, habe ich als solche gekennzeichnet. Mir ist bekannt, dass andernfalls der Senat gemäss Artikel 36 Absatz 1 Buchstabe o des Gesetzes vom 5. September 1996 über die Universität zum Entzug des auf Grund dieser Arbeit verliehenen Titels berechtigt ist.
Ich gewähre hiermit Einsicht in diese Arbeit.

Bern, 23. August 2021